KWARTALNIK
ELEKTRONIKI I TELEKOMUNIKACJI

ELECTRONICS AND
TELECOMMUNICATIONS

QUARTERLY

Ark. wyd. 16,56	Ark. druk. 13,25	Podpisano do druku w listopadzie 2004 r.
Papier offset. kl. III 80 g. B-1		Druk ukończono w listopadzie 2004 r.

Szanowni Autorzy

„Kwartalnik Elektroniki i Telekomunikacji" — Electronics and Telecommunications Quartery jest kontynuatorem tradycji powstałego 50 lat temu kwartalnika p.t. „Rozprawy Elektrotechniczne".

Kwartalnik jest czasopismem Komitetu Elektroniki i Telekomunikacji Polskij Akademii Nauk. Wydawany jest przez Warszawską Drukarnię Naukową PAN. Kwartalnik jest czasopismem naukowym, na którego łamach są publikowane artykuły i komunikaty prezentujące wyniki oryginalnych prac teoretycznych i doświadczalnych, a także przeglądowych. Związane są one z szeroko rozumianymi dziedzinami współczesnej elektroniki, telekomunikacji, mikroelektroniki, oproelektroniki, radiotechniki i elektroniki medycznej.

Autorami publikacji są wybitni naukowcy, znani specjaliści o wieloletnim doświadczeniu, a także młodzi badacze — głównie doktoranci.

Artykuły charakteryzują się oryginalnym ujęciem zagadnienia, interesującymi wynikami badań, krytyczną oceną teorii lub metod, omówieniem aktualnego stanu, lub postępu danej gałęzi techniki oraz omówieniem perspektyw rozwojowych. Sposób pisania matematycznej części artykułów zgodny jest z wytycznymi IEC (International Electronics Commision) oraz ISO (International Organization of Standarization).

Wszystkie publikowane w Kwartalniku artykuły są recenzowane przez znanych krajowych specjalistów, co zapewnia że publikacje te są uznawane jako autorski dorobek naukowy. Opublikowane w kwartalniku wyników prac naukowych zrealizowanych w ramach „GRANTów" Komitetu Badań Naukowych spełnia więc jeden z wymogów stawianych tym pracom.

Czasopismo dociera do wszystkich zajmujących się elektroniką i telekomunikacją krajowych ośrodków naukowych oraz technicznych, a także szeregu instytucji zagranicznych. Jest ponadto prenumerowane przez liczne grono specjalistów i biblioteki.

Każdy Autor otrzymuje bezpłatnie 20 egzemplarzy nadbitek swojego artykułu, co ułatwia przesłanie go do indywidualnych wybranych przez Autora osób i instytucji w kraju lub za granicą. Ułatwia to dodatkowo fakt, że w Kwartalniku są publikowane artykuły w języku angielskim.

Nadesłane do redakcji artykuły są publikowane w terminie około pół roku, w przypadku sprawnej współpracy Autora z Redakcją. Wytyczne dla Autorów dotyczące formy publikacji są zamieszczone w zeszytach Kwartalnika, można je także otrzymać w siedzibie Redakcji.

Artykuły można dostarczać osobiście, lub pocztą pod adresem zamieszczanym na stronie redakcyjnej w każdym zeszycie.

Redakcja

CONTENTS

Fore

T
to th
muni
is wi
Expre
histor

I
the s
techn
crowa
expan
comn
foreig
been
Polish
of Ele
resear
nolog
has b
radar
micro
imme
centre
and li
for the
claw (
event

T
cepted
those
of the
were
and L
Nethe
the U
MIKC
stream
wirele
10 ses
metho

Foreword

The special issue of *the Electronics and Telecommunications Quarterly* is devoted to the **15th International Conference on Microwaves, Radar and Wireless Communications MIKON'04**, which was held on 17–19 May 2004 in Warsaw. The event is widely considered one of the highest ranking microwave conference in Europe. Expressing my gratitude towards the Editorial Board, I would like to present a brief history of the Conference as well as a short summary on this year's MIKON.

In the course of MIKON's 35-years long history, this year conference was already the sixth truly international meeting. It started in 1969 as a microwave solid state technology conference MECS and in 1983 it was transformed and renamed into a microwave conference. All over the years, MIKON has been continuously modified and expanded. The first nine conferences were national assemblies of the Polish microwave community, organized every two or three years with only a limited number of invited foreign guests. In 1994 MIKON received the international status. Since then it has been organised biannually in May under the auspices of two parent institutions: the Polish Academy of Sciences, being the original one, and the new one – the Institute of Electrical and Electronics Engineers, and is hosted by various Polish cities - biggest research and culture centres. Due to the fact that telecommunications and radar technology are the principal driving forces behind microwave research, recently MIKON has been transformed once again, into an international conference on microwaves, radar and wireless communications. Nowadays, MIKON assembles the whole Polish microwave and radiolocation community as well as numerous representatives of our immediate neighbours. It is also privileged to host the leaders of other foreign research centres collaborating with Poland as well as scientists of Polish origin, now working and living abroad. Almost 140 papers were accepted for the MIKON-1994 as well as for the MIKON-1996. Each of the following three conferences in Krakow (1998), Wroclaw (2000) and Gdansk (2002) featured about 190 papers, making MIKON a leading event in Central and Eastern Europe.

This year MIKON moved to Warsaw, with the record number of 234 papers accepted for presentation: 105 from Poland and, what we highly appreciate, 129 of those come from abroad, from 31 countries. These figures are certainly indicative of the enhanced international dimension of MIKON. The majority of foreign papers were submitted by the neighbouring countries – Russia, Ukraine, Germany, Sweden and Lithuania as well as other European countries including France, Italy and the Netherlands. From overseas, the largest number of papers came from Australia and the USA. Out of the accepted papers, 137 were oral and 97 poster presentations. The MIKON-2004 program comprised 36 sessions in total: 30 oral ones, held in 3 parallel streams, and 3 interactive forums. The number of contributions from the area of wireless communications and antennas has been constantly increasing, and this year 10 sessions were organized on these subjects. Traditional MIKON topics such as CAD methods, measurement techniques, active and passive components were also very well

covered. Although millimetre technology, integrated circuits and optoelectronics have attracted less interest in regular papers, they were well represented by invited speakers. This year's MIKON constituted the kernel of the Microwave and Radar Week-2004 in Poland, which was comprised, besides MIKON, of the following events: the *5th International Radar Symposium, the 17th International Conference on Electromagnetic Fields and Materials and the East-West Workshop on Advanced Techniques in Electromagnetics.* A total number of 506 participants from 40 countries attended the whole Week, for which 374 papers were presented.

The Polish microwave and radar community felt privileged to have many distinguished guests among the Conference participants. We took the chance of listening to welcome addresses given by Prof. Michał Kleiber, Minister of Scientific Research and Information Technology, IEEE MTT 2004 President, Prof. Robert Trew and Prof. Władysław Włosiński of the Polish Academy of Sciences.

This special issue comprises 14 papers — 4 ones chosen from those presented by invited speakers as well as 11 papers selected and expanded from among regular papers. The majority of these papers is devoted to new technologies and components for wireless communications and radar systems. A few papers concern advanced CAD methods and modelling, planar antennas, low-noise systems and microwave photonics. It is my hope that this volume addresses issues of interest to the Readers and will prove relevant in terms of practical application.

Józef Modelski
Guest Editor

Welcome Address by Professor Michał Kleiber, Minister of Scientific Research and Information Technology, given at the Conference Opening Session

Ladies and Gentlemen, Dear Guests

I'd like to extend my warmest welcome to all gathered in this venue. First of all, I'd like to thank the Organisers for inviting me to this Conference and at the same time congratulate on the jubilee, which the 15-th meeting at MIKON Conference makes.

Dear Colloquies,

Topics, which you'll discuss at this conference, constitute in today's world a very important discipline of science as well as touch many aspects of everyday living.

Modern communication systems are designed according to the basic laws governing relations between electric charges and magnetic poles. Certain of these relations were already discovered in the seventeenth, while others in the eighteenth and nineteenth centuries. Without these laws, electric, electronic and computer engineering as well as microwave technology and radiolocation in the form we know it and experience it today, would not have come into existence. Pioneer work by Maxell and experiments by Hertz built fundaments and gave a significant impulse for the creation of high frequency technology. Microwave technology, which right from the start of its engineering history embodied electromagnetism, in the beginning stages of its development was identified with military technology of radiolocation. Even though radiolocation, whose beginnings fell in the years prior to the outbreak of the Second World War, remain in the direct symbiosis with the technology of very high frequencies, it is really a specific discipline applying the theory of electromagnetic waves. Due to enormous superiority in radiolocation, military operations in the forties proceeded according to the plot advantageous to the Allied forces. Although, significance of radiolocation technology for military needs should not be overvalued, we cannot underestimate it. This technology has come broadly into all disciplines of human activity, associated alike with military sector as well as civil sectors where remote locating, tracking, piloting or identifying objects as well as exchanging data are required.

Additionally to these applications, the theory of electromagnetic field led to the creation of possibilities of using the energy of electromagnetic waves in the processes reacting with organic and non-organic matter.

Thermal processes, the result of interaction between electromagnetic waves and matter, are nowadays used on industrial scale in agricultural and food processing (cooking, baking, defrosting, drying, sterilisation), wood processing (drying of wood, cartoons, paper), chemical processing (vulcanisation, polymerisation) and pharmaceutical industry (speeding up of granular processes) and also in direct medical therapy, particularly in the fight against cancer.

Right from the start of its existence, "the world of high frequencies" dressed in technical frame has made and still makes significant marks on the technical civilisation of our times and the generations to come. We believe that the technology of microwaves together with other technologies will be an effective tool in forecasting and preventing global threats.

Please, allow me to express my opinion that this gathering in Warsaw is an important step in strengthening our community, encouraging exchange of information, scientific experiments and research in the field of topics discussed at this conference.

Wishing you effective proceedings, I'd like to start our conference. Thank you for your attention.

N

with

devic

powe

of hi,

solid

vacu

vices

for b

plied

area

F

Wide Bandgap Transistor Amplifiers for Improved Performance Microwave Power and Radar Applications

(Invited Paper)

R.J. TREW

Abstract — The generation of high RF output power, on the order of 100's to 1000's of watts necessary for transmitters for radars and wireless communications systems, remains a difficult challenge for semiconductor devices. RF power devices fabricated from standard semiconductors such as Si and GaAs are limited in the RF output capability by the inherent breakdown voltage of the semiconductor material. Recently, the development of wide bandgap semiconductors, such as SiC and GaN and related heterostructures, offers the potential to fabricate transistors with an order of magnitude improved RF output power compared to traditional devices. The wide bandgap semiconductor transistors offer the potential to fabricate high power transmitters for radars and communications systems, thereby permitting full semiconductor realization of advanced systems. However, the wide bandgap semiconductor devices currently suffer from several physical effects that are limiting the RF performance, and thereby, their application. These limitations are discussed and solutions presented.

1. INTRODUCTION

Many microwave radars and communications transmitters require active devices with RF output power capability on the order of kW to MW. Although semiconductor devices can be used to generate kW level RF output power, it is necessary to use power-combining and/or phased array techniques. Many other systems require the use of high power RF sources with RF performance capability beyond that available from solid state devices. High power transmitters currently require the use of microwave vacuum tube devices. The vacuum tube sources are required since semiconductor devices are limited in the dc voltage that can be applied by the inherent critical field for breakdown that the semiconductor can sustain. Since limited dc voltage can be applied, high RF power operation requires large dc and RF currents, which require large area devices. High current operation is inefficient due to series losses, and large area

ECE Department, North Carolina State University, Raleigh, NC, USA

504   R.J. TREW   *Kwart. Elektr. i Telekom.*

TOM

devices have inherently high capacitance and low impedance, which limit operating frequency.

Recently, the development of wide bandgap semiconductor materials, such as SiC and GaN-based composites, particularly the AlGaN/GaN heterostructure, offer the potential to fabricate RF active devices with significantly improved output power performance. The improved RF output power is possible due to much improved critical field for breakdown in the wide bandgap semiconductors. Both SiC and GaN have breakdown fields greater than $E_c > 10^6$ V/cm, compared to comparable fields of slightly over $E_c > 10^5$ V/cm in standard semiconductors such as Si and GaAs. The increase in critical field results in the ability to sustain a much increased bias voltage, and this, in turn, permits much improved RF output power to be developed. In fact, RF output power an order of magnitude higher than for standard devices has been demonstrated [1]. Field-Effect Transistors fabricated from SiC and the AlGaN/GaN heterostructure demonstrate the ability to produce RF output power on the order of 100's of watts, and these devices can be easily combined to fabricate kW level and higher transmitters.

However, the wide bandgap semiconductor devices are currently limited in performance due to several physical effects associated with material-related and design-related issues. Solutions to these problems are emerging, and these devices will soon find practical application.

2. RF PERFORMANCE

The current state-of-the-art of microwave solid state devices and microwave tubes is shown in Fig. 1 [1], and the RF output power capability of commercially available GaAs field-effect transistors is shown in Fig. 2. As indicated, semiconductor transistors produce RF power levels less than about 100 W at S-band frequencies and below, and the RF output power degrades with increasing frequency. The RF output power capability of GaAs field-effect transistors approaches 50 W at S-band and at Ka band is limited to about 1 watt. The GaAs FET's are limited in RF output power capability primarily by the gate-drain breakdown voltage, which generally limits the drain bias voltage that can be applied to the order of $V_{ds} = 10 - 12v$.

Semiconductor devices fabricated from wide bandgap semiconductor devices offer significantly improved RF performance capability. For example, the predicted RF performance for class A amplifiers fabricated using SiC MESFET's are shown in Fig. 3 [1]. For these amplifiers the transistor is biased with a drain voltage of $V_{ds} = 40v$, which is possible since the gate-drain breakdown voltage for these devices is about $V_{bgd} = 100v$.

The SiC field-effect transistor can produce RF output power density of 4-6 W/mm of gate periphery, and a single device can produce RF output power greater than 50 W [2], and recent results demonstrate RF output power on the order of $P_o = 80 - 100$ W at C-band frequencies with near-ideal power-added efficiency. RF performance
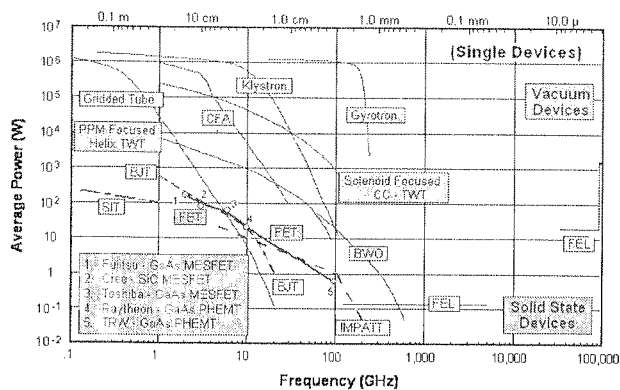
Fig

Fig. 3.

Fig. 1. Power-Frequency Performance of Microwave Tubes and Solid State Devices
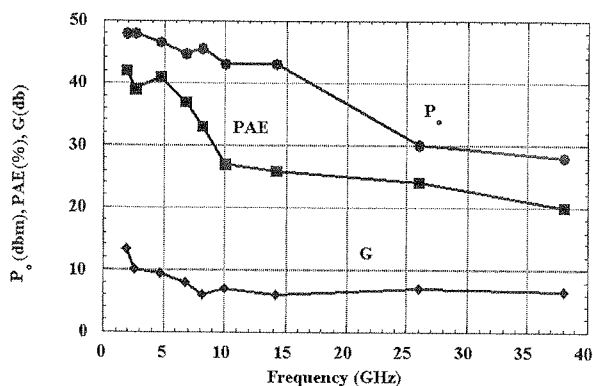

Fig. 2. Power-Frequency Performance of Commercially Available GaAs Field-Effect Transistors
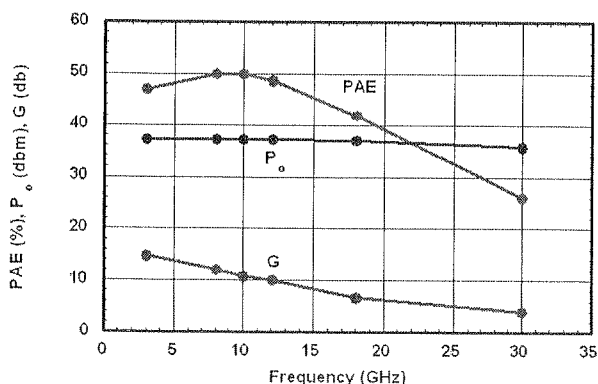

Fig. 3. Predicted Power-Frequency Performance of SiC MESFET's for a Device with 1 mm Gate Width

degrades at higher frequencies due to relatively high series losses, and it will be difficult to obtain good RF power performance above X-band due to a decrease in the gain that can be obtained.

The predicted RF output power capability of AlGaN/GaN HFET's is shown in Fig. 4. These devices are capable of RF output power density on the order of 10-12 W/mm of gate periphery when biased at $V_{ds} = 40v$, and recent results have demonstrated RF output power density greater than 20 W/mm when biased at $V_{ds} = 80-90v$. Bias voltages of this magnitude are possible by use of field-plate technology [3]. The field-plate consists of a layer of metal that is placed over the gate, extending into the gate/drain region. This plate produces a suppression of the gate leakage current that normally occurs under high voltage conditions. The suppression of the gate leakage current produces an increase in gate/drain breakdown voltage since high drain bias can be applied before significant gate leakage occurs.
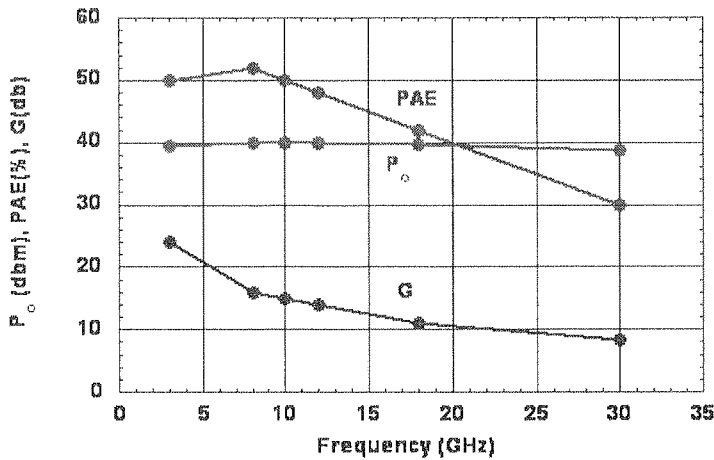
Fig. 4. Predicted Power-Frequency Performance of AlGaN/GaN HFET's
for a Device with 1 mm Gate Width

SiC MESFET's are rapidly approaching commercial applications. However, the AlGaN/GaN HFET's are currently limited in RF performance by a series of physical effects that prevent reliable operation from being achieved on a consistent basis. The main problem is caused by gate leakage current caused by thermally assisted tunneling of electrons from the gate metal to the surface of the semiconductor [4] where they introduce RF performance limitations through electrostatic interaction of the surface and conducting channel electrons. A variety of design techniques are being developed to control these effects. Approaches include the use of field-plates and other approaches intended to isolate the surface from the device channel.

3. PHYSICAL LIMITATIONS IN NITRIDE-BASED HFET'S

Although the nitride-based HFET's have been demonstrated, both theoretically and experimentally, to be capable of producing RF output power and performance an order of magnitude superior to standard semiconductor devices, the nitride-based HFET devices currently produce inconsistent RF performance. While spot experimental data indicate RF performance approaching theoretical predictions, these results are not consistently obtained, and RF performance varies from device-to-device and from run-to-run. The greatest variation in performance occurs under large-signal RF conditions associated with high RF power operation. The devices experience a series of physical phenomena that affect and limit RF performance.

The most significant limitations to obtaining optimum RF performance occur under the extremes of the RF voltage-current swing. For example, the ideal RF voltage-current behavior for an AlGaN/GaN HFET operating under ideal conditions is shown in Fig. 5, which shows predictions from a physics-based large-signal device/circuit simulator.
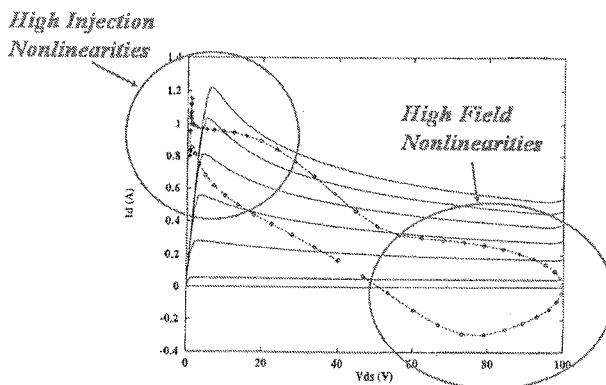
Fig. 5. dc and RF Current-Voltage Characteristics for an AlGaN/GaN HFET Class A Amplifier under Optimum Power-Added Efficiency at 10 GHz (Vds=40 v)

The device has a gate length of $L_g = 0.5\mu m$ and a gate width of $W = 1$ mm. The device was biased with a drain bias of $V_{ds} = 40$ v, and tuned for optimum power-added efficiency under class A conditions at a frequency of $f = 10$ GHz. Under these conditions the device produces RF output power of $P_o = 10$ W (i.e., RF output power density of 10 W/mm). The simulation includes thermal effects and the decrease in the I-V characteristics at high drain current and increasing drain bias are due to thermal degradation. The dynamic i-v load line is observed to optimally make use of the allowed i-v operating region, thereby producing maximized RF output power and power-added efficiency. The dynamic RF voltage extends from essentially zero drain voltage to 100 v, where RF breakdown begins to occur. The RF current extends from maximum channel current conditions (under forward biased gate voltage) to about a negative value of 0.4 A. The negative RF current is permitted due to the capacitive

reactance of the device. That is, conduction current is not permitted to go negative since this would indicate a reversal in direction, which is not permitted by the device bias conditions. However, the RF current is permitted to reverse direction due to the device capacitance, which results from charge storage in the device. The charge storage maintains the terminal current to satisfy Kirchoff's Law, thereby permitting RF current direction reversal.

Fig. 6 shows the real-time RF voltage and current waveforms that correspond to the RF cycle for the dynamic load line shown in Fig. 5.
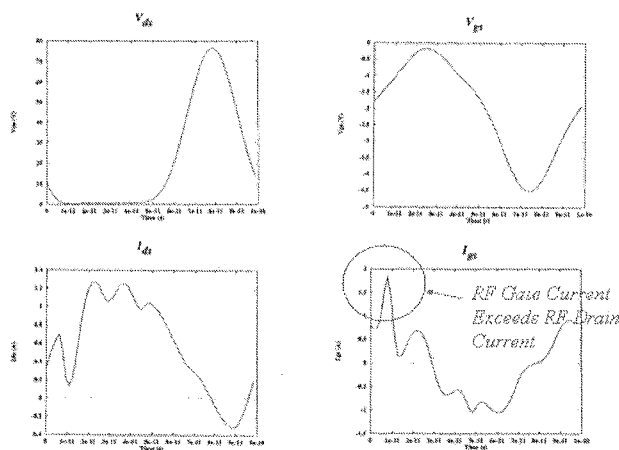
Fig. 6. Real-Time RF Voltage and Current Waveforms for Optimum Power-Added Efficiency Tuning Conditions for a Class A AlGaN/GaN Amplifier

In Fig. 6 the RF drain voltage and current are shown on the left and the RF gate voltage and current are shown on the right. The waveforms for the RF drain and current indicate the high frequency switch characteristic of RF performance. That is, the RF voltage and current are essentially 180 degrees out-of-phase at the output of the device across the load impedance, with the voltage low when the current is high, and vice versa. This represents near-ideal operation. The high frequency variation in the RF current is due to the introduction of higher order harmonics when the RF voltage is clipped during the low voltage portion of the RF cycle. The RF waveforms on the gate electrode indicate the input to the device. The RF voltage and current are only slightly out-of-phase, indicating a low magnitude capacitive input to the device. The degree to which the RF voltage and current are out-of-phase varies directly with the input drive level, with increasing drive levels producing lower input impedance and increased phase shifts between the voltage and current. Again, the high frequency variations in the RF gate current are due to the introduction of harmonics resulting from waveform clipping. As indicated in Fig. 6, the RF gate current achieves very large magnitude during the high injection portion of the RF cycle. In fact, the RF gate current during this portion of the RF cycle is larger than the RF drain current,

indicating an f_T (i.e., current drive) less than unity. This would, of course, introduce a drive-dependent limitation to obtaining good RF performance.

The dynamic RF load-line and voltage-current waveforms shown in Figs. 5 and 6 represent ideal operating conditions, and do not necessarily indicate practical and realistic operation. The simulation permitted full development of the dynamic RF voltage and current and did not include several physical effects that have been found to affect the extent to which the RF voltage-current can develop, and thereby limit, device RF performance. In particular, the behavior of the dynamic voltage and current at the extremes of the RF cycle need to be examined in more detail. As indicated in Fig. 5 nonlinear effects are introduced under extremes of the RF cycle. Under low voltage/high current conditions nonlinearities associated with high charge injection conditions are introduced, and under high voltage/low current conditions nonlinearities associated with high gate leakage and surface trapping phenomena are introduced. These nonlinearities account for the most significant of the RF performance limiting effects observed in experimental devices.

It should be noted that these nonlinear effects also exist in field-effect transistors fabricated from conventional semiconductors such as GaAs. However, the ramifications of the nonlinear effects are amplified for nitride-based devices by the significantly higher current densities and electric fields associated with the operation of the wide bandgap transistors. Current densities in the nitride-based devices can easily exceed $J \sim 10^6$ A/cm^2, whereas in GaAs MESFET's the current density seldom exceeds $J \sim 10^5$ A/cm^2. Also GaAs transistors generally can sustain a drain voltage in the range of $V_{ds} = 10 - 12$ v, and internal electric fields are limited to the order of $E \sim 10^5$ V/cm or less. The bulk avalanche breakdown field for GaAs is about $E_c \sim 5 \times 10^5$ V/cm. However, the bulk breakdown electric field for SiC and GaN is almost an order of magnitude higher and over 10^6 V/cm, and the SiC and nitride-based HFETs can easily sustain drain bias voltages in the range of $V_{ds} = 40 - 50$ v. Suppression of the electric field at the gate permits drain voltages on the order of $V_{ds} = 80 - 90$ v to be applied, and drain bias voltages of $V_{ds} = 120$ v have been reported. Indeed, the high RF output power capability of the wide bandgap semiconductor FETs stems directly from the ability to operate at high current and high bias voltage.

The high current injection and high electric field nonlinearities are associated with physical phenomena within the device that affect the ability of electrons to freely move in response to applied electric fields. The RF performance of the device is especially sensitive to the behavior of electronic charge in certain areas of the device structure, as indicated in Fig. 7 for an AlGaN/GaN HFET. In particular, the gate/source region, the channel region under the drain edge of the gate electrode, and the surface region near the drain side of the gate are areas of concern. The GaN/buffer interface can also introduce deep traps that can cause current anomalies, particularly under high gate and drain bias conditions. These interface problems are strongly related to material growth conditions and can be minimized by improved material quality. Generally, these interface effects are less significant than those associated with the other areas.

As indicated, the two most significant effects limiting the RF performance of the AlGaN/GaN HFET's occur due to high current injection conditions through the source contact during the high current portion of the RF cycle, and charge leakage from the gate metal to the surface of the semiconductor during the field voltage portion of the RF cycle. It has been demonstrated that the high current injection in the
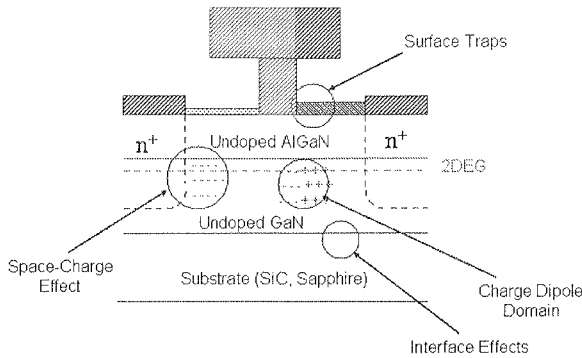
Fig. 7. AlGaN/GaN HFET Structure and Sources of Operational Nonlinearities
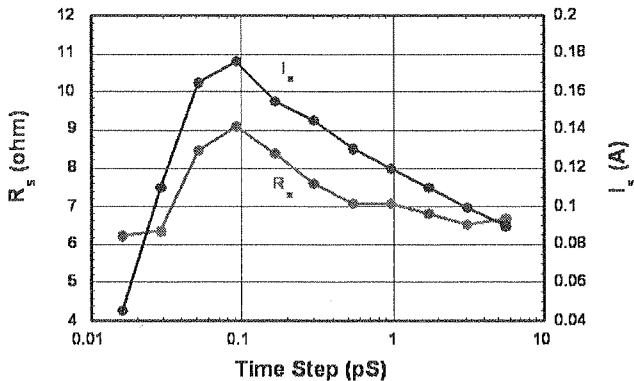
Fig. 8. HFET Source Resistance Modulation Due to High Current Injection Conditions (Vds=8 v)

source region produces an increase in source resistance due to space-charge limited current phenomenon [1, 5]. The current density in the AlGaN/GaN HFET's under high current conditions can exceed the critical magnitude to achieve space-charge limited conditions, thereby producing a significant increase in source region resistance. The source resistance is modulated by the channel current, as shown in Fig. 8 [1].

During the high current portion of the RF cycle the source resistance can increase to a significant extent, thereby introducing an undesirable nonlinear source region resistance, as shown in the equivalent circuit model in Fig. 9.
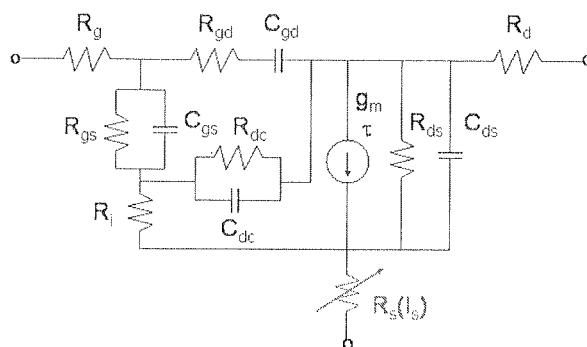
Fig. 9. AlGaN/GaN HFET Equivalent Circuit with a Nonlinear Modulated Source Resistance Under High Current Injection Conditions

This effect can be minimized, or eliminated, by tuning the circuit so that the dynamic load line does not enter into the high current, low voltage portion of the i-v characteristic, as shown in Fig. 5. This requires use of high impedance circuits with a resistive load line. Also, the source/gate region of the transistor can be intentionally doped to produce an increase in threshold current for the on-set of space-charge effects. Each order of magnitude increase in impurity doping produces an order of magnitude increase in the threshold for the on-set of space-charge resistance.
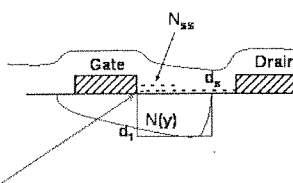
During the high voltage, low current portion of the RF cycle, the electric field at the edge of the gate metal on the drain side obtains a very high magnitude, and on the order of $E\sim 10^6$ V/cm or greater. Under these conditions it has been shown that electrons transfer from the gate metal to the surface of the semiconductor by a thermally assisted tunnel mechanism [4]. This phenomenon creates a „virtual gate" where the physical length of the gate appears to increase with increasing RF drive level. The performance of the device thereby degrades, producing a premature saturation in amplifier performance. This mechanism has been investigated in detail for GaAs-based MESFET's and HEMT's and a comprehensive model developed [6, 7]. The effect is illustrated in Fig. 10 [7], along with the mathematical formulation for the magnitude of the electric field at the gate edge.

The phenomenon can be modeled with introduction of an additional current generator between he gate and drain electrodes, as shown in Fig. 11 [7].

The influence of gate/drain breakdown upon the RF performance of field-effect transistor amplifiers has previously been described [7, 8]. It has been observed that there can be a significant difference between dc and RF breakdown, and the breakdown voltage, as observed in dc I-V characteristics, is not necessarily the voltage that determines the gate/drain breakdown characteristics. In order to increase RF output power it is necessary to decrease the leakage current resulting from the tunneling of electrons from the gate metal to the surface of the semiconductor. This can be accomplished by decreasing the magnitude of the electric field at the gate edge. The use of field plate

$$E_g = \frac{q}{\varepsilon f_G L_g} \left[d_s \int_0^{d_1} N_D(y)\,dy - \int_0^{d_s} N_{ss}(x)\,dx \right] \qquad n_t = \frac{J_t(E_g)}{q v_s}$$

$$I_t = f_G L_g W_g J_t(E_g) = I_{tf} - I_{tr}$$

Fig. 10. Gate Thermally Assisted Tunnel Leakage Model Formulation for Virtual Gate Effect
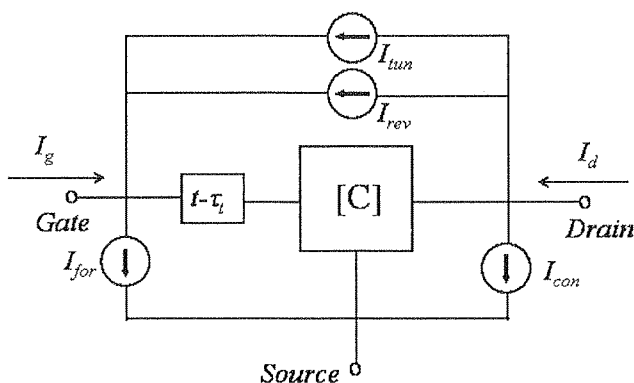
Fig. 11. Large-Signal Equivalent circuit Model Including Gate Tunnel Leakage Current Effect

technology has long been recognized as a useful technique for suppression of voltage at critical locations within a semiconductor device [9-12]. The concept has recently been revisited for use in AlGaN/GaN HFET's with excellent success [3]. Basically, the field plate consists of an additional metal layer located over the gate metal and extending into the region between the gate and drain. The gate metal provides an electric field termination layer that reduces the magnitude of the electric field at the gate edge, thereby suppressing the gate leakage current. The use of field-plate technology permits high drain bias voltages to be applied, thereby producing improvements in RF output power. In fact, the degree of gate leakage suppression is sufficient to permit drain bias on the order of $V_{ds} = 100-120$ v to be applied. High RF output power results. However, the field-plates also introduce additional capacitance and reduce the transconductance of the transistor. Therefore, a degradation in frequency performance results. For this reason, a minimum field-plate length should be employed.

4. SUMMARY

Field-Effect Transistors fabricated from the wide bandgap semiconductors SiC and GaN have the capability to produce RF output power an order of magnitude greater than devices fabricated from traditional materials, such as Si and GaAs. Amplifiers fabricated using SiC FET's have produced RF output power in the range of 80-100 w at C-band and the nitride-based HFET's have produced RF output power density greater than 20 W/mm. Amplifiers fabricated using these devices will produce greater than 100 w RF and will operate to beyond Ka-band. These devices will find use as amplifiers for communication and radar transmitters.

5. ACKNOWLEDGEMENT

6. REFERENCES

1. R . J . T r e w, "SiC and GaN Transistors: Is There One Winner for Microwave Power Applications?" *Proc. IEEE, Special Issue on Wide Bandgap Semiconductors*, vol. 90, pp. 1032-1047, June 2002.
2. R . A . S a d l e r, S . T . A l l e n, T . S . A l c o r n, W . L . P r i b b l e, J . S u m a k-e r i s, and J . W . P a l m o u r, "SiC MESFET with Output Power of 50 Watts CW at S-Band", 1998 Device Research Conference Digest, pp. 92-93.
3. S . K a r m a l k a r and U . K . M i s h r a, "Enhancement of Breakdown Voltage in AlGaN/GaN High Electron Mobility Transistors Using a Field Plate", IEEE Trans. Electron Dev., Vol. 48, pp. 1515-1521, Aug. 2001.
4. R . J . T r e w and U . K . M i s h r a, "Gate Breakdown in MESFETs and HEMTs", *IEEE Electron Dev. Lett.*, vol. 12, pp. 524-526, Oct. 1991.
5. R . J . T r e w, (Invited) "AlGaN/GaN HFET Amplifier Performance and Limitations", *2002 IEEE International Microwave Symposium Digest, Seattle*, WA, pp. 1811-1814.
6. T . A . W i n s l o w, R . J . T r e w, and A . S . M o r r i s, "An Improved Gate Breakdown Model for Studying High Efficiency MESFET Operation", *Proc. of the IEEE/Cornell University Conference on Advanced Concepts in High Speed Semiconductor Devices and Circuits*, Ithaca, NY, Aug. 2-4, 1993, pp. 401-410.
7. T . A . W i n s l o w and R . J . T r e w, "Principles of Large-Signal MESFET Operation", *IEEE Trans. Microwave Theory Tech.*, vol. 42., pp. 935-942, June 1994.
8. T . A . W i n s l o w, D . F a n, and R . J . T r e w, "Gate-Drain Breakdown Effects Upon the Large Signal RF Performance of GaAs MESFETs", *1990 IEEE MTT-S International Microwave Symposium Digest*, pp. 315-317.
9. F . C o n t i and M . C o n t i, „Surface breakdown in silicon planar diodes equipped with a field plate", *Solid State Electron.*, vol. 15, pp. 93-105, Jan. 1972.
10. M . C h a n g, G . P i f e r, H . Y i l m a z, and E . W i l d i, "Lateral HV-IC with 1200 V bipolar and FET devices", *IEEE Trans. Electron Devices*, vol. 33, pp. 1992-2001, 1986.

11. Y. H o r i, M. K u z u h a r a, Y. A n d o, and M. M i z u t a, "Analysis of electric field distribution in GaAs metal-semiconductor field effect transistor with a field-modulating plate", *J. Appl. Phys.*, vol. 87, pp. 3483-3487, Apr. 2000.

12. C. B. G o u d and K. N. B h a t, "Two-dimensional analysis and design considerations of high-voltage planar junctions equipped with field plate and guard ring", *IEEE Trans. Electron Devices*, vol. 38, pp. 1497-1504, June 1991.

CMOS MMICs for microwave and millimeter wave applications

(Invited Paper)

M. FERNDAHL[1], H. ZIRATH[1,2], B. M. MOTLAGH[1], A. MASUD[1],
I. ANGELOV[1], H.-O. VICKES[3], S. GEVORGIAN[1,2], F. INGVARSSON[1]

Abstract — Recent results on MMICs based on a 90-nm CMOS process are presented. Linear and nonlinear models were developed for the transistors based on S-parameters, noise parameters, and power spectrum measurements. Based on em-simulations, models for multilayer capacitances, MIM-capacitances, various transmission lines etc were also developed. Amplifiers, frequency mixers, and frequency multipliers were then designed, fabricated and characterized. Amplifiers with a gain of 6 and 3.5 dB per stage at 20 and 40 GHz respectively, were demonstrated as well as frequency multipliers from 20 to 40 GHz with 15.8 dB conversion loss, and 30 to 60 GHz multipliers with 15.3 dB conversion loss. Resistive mixers at 20, 40, and 60 GHz were also demonstrated with promising results.

Index Terms - MMIC, CMOS, 90-nm, microwave, millimeter wave

1. INTRODUCTION

MILLIMETER-WAVE wireless communication systems have attracted interest for data communication up to frequencies of 60 GHz, due to the higher available band width and the related increased information capacity. In particular 60 GHz systems are interesting due to its high information capacity, 1 Gbps and small co-channel interference. So far, most system demonstrators are designed with GaAs MMICs [1-2]. Due to the possible lower cost of silicon, and feasibility of backend integration, silicon CMOS is an interesting alternative as the technology has achieved impressive improvement of the high frequency performance due to downscaling of feature dimensions [10-13]. The aim of this work is to demonstrate that it is possible to realize circuits for wireless

[1] *Chalmers University of Technology, Department of Microtechnology and Nanoscience, Microwave Electronics LaboSE - 412 96 Göteborg, Sweden*
[2] *Ericsson AB, Microwave and Speed Electonics Center, SE - 431 84 Mölndal, Sweden*
[3] *Ericsson Microwave System, SE - 431 84 Mölndal, Sweden*

communication such as amplifiers, frequency multipliers and mixers up to millimeter wave frequencies.

2. TECHNOLOGY

The technology used in this work is 90-nm gate length CMOS from IMEC, Belgium, with a 5 metal layer copper damascene backend process. The silicon substrate resistivity is 20 Ohm.cm.

3. ACTIVE DEVICES

On-wafer measurements on CMOS devices revealed a de embedded f_{max} of 100 GHz and an ft of 130 GHz. This transistor has a gate width of 40 μm, the sub cell width is 2 μm. In Fig 1, Masons gain calculated from measured S-parameters is plotted as a function of frequency. In addition, deembedded performance is also shown. This figure indicates that the transistor can be practically in amplifier designs up to about half of f_{max} i e 40 GHz. Noise parameters were also measured by using an ATN NP5 noise parameter system. F_{min} versus frequency is plotted in Fig 2. This data was used for building a noise model based on Pospieszalski's mod-
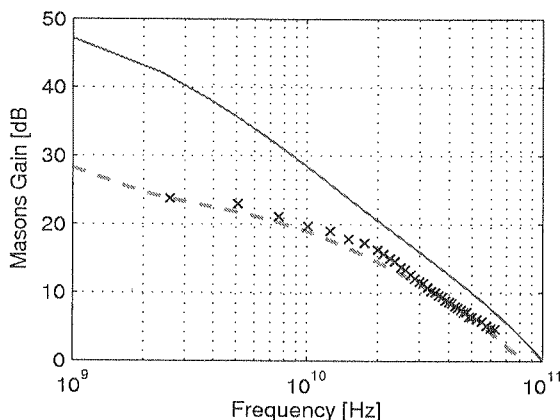
Fig. 1. MASON. Mason's gain[dB]. Measured (Bl crosses) and model (Green, dashed). Solid line shows deembedded performance

el. Deembedded noise data is also shown in Fig. 2. At 25 GHz, F_{min} is approximately 3 dB which is acceptable for many commercial applications. As a comparison, a GaAs PHEMT technology would give an F_{min} of approximately 1 dB. Due to the thin gate oxide of the CMOS-transistors, there will be some gate current due to quantum mechanical tunnelling which will increase F_{min} at lower frequencies.

Fig. 2. FMIN. F_{min} [dB]. Measured (crosses) and model (dashed). De-embedded performance (solid)

A. Large signal CMOS model

When designing highly non-linear microwave circuits like mixers and frequency multipliers, an accurate and converging transistor model is of key importance. The model used in the circuit design of the mixers and frequency multipliers have been developed in-house and is quite simple with a limited number of parameters, accurate, well converging and easy to extract. The modeling approach we used is from a microwave-engineering point of view, i.e. a set of empirical continuous model equations is used. This approach has been very successful for compact modeling of III-V high frequency transistors and we have showed that this approach is also viable for CMOS transistors.

Fig. 3. Equivalent circuit of the transistor

We have previously successfully modeled MESFETs and HEMTs using a non-linear FET model [3]. However, the specifics of the CMOSFET require a quite complicated model structure, see Fig. 3, and some changes and additions to the model were required.

An example is the addition of a bulk terminal together with related components in order to include the bulk effect at very high frequencies. Furthermore, a symmetric description of the drain current is employed for accurate modeling of the transistor behavior for both positive and negative V_{ds}. This is important for devices operating at low drain voltages as well as switches and resistive mixer applications. To obtain this in a proper manner, both V_{gs} and V_{gd} control the current source, respectively:

$$I_{ds} = I_{dsp} - I_{dsn} ; \tag{1}$$

$$I_{dsp} = I_{pk}(1 + \tanh(\psi_p)(1 + \tanh(\alpha_p V_{ds})) \cdot (1 + \lambda_p V_{ds} + \lambda_{1p} \exp(V_{ds}/V_{kn}) - 1). \tag{2}$$

$$I_{dsn} = I_{pk}(1 + \tanh(\psi_n)(1 + \tanh(\alpha_n V_{ds})) \cdot (1 + \lambda_n V_{ds} + \lambda_{1n} \exp(V_{ds}/V_{kn}) - 1). \tag{3}$$

where $\psi_{p,n}$ are power series functions centered at V_{pk}

$$\psi_p = P_1(V_{gs} - V_{pk}) + P_2(V_{gs} - V_{pk})^2 + P_3(V_{gs} - V_{pk})^3. \tag{4}$$

$$\psi_n = P_1(V_{gd} - V_{pk}) + P_2(V_{gd} - V_{pk})^2 + P_3(V_{gd} - V_{pk})^3. \tag{5}$$

Typically 3 terms of the power series are enough to produce a model accuracy of 2-5%. V_{pk} and I_{pk} are the gate voltage and the drain current at which the maximum of the transconductance occurs, $\alpha_{p,n}$ are the saturation parameters, and the λ parameters account for channel length modulation. Some parameters, like V_{pk} and $P_{1,2,3,...}$ exhibit V_{ds} dependence and this was accounted in a similar way as in [Chalmers model extension]. Fig. 4 shows the good fit between measured and modeled DC-current.
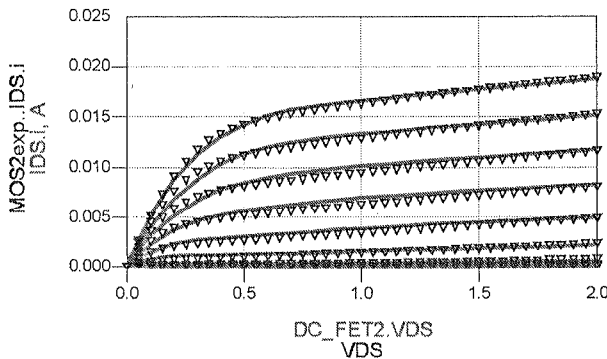

Fig. 4. Measured (triangles) and simulated (solid) drain current

The model uses a capacitance implementation rather than charge so that the resulting small-signal equivalent circuit consists of the capacitance value at the corresponding DC-voltage. In this way the small and large signal capacitances are consistent and

no trans-capacitances are needed. The capacitances were modeled with the following equations.

$$C_{gs} = C_{gsp} + C_{gs0}(1 + V_{gs} + P_{10}/(P_{11} + (V_{gs} - P_{10})^2)^{0.5})(1 + \tanh[P_{20} + P_{21}V_{ds}]);$$

$$C_{gd} = C_{gdp} + C_{gd0}(1 + V_{gd} + P_{40}/(P_{41} + (V_{gd} - P_{40})^2)^{0.5})(1 + \tanh[P_{30} + P_{31}V_{ds}])$$

The problem with a capacitance approach is that the derivatives must be continuous in order for the harmonic balance simulator to converge. This has, as can be seen from the equations above, been taken care of.

The model shows good agreement with measured S-parameters, see Fig. 5 a, b.
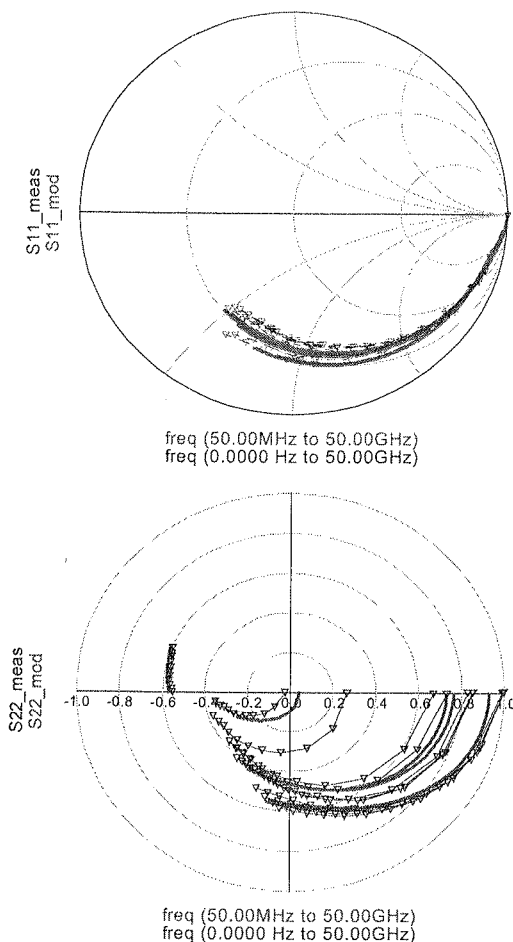

freq (50.00MHz to 50.00GHz)
freq (0.0000 Hz to 50.00GHz)

freq (50.00MHz to 50.00GHz)
freq (0.0000 Hz to 50.00GHz)

Fig. 5a . Measured (blue w. markers) and simulated S_{11} and S_{22} parameters up to 50 GHz for different bias-conditions
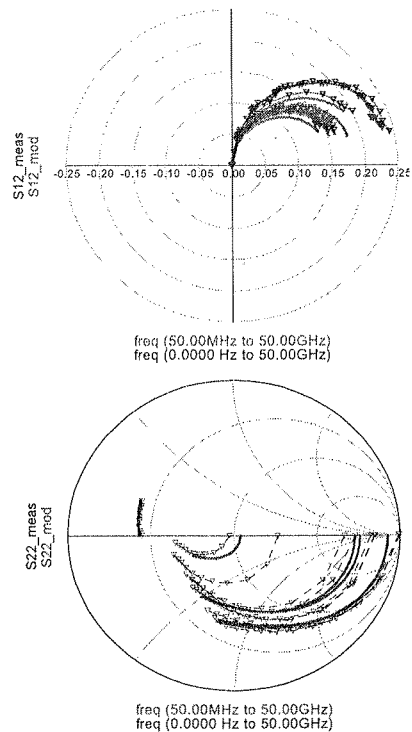
Fig. 5b . Measured (blue w. markers) and simulated S_{12} and S_{21} parameters up to 50 GHz
for different bias conditions

The harmonic generation was evaluated using power spectrum measurements, see Fig. 6, a very good agreement between measurements and simulations is observed.
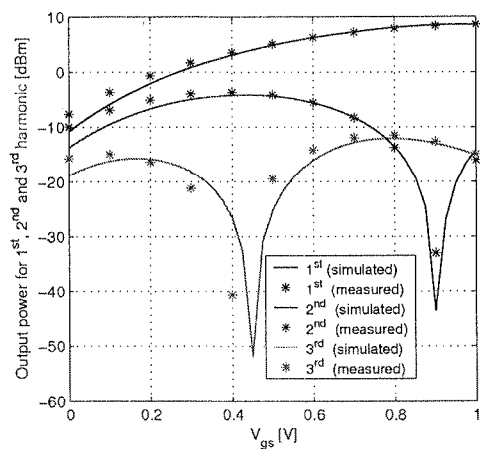

Fig. 6. Measured (*) and simulated (-) power spectrum at 1 GHz input frequency

4. PASSIVE STRUCTURES

A. Characterization of Silicon dioxide

The large difference in the published dielectric constant and loss tangent of the Silicon-dioxide ([4]-[8]) indicates that its dielectric properties are process dependent. In order to properly model the lines, it is necessary to evaluate the substrate parameters i.e. the dielectric constant and loss tangent of the Silicon-dioxide. In this paper we used a simple method originally proposed by Ma et al [9]. Special test structures have been designed and fabricated for microwave characterization of Silicon dioxide according to this method. The cross sectional and top views of the structures are shown in Fig. 7.
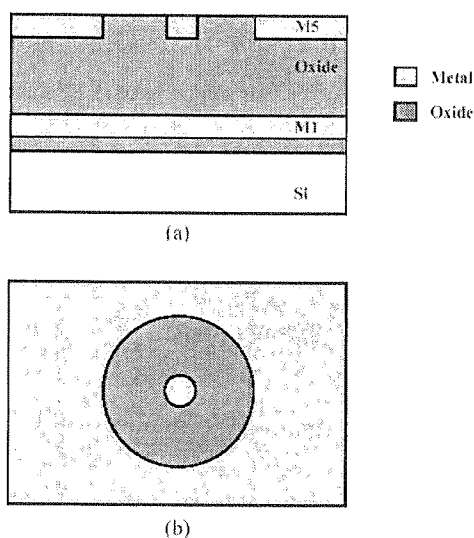
(a)

Metal

Oxide

(b)

Fig. 7. (a) Cross sectional view (b) top view of the teststructures for cahracterization of Silicon dioxide

Using this method the loss tangent, $\tan\delta$, of the Silicondioxide is measured to be 0.07. It is also worth mentioning that using a method of trial and error Six et al [6] have come to this same conclusion, i.e. 0.07.

B. Transmission Line

The transmission lines were realized using the top metal (metal 5) as signal and the bottom metal (metal 1) as ground thus utilizing SiO_2 as dielectric. Because of the chemical mechanical polishing procedure, a slotted ground plane using metal stripes had to be designed rather than a uniform metal plane, see Fig 8. HFSS was used in order to investigate the quality of such a ground plane in terms of a shield against

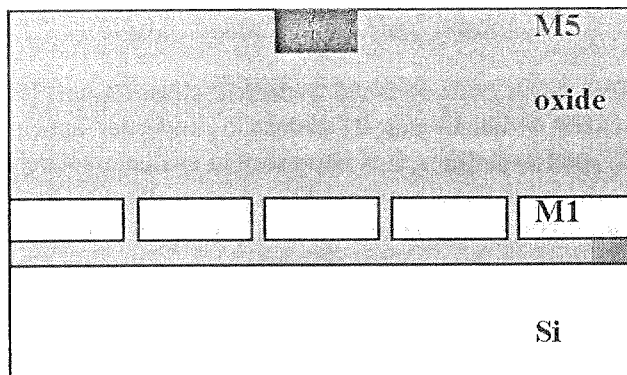the losses in the Silicon, and possible effects on the characteristic impedance and the losses of the line.

Fig. 8. Cross sectional view of the microstrip transmission line layout

Two 50 Ω-lines, one with uniform ground plane and one with a slotted ground plane were simulated. Following parameters were used in the simulations; for the silicon, $\varepsilon = 11.7$, $\rho = 20\Omega$ cm, 700μ m substrate thickness. For the oxide, $\varepsilon = 4.2$, $\tan \delta = 0.07$, the thickness is about 4.8 μm. Metal layers 1 and 5 are made of 0.65 μm thick Copper, Rs=35 mΩ/square. The width of the lines was chosen to be 8 μm to achieve a characteristic impedance of 50 Ω. The results of the simulations are shown in Fig. 9.
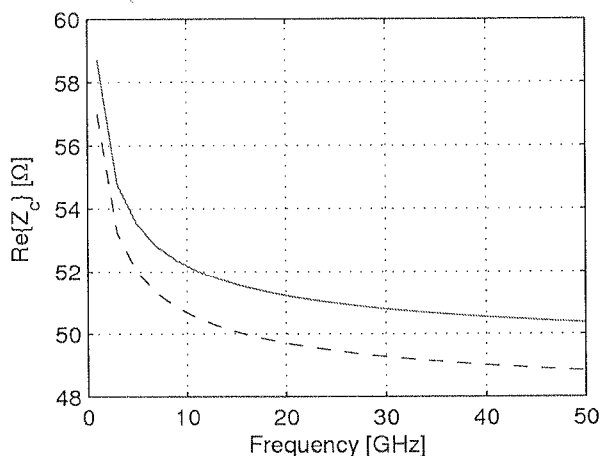
Fig. 9. Simulated characteristic impedance Z_c with (–) uniform and slotted (-) ground plane

In order to be able to fully characterize the lines, both S-parameter-measurements and DC-measurements were performed on 1, 2 and 4 mm long lines.
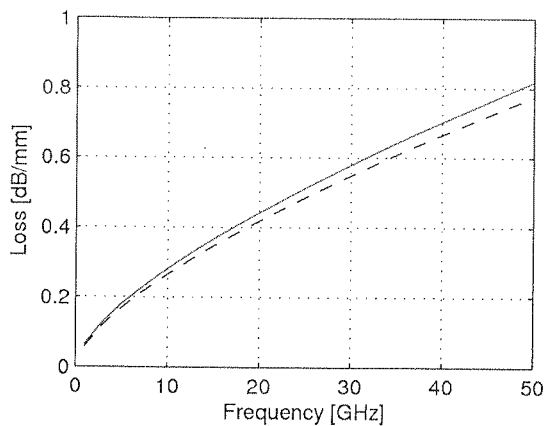
Fig. 10. Simulated losses with (--) uniform and slotted (-) ground plane

S-parameter-measurements

Fig. 11 shows the measured vs. simulated reflection and insertion loss for the 1 mm long line. Good agreement between simulated and measured result is observed.
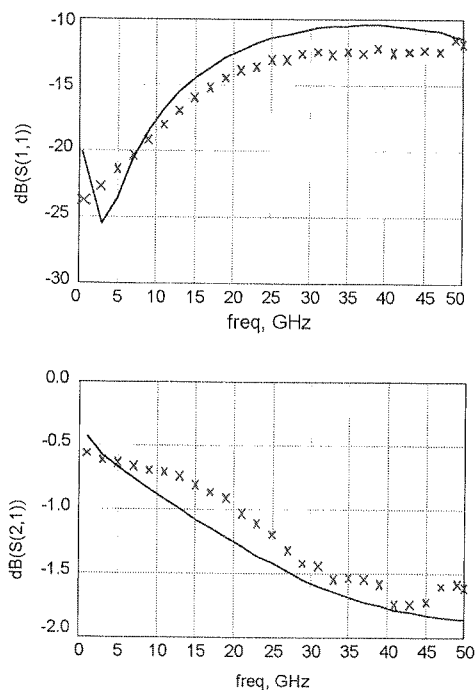
Fig. 11. Simulated (-) and measured (cross) S_{11} and S_{21} of a 1 mm long line

DC-measurements

DC-measurements on 1, 2 and 4 mm long lines, revealed a 5.3 Ω/mm DC-resistance for the lines, which assuming a contact resistance of approximately 0.5 is consistent with the nominal sheet resistance of 35mΩ/square.

Theoretically the DC-losses, α, can be evaluated according to

$$\alpha = 20 \log(1 + R_{DC}/2Z_0) \tag{6}$$

From Fig. 11 we can estimate the dc-losses to be approximately 0.5 dB/mm. Using (6) we can now extract RDC to be 5.6 Ω/mm which is in agreement with DC-measurements.

MIM-capacitors

In the present process, the MIM-capacitors are placed in between metal layers M2 and M3 with no Copper wiring directly below the capacitor. The cross sectional view of this capacitor is shown in Fig. 12. The top and bottom electrodes are made of 500 Å thick TaN (Rs=50Ω/square) and the MIM-dielectric is 350 Å thick Silicon dioxide ($\varepsilon = 4.2$ and $\tan \delta = 0.07$). The ground plane is placed at the back side of the Silicon substrate.

(a)   (b)
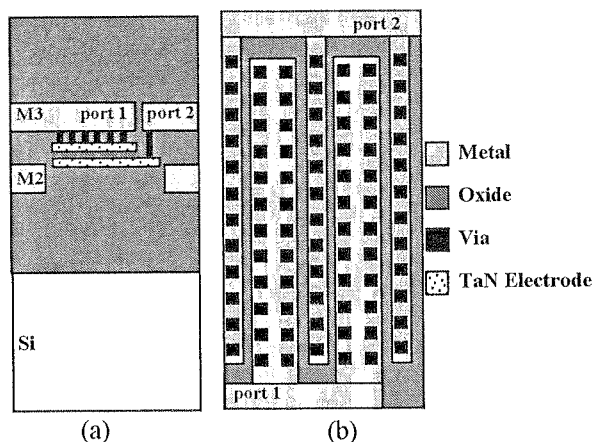
Fig. 12. (a) Cross sectional view of MIM-capacitor,
(b) top view of multi-finger MIM-capacitor

A capacitance of 1.2 fF /μm^2 is achieved with this structure. The main drawback of this structure is the high series resistance caused by the low conductivity of the electrodes. Due to this high series resistance the Q-factor of such a capacitor is rather low, typically around 10. One way to increase the Q-factor substantially is to design multi finger capacitors by connecting long narrow capacitors in parallel as shown in Fig. 12 b. The series resistance is then reduced and as a result the Q-factor is improved.

Ef
capaci
betwee
at the
layers
By co
increas

Fig. 13.

Fig
between

Multilayer capacitors

Efforts have been made to extract the equivalent circuit model of the MIM-capacitors using EM-simulation and finally using measurement results. Good agreement between simulation and measurement results at one side and measurement and model at the other side is observed as shown in Fig. 13. The idea is to make use of two metal layers as top and bottom electrodes utilizing the interlayer Silicon-dioxide as dielectric. By connecting several of these capacitors in parallel the capacitance per unit area is increased.
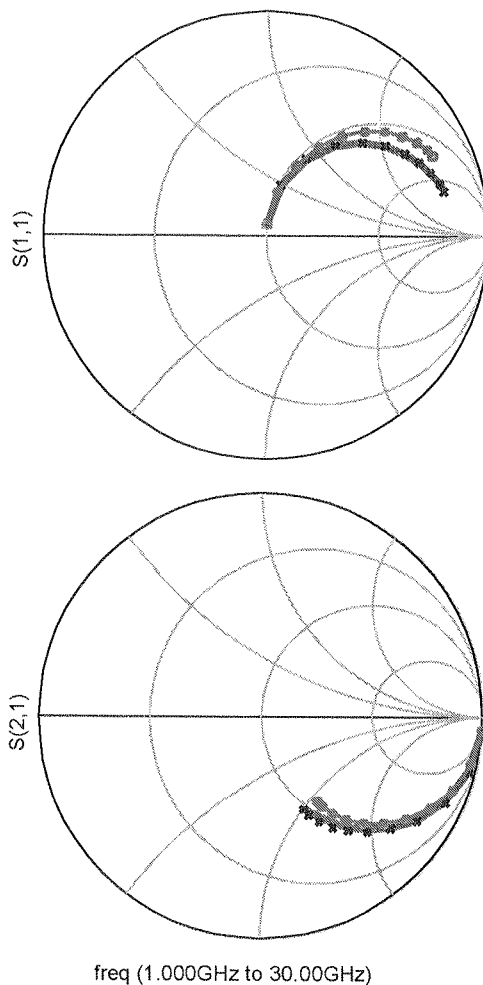
freq (1.000GHz to 30.00GHz)

Fig. 13. Simulated (circle), measured (cross) and modeled (-) S11 and S21 of a 0.1 pF MIM-capacitor

Fig. 14 shows an example of a multilayer capacitor structure using the capacitor between metal layers 3, 4 and 5. The top and bottom electrodes are made of Copper

(Rs= 35 mΩ/square) and by connecting the capacitors in parallel the series resistance is decreased thus increasing the Q-factor. However a larger area is needed to achieve the same capacitance as MIM-capacitor. The equivalent circuit models of these capacitors are also extracted using measurement results. A capacitance of 0.13 fF/μm^2 is achieved with this structure.
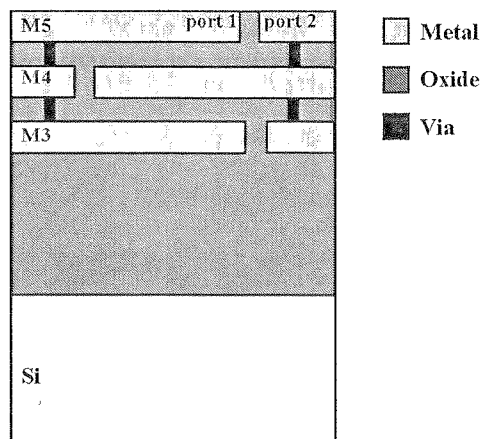

Fig. 14. Cross sectional view of Multilayer-capacitor

Fringing-Field-Enhanced[*]*capacitor*

A novel high-Q capacitor called Fringing-Field-Enhanced Capacitor (FFE-capacitor) is introduced. The idea is to take advantage of the fringing fields in between two adjacent vias. Fig. 15 (a) shows a simple parallel plate capacitor while Fig. 15 (b) shows the proposed design. Placing stacks of vias connected to two different plates within a close distance as shown in Fig. 15 (b) increases the capacitance between the two plates, thanks to the fringing fields between vias and connection pads. At the same time, since the vias are effectively connected in parallel, the series resistance decreases, increasing the Q-factor of the capacitor. The vias are placed within a matrix in the way that each via is surrounded by four other vias connected to the opposite plate as seen in Fig. 15 (c).

Full wave simulations by HFSS showed that a capacitance of 0.18 fF/μm^2 can be achieved with this structure. A 20 μm by 20 μm capacitor of this kind have a Q-factor of about 27 at 20 GHz. The distance between the vias and connection pads are of course decided by the design rules. In this particular process (like many others) the design rules for the layers M4 and M5 are different from the rules for the remaining three metal layers, excluding M5 from the structure allows for vias and pads to be

---

[*] Patent Pending

(a)

(b)

(c)
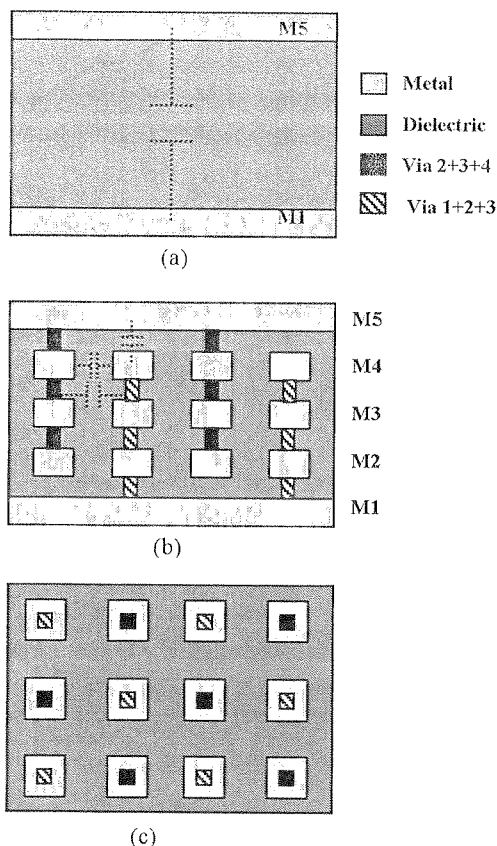
Fig. 15. (a)Cross sectional view of a simple parallel plate capacitor, (b) Cross sectional view of FFE-capacitor, (c) top view of FFE-capacitor

placed within a shorter distance hence adding to the capacitance of the structure. A capacitance of 0.47 fF/μm^2 is achieved with this structure. A 10μm by 10μm capacitor of this kind will have a Q-factor of about 34 at 20 GHz.

5. AMPLIFIERS

Several one and two-stage amplifiers were simulated at center frequencies 20, 40, and 60 GHz. The transistor model in this work is a lumped element small-signal transistor model based on S-parameter measurements from 1 GHz to 65 GHz. This model was also used as a two-temperature noise model by fitting noise parameter data from 2-26 GHz. High frequency fit is presented in Fig. 16. The equivalent circuit of the small signal model is presented in Fig. 17.
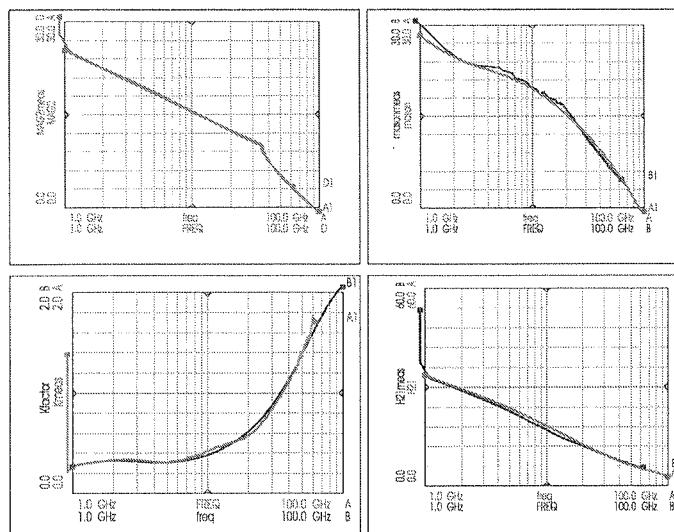
Fig. 16. Measurements to 62.5 GHz and simulation from small signal model. (a) Maximum available gain, (b) Stability factor, (c) Mason's unilatreral gain and (d) Current gain, h_{21}
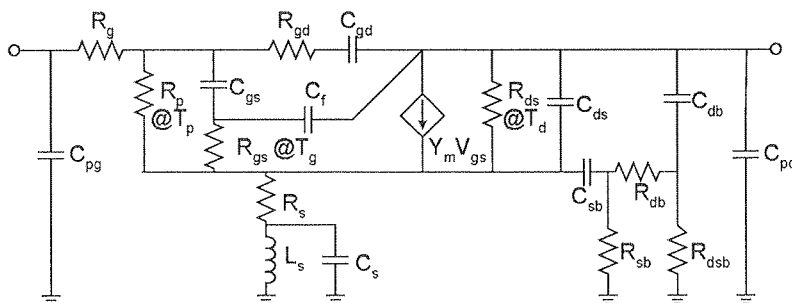
Fig. 17. Equivalent circuit of small signal model using an extended Pospieszalski noise model

20 GHz single stage small signal amplifier

The chosen topology is of single ended type with the input and output matched to 50Ω, see Fig. 18. Series transmission lines and shorted stubs are used in order to match the input and output. The design is optimized for maximum gain. Due to the use of distributed element in the matching network, the resulted transmission lines were rather lengthy. This made the circuits difficult to accommodate in the target area of 1.0 mm^2. For this reason, transmission lines are meandered with proper margin between the adjacent lines to minimize mutual coupling. A sensitivity analysis on all critical components in the amplifier showed that the q-value of the shorting capacitance at the end of the matching stubs were critical. Therefore, we use specially designed 5-layer multilayer capacitors with metal 1 ground.
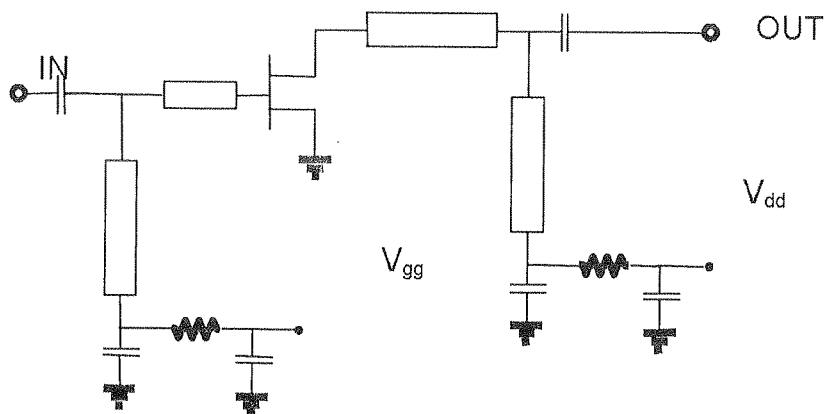
Fig. 18. Circuit schematic of the 20 GHz one-stage amplifier
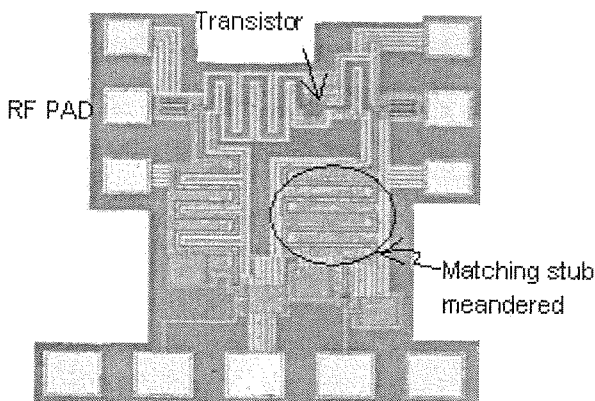
Fig. 19. Die photo of the 20 GHz amplifier

Simulation of the circuit has been done with HP ADS software. The circuit uses a drain voltage of 1.5 Volts with a gate bias of 0.65 volts. In Fig 20, simulated and measured S-parameters are plotted for the one-stage 20 GHz amplifier.

An Anritsu 37397 network analyzer was used for the S-parameter measurements. The measured maximum gain is approximately 6 dB, about 1 dB larger than predicted, and the gain peak is approximately 10% lower in frequency.

The circuit is well matched to 50 ohm at both the input and the output ports. S22 is very well predicted by the simulations, while the measured S11 dip is 10% lower in frequency. The noise figure of the amplifier was also studied. Figure 21 shows the measured and the simulated results. A value of 6.4 dB has been obtained from the measurement. This value is quite reasonable for a high frequency CMOS small signal amplifier, if not optimized for minimum noise.
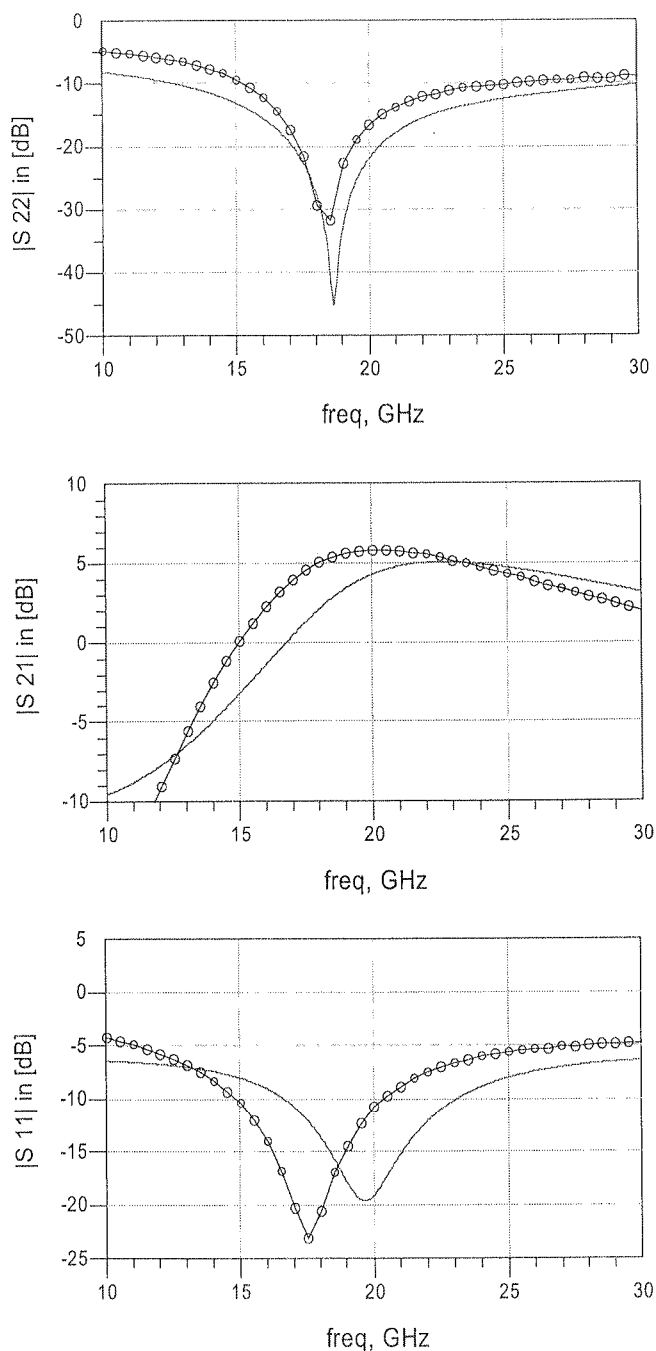
Fig. 20. Measured (circles) and modeled (solid) S-parameter responses of 20 GHz single stage amplifier. The device width is 40 μm

The

with pro

order to

circuit.

Bias

amplifier

stage am

figure. A

has been

line loss

maximum

figure of
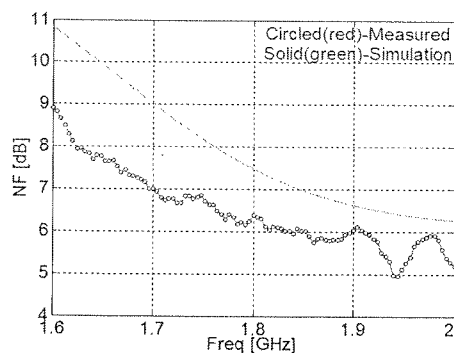
Fig. 21. Noise figure of the 20 GHz amplifier

Two-stage 40 GHz small signal amplifier

The basic circuit arrangement consists of cascading two single stage amplifiers with proper matching network. Like before, matching stubs have been meandered in order to reduce die chip area without affecting the microwave characteristics of the circuit.
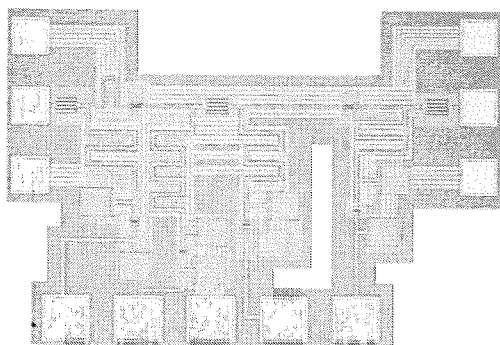
Fig. 22. Die photo of the 40 GHz two stage amplifier

Biasing of the circuit was done by the same bias voltage like the single stage amplifier but the DC power consumption is almost double the amount of the single stage amplifier. The S-parameter, output power has been measured and is shown in the figure. A very good match between the measurement and simulation for the $|S21|$ curve has been obtained, see Fig. 23. All the simulations have been carried out taking the line loss into account. At 40 GHz, a gain of 6.1 dB has been measured. The measured maximum gain occurs at around 35 GHz giving a value of 7.3 dB. The simulated noise figure of the circuit is 8.3 dB at 40 GHz.
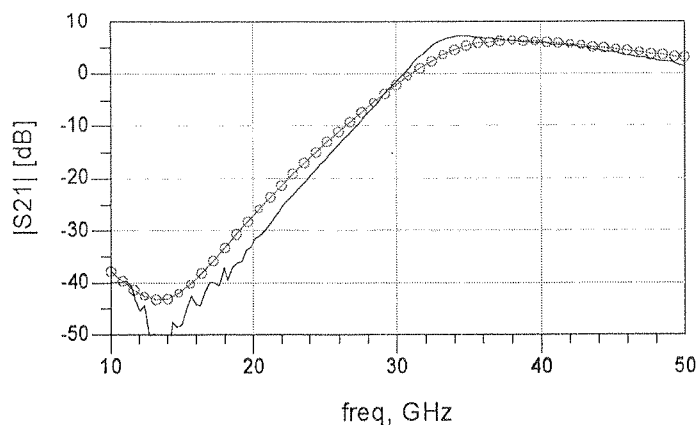
Fig. 23. Simulated (circles) and measured (solid) S-Parameter responses
of the 40GHz two stage amplifier

6. FREQUENCY MULTIPLIERS

Two frequency doublers have been realized, one 20 to 40 GHz and one 30 to 60 GHz. Both show about 15 dB conversion loss, see Section VI. B and C for details.

A. Topology

The frequency multipliers were realized as active multipliers similar to [14] with input matching network and an output filter to suppress fundamental and match the 2nd . See Fig. 24 for schematic and Fig. 25 for die photo.
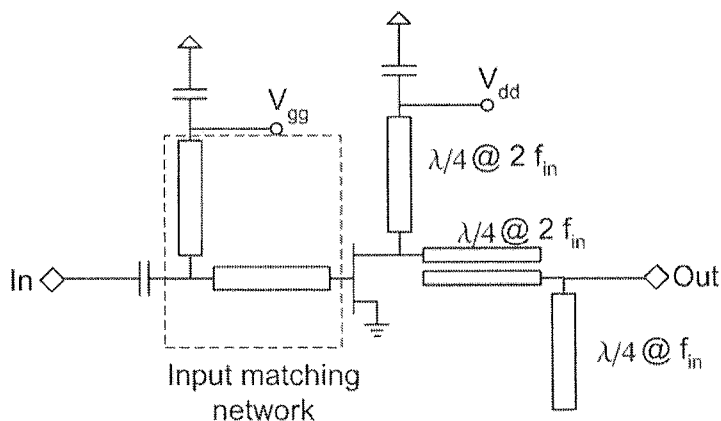
Fig. 24. Circuit diagram of the frequency doublers
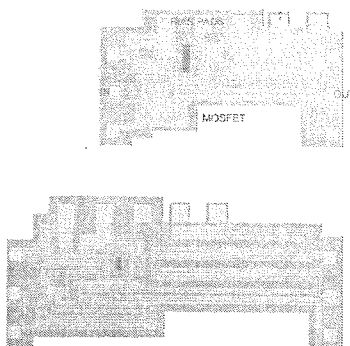
Fig. 25. Die photo of 30 to 60 (top) and 20 to 40 (bottom) GHz frequency doublers

B. 20 to 40 GHz: Measured and simulated results

At 20 GHz input frequency a minimum conversion loss of 15.8 dB was achieved at 3 dBm input power, see Fig. 26. The measured value is close to the simulated with only a shift in optimum input power from 0 dBm in simulation to 5 dBm in measurements. Better than 20 dB suppression of fundamental was achieved, some difference compared to simulations.

C. 20 to 40 GHz: Measured and simulated results

At 20 GHz input frequency a minimum conversion loss of 15.8 dB was achieved at 3 dBm input power, see Fig. 26. The measured value is close to the simulated with only a

Better than 20 dB suppression of fundamental was achieved, some difference compared to simulations. shift in optimum input power from 0 dBm in simulation to 5 dBm in measurements.
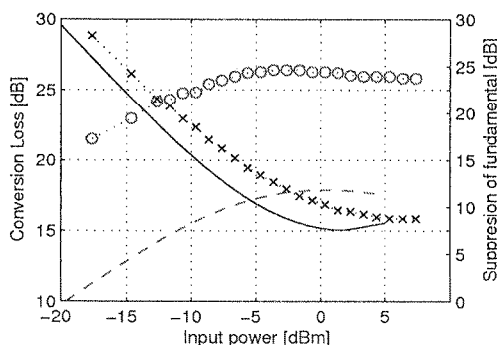
Fig. 26. Conversion loss: Measured (-x), simulated (-) and Suppression of fundamental harmonic: Measured (-o), simulated (--) vs input power at 20 GHz input frequency

D. 30 to 60 GHz: Measured and simulated results

With an input power of 3 dBm a conversion loss of 15.3 dB was achieved at 30 GHz input frequency. The measured conversion loss shows good agreement with simulation with 0.5 dB higher conversion loss than simulated and 3 dB shift in optimum input power. Suppression of fundamental better than 20 dB was also achieved, see Fig. 27.
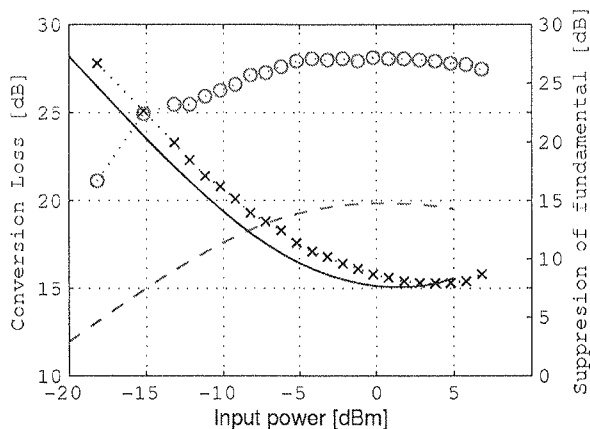
Fig. 27. Conversion loss: Measured (-x), simulated (-) and Suppression of fundamental harmonic: Measured (-o), simulated (–) vs input power at 20 GHz input frequency

7. MIXERS

Three resistive mixers with RF-frequencies of 20, 40 and 60 GHz have been designed. The conversion loss of these mixers is 8.5, 8.1 and 13.2 respectively.

Topology

The mixers were realized using according to passive single-ended topology, refs. [15-22] describe this and other mixer types. The schematic of the mixer is shown in Fig. 28.

The LO-signal is applied to the transistor gate while the RF-signal is applied to drain. The IF-signal is then extracted from the drain via a low pass filter.

The low pass filter at IF-output is needed to suppress the harmonics and the mixed products with frequencies higher than 5 GHz. This is a 4-section-lumped element filter with equi-ripple characteristics. The low IF-frequency make it more appropriate to use lumped elements in filter design. The large wavelength at lower frequencies would result in long lines if any kind of transmission line configurations were to
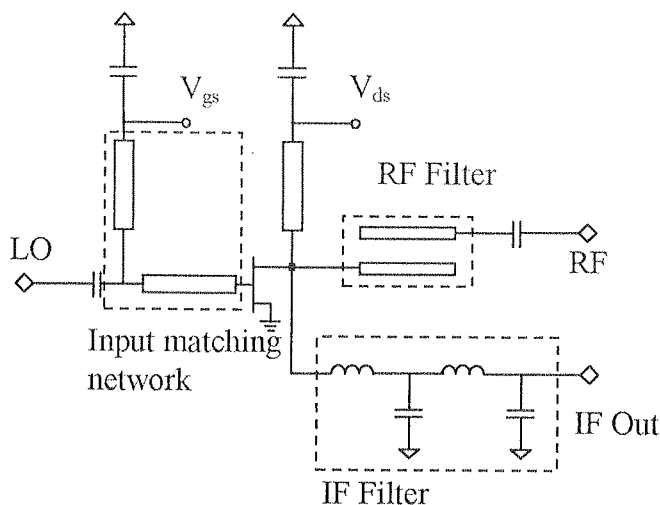
Fig. 28. Schematics of the mixers

be used. The long lines would apart from the large component sizes; contribute to increasing the total losses of the circuit and degrading the circuit performance considerably.

At the RF-input of the mixer a band pass filter has been placed. Since the cut off frequency of the IF-filter is at 5 GHz, the RF-filter will naturally have to have a band pass between 15-25 GHz for a LO-frequency of 20 GHz, 35-45 GHz for a LO-frequency of 40 GHz, 55-65 GHz for a LO-frequency of 60 GHz. Two-section-coupled line filters realised in microstrip line technology, a suitable filter configuration at higher frequencies, were designed for each of this frequencies. Also gate and drain matching networks consist of stubs realised in microstrip line technology.

Simulation Result

The result of the harmonic balance simulation on the mixers is summarized in Table 1.

Table 1

Simulation results for the mixers

Frequency	Conversion Loss	LO-IF isolation	LO-RF isolation
20 GHz	9.5 dB	> 44 dB	> 9 dB
40 GHz	7.5 dB	> 43.5 dB	> 5dB
60 GHz	10.6 dB	> 43.7 dB	> 2 dB

The conversion Loss and the LO-IF-isolation is very promising and show a performance comparable to GaAs-based circuits, while the LO-RF-isolation is very low. This is however normal for a single-ended mixer.

Measurement Results

Conversion loss measurements on the mixers were performed with 0.4 V DC-bias on the gate, the drain was grounded. An LO-power of 0 dB was applied to gate while the RF-power applied to drain was 0 dB.

First set of measurements on the mixers revealed problems with the RF-filter's high attenuation at the pass band. However since the break out of the filters were available the filter losses could be measured and omitted from the overall loss of the circuit. Doing this the Conversion loss of the mixers was within close agreement with the simulations.

Table 2 shows the summarized result of the measurements vs. simulation result.

Table 2

Simulation vs. measurements for mixers

Frequeny	Simulation	Measurement	Measurement -filter losses omitted
20 GHz	9.5 dB	19.5 dB	8.5 dB
40 GHz	7.5 dB	24.9 dB	8.1 dB
60 GHz	10.6 dB	28.5 dB	13.2 dB

Due to above mentioned problem with the RF-filter aside from conversion loss measurement no other measurement was performed and a full characterization of the mixers was not possible. Nevertheless, ignoring the additional losses presented by the filters, conversion losses of the mixers are within reasonable margins in agreement with the simulation results and are proof of the functionality of the mixers.

8. CONCLUSION

Recent result in both circuits and modeling for micro- and millimeter-wave in 90 nm CMOS is demonstrated. Amplifiers, frequency multipliers, and mixers were successfully demonstrated up to 60 GHz for some circuits. It is likely to be expected that the gain of the circuits etc will be further improved by improving the losses in passive circuits, and by increasing the gain in CMOS devices.

9. ACKNOWLEDGEMENT

10. REFERENCES

1. H. Z i r a t h, "Development of 60 GHz front end circuits for high data rate com munication systems in sweden and Europe", *2003 IEEE-GaAs IC, Gallium Arsenide Int. Circ. Symp.*, Dig., pp. 93-96, 2003.

2. Y. M i m i n o, *et al*, "A 60 GHz millimeter-wave MMIC chipset for broad band wireless access system font-end ", *IEEE MTT-S International Microwave Symposium Digest*, vol. 3, pp. 1721-1724, 2002.

3. I. A n g e l o v, L. B e n g t s s o n, M. G a r c i a, "Extensions of the Chalmers nonlinear HEMT and MESFET mode",*IEEE- MTT, Trans. on Microwave Theory and Tech.* Vol. 44, pp. 1664-7, Oct. 1996.

4. G. B a r t o l u c c i, F. G i a n n i n i, E. L i m i t i, a n d S. P. M a r s h, "MIM Capacitor Modeling: A Planar Approach", *IEEE Trans. Microwave Theory and Tech.*, vol. 43, no. 4, pp. 901-903, April 1995.

5. M. A r m a c o s t, A. A u g u s t i n, P. F e l s n e r, *et al*, "A High Reliability Metal Insulator Metal Capacitor for 0.18 μm Copper Technology" *Proc. IEEE Int Interconnect Technol. Conf.* 2001, pp. 113-115, 2001.

6. C. C. L i n, H. M. H s u, Y. H. C h e n, *et al*, "A Full Cu Damascene Metallization Process for Sub −0.18 μm RF CMOS SoC High Q Inductor and MIM Capacitor Application at 2.4 GHz and 5.3 GHz" *Proc. IEEE Int Interconnect Technol. Conf. 2001*, pp. 113-115, 2001.

7. C h e n Z h e n, G u o L i h u i, Y u M i n g b i a n a n d Z h a n g Y i, "A Study of MIMIM On-Chip Capacitors Using Cu/SiO2 Interconnect Technology" *IEEE Microwave and Wireless Components Letters*, vol. 12, no. 7, pp. 246-248, July 2002.

8. K a i S h a o, S a n f o r d C h u, K o k - W a i C h e w, *et al*, "A scaleable metal-insulator-metal capacitors process for 0.35 to 0.18 μm analog and RFCMOS" *Proc. IEEE. 6th International Conf Solid-State and Integrated-Circuit Technology. 2001*, vol. 1, pp. 243-246, 2001.

9. C. H. N g, K. W. C h e w, J. X. L i, *et al*, "Characterization and comparison of PECVD silicon nitride and silicon oxynitride dielectric for MIM capacitors", *IEEE Electron Device Lett.*, vol. 3, no. 9 pp. 529-531, September 2002.

10. X. G u a n, A. H a j i m i r i, "A 24-GHz CMOS Front-End", *IEEE-Journal of solid-state circ.* Vol. 39, no. 2, pp. 368-373, Feb. 2003.

11. S. H a c k l, J. B o c k, G. R i t z b e r g e r, M. W u r z e r, H. K n a p p, L. T r e i t i n g e r, A. L. S c h o l t z, "A 45 GHz SiGe active frequency multiplier", *2002 IEEE-ISSSC Int. Solid State Circuits Conf*, vol. 1, pp. 82-447, Feb 2002.

12. M. T i e b o u t, H.-D. W o h l m u t h, W. S i m b u r g e r, "A 1 V 51 GHz fully-integrated VCO in 0.12 um CMOS", *2002 IEEE-ISSCC Int. Solid State Circuits Conf.*, vol. 1, pp. 300-468, Feb. 2002.

13. H. W a n g, "A 50 GHz VCO in 0.25 um CMOS", *2001 IEEE-ISSCC Int. Solid State Circuits Conf.*, pp. 372-3, Feb. 2001.

a per-
ry low.

DC-bias
e while

-filter's
rs were
s of the
nt with

result.

Table 2

ion loss
n of the
d by the
reement

wave in
rs were
xpected
osses in

14. C. Fager, L. Landen, H. Zirath, "High output power, broadband 28-56 GHz MMIC frequency doubler", *2000 IEEE-MTT-S Int. Microwave Symp*, Dig, vol. 3, pp. 1589-1591, June 2000.

15. V. Geffroy, *et al*, "RF mixers using standard digital CMOS 0.35 μm process", *IEEE MTT-S International Microwave Symposium Digest*, vol. 1, pp. 83-86, 2001.

16. P. Gould, *et al*, "A CMOS resistive ring mixer MMICs for GSM 900 and DCS 1800 base station applications", *IEEE MTT-S International Microwave Symposium Digest*, vol. 1, pp. 521-524, 2000.

17. J. J. Kucera, *et al*, "A zero DC-power low distortion mixer for wireless applications", *IEEE Microwave Guided Wave Lett.*, vol. 9, pp. 157-159, Apr 1999.

18. L. Verweyen, *et al*, "LMDS up- and down-converter MMIC2", *IEEE MTT-S International Microwave Symposium Digest*, pp. 1685-1688, Boston, MA, June 2000.

19. B. M. Frank, *et al*, "A novel common gate mixer for wireless applications", *IEEE transactions on Microwave Theory and Techniques*, vol. 50, pp. 1433-1435, May 2002.

20. F. Ellinger, *et al*, "Compact monolithic integrated resistive mixers with low distortion for HIPER-LAN", *IEEE transactions on Microwave Theory and Techniques*, vol. 50, pp. 178-180, Jan 2002.

21. L. M. Devlin, *et al*, "A monolithic 2 to 18 GHz Upconverter", *IEEE MTT-S International Microwave Symposium Digest*, vol. 1, pp. 257-261, 2002.

22. K. Andersson, *et al*, "Resistive SiC-MESFET mixer", *IEEE Microwave and Wireless Components Lett.*, vol. 12, pp. 119-121, Apr 2002.

A SiGe Bipolar WCDMA Power Amplifier with 52% PAE at 3.3 V

K. KITLINSKI, G. DONIG, W. BAKALSKI, B. KAPFELSPERGER, R. WEIGEL

Abstract — A monolithic radio frequency power amplifier for WCDMA handheld applications has been fabricated in a 0.35 μm, 40 GHz f_T - volume production SiGe bipolar technology. The process technology features a doped ground connection for on-chip devices to improve the overall performance. At 3.3 V supply voltage saturated output power of 29 dBm with a PAE of 52% has been achieved; simultaneously OP1 dB reaches 28 dBm and the small signal gain is 32 dB.

Index Terms — Microwave power bipolar transistor amplifiers, MMIC amplifiers, Code division multi-access, Inductors

1. INTRODUCTION

Today's power amplifier (PA) market is dominated by III/V-technologies. While enabling outstanding performance [1], it stills suffers from high cost in mass-production technologies compared to Si based technologies.

Todays silicon germanium (SiGe) semiconductor processes already feature HBTs with f_T and f_{MAX} values of 200 GHz and beyond [2], but with low breakdown voltages in volume processes. In the past years several Si-based high efficient PAs for the most different applications have been presented [3], [4]. Single output-stages were developed [5] but most examples suffer from low linearity [5], [6], [7]. This paper demonstrates a high gain, high linearity 3-stage amplifier designed for WCDMA systems.

As typical Si volume production processes are not suited for PA applications due to low avalanche breakdown voltages (BV_{ceo} and BV_{cbo}) the process was modified for higher ruggedness and an additional low inductance ground connection feature was applied to connect the transistor emitters to ground using a very low resistance substrate.

With this technique, a single-ended PA for WCDMA applications was realized [8]. As a result the main system requirements are fulfilled and the suitability of SiGe bipolar technology for mobile phone PA realizations has been proved.

A key design feature is a high output compression point (OP1dB) being very close to the saturated output power. Furthermore, this design and technology approach can be used for non-constant envelope systems, like EDGE or WLAN.

2. TECHNOLOGY

The chip was manufactured in modified standard 0.35 μm SiGe bipolar technology (B7HF) by Infineon Technologies described in [9], [10]. The worst case collector base breakdown voltage (BV_{cbo}) is 15.5 V and the collector emitter breakdown voltage (BV_{ceo}) is 4.4 V. The achieved maximum transit frequency (f_T) is 40 GHz and $f_{MAX} = 60$ GHz. Additionally, a sinker for ground contacting is introduced to overcome the problem of emitter degradation being an important issue in single-ended designs for high frequencies. Therefore, a huge amount of bondwires or other costly low-inductance ground connections are no more required.
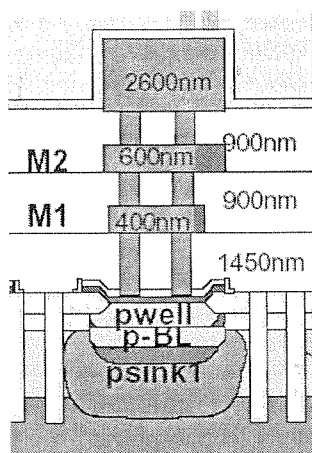
Fig. 1. Metallization cross section with sinker contact. The usage of a low resistive substrate and a high doped psink1 (epi layer) allows a low inductance ground connection

Fig. 1 shows the schematic metallization cross section view of the SiGe-bipolar technology with the sinker structure used for the low inductance ground connection. For the realization of the sinker the substrate resistance is enormously decreased - down to 15mΩcm. Using highly doped epi layers a low inductance connection between the lowest layer of metal and the substrate is achieved. The structure created in this way has a series resistance of only 50Ωm / 100000μm^2 and a neglectable series inductance. Used at the emitter finger contacts of an RF transistor, it allows the realization of single-ended high frequency amplifier stages with the possibility to adjust the emitter degradation. In contrast to conventional process technologies no ground bondwires [11] are necessary - the inductive feedback is almost none, additionally chip area is saved

due to no more required pads. Moreover it is possible to get a high-quality connection for the shunt elements in the matching networks in every place of the chip.

Thinking of a possible technology disadvantage, the factor $f_T \times BV_{cbo}$ remains at the same level as without the modification of the technology. Hence, it does not produce any drawbacks in the transistor's behaviour.

3. CIRCUIT DESIGN

Fig. 2 shows the simplified circuit diagram of the PA. The circuit is a three-stage single-ended design using two on-chip interstage matching networks. The input stage consists of an input matching network using an on-chip shunt inductance and only one small external shunt capacitor. The input HBT T1 has an effective emitter area of $126\mu m^2$ and is designed to work in class-A mode. Using a T-match, the input stage feeds the HBT T2 operated in class-A as well. Its effective emitter area is $336\mu m^2$. The most critical matching in the design is found between T2 and T3. As the input impedance of T3 is very low, the base inductance quality factor limits the impedance transformation. This implies the usage of an inductor with a maximum in its quality factor at the operating frequency. For this reason, an octangular single-winded inductor was used (see Fig. 8). Finally, the output stage HBT T3 with an effective emitter area of $2184\mu m^2$ is matched externally and operates in class-AB mode. All HBTs use a triple base connection, to keep the transistor base resistance as low as possible.
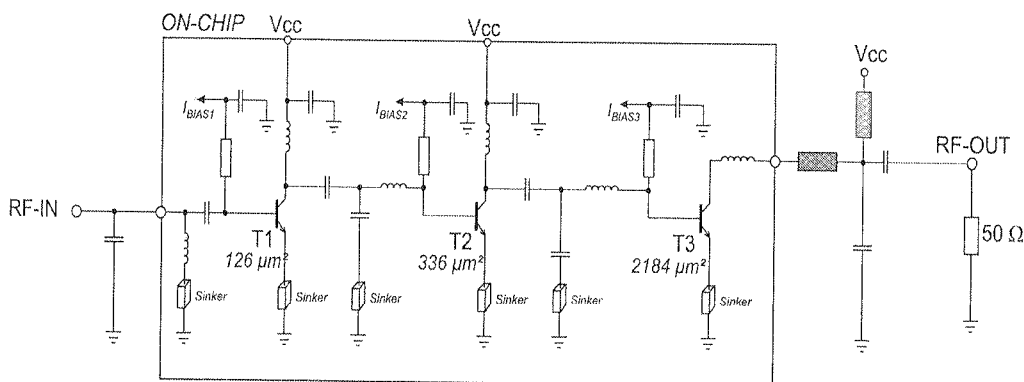
Fig. 2. Simplified schematic of the three-staged single-ended power amplifier

As the output match was realized externally, four bondwires were used to keep the connection inductance as low as possible. However, load-pull tuning using a manual harmonic load-pull tuner was done to obtain the optimum matching to achieve a high Power Added Efficiency (PAE) as well as linearity considerations. The required output matching network was synthesized out of the load-pull data and realized using

microstrip transmission lines and high-Q Epcos capacitors. The output match consists of the connection inductance, a short transmission line and a shunt capacitor. A $\lambda/4$-transformer is used at this position for the supply voltage feeding and the second order harmonic block. Efficiency issues for the optimum matching can be found in [12].

All circuit stages are biased using a current mirror circuit using a resistor connected to the HBT base. The current mirror transistor is placed directly next to the output transistor to achieve similar temperature levels. The current mirrors are controlled by the bias circuitry enabling features like power-down as well as the output power reduction facility.

The design was simulated using the Agilent Advanced Design System ADS [13] as well as with Cadence Spectre [14]. The used transistor model used for ADS is a standard SPICE Gummel Poon (SGP) model [15], [16]. The used transistor equivalent circuit is shown in Fig. 3.
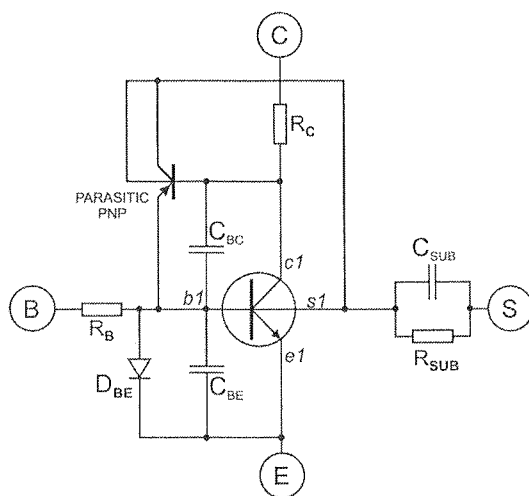
Fig. 3. Transistor equivalent circuit of the transistor model.
S represents the substrate contact

4. INDUCTOR SIMULATION AND MODELING

The realization of the sinker structure resulted in the change of the p+ silicon substrate conductivity. Unfortunately, this parameter has an impact on the quality factor and thus the modelling of the inductor structures. The substrate resistance is reduced to $15 m\Omega cm$, causing an increasing metal to substrate capacitance. Thus the substrate capacitance is now dominant in the inductor equivalent circuit shown in Fig. 4

(C_{SUB})
decreas

Prev
simulator
dependen
The indu
current d
stage bas

(C_{SUB}). In consequence the substrate losses increase and the Q-factor of the inductors decrease.
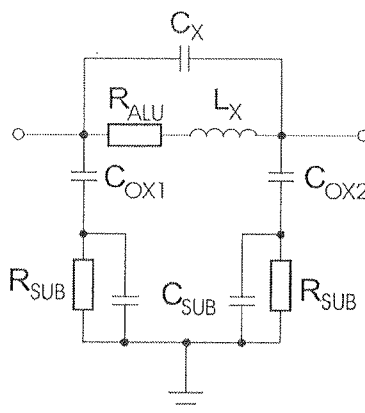
Fig. 4. Equivalent circuit of an inductor
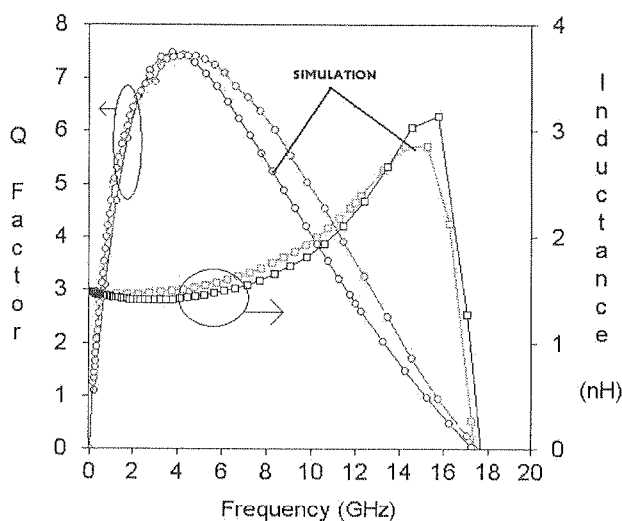
Fig. 5. Simulation and measurement of a 1.47 nH inductor on 15mΩcm substrate.
The quality factor Q reaches up to 7.5

Previous inductor models were no longer valid and a full-wave electromagnetic simulator (Sonnet 9.52 [17]) was used to predict the quality factor with its frequency dependence, ohmic resistances and the desired inductances including their connections. The inductors were optimized to achieve the highest possible quality factor for the given current densities and their geometric outline. The most critical inductance at the output stage base contact was designed as an octangular structure, as the low input impedance

of the output transistor requires high quality factors to achieve the desired linearity. To prove the simulation results, additional inductor test structures were realized for the verification. Fig. 5 shows the comparison between measurement and simulation for a collector inductance in the interstage section.

Fig. 1 shows the cross section of the metal layer stack, and the sinker underneath, in the presented technology. Fig. 6 displays a photo of the metal stack.
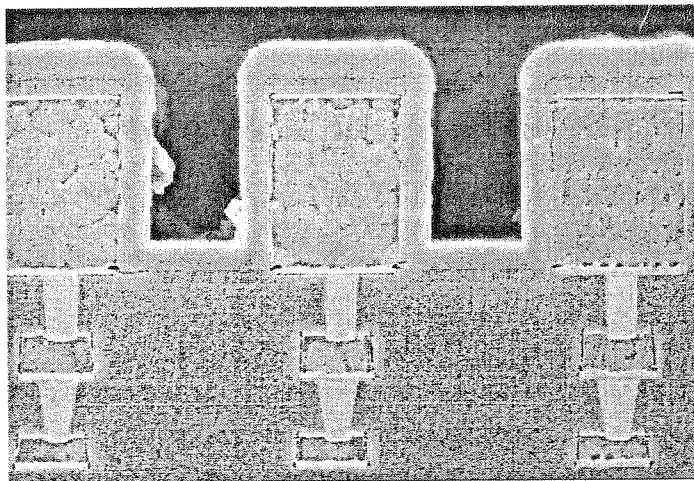
Fig. 6. Photo of the metal stack

All inductors are presumably made in the thick upper aluminium layer to reduce the series resistance of the inductor (R_{ALU} in the equivalent circuit in Fig. 4) and reduce the capacitance to substrate (Fig. 4 — C_{SUB}).

The layers underneath the thick metal are used for short connections and under-passes — marked with M2 and M1 in Fig. 1.

5. MEASUREMENT RESULTS

Fig. 7 shows the application board, build on an FR4 substrate used for the amplifier measurement setup. External input and output matching networks have been build and optimized to get the desired performance with use of transmission lines and high-Q Epcos capacitors. The $\lambda/4$ transmission line is not visible in the Fig. 7 due to its placement on the backside of the measurement board.

The chip was packaged into a VQFN 20 package with a heat sink. To ensure proper heat dissipation, the PCB features several via contacts. The chip micrograph is shown in Fig 8. The RF-section requires a die area of only $1 \times 1.3 \text{mm}^2$. The absence of ground-bonds can be seen as well.

Fig.
3.3 V wi
to the ou
consump
To c
plotted f
measurer
The
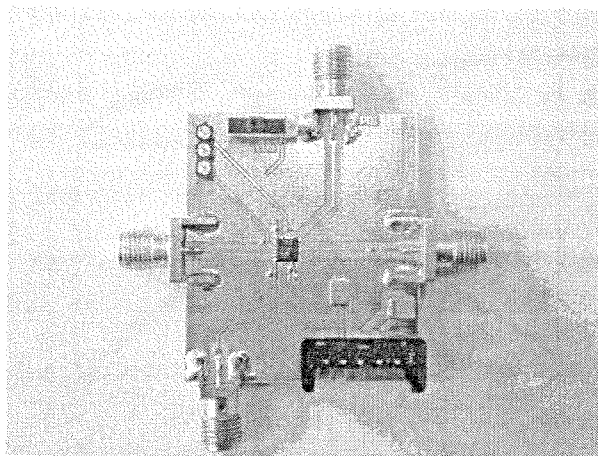
Fig. 7. Test board for the UMTS Power Amplifier
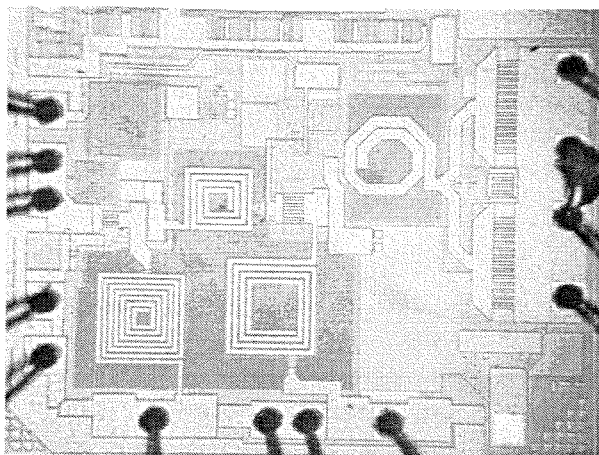
Fig. 8. The die micrograph of the power amplifier. The die size is 1×1.3 mm^2.
No bond wires needed for the emitter ground contact

Fig. 9 shows the measured power transfer characteristic for the supply voltage of 3.3 V with a quiescent current of 90mA. The maximum PAE of 52% can be found near to the output 1dB compression point (OP1dB) of 28dBm. The corresponding current consumption and gain behaviour are in Fig. 10.

To observe, if class AB is reached or not, the power transfer characteristic was plotted for the small signal gain and the required current as well. Fig. 9 shows the measurement results, hence the class-AB operation starts up very early.

The measurement results were compared with the simulations and show excellent
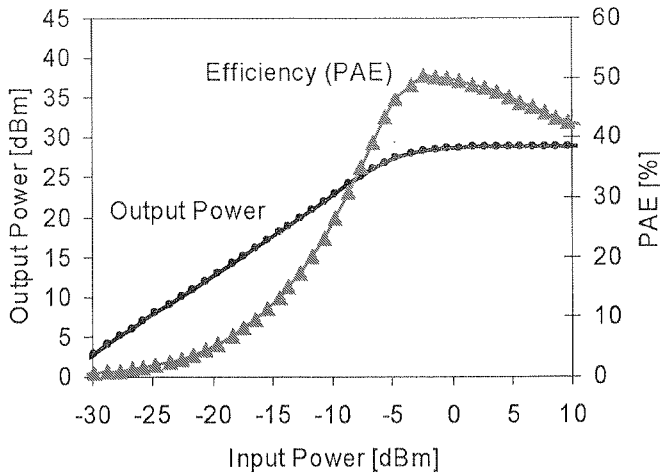
Fig. 9. Measured power transfer characteristic and PAE at V_{cc}=3.3 V
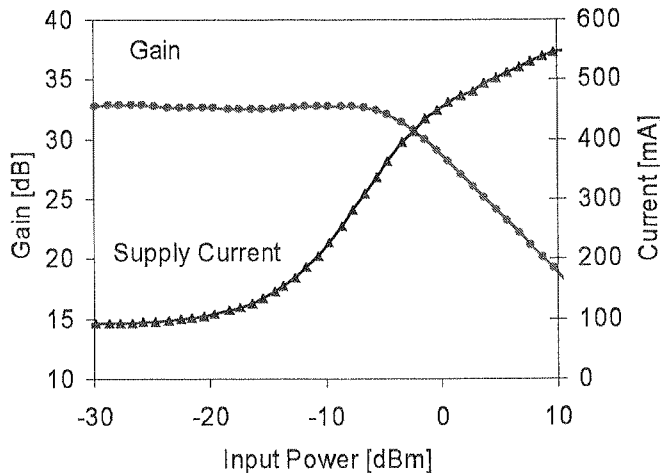
Fig. 10. The measured gain and supply current at V_{cc}=3.3 V

match. Fig. 11 shows the measured and simulated power transfer characteristic and Fig. 12 the PAE curves.

Fig. 13 shows the comparison of the simulated and measured small signal gain. The difference in the current consumption curves in Fig. 14 can be explained by the not enough precise transistor models used for high current operation.

As cellular phones have always to struggle with differing supply voltage due to different battery status, measurements for a supply voltage range between 2.4V up to 3.6 V were done. Fig. 15 shows the power transfer characteristic plots vs. supply voltage. The amplifier remains linear down to the supply voltage of 2.4 V.
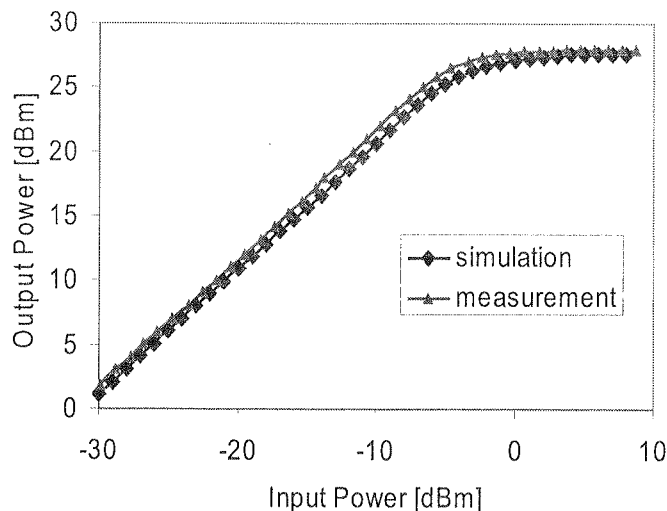
Fig. 11. Measured and simulated output power transfer characteristic at V_{cc}=3.3 V
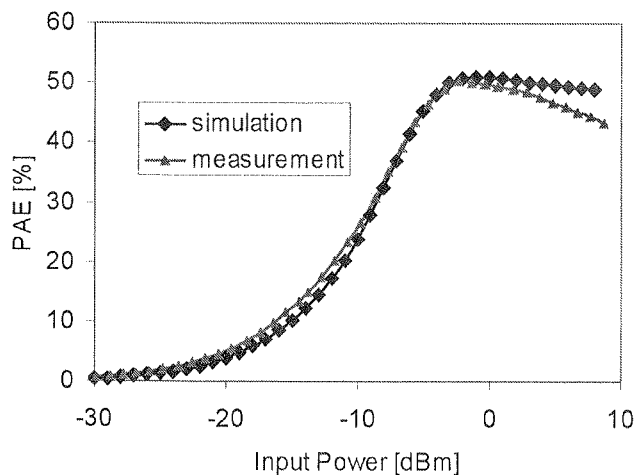
Fig. 12. Measured and simulated power added efficiency at V_{cc}=3.3 V

Another interesting point is the frequency response as it shows mistuning of the amplifier and matching stages, but also the usability for different applications. Fig. 16 shows the measured frequency response for an input power of -3dBm corresponding to the OP1dB. The amplifier center frequency is slightly shifted and the maximum output power is reached at 2.15 GHz.

As the PA was designed for WCDMA, linearity is an important issue. For the measurement setup the PA was fed with a WCDMA test signal and the output signal was observed using a Vector Signal Analyzer. The output spectrum under WCDMA conditions is presented in Fig. 17. The Adjacent Channel Power Ratio (ACPR) level
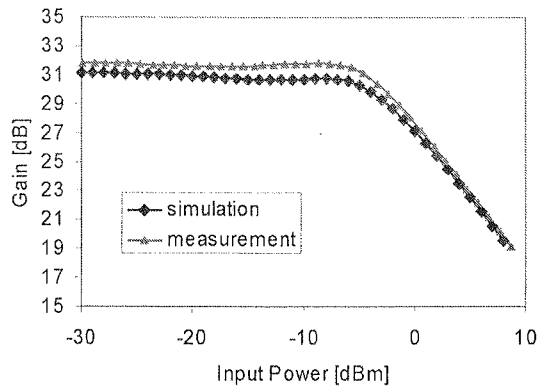
Fig. 13. Measured and simulated gain at V_{cc}=3.3 V
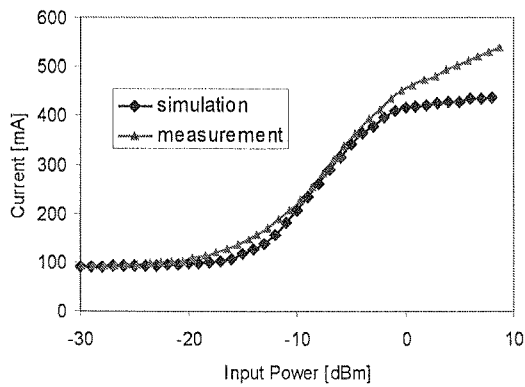
Fig. 14. Measured and simulated current consumption at V_{cc}=3.3 V
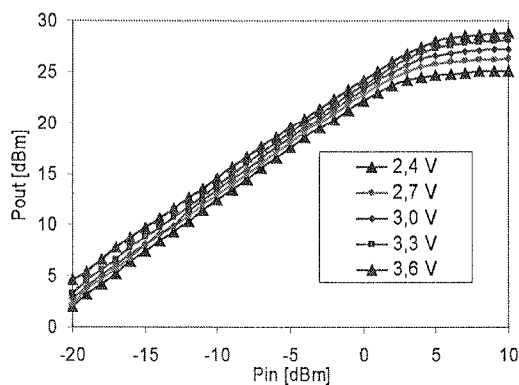
Fig. 15. Power transfer characteristic for varied supply voltage

of −36 c
efficienc
output p
Ano
Vector N
input po
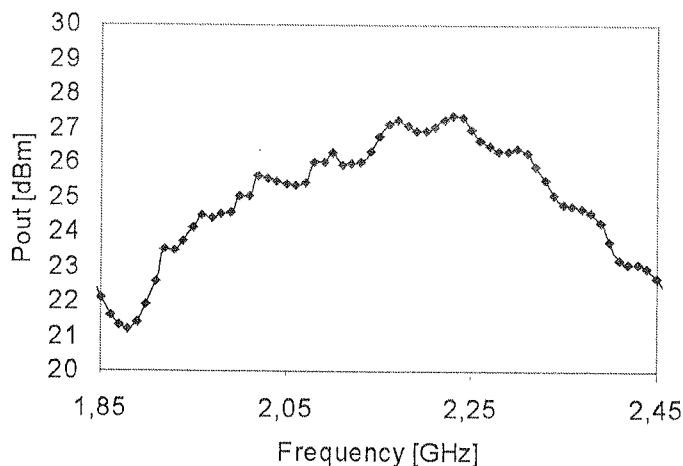
Fig. 16. Measured frequency response for
Pin = -3dBm and V_{cc}=3.3 V and I_q= 90mA
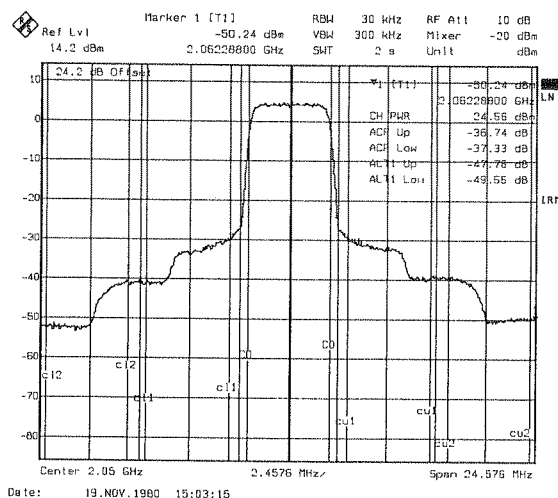
Fig. 17. Output spectrum under WCDMA conditions,
for V_{cc}=3.3 V and I_q= 90mA

of −36 dBc for the first channel is reached for the output power of 25.4 dBm with an efficiency of 34%. The ACPR levels of the first and the second channel $(n + 1)$ vs. output power are shown in Fig. 18.

Another often found linearity characterization of the power amplifier is the Error Vector Magnitude (EVM). Fig. 19 shows the measured EVM characteristics vs. the input power. The EVM remains under 4% up to the output power of 28 dBm.
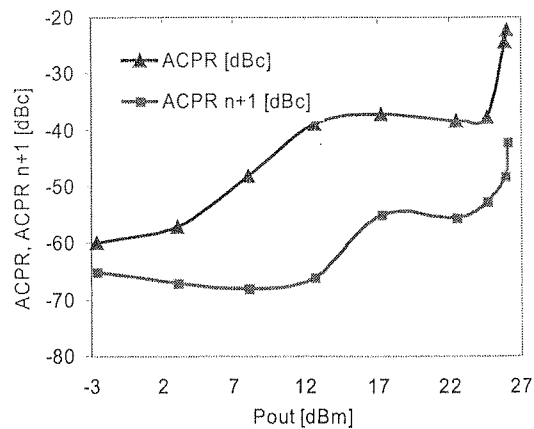
Fig. 18. ACPR level for the first and second channel
vs. output power for V_{cc}=3.3 V and I_q= 90mA
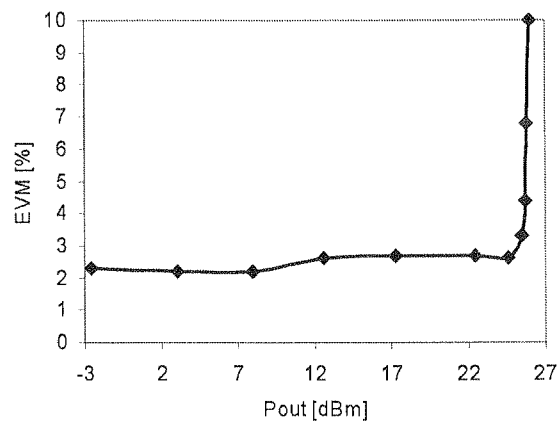
Fig. 19. Error Vector Magnitude measurement under WCDMA
conditions for V_{cc}=3.3 V and I_q= 90mA

6. CONCLUSION

A WDCMA power amplifier in a 0.35 μm-SiGe-bipolar technology has been de-
signed and fabricated. It is based on a 3-staged single-ended PA design using on-chip
inductors for the interstage matching and a sinker for low inductance ground connec-
tions. A maximum output power of 29 dBm at 3.3 V supply voltage with PAE of 52%
and small signal gain of 32 dB has been achieved. In summary it has been demonstrated
that inexpensive SiGe bipolar technologies allows to achieve attractive performance in
terms of linearity and efficiency, as required for 3 G handheld applications.

7. ACKNOWLEDGMENT

8. REFERENCES

1. T. B. Nishimura, M. Tanomura, K. Azuma, K. Nakai, Y. Hasegawa, H. Shimawaki, "A 50% efficiency InGaP/GaAs HBT power amplifier module for 1.95 GHz wide-band CDMA handsets"; *Radio Frequency Integrated Circuits (RFIC) Symposium, 2001. Digest of Papers. 2001 IEEE*, May 2001, pp. 31-34.
2. T. F Meister, *et al.*, "SiGe bipolar technology with 3.9ps gate delay", *Proceedings of the Bipolar/BICMOS circuits and technology meeting, IEEE*, Sept. 2003.
3. R. Parkhurst *et al.*, "Silicon Bipolar 3V Amplifier for GSM900/GSM1800 Handsets", in *Bipolar/BiCMOS Circuits and Technology Meeting, IEEE*, Sept. 1998, pp. 117-119.
4. P. Baltus and A. Bezooijen, "Design considerations for RF power amplifiers demonstrated through a GSM/EDGE amplifier module", *AACD 2001 Workshop*, April 2001.
5. M. Kondo, I. Miyashita, M. Koshimizu, Y. Kagotoshi, H. Nagai, K. Washio, "High-efficiency power characteristics for WCDMA applications of SiGe HBT devices using a novel form of base-bias resistance", in *2003 IEEE MTT-S International Microwave Symposium Digest*, Volume 3, 8-13 June 2003, pp. 2205 -2208.
6. F. Carrara, A. Castorina, A. Scuderi, G. Palmisano, "High performance silicon bipolar power amplifier for 1.8 GHz applications" in *2002 IEEE MTT-S Microwave Symposium Digest*, Volume 2, June 2002, pp. 1015-1018.
7. T. Biondi, F. Carrara, A. Scuderi, G. Palmisano, "A silicon bipolar technology for high-efficiency power applications up to C-band"", *Radio Frequency Integrated Circuits (RFIC) Symposium, 2003 IEEE*, June 2003, pp. 155-158.
8. K. Kitlinski, G. Donig, B. Kapfelsperger, R. Weigel, "Si-Ge Power Amplifier for WCDMA Handheld Applications", *Proceeding of Mikon 2004, IEEE*, May 2004.
9. W. Klein and B. U. H. Klepser, "75 GHz Bipolar Production Technology for the 21 th Century", *Proceedings of the European Solid-State Device Research Conference (ESSDERC) 1999, IEEE*, Sept. 1999, pp. 88-94.
10. K. Wolf, W. Klein, N. Elbel, A. Berthold, S. Gröndahl, T. Huttner, S. Drexl, and R. Lachner, "SiGe-HBTs for bipolar and BICMOS applications: from research to ramp up of production", *IEICE Transactions on Electronics*, Vol. E84-C, no. 10, 2001, pp. 1368-82.
11. Steven L. March "Simple equations characterize bond wires", *Microwave & RF*, Nov. 1991, pp. 105-110.
12. S. A. El-Hamamsy, "Design of High-Effciency RF Class-D Power Amplifier", *sIEEE Transactions on Power Electronics*, vol. 9, May 1994, pp. 297-308.
13. Advanced Design System 2003C, *www.agilent.com*
14. Cadence RF Spectre, 2003' *www.cadence.com*
15. J. Berkner, "Kompaktmodelle für Bipolartransistoren", *Expert Verlag*, 2002.
16. M. Reisch, "High frequency bipolar transistors", *Springer Verlag, First edition*, 2003.
17. Sonnet Software, v. 9.52, 2003, *www.sonnetusa.com*

Dou

Ab
0.3
wi
Ex
nor
orc
any
wa
and

Ina

Curr
tifunction
process
well as n
to suppo
are neede
gether di
include te
as well a
It will im

Double Balanced Resistive Mixer For Mobile Applications

RADU CIRCA, DARIUSZ PIENKOWSKI, GEORG BOECK, MARKUS MÜLLER

Abstract — We present a double balanced resistive mixer for mobile applications using a 0.35 μm MOSFET-technology. The mixer has been designed for direct conversion receivers with RF — and IF — frequency ranges of 2-3 GHz and DC to 50 MHz, respectively. Excellent performance has been achieved. Typical values are 6 dB conversion loss, 7 dB noise figure, 6.5 dBm 1 dB power compression, 16.5 dBm third order and 55 dBm second order intercept point, and 50 dB isolation between all ports. The mixer does not consume any DC-power and the needed LO-voltage amplitude is 1 V typical. No low frequency noise was detectable down to 10 kHz. We report on the design strategy and present simulated and measured results.

Index Terms - MMIC, CMOS, 90-nm, microwave, millimeter wave

1. INTRODUCTION

Current development trends in the mobile communication area tend towards multifunctional or re-configurable systems. That means systems being in the position to process more than one communication standard in one transceiver (base station as well as mobile terminal). As a consequence special functional blocks, which are able to support a wide range of frequency bands, signal types, and modulation schemes are needed. The 4th generation of mobile communication systems intend to bring together different domains of information exchange under the same environment. It will include technologies with innovations in system architectures and spectrum allocation as well as utilization in radio communication, networking, services and application. It will improve and revolutionize wireless/wire-line data and voice networks. Gigabit

Radu Circa, Dariusz Pienkowski, and Georg Böck are with the Microwave Department, Technische Universitaet Berlin, Berlin 10587, Germany (http://www-mwt.ee.tu-berlin.de).
Markus Müller is with Nokia Research Center, Bochum, Germany

wireless communications will be among one of them. Mobility and data-rate will be the keywords of the future.

The implementation of a reconfigurable system causes a lot of problems especially if the different standards require different receiver architectures. Two fundamentally different architecture concepts are conceivable: implementation of reusable functional blocks or use of redundant systems that provide separate functional blocks for each communication standard. Reusable function blocks require higher research and development efforts but will lead to systems of higher integration density, lower power consumption, size, weight, and finally, cost. Re-usable functional blocks of re-configurable systems have to take into account the requirements of the selected different standards very carefully.

The RF transceiver will remain one of the research hot spots in the development of such re-configurable or 4G systems. The successful development of innovative solutions for wireless components and function blocks will be based on the success in innovative semiconductor device technology development. Semiconductor device technology will be finally responsible for the overall RF-transceiver performance. A broad overview about different types of reconfigurable mobile RF-transceivers is presented in [1].

In this paper we will focus on one function block of a re-configurable RF-receiver, a double balanced passive FET-mixer based on a 0.35 (m MOSFET technology first presented in [2]. Compared to active mixers of the same technology (e.g. Gilbert cell) passive mixers offer some advantages: no power consumption, lower RF — and low frequency noise, higher linearity, higher port isolation. The lack of conversion gain can be balanced in the IF- or baseband amplifier with little additional DC-power. We will discuss the design flow and present simulated and measured results. The circuit was simulated using ADS from Agilent and the layout work has been carried out in Cadence. The complete set of features makes this mixer type a well suitable candidate for 4G mobile communication transceivers.

2. FUNDAMENTALS OF RESISTIVE MIXERS

After thorough study of the different receiver architectures proposed in the literature a decision has been made in favour of a resistive mixer as the best solution with respect to our system requirements. Because of the mentioned advantages compared to their active counterparts resistive FET mixers seem to be well suited candidates especially for direct conversion receivers. Besides of no DC power consumption passive FET mixers show very good performance with respect to port isolations, second and third order intermodulation and low frequency noise. These are key parameters of direct conversion receivers. Different resistive mixer solutions are presented in [3]-[6]. The advantages of passive FET mixers in comparison to active ones are discussed in these papers, too.

In this work a double balanced FET-ring mixer has been chosen. An excellent electrical balance of the whole structure is realizable with this circuit principle. Elec-

trical circuit balance is the key parameter especially with respect to low second order intermodulation and 1/f noise generation [7], [8], [9].

The design considerations have started from the basic functional cell of a single FET mixer presented in the left side of Fig. 1. Such mixer architecture has the advantage of simplicity. Therefore, it can be useful for low-level systems. The disadvantage is the poor port isolation and the LO coupling to the drain. LO coupling to the drain causes self mixing and consequently DC current and noise. Because of these drawbacks, this mixer type is unusable for direct conversion applications. Some problems can be overcome by a single balanced architecture as presented in the right side of Fig. 1.
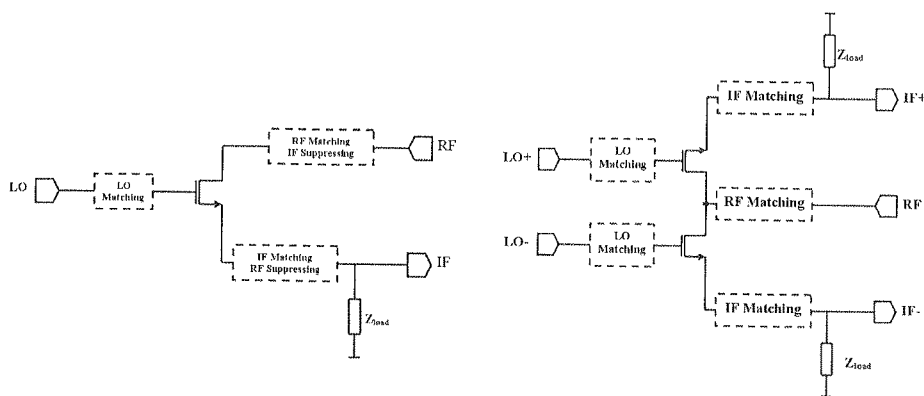
Fig. 1. Unbalanced resistive FET mixer (left) and single balanced resistive FET mixer (right)

The single balanced mixer shows good LO-RF isolation because of the virtual LO ground at the RF feeding point. Also, this mixer type suppresses self-mixing and DC current generation leading to considerable improved 1/f noise behavior. However, the LO-IF port isolation is not satisfactory and has to be improved.
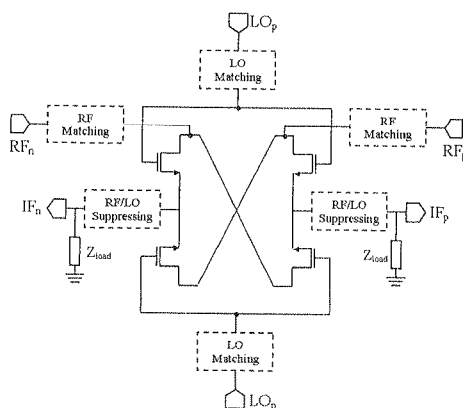
Fig. 2. Double balanced FET mixer

For this reason a double balanced resistive mixer, shown in Fig. 3 has been developed. This mixer unifies all the advantages mentioned above and shows additionally the highest isolation between all ports because of the overall electrical symmetry realizable for the whole circuit. The matching circuits are simple reactive networks with a few elements and are added to the double balanced mixer cell given in Fig. 3.

3. CIRCUIT DESIGN

The resistive mixer described in this article is designated to be used in a reconfigurable RF receiver that is able to process both Universal Mobile Telecommunication System (UMTS) and Wireless LAN IEEE 802.11a standards. In this complex front-end, the mixer acts as direct conversion mixer in the UMTS-standard and as a second stage heterodyne mixer if the WLAN standard is required. This fact defines a range of very demanding requirements that the mixer has to fulfil. From the DCR (direct conversion receiver) point of view, the mixer must provide a very high isolation between the LO and RF port to avoid the re-radiation problem and therefore the DC generation in the baseband. A high 1/f noise will also increase the DC level in the baseband and therefore is a critical parameter of the mixer. The second order intermodulation products which are not mixed with the LO signal generate in principle the same problem. These products are transferred directly to the baseband as frequency difference of the two injected RF carriers. Not only the second but also the third order intermodulation products are of great interest in the design process. Both inter-modulation products lead to more or less unwanted spurious responses in the baseband. Another requirement that resides in the nature of the reconfigurable receiver is the wide frequency range (between 2 and 3 GHz for the chosen multi-standard architecture) in which the mixer must provide a relatively constant conversion loss.

The mixer has been realized in a 0.35 μm BiCMOS process from ST Microelectronics and simulated using Agilent ADS2002 design environment. Circuit simulation and optimization were performed using the harmonic balance simulation tool. Layout work, design rules check and parasitic extraction were carried out in a Cadence environment.

As described in the previous section we have designed a double balanced resistive mixer using a transistor bridge together with matching networks. The LO input port can be seen as a nearly pure capacitive port with the capacitance Cgs of each transistor. Our goal was to transform the input port into a virtual open in order to reduce the consumed power at the LO port. We have achieved this goal by applying an AC coupled shunt inductance at the LO port. In contrary to the LO port, the RF port should be well matched. For a specific value of the transistor gate width, one can achieve a drain input impedance being on the normalized unity circle of the Smith Chart. In this case only a small serial inductance is needed for realizing a good matching of the RF port.

A very important step during the design process is the realization of the layout presented in Fig. 3. Total geometrical layout symmetry is necessary if extraordinary

port isolation values should be obtained. Therefore careful extraction of all parasitic elements has to be carried out. It has been found that the isolation values can be dramatically worse if parasitic couplings are not adequately taken into account, because of violation of electrical symmetry conditions. As mentioned above, perfect electrical symmetry is necessary also for suppressing 1/f noise generation.
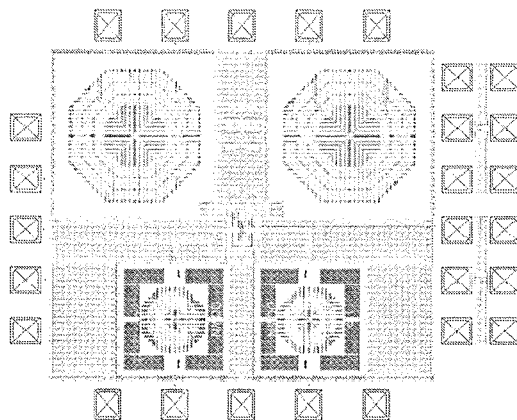
Fig. 3. Double balanced resistive mixer layout

The total chip area of the mixer is about 1.6 mm^2 without the transistor test structures on the right side of Fig. 3.

4. MEASUREMENT ENVIRONMENT

The measurements have been carried out on-wafer using balanced probe heads with 150 um pitch. For adaptation of the balanced structures to the single ended RF and LO signal sources two 180° hybrids have been used. At the IF port a coiled transformer with the transformation factor 1:6 has been applied for double to single ended conversion and impedance transformation to 50 Ω. The measurement environment is shown in Fig. 4.
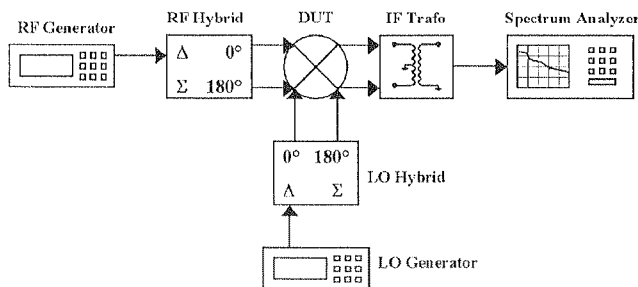
Fig. 4. Mixer measurement system

558   R. CIRCA, D. PIENKOWSKI, G. BOECK, M. MÜLLER   *Kwart. Elektr. i Telekom.*

TOM 50 -

The whole network between signal generators and mixer as well as between mixer and measurement units, respectively are non-ideal elements. Their overall amplitude and phase errors have to be de-embedded for an accurate measurement. That implies the characterization of hybrids, IF transformers, cables, bias tees and the probe heads. The total loss along these elements in the RF frequency range 2 and 3 GHz is around one dB. The characterization of the 180° hybrids and the IF transformer has to be carried out very carefully because the influence of their amplitude and phase imbalance on the overall mixer performance is very critical. This imbalance not only increases the measured conversion loss of the mixer but shows a high sensitivity also with respect to port isolation measurements.

Fig. 5 shows the insertion losses of the two branches of the RF — 180° hybrid. The characteristics of the two hybrids at the LO and RF port are very similar. As a consequence of increasing imbalance at RF and LO port the measured conversion loss increases, too. The total phase imbalances of the LO and RF path have been found in the order of a few degrees and has been de-embedded as well.
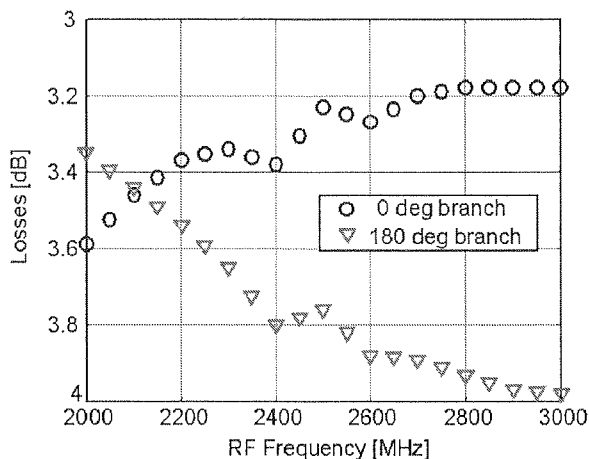
Fig. 5. Insertion loss of the two hybrid branches

After S-parameter characterization of all components used in the measurement environment, we have transferred these data into the simulation environment and de-embedded the influence of the whole surrounding measurement equipment.

The test bench for the noise figure measurements is given in Fig. 6. Because of a conversion loss (instead of a gain) a low noise amplifier has been added at the mixer output port for the measurements. Another problem involved with noise figure measurements at frequency converting circuits is the calibration of the noise figure meter. Because of the different frequency ranges of RF hybrid and IF transformer, these components could not be introduced into the calibration procedure. Their influence has to be eliminated by a de-embedding procedure, too.

The
hybrid a
total syst
been extr
figure ha
all these

A bi
other par
were swe
to the IF
MHz, alt
Fig.
IF freque
between
power co
an open
the linear
embedded
and de-er
conversio
The c
and IF fr
was 7 dB
input pow
simulation
third orde
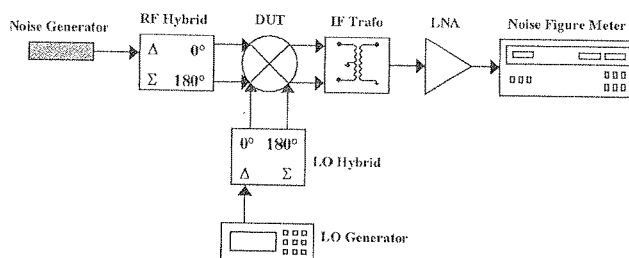
Fig. 6. Noise figure measurement system

The calibration has been performed at a IF frequency of 10 MHz without the RF hybrid and IF transformer. Therefore, the measured result is the noise figure of the total system, RF hybrid and IF transformer included. The noise figure of the DUT has been extracted applying the Friis' formula. Further on, measured double sideband noise figure has been transformed to single side band one by adding 3 dB. After performing all these procedures we obtain the single side band noise figure of the mixer.

5. RESULTS

A bias voltage of 0.45 V has been used at the LO port for all measurements. All other parameters like RF, LO and IF frequencies as well as LO and RF power levels were sweeping parameters and will be specified for each measurement. With respect to the IF port the mixer parameters show no dependence on IF frequency up to 50 MHz, although the IF frequency will be specified for each measured result, too.

Fig. 7 shows the conversion loss. The measurement has been done at a fixed IF frequency of 50 MHz. We have swept synchronously the RF and LO frequencies between 2 and 3 GHz. The available LO power was 7 dBm although the actually power consumed by the LO port was less than 0 dBm (because the LO port is nearly an open circuit). The RF input level was −20 dBm assuring that the mixer works in the linear domain. Fig. 7 shows a comparison between simulated, measured and de-embedded measured results. A very good agreement can be seen between the simulated and de-embedded measured behavior of the mixer. The measured value for the mixer conversion loss was established at 6 dB.

The determination of 1 dB power compression point has been performed at RF and IF frequencies of 2.5 GHz and 10 MHz, respectively. The available LO power was 7 dBm, again. The RF power level was swept between −30 and 10 dBm. A 1 dB input power compression point of about 6.5 dBm has been found which is close to the simulations. The compression point is depicted in Fig. 8 together with the second and third order inter-modulation products. The simulation results are not depicted in the
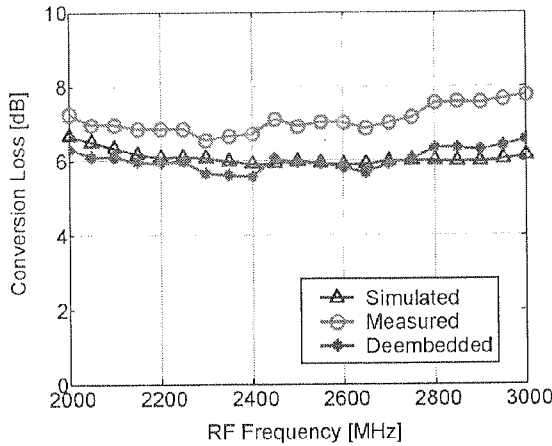
Fig. 7. Conversion loss (CL) vs. RF frequency, $P_{LO} = 7$ dBm, $P_{RF} = -20$ dBm

figure for simplicity and because the differences to the measurement results are very small.

For the third order intercept point (TOI) measurements we have used two RF signal generators with a spacing of 100 kHz between the two carriers. The middle RF frequency was 2.5 GHz and the IF frequency was 10 MHz, too. The available LO power level was 7 dBm, again. As expected, the third order intercept point as depicted in Fig. 8 is approximately 10 dB above the 1 dB compression point and has been determined to 16.5 dBm at the input. Power compression and IIP3 are considerable higher as needed in our system and also as provided by active mixers with DC power consumption up to about 10 mW.
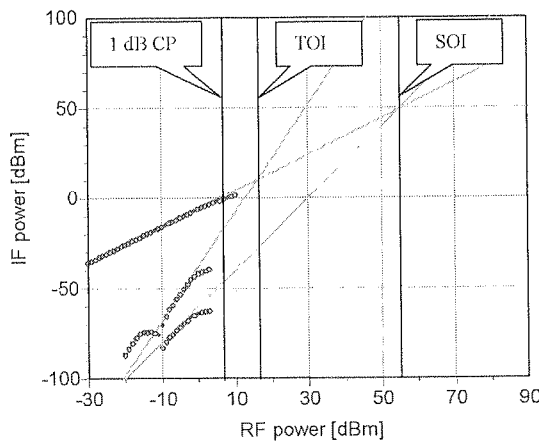
Fig. 8. Measured intercept points of the mixer at RF frequency 2.5 GHz, RF frequency spacing 100 kHz, available LO power 7 dBm, IF frequency 10 MHz

The second order intercept point (SOI) was measured under the same circumstances as the TOI. In mixer circuits one can differentiate between two different definitions of SOI. The first definition is the same as used for amplifiers and the frequencies of the inter-modulation products can be calculated by the formula

$$\omega_{SOI} = |\omega_{RF1} \pm \omega_{RF2}| \tag{1}$$

where ω RF1 and ω RF2 are the injected RF frequencies. The power level of these products is nearly independent on LO power level.

The second definition is applicable only for mixer circuits and the inter-modulation products can be calculated by

$$\omega_{SOI} = |\omega_{RF1} \pm \omega_{RF2} \pm \omega_{LO}| \tag{2}$$

where ω LO is the local oscillator frequency. The products related to this definition are strongly dependent on LO power level. The inter-modulation products defined by (1) are important for direct conversion receivers because they occur in the baseband. In our measurement, we have used a frequency spacing between the two RF fundamentals of 100 kHz and consequently, the SOI was measured at 100 kHz. A high value of about 55 dBm at the input port was measured for the SOI depicted in Fig. 8. This result is higher than the required performance for our receiver.

It has been found that the simulation of the inter-modulation behavior is a critical issue. Correctness and stability depend on some parameters: power level, circuit model, number of harmonics during the harmonic balance simulation and spacing of the carriers. With respect to all these difficulties the high grade of agreement of simulated and measured IIP3 can be seen as an excellent result with respect to both, simulations and measurements.

Fig. 9 depicts the measured independence of the input SOI based on (1) on the LO power. In this measurement, we have used a constant RF power level of −5 dBm and swept the available LO power between −1 and 14 dBm. The measurement frequency is the same as for the intermodulation measurements given in Fig. 8. The obtained result is explained by the fact that no LO harmonic participates at the generation of the second order inter-modulation product defined by (1). On the other hand, the same measurement made with respect to the input TOI (showed in Fig. 10) shows a strong dependence on the LO power level. The behavior is similar to the dependency of the conversion loss on LO power. This result is based on the fact that the third order inter-modulation products of the mixer are calculated by the formula

$$\omega_{TOI} = |2\omega_{RF1} \pm \omega_{RF2} \pm \omega_{LO}| \tag{3}$$

where the LO fundamental frequency is used for frequency conversion similar to the standard RF-IF conversion process.

In (Fig. 11) the leakage of the LO signal into the RF port is shown. The isolation is better than 50 dB nearly in the whole frequency range. With respect to the large bandwidth, these results belong to the best ones ever reported (Fig. 11). The measurements
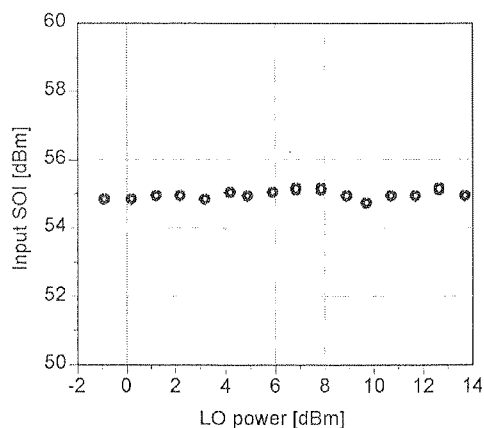
Fig. 9. Measured input second order intercept point versus LO power at RF frequency 2.5 GHz,
with a frequency spacing 100 kHz and a RF power level of −5 dBm
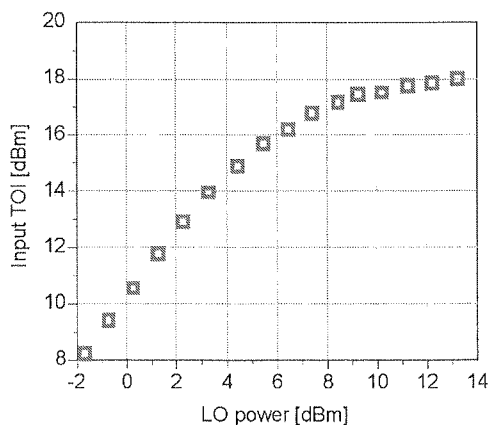
Fig. 10. Measured input third order intercept point versus the LO power at RF frequency 2.5 GHz,
with a frequency spacing 100 kHz and a RF power level of −5 dBm

have been carried out under large signal conditions by sweeping the LO frequency in the whole 2 to 3 GHz frequency range and measuring at the RF port by using a low pass filter for rejection of all spurious signals above the RF frequency.

The LO-IF isolation is depicted in Fig. 11, too. Because the IF transformer has an upper frequency limit of about 300 MHz the 180° hybrid combiners have been used at RF and LO ports for this measurement, too, although the IF port is mismatched in this case. This mismatch and the amplitude imbalance of the hybrids have been de-embedded. However, the phase errors could not been eliminated. Hence, the minimum measured isolation is limited. Therefore, the real intrinsic chip-isolation is still higher as the measured one.

The noise figure measurement procedure is extensively described in section IV of
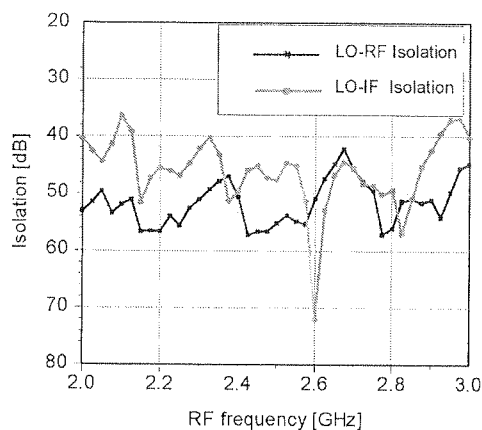
Fig. 11. LO-RF and LO-IF isolations, measured under large signal condition
with a available LO power of 7 dBm

this paper. The measurement was done with the same available LO power of 7 dBm at
the LO port and by sweeping the LO frequency between 2 and 3 GHz. The noise level
was measured at a frequency of 50 MHz. A comparison between the single side band
noise figure and the conversion loss depicted in the Fig. 12 shows that noise figure
values are slightly higher then the conversion loss (up to one dB).
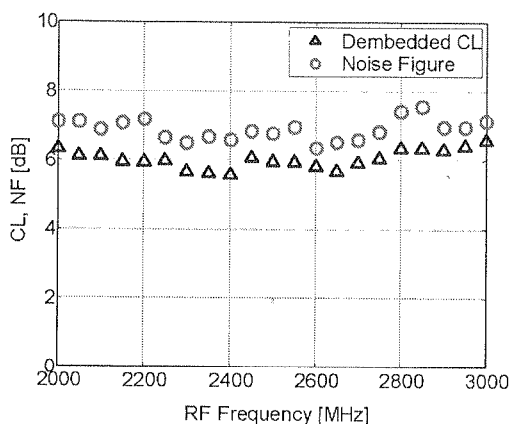
Fig. 12. Single side band noise figure and conversion loss measured at a IF frequency of 50 MHz
with an available LO power of 7 dBm

Because of the application of this mixer in a direct conversion mobile terminal
and in order to characterize its noise behavior completely, we also have carried out
low frequency noise measurements.

1/f noise behavior of resistive mixers and the measurement procedure are described
in [8], [9]. To perform the 1/f noise characterization, we followed the cited literature

and used a cascaded low noise amplifier chain to obtain the required sensitivity and amplification. Nevertheless, the 1/f noise level was under the measurable limit at the IF port from 80 kHz down to 10 kHz. The measurements were performed at different LO levels and frequencies. The measured excellent low frequency noise behavior is a consequence of a well established semiconductor technology and an eminent electrical balance of the whole structure. Small deviations from a correct balancing would lead to DC current generation and 1/f noise.

A comparison of our work has been carried out with other ones on a similar field (Table I). The table shows the advantage of the presented mixer with respect to nearly all parameters.

TABLE 1

Performance comparison with recent papers

Process	Architecture	RF [MHz]	IF [MHz]	P_{cons} [mW]	Conversion Gain [dB]	$IP_{1\,dB}$ [dBm]	ITOI [dBm]	NF [dB]	Ref.
0.35 µm CMOS	Resistive	2000–3000	50	0	−6	6.5	16.5	7 SSB	Our Work
CMOS	Gilbert Cell	2400	100	1.8	26.6	–	−0.1	8.9 DSB	[10]
0.35 µm CMOS	Gilbert Cell	2400	10	10	9	–	5	18 SSB	[11]
0.35 µm CMOS	Offset canceling	2400	28	11	−5		11	–	[12]
0.35 µm BiCMOS	Gilbert Cell	1900	1000	24	7.5	−8	−3	10 SSB	[13]
BiCMOS	3rd order cancellation	2150	–	5.9	15	–	6.0	7.7 DSB	[14]

6. CONCLUSION

We have simulated, designed and characterized a double balanced resistive MOS-FET mixer for use in mobile direct conversion receivers. Because of the chosen broadband architecture (2 to 3 GHz) the mixer is well suited for future reconfigurable systems. Very good performance has been achieved with respect to conversion loss, matching and RF noise. The mixer has no DC power consumption and simply needs a supply voltage in the order of the threshold voltage at the gates. The LO power consumption is in the order of 0 dBm.

With respect to port isolation, 1/f noise and intermodulation behavior excellent results have been achieved. Typical LO-RF isolation values of 55 dB and LO-IF isolation values of 45 dB have been measured. At the low frequency end of the IF band an increase in noise power down to 10 kHz was not detectable. Third and second

order intercept points of 16.5 and 55 dBm have been measured at the input. In context, these features make the mixer a superior candidate for mobile direct conversion and re-configurable receivers.

As an outlook we have implemented a similar mixer in a 0.13 HCMOS technology. First measurements at this mixer show further improved results with respect to conversion loss, LO power consumption and port isolation. We will report on this mixer in the near future.

7. REFERENCES

1. *2003 IEEE MTT-S Int. Microwave Symp. Dig.*, "Future Multiband and Multimode Communications", Philadelphia, Pennsylvania, June 8, 2003.
2. R. Circa, D. Pienkowski, G. Boeck, M. Mueller, "Double Balanced Resistive Mixer for Mobile Applications", 15th Int. Conf. On Microwaves, Radar, and Wireless Communications, MIKON, Poland Warszawa, May 17-19, 2004, to be published.
3. S. A. Maas, *Microwave Mixers, Norwood*, MA, Artech House, Inc, 1986.
4. K. S. von Behren, M. Tempel and G. Boeck, W. Schwartz, D. Leipold, "5-6 GHz Resistive Image Reject Mixer in a 2.5 V CMOS Technology", IP2000 Europe - New Technologies for RF Circuits, Scotland, 23-24 October 2000.
5. S. A. Maas, "A GaAs MESFET Mixer with Very Low Intermodulation", *IEEE Trans. Microwave Theory and Techn.*, vol. 35, issue 4, Apr. 1987, pp. 425-429.
6. F. Ellinger, R. Vogt, W. Baechtold, "Compact Monolithic Integrated Resistive Mixers With Low Distortion for HIPERLAN", *IEEE Trans. Microwave Theory and Techn.*, vol. 50, issue 1, Jan. 2002, pp. 178-182.
7. M. Margraf, G. Boeck, "A New Scalable Low Frequency Noise Model for Field- Effect Transistors used in Resistive Mixers", in *2003 IEEE MTT-S Int. Microwave Symp Dig.*, vol. 1, 8-13 June 2003, pp. 559-562.
8. M. Margraf, G. Boeck, "Scaling of Low-Frequency Noise in Resistive FET Mixers" in *Proc. Int. Microwave and Optoelectronics Conference, IMOC 2003. of the 2003 SBMO/IEEE MTT-S Int.*, vol. 2, 20-23 Sept. 2003, pp. 873- 876.
9. M. Margraf, G. Boeck "1/f Noise Optimum for Field- Effect Transistors in Single- Ended Resistive Mixers", presented at the 33rd European Microwave Conference, vol. 3, 7-9 Oct. 2003, pp. 1015-1017
10. Cheng-Chih Chang, Ro-Min Weng, J. C. Huang, Kang Hsu, Kun-Yi. Lin, "A 1.5V High Gain CMOS Mixer for 2.4 GHz applications", in *2001 IEEE Int. Symp. on Circuits and Systems ISCAS 2001*, 6-9 May 2001, vol. 4.
11. Tang Jing Jung, Cary Cheung King Sau, Jack Lau, "A 2.4 GHz Four Port Mixer for Direct Conversion Used in Telemetring", in *2001 IEEE Int. Symp. on Circuits and Systems ISCAS 2001*, 6-9 May 2001, vol. 4.
12. Chih-Chun Tang, Kun Hsien Li, Shen-Tuan Lin, "2.4 GHz Offset-Cancelling Down-Conversion Mixer", in *Electronic Letters*, vol. 38, no. 9, April 2002.
13. K. Nimmagadda, G. M. Rebeiz, "A 1.9 GHz Double-Balanced Subharmonic Mixer for Direct Conversion Receivers", in *Radio Frequency Integrated Circuits (RFIC) Symp., 2001. Digest of Papers. 2001 IEEE*, 20-22 May 2001, pp. 253-256.
14. L. Sheng, L. E. Larson, "A Si/SiGe BiCMOS Mixer with 3rd-Order Nonlinearity Cancellation for WCDMA Application (Student paper)", in *Radio Frequency Integrated Circuits (RFIC) Symp., 2003. Digest of Papers. 2003 IEEE* June 8-10, 2003.

Ab
ad
Ca
fee
the
pha
set
lev
rep

A. Struct

The
with a ne
the greate
of this te
types of
the achiev
of telecor
approach.

B. Genera

Havin
ments, is

Strongly nonlinear feedback technique for significant phase noise suppression at microwave harmonic oscillators

TAMÁS BÁNKY[1], ATTILA ZÓLOMY[1], TIBOR BERCELI[1]

Abstract —— Calculations are presented to study the phase noise suppression effects of an additionally introduced highly nonlinear feedback loop in microwave harmonic oscillators. Calculations are done for determining the optimal structure and parameter set of nonlinearly feedbacked harmonic oscillators, with respect to the effects of the nonlinear properties on the behavior of the phase noise characteristics. Using the calculated analytical form 6dB of phase noise suppression was achieved. Experiments have been also performed on a practical setup, specifically on an opto-electronic oscillator structure operating with high harmonic levels. Measurement and simulation results for confirming our theoretical principles are also reported.

1. INTRODUCTION

A. Structure of the Paper

The paper is organized as follows. The core of this paper is mainly concerned with a new technique which gives easy-to-apply solution for fighting against one of the greatest problem of the RF signal generation: the phase noise. Detailed description of this technique will appear in Section II. Before that, in Section I. shows the main types of previously published noise reduction techniques. Section III. will report on the achieved results (both measured and simulated) and their significance in the field of telecommunications, whereas Section IV. summarizes the basic concept of our new approach.

B. General Types of Phase Noise Reduction Techniques

Having millimeterwave oscillators that meet the most recent performance requirements, is one of the most important and actual need in the field of telecommunications.

[1] Budapest University of Technology and Economics, Goldmann Gy ter 3., Budapest, HUNGARY H-1111 Tel:+36-1-463-3684 Fax:+36-1-463-3289 banky@mht.bme.hu, zolomy@mht.bme.hu, berceli@mht.bme.hu

With improved phase noise characteristics, high temperature stability, precise frequency stability RF oscillators, high quality transmitter- and receiver-end applications are able to be constructed, in today breezily extending RF data communication field.

In the last decade huge effort had been taken for developing design methods that can improve the above mentioned characteristics of oscillators. There are three main category of available solutions for phase noise reduction at microwave oscillators: overall loaded Q-factor improvement, noise source minimization, amplifier linearization.

The loaded Q-factor (and so the stored energy) can be enhanced in several ways. Mostly, techniques use coupling between resonator elements having different quality factor for that, like in the case of [3], [4], [6], [7]. As high-Q elements, today instead of the metal cavities [3], [6], dielectric resonators in $TE_{01\delta}$ mode (unloaded Q is in the range of several 1000) and sapphire resonators in whispering-gallery-mode (WGM) (unloaded Q is in the range of 100.000) are frequently utilized [4]. Most widely used are the dielectric resonator approaches, which can offer SSB phase noise as low as e.g. −125 dBc/Hz at 10 kHz off from the 10 GHz carrier. Another technique, becoming popular in the last years, is the opto-electronic type RF oscillators (~ −140 dBc/Hz at 10kHz SSB phase noise @10 GHz oscillators).

Except for resonator Q enhancements, other special noise reduction techniques have also been published. Experiments for reducing the effects of noise sources in the oscillator circuit have also been published. One type of these approaches utilizes phase-locked-loop (PLL) techniques [7]. The other type apply a suitable low frequency (LF) matching network (for example by bias optimization) to provide a load for the noise source that matches it into low noise regime [2], [8].

Linearization of the active element (as a central part of the oscillator) is also a widespread technique. The need for linearization will be explained in the subsequent section. This can be achieved by using well known configurations of transistor structures representing the amplifier part of the oscillator. Example for that can be the source-coupling of the transistors (eliminating the effect of input capacitance-nonlinearities by capacitive compensations), or using push-push configuration, etc.

2. THEORY

A. The Concept

Here, a new technique is to be introduced, which heals the general problem of the phase noise in microwave oscillators from point of view which is different from the ones listed above. Principally, it concentrates on the noise sources themselves of the electrical active element.

Instabilities in the oscillators' frequency can have a wide variety of sources, such as internal noise sources, thermal changes in the circuit, effects of environmental interferences, etc. Excluding the internal noise sources, all the other effects may be significantly

reduced by proper design (temperature stabilization, shielding, etc.). Effects of internal noise sources need different kind of treatment.

Generally, phase noise development in a conventional oscillator structure occurs as follows. Existence of flicker noise sources inside of the active element is a consequence of normal operation of the active device. Depending on the type of the active element number and location and hence importance of them may vary. These sources produce noise signal, which has spectral density function inversely proportional to the frequency. This way taking a given realization of them, these signals can be understood and handled as low frequency signals.

Amplitude limiting nonlinearity is a usual condition of self-sustained oscillation operation. Taking the most simple case (e.g. FET transistor loaded by a resonator) operation characteristics of the active element (FET) automatically provides system with this nonlinearity (nonlinear transconductance, nonlinear internal capacitances, etc.). Above mentioned noise signals also enter this nonlinearity together with the fundamental oscillation tone. Those two, combined in the nonlinearities of the active device produce several harmonic components, *with the upconverted noise signal around*. As usual, one could get rid of all the harmonics by proper filtering and matching. However, this way also some "information" regarding the actual realization of our noise would be lost. According to our approach, detailed in this paper, we try to profit from this information instead. The reason we can make use of it is that right after the upconversion the noise skirts around the oscillation tones still remain strongly correlated to the signal of the original noise sources.

According to the above described procedure, the active device can be modeled as a series of noise source and nonlinear gain:
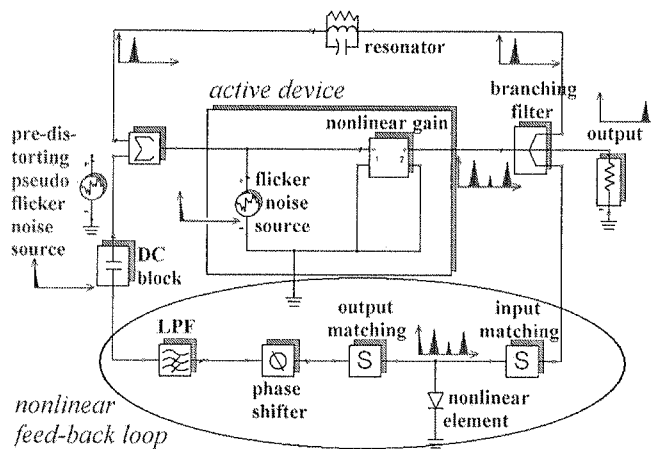
Fig. 1. General concept of nonlinear feedback in microwave harmonic oscillators

The following sections will give theoretical basis to the nonlinear feed-back loop approach, and also proves the beneficial effect of it regarding the phase noise around the harmonic oscillation frequencies (ref. Fig. 1.).

B. Nonlinearity in Harmonic Oscillators

By frequency multiplication high output frequency can be achieved with a cheaper technology. Beside the varactor based frequency multipliers an efficient way for that is the profiting from the (second or) third harmonic component generation of the active part of the oscillator [5]. To achieve high enough harmonic level the active device must be biased properly and operated in a strongly nonlinear regime. (This characteristics will be used also by the nonlinear feedbacking technique.)

The strong nonlinearity of the active device in the feedback system can be described by its transfer characteristics ($V_{GS} - I_{DS}$ in FETs and HEMTS). Mathematical characterization of this function can be easily simplified as follows. Three sections are defined: between the pinch-off (V_p) and the saturation voltage (V_s) the nonlinear characteristic can be approximated by a third order polynomial; while outside of this region by constant level as it is shown in Fig. 2. Third orderly nonlinear section of the $V_{GS} - I_{DS}$ function are represented by ai parameters in the following equation, which describes the overall mathematical transfer characteristics of the active device:

$$I(t) = \begin{cases} I_S & , V_S \leq V(t) \\ I_0 + a_1 V(t) + a_2 V(t)^2 + a_3 V(t)^3 & , V_P \leq V(t) < V_S \\ 0 & , V(t) < V_P \end{cases} \tag{1}$$

By the variation of the input amplitude (x_1) and the input (gate) bias voltage (V_0) symmetrically or asymmetrically truncated output waveform can be achieved. The former case results in high fundamental and third whereas the latter case results in high second harmonic content in the output spectra.
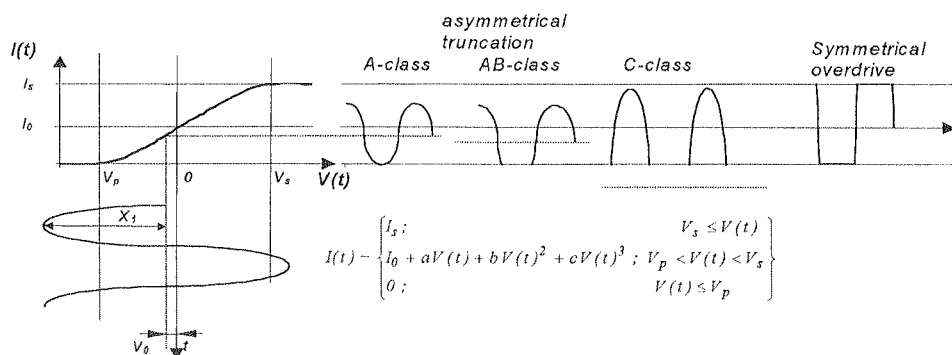
Fig. 2. General concept of nonlinear feedback in microwave harmonic oscillators

In the following calculations, amplitudes of the output signal components at fundamental, 2nd order and 3rd order harmonics are designated by A_1, A_2 and A_3, respectively. Values of these amplitudes can be calculated by taking the Fourier series of the signal waveform at the output of the active element (4-6). For the easier calculation A, B, L_1 and L_2 variables are introduced:

$$A = \frac{V_P - V_0}{x_1}, \quad B = \frac{V_S - V_0}{x_1}, \quad L_1 = (\arccos B - \arccos A),$$
$$L_2 = (\arccos B - \arccos A) \tag{2}$$

transconductance components are:

$$G_0 = I_0 + a_1 V_0 + a_2 V_0^2 + a_3 V_0^3, \quad G_1 = \left(a_1 + 2a_2 V_0 + 3a_3 V_0^2\right) x_1,$$
$$G_2 = (a_2 + 3a_3 V_0) x_1^2, \quad G_3 = a_3 x_1^3 \tag{3}$$

where all the input parameters $(a_1, a_2, a_3, V_P, V_0, V_S, x_1)$ can be easily measured or set!

$$A_1 = \frac{1}{\Pi}\left\{ 2I_0 \sin(\arccos A) + \left(G_1 + \frac{3}{4}G_3\right)L_1 + (G_1 + G_3)\sin L_1 \cos L_2 + \right.$$
$$+ (3G_2 + 4G_0)\sin\frac{L_1}{2}\cos\frac{L_2}{2} + \frac{G_2}{3}\sin\left(\frac{3L_1}{2}\right)\cos\left(\frac{3L_2}{2}\right) + \tag{4}$$
$$\left. + \frac{G_3}{8}\sin(2L_1)\cos(2L_2) \right\}$$

$$A_2 = \frac{1}{\Pi}\left\{ \frac{G_2}{2}L_1 + I_0 \sin(2\arccos A) + 2(G_1 + G_3)\sin\frac{L_1}{2}\cos\frac{L_2}{2} + \right.$$
$$+ (2G_0 + G_2)\sin L_1 \cos L_2 + \left(\frac{2}{3}G_1 + \frac{G_3}{2}\right)\sin\left(\frac{3}{2}L_1\right)\cos\left(\frac{3}{2}L_2\right) + \tag{5}$$
$$\left. + \frac{G_3}{10}\sin\left(\frac{5}{2}L_1\right)\cos\left(\frac{5}{2}L_2\right) + \frac{G_2}{4}\sin(2L_1)\cos(2L_2) \right\}$$

$$A_3 = \frac{1}{\Pi}\left\{ \frac{G_3}{4}L_1 + \frac{2}{3}I_0 \sin(3\arccos A) + G_2 \sin\frac{L_1}{2}\cos\frac{L_2}{2} + \right.$$
$$+ \left(G_1 + \frac{3}{4}G_3\right)\sin L_1 \cos L_2 + \frac{G_3}{12}\sin(3L_1)\cos(3L_2) +$$
$$+ \left(\frac{4}{3}G_0 + \frac{2}{3}G_2\right)\sin\left(\frac{3}{2}L_1\right)\cos\left(\frac{3}{2}L_2\right) + \frac{G_5}{2}\sin\left(\frac{5}{2}L_1\right)\cos\left(\frac{5}{2}L_2\right) + \tag{6}$$
$$\left. + \left(\frac{3}{8}G_3 + \frac{G_1}{2}\right)\sin(2L_1)\cos(2L_2) \right\}$$

By tuning x_1 and V_0, one can set the dynamic polynomial nonlinearity parameters $(\alpha_1, \alpha_2, \alpha_3)$ for the operation of the active device [1]. The overall transfer function between the input (v_{in}) and the output (v_{out}) signal of the active device can be expressed as:

$$v_{out} = \sum_i \alpha_i \cdot v_{in}^i, \qquad i = 1, 2, 3 \tag{7}$$

C. Phase Noise Suppression Effect of Nonlinear Feedback Loop

Since internal noise sources are mainly working in the low frequency region, signals produced by them remain correlated for "longer distance" through the oscillator circuit (even when they are up and/or downconverted). This way one may modify the signal of these sources for example by utilization of feed-back techniques, as it happens in our approach, as well.

The signal of the flicker noise source can be observed mathematically, by taking one — ω frequency — component of our actual noise signal realization. This way all the signals that are entering the nonlinear gain (noise component plus fundamental oscillation tone) can be represented as:

$$v_{in} = \cos(\Omega t) + z_\omega \cdot \cos(\omega t + \Phi_\omega) \tag{8}$$

where a value of 1 is the voltage amplitude of the oscillation signal at Ω fundamental oscillation frequency, while z_ω and Φ_ω are the amplitude and phase of the actual realization of the flicker noise's ω frequency component, respectively (relative to the oscillation tone).

v_{out} contains components at frequencies Ω, ω and their harmonics and combination frequencies (up to 3$^{\text{rd}}$ order). Just taking the terms in which z_ω is on the 0$^{\text{th}}$ or 1$^{\text{st}}$ power[2], we can write:

$$\begin{aligned}
v_{out} \cong &\ \frac{1}{2}\alpha_2 + \alpha_1 z_\omega \cos(\omega t + \Phi) + \frac{3}{2}\alpha_3 z_\omega \cos(\omega t + \Phi) + \left(\alpha_1 + \frac{3}{4}\alpha_3\right)\cos(\Omega t) + \\
&+ \frac{1}{2}\alpha_2 \cos(2\Omega t) + \frac{1}{4}\alpha_3 \cos(3\Omega t) + \alpha_2 z_\omega \cos(\Omega t + \omega t + \Phi) + \\
&+ \alpha_2 z_\omega \cos(\omega t - \Omega t + \Phi) + \frac{3}{4}\alpha_3 z_\omega \cos(2\Omega t + \omega t + \Phi) + \\
&+ \frac{3}{4}\alpha_3 z_\omega \cos(\omega t - 2\Omega t + \Phi)
\end{aligned} \tag{9}$$

All the components in 9, present at the output of the active element. They also include the "noise information", ω distance off from the oscillation tones, forming

---

[1] $\alpha_1 = 4A_3$, $\alpha_2 = 2A_2$, $\alpha_3 = A_1 - 3A_3$

[2] since $z_\omega \ll 1$ multiplication by z_ω means several order of degradation, hence terms with z_ω on higher than 1$^{\text{st}}$ power are negligible compared to the others

noise sidebands around. By effectively converting these noise sidebands down to the baseband again through an appropriately set nonlinearity, ideally, we can have a signal identical to the one that was produced by the original noise source. We should properly phase shift this signal and feed it back to the (e.g. Gate-Source) noise source located at the input of the amplifier, to be able to suppress its signal in real time. (Naturally, a strong condition of this operation is the correlation of the fed-back and the originally produced noise signal, which can be ensured by a short, passive loop.)

For being able to effectively downconvert, it is strongly advisable to choose an appropriate type of nonlinear element into the feed-back loop (either 2nd or 3rd order, as needed). Otherwise, it is impossible to produce high enough power ω frequency component at the end of the loop to effectively compensate the noise source's signal. Transmission through the nonlinearity can be described as:

$$v_{feedback} = \sum_j \beta_j \cdot v_{out}^j = \sum_j \beta_j \left(\sum_i \alpha_i \cdot v_{in}^i\right)^j, \qquad j = 1, 2, 3, \qquad (10)$$

where $\beta_1, \beta_2, \beta_2$ are the polynomial nonlinearity parameters of the feedback loop and $v_{feedback}$ is the signal waveform at the output of it.

10 produces new frequency components as the mixing products of the terms appearing in (9). We need to investigate these products to be able to determine what the optimal values for β_j-s are. Again, we should just take those which contains z_ω on less than 2nd power and representing low frequencies (since this signal is passed through a Low-Pass-Filter before entering the active device again).

Using these terms we can get the diagram presented in Fig. 3. From Fig. 3. one can easily read out how the ratio of the α_i parameters ($\alpha_2 : \alpha_3$), affect the weight of the contribution of β_2 and β_3 parameters to the overall signal production at the ω frequency component output signal of the feedback loop. Other low frequency components will have negligible powers, since the $n(\omega, (n > 1)$ frequency components will always get z_ω multiplication on the pth power, where $p = n, n + 2, n + 4, \ldots$

In Fig. 3. it can be seen that for having high level of feed-backed low frequency power, in case of an active device with strong 3rd order nonlinearity ($\alpha_2 << \alpha_3$), a feedback element with strong 3rd order nonlinearity should be applied as well. This requirement is easy to be satisfied, since the amplifier in the oscillator is typically a 3rd order nonlinear device (as also shown in Fig. 2.), while feed-back nonlinearity can be easily realized by for example an antiparallel diode pair. (The other side of the diagram would mean a need for 2nd order active element ($\alpha_2 >> \alpha_3$) (which is not usual), and strong 2nd and 3rd order nonlinear device at the same time, which is not possible to be effectively realized.)

D. Effect#2 (on the Incident Noise Content)

Another effect of the nonlinear feed-back circuit, different from the one described above, can also be observed, since noise content of the oscillation tone at the input of
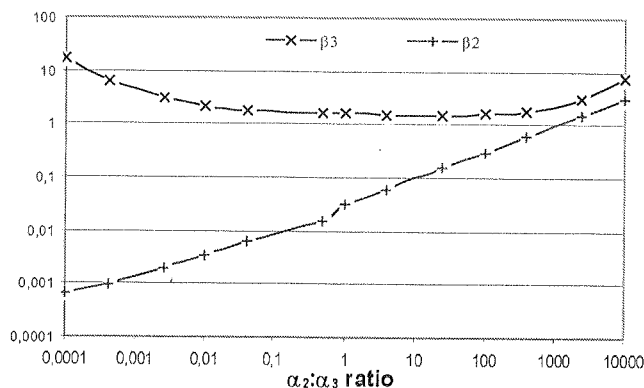
Fig. 3. Relative weight of β_2 and β_3 contribution in vfeedback signal as
a function of active device's nonlinearity parameters

the active device may also be affected by the inserted feed-back loop. We can follow its operation by the modification of our model as follows.

To keep track of the behavior of noisy incident signal, we assume single frequency operation from the input, as it was also done before , but in this case we let the incident signal have phase noise sidebands at both sides. Since the incident noise is not correlated with the signal of the amplifier's noise source noise, they can not coherently interfere with each other (we can handle them independently). That's why we eliminate the internal noise source from our recent model. The modified model is as shown in Fig. 4.:
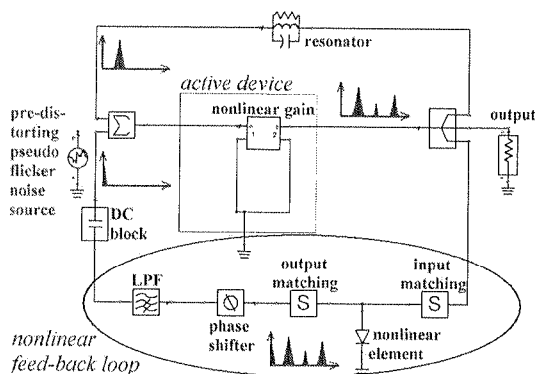
Fig. 4. Modified model used for analyzing Effect #2

As shown in the diagram, also in this case downconversion of the noise to the baseband happens through the nonlinear feed-back loop. At the end of the loop, a simple baseband signal is to be produced, which will act as an imaginary flicker noise source. The signal of this "noise source" propagates through the amplifier's nonlinearity

once m
which i
of elem
the nois
are able
the sam
level du
nonline

At t
for being
signal" a

where v_{i}
done onl
from the
in (8).

Durir
the Low-
selection
get the fo

$v_{inv.nois}$

Based
type of fee
in Fig. 5.

Consi
content of
dominant i
linearity (r
use 2nd or
weight in f

once more, where it will be combined with the oscillating fundamental spectrum (from which it was originally created). Since there are no relatively long delays or any kind of elements in the feed-back loop which would insert incoherency in the noise, all the noise sidebands appearing in Fig. 4. are coherent with the others. That's why they are able to interfere (constructively or destructively) with the others when getting in the same spectral domain. Obviously, our aim is to avoid the enhancements of noise level due to this operation. Calculations determine exactly how one should choose the nonlinear characteristics (β_1, β_2, β_2) of the feed-back loop for that.

At the end of the feed-back loop $v_{feedback}$ is produced. It enters the amplifier again for being upconverted through its nonlinearities, so in final state the "inverted noise signal" around Ω frequency can be written as:

$$v_{inv.noise} = \sum_k \alpha_k \cdot v_{feedback}^k = \sum_k \alpha_k \left(\sum_j \beta_j \left(\sum_i \alpha_i \cdot v_{in}^i \right)^j \right)^k , \qquad (11)$$

where $v_{in} = A \cdot \cos(\Omega t) + A \cdot z_\omega \cdot \cos(\Omega t \pm \omega t + \Phi_\omega)$ since the calculations are to be done only with a single frequency component of the noise spectrum (spaced by ω from the funda mental oscillation frequency). A, Ω, z_ω, Φ_ω have the same meaning as in (8).

During calculation we can omit those terms of $v_{feedback}$, which are filtered out by the Low-Pass-Filter and those which have z_ω on higher than 2nd power. We can do selection of terms after the upconversion, around Ω frequency, as well. This way we get the following expression:

$$v_{inv.noise}|_{(\Omega+\omega)} \cong \left(\frac{15}{8}\alpha_2\alpha_3^2\beta_2 + \alpha_1^2\alpha_2\beta_2 + \alpha_2^2\beta_1 + \frac{105}{16}\alpha_2^2\alpha_3^2\beta_3 + \frac{9}{2}\alpha_1^2\alpha_2^2\beta_3 + \right.$$
$$\left. +3\alpha_1\alpha_2\alpha_3\beta_2 + \frac{45}{4}\alpha_1\alpha_2^2\alpha_3\beta_3 + \frac{3}{2}\alpha_2^3\beta_2 \right) \cdot z_\omega \cdot \cos(\Omega t + \omega t + \Phi) \qquad (12)$$

Based on (12) we are able to create the weighting diagram which tells us what type of feedback we whould choose in this case. The weighting diagram is depicted in Fig. 5.

Considering 3rd order nonlinearity, Effect#2 has significant effect on the noise content of the incoming oscillation signal when 2nd order nonlinearity parameter is dominant in the feed-back loop. If active element would realize strong 2nd order non-linearity (right hand side of diagram), then it would be almost indifferent whether we use 2nd or 3rd order nonlinearity in the feed-back loop, since here they have the same weight in forming the power of the resulting "inverted noise signal".
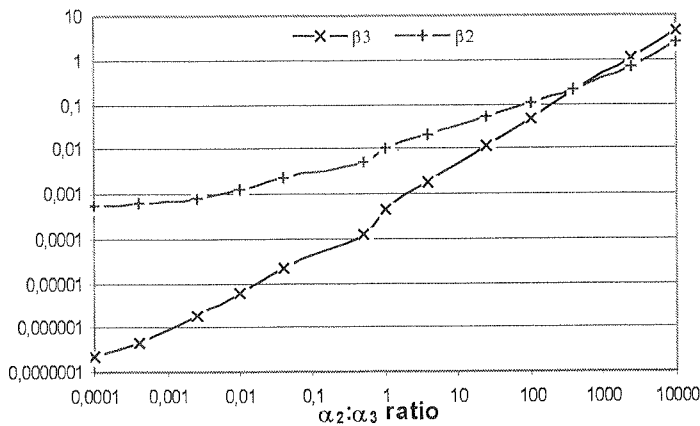
Fig. 5. Relative weight of β_2 and β_3 as a function of active device's nonlinearity

3. TEST RESULTS

For testing the feedback technique we applied feedback structure to an opto-electronic oscillator (OEO). α_i nonlinearity parameters were calculated according to Section II.B., while feedback nonlinearity (β_j) according to Section II.C. Tests were performed both in simulator environment (Agilent's ADS RF Design) and in experiments.

Opto-electronic oscillator structure is formed by a series of an electrical amplifier, a Mach-Zehnder Modulator, a high Q (long) optical fiber, a photodetector and an electrical band-pass filter. The main noise sources of OEOs are located inside of the electrical amplifier, driving the Mach-Zehnder Modulator. This is why there is a need for easy-to-apply and cost effective solutions which may reduce the noise produced by the electrical active element. In this matter OEO is a perfect application to demonstrate the beneficial effect of the nonlinear feed-backing on.

So far great effort has been taken in order to get rid of the electrical amplifier, although no effective solution has been developed to replace it. That is why the only way we can reduce its phase noise is to suppress the effects of the noise sources in the system.

In the experimental setup low noise amplifiers were compensating the loss of the electrical-optical and optical-electrical conversion ($\sim$ 55 dB). At the last stage of the amplification an ATF-36077 pHEMT transistor was utilized, which was also responsible for the introduction of the nonlinearity to the system. The whole set-up worked with 2.5 GHz fundamental oscillation frequency. Due to the strong 3rd order nonlinearity high power signal at 7.5 GHz was also produced at the output. Feedback was realized by HSMS-8002 antiparallel diode pair. Results are depicted in Fig. 6.

Si
good a

Fu
noise s
microv
V_S, x_1
suitabl
for the
opto-el
SSB p

1. H e
    Noi
    vol.
2. M .
    Loa
    35,
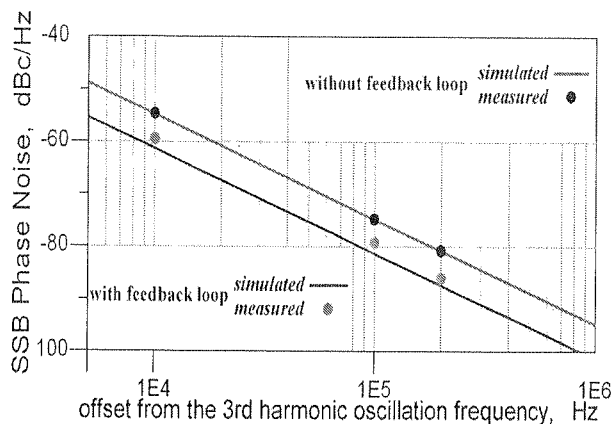3. T .
4. M .
    g o
    IEE

Fig. 6. SSB Phase Noise (both simulated and measured data) both with
and without the nonlinear feedback loop

Simulation results given by Agilent's ADS RF Design environment showed fairly good accordance with the data served by our measurements.

4. CONCLUSIONS

Full-scale calculation is presented for being able to reach maximum available phase noise suppression by the utilization of an additional strongly nonlinear feedback loop in microwave oscillators. Analytical formulas show how to set tunable parameters (V_P, V_0, V_S, x_1) of active device in harmonic oscillators to reach to nonlinearity parameters (α_i) suitable for significant noise reduction. Selection of optimal β_j parameter distribution for the set α_i parameters is also given. Experiments on a 2.5 GHz/7.5GHz harmonic opto-electronic oscillator with this way optimized parameters, resulted in ~ 6 dB of SSB phase noise suppression.

5. REFERENCES

1. Heng-Chia Chang, Xudong Cao, Umesh K. Mishra, R. A. York, "Phase Noise in Coupled Oscillators: Theory and Experiment" *IEEE Trans. Microwave Theory and Tech.*, vol. MTT-45, no. 5, May 1997, pp. 604-615.
2. M. Prigent, J. Obregon, "Phase Noise Reduction in FET Oscillators by Low-Frequency Loading and Feedback Ciruitry Optimization" *IEEE Trans. Microwave Theory and Tech.*, vol. MTT-35, no. 3, March 1987, pp. 349-352.
3. T. Berceli, "Nonlinear Active Microwave Circuits" *Akadémiai Kiadó*, Budapest, 1987, pp. 31-68.
4. M. Prigent, M. Camiade, J. C. Nallatamby, J. Guittard, J. Obregon, "An Efficient Design Method of Microwave Oscillator Circuits for Minimum Phase Noise" *IEEE Trans. Microwave Theory and Tech.*, vol. MTT-47, no. 7, July 1999, pp. 1122-1125.

5. A. Zólomy, V. Bíró, T. Berceli, G. Járó, A. Hilt, "Design of Nonlinear Oscillators for Millimeter Wave Signal Generation in Optical Systems", *European Microwave Conference '98*, Vol. I, Amsterdam, October 1998, pp. 74-79.

6. R. A. Strangeway, T. Koryu Ishii, J. S. Hyde, "Low-Phase-Noise Gunn Diode Oscillator Design" *IEEE Trans. Microwave Theory and Tech.*, vol. MTT-36, no. 4, April 1988, pp. 792-794.

7. Tadao Nakagawa, Takashi Ohira, "A Phase Noise Reduction Technique for MMIC Frequeny Synthesizers that Uses a New Pulse Generator LSI" *IEEE Trans. Microwave Theory and Tech.*, vol. MTT-42, no. 12, December 1994, pp. 2579-2582.

8. A. N. Riddle, R. J. Trew, "A New Method of Reducing Phase Noise in Ga As FET Oscillators" *IEEE Tr. MTT.*, n. 2, 1984, pp. 274-276.

The control of the output signal of semiconductor synchronized microwave oscillators by the bias voltage

D. A. USANOV, A. V. SKRIPAL, A. V. ABRAMOV, V. A. POZDNYAKOV

Abstract —— The use of the scheme of coherent signals subtraction (the synchrosignal and the synchronized oscillator output signal) for realization of the simple method of control of the output power of semiconductor microwave oscillators on the example of Gunn oscillator by the changing the bias of an active element has been proved theoretically and experimentally. The change up to 40 dB of the oscillator output power at the constant output frequency, when bias changes on 2.7%, has been achieved.

1. INTRODUCTION

The control of the output power of semiconductor microwave oscillators by the bias changing on the one hand is the attractive one because of its simplicity [1]–[4], but on the other hand there are several difficulties. For example, to achieve hard-driving amplitude modulation the bias variation must be comparable to the active element bias voltage. At that the change of the stationary electrical and thermal mode of an active element [5]–[8], which can accompany with the rise of the complicated dynamic operation modes, namely: subharmonics generation, frequency and amplitude modulation, chaotic oscillations [9]–[15].

In this work the possibility of using the scheme of coherent signals subtraction (the synchrosignal and the synchronized oscillator output signal) [16]–[21] for realization of the control of the semiconductor microwave oscillators output power by the change of an active element bias at the constant output frequency is investigated on the example of Gunn oscillator.

Saratov State University, Physical Department, Moskovskaya str., 410012 Saratov, Russia, usanov-da@info.sgu.ru

2. ANALYTICAL MODEL

To increase the dynamic range of the change of the microwave power come to the load let's consider the mode of subtraction of the synchrosignal and the Gunn oscillator output signal on the common load, which can be realized in the scheme shown in fig. 1. The optimal subtraction mode can be selected by changing the frequency or the power of synchrosignal [16]–[21], the bias of Gunn diode or the output load.
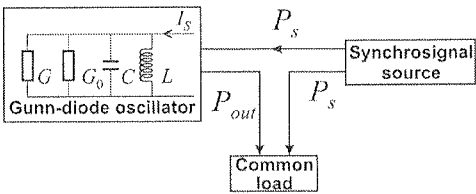
Fig. 1. Experimental setup
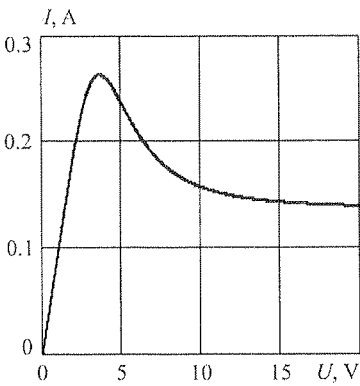
Fig. 2. The IV-curve of the Gunn diode

Consider the model of the single-circuit diode locked oscillator (fig. 1) with the resistive active semiconductor element, IV-curve of which has a section of negative differential conductivity $G(U)$ (fig. 2), which depends on the amplitude of AC voltage as [16]-[21] $G(U = -G_A + \alpha U^2$, where $-G_A$ is the small-signal negative differential resistance, is the nonlinearity factor.

The gain-frequency characteristic $y(x)$ and the phase-frequency characteristic $\varphi(x)$ of such synchronized oscillator are described by the equations [22]:

$$y\left((y-1)^2 + x^2\right) = F, \tag{1}$$

$$tg\varphi = \frac{x}{y-1}, \tag{2}$$

and oscillations stability conditions in the steady-state mode are: $y > 0.5$ and $x^2 + (y-1)(3y-1) > 0$.

If load conduction equals oscillator's output conduction and internal conduction of the synchrosignal source in the reflective scheme the power P_S of the synchrosignal source is constant and does not depend on frequency detuning, and the amplitude of the synchronizing current at the oscillator input is determined by the expression $I_S = \sqrt{8P_S G_0}$.

Since with the external synchronization in the steady-state mode at the fixed x detuning and synchrosignal amplitude F the constancy of phase difference φ between output signal of self-oscillator and synchrosignal is provided, then the investigation of the behavior of the gain-frequency and phase-frequency characteristics of the signal in the common load G_L when subtraction of the output signal p_{out} of the self-oscillator and synchrosignal p_S is of interest.

The current in the load G_L can be represented as

$$I_L = I_{SL} \sin(\omega t + \Delta_\alpha) + I_{out} \sin\left(\omega t + \Delta_\beta + \varphi(x)\right), \tag{3}$$

where I_{out} and I_{SL} are the amplitudes of currents, induced by the output signal of the synchronized oscillator on the load G_L and the synchrosignal on this load when conveying directly to the load G_L, $\phi(x)$ is the phase difference which depends on the frequency detuning within the locking range, Δ_α and Δ_β are the initial phase difference which defined by the electrical length of the transmission lines to the load G_L. Since the synchrosignal and synchronized oscillator output signal frequencies change in the locking range not more then 1%, then the variation of Δ_α and Δ_β may be neglected in comparison with and consider Δ_α and Δ_β as constants in every particular scheme.

The amplitudes of the currents I_{out} and I_{SL} in the load G_L, if load conduction equals oscillator's output conduction G_0 and internal conduction of the synchrosignal source, are defined from relations:

$$I_{out} = \sqrt{2P_{out}G_L}, \tag{4}$$

$$I_{SL} = \sqrt{k_2 2P_S G_L}, \tag{5}$$

where P_{out} is the output power of the synchronized oscillator, k_1 and k_2 are power-transfer coefficients of oscillator's output signal and synchrosignal to the common load defined by the power loss in transmission lines.

The amplitude I_{L0m} and the phase ψ of the resulting current $I_L = I_{L0m} \sin(\omega t + \psi)$ in the load are defined by the following expressions:

$$I_{L0m} = \sqrt{I_{SL}^2 + I_{out}^2 + 2I_{SL}I_{out}\cos\left(\Delta_\beta + \varphi - \Delta_\alpha\right)}, \tag{6}$$

$$\psi = arctg\left[\frac{I_{SL}\sin(\Delta_\alpha) + I_{out}\sin\left(\Delta_\beta + \varphi\right)}{I_{SL}\cos(\Delta_\alpha) + I_{out}\cos\left(\Delta_\beta + \varphi\right)}\right], \tag{7}$$

e to the
scillator
n fig. 1.
e power

with the
negative
C voltage
fferential

stic $\varphi(x)$

(1)

(2)

If amplitudes I_{out} and I_{SL} are equal and phase condition

$$\beta - \alpha + \varphi = \pi \qquad (8)$$

is fulfilled then almost absolute damping of I_L is possible.

In the locking range the phase difference φ between oscillator output signal and synchrosignal can vary from $-\pi/2$ to $\pi/2$. It allows one if $\dfrac{\pi}{2} < \beta - \alpha < \dfrac{3}{2}\pi$ to achieve the adding signals to be antiphase ones during the detuning x changing. The power on the load G_L at the current I_L is defined by the following relation:

$$P_L = \frac{I_{L0m}^2}{2G_L}, \qquad (9)$$

If the bias voltage U_d of Gunn diode considerably exceeds the threshold voltage, then the increase of U_d results in the change of the negative differential resistance $-G_A = qn_0 dv\,(E)\,/dE$, where $v\,(E) = \left[\mu_0 + v_S \left(\dfrac{E}{E_n}\right)^4\right] / \left[1 + \left(\dfrac{E}{E_n}\right)^4\right]$ is the dependence of the electron-drift velocity on the electrostatic intensity E, $E = U_d/L_d$, $\mu_0 = 0.6\text{m}^2/V \cdot s$; $v_S = 8.5 \cdot 10^4 m/s$; $E_n = 4 \cdot 10^5 V/m$; $L_d = 10\mu m$ is the length of the diode, q is the electron charge, n_0 is the concentration of fully ionized donors [1], [23]. This results in the change of the amplitude U_0 of oscillations of free-running oscillator and its output power.

Since, when the output signal of the self-oscillator and the synchrosignal are subtracted on the load G_L in the locking range, the power on the load depends, according to (6) and (9), on the frequency and the power of self-oscillator, then the change of the Gunn diode bias voltage, which results in insignificant change of the frequency and the power [1], [23] of the synchronized oscillator, causes the abrupt change of the output signal power at its constant frequency.

3. RESULTS OF COMPUTER CALCULATIONS

The optimal subtraction mode of the synchrosignal and the Gunn oscillator output signal on the common load can be achieved by selecting the frequency and power of synchrosignal.

The results of computations of power-frequency $P_L(x)/P_0$ and phase-frequency $\psi(x)$ (in polar coordinates) characteristics of signal in the load G_L at the different values of F, which were carried out with the use of relations (3), (4) and (5), are shown in fig. 3 and fig. 4. The power magnitude in the minimum of power-frequency characteristic depends non-monotonely on synchrosignal. At the optimum synchrosignal value F_0 (solid curve in fig. 3) on the frequency corresponded to the minimum of power-frequency characteristic the maximum power suppression of output signal is

observed on the load G_L. On the phase-frequency characteristics $\psi(x)$ at the minimum of power-frequency characteristic the abrupt change of the output signal phase ψ up to $\sim \pi$ (fig. 4) is observed. At the values of F less then F_0 the rate of the phase changing at the minimum of power-frequency characteristic is positive and increase when F approaches to F_0. When F becomes more then F_0 the rate of the phase changing at the minimum of power-frequency characteristic change the sign stepwise from positive to negative. Further increase of the F decreases the rate of the phase changing on the phase-frequency characteristic. In the inset of the fig. 4 the phase-frequency characteristics for the positive x are shown.
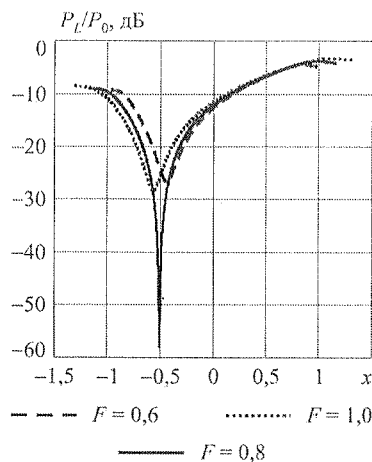

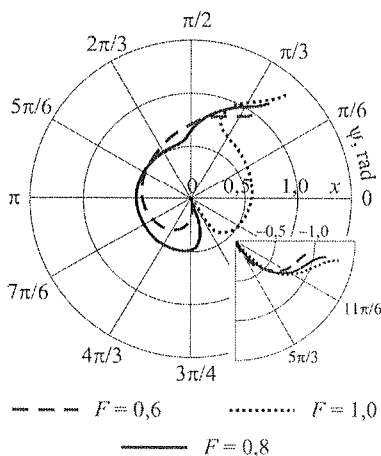Fig. 3. Calculated power-frequency characteristics at the different values of F

Fig. 4. Calculated phase-frequency characteristics at the different values of F

It is follows from the results of calculations, carried out with the use of (3), (4) and (5), that in the mode of subtraction of coherent signals at the constant synchrosignal power the change of the bias voltage of the active element on several percents results in the change of the position of power-frequency characteristic minimum (fig. 5). At that the rate of phase changing at a point of PFC minimum with the growth of Gunn diode bias voltage can change its sign at the certain syncrosignal power (see solid curve in fig. 6).

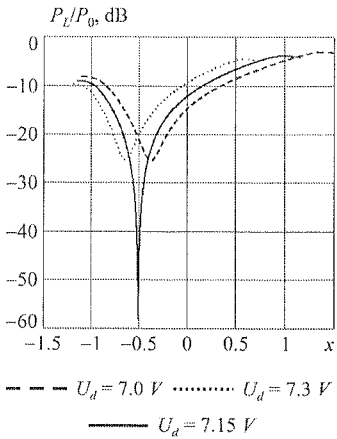Fig. 5. Calculated power-frequency characteristics at the different values of the oscillator active element bias voltage
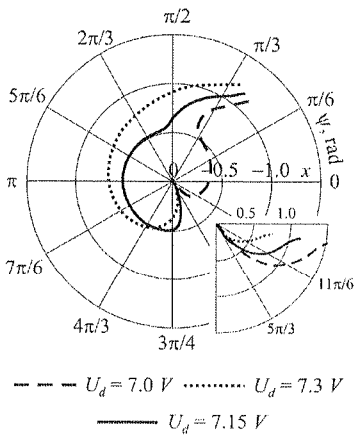

Fig. 6. Calculated phase-frequency characteristics at the different values of the oscillator active element bias voltage

At the constant synchrosignal power the change of the active element bias voltage U_d results in significant change of the power (fig. 7) and the phase (fig. 8) of the

output signal on the common load in the comparison circuit under investigation. As it follows from these results, selecting the detuning x and bias voltage range one can obtain both monotonous and non-monotone dependence $P_L/P_0(U_d)$. At that the change of the output signal phase with the growth of the Gunn diode bias on about 0.1 V may reach π (see solid, dotted and dashed curves in fig. 8). Selecting power and frequency of the synchrosignal one can reach the change of the output power more than 40 dB at the constant frequency of the output signal and at the change of the bias voltage on 0.15 V.

P_L/P_0, dB

— — — $x = -0.484$ ·········· $x = -0.539$

——————— $x = -0.513$
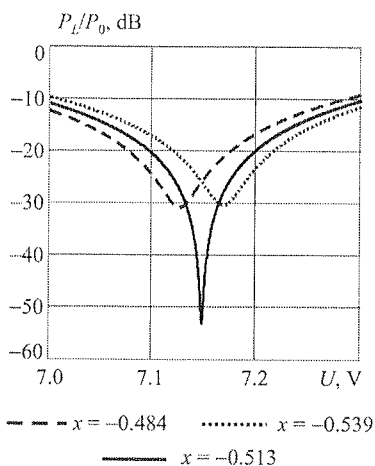
Fig. 7. Calculated dependencies of the power
of the signal in the load on the active element bias voltage

— — — $x = -0.484$ ·········· $x = -0.539$

——————— $x = -0.513$
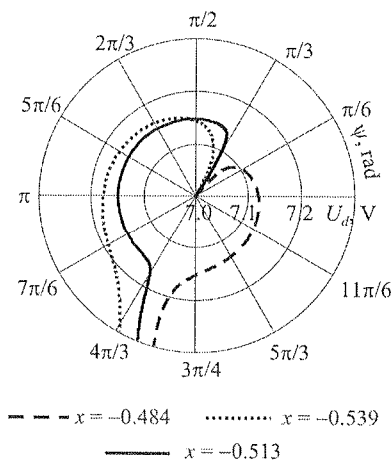
Fig. 8. Calculated dependencies of the phase
of the signal in the load on the active element bias voltage

586   D. A. USANOV, A. V. SKRIPAL, A. V. ABRAMOV, V. A. POZDNYAKOV   *Kwart. Elektr. i Telekom.*

TOM 5(

4. EXPERIMENT

In experimental investigations in one of the arms of the bridge circuit (fig. 1) the synchrosignal source was placed. In the other arm the Gunn oscillator 3A703 was placed. At the output of the bridge circuit the synchrosignal and the Gunn oscillator output signal were summarized on the common load. The resultant signal was observed with the spectrum analyzer and power meter.

Selecting the bias of the Gunn diode, power level and frequency of the synchrosignal and tuning elements of the bridge circuit we realized the mode of subtraction of synchrosignal and Gunn oscillator output signal on the common load. During the change of the synchrosignal frequency in the locking range the change of the power of the first harmonic on the output of the bridge circuit in the load was observed. The magnitude of this change at the optimal synchrosignal power P_{S0} reached 40 dB.

The results of measurements of power-frequency characteristics at the fixed synchrosignal power for different values of bias voltage of the Gunn oscillator active element are shown in fig. 9. At the bias voltage of 7.14 V the mode of maximum subtraction of signals on the common load was realized. It is follows from these results that the change of the bias voltage results in changing of the position of the PFC minimum.
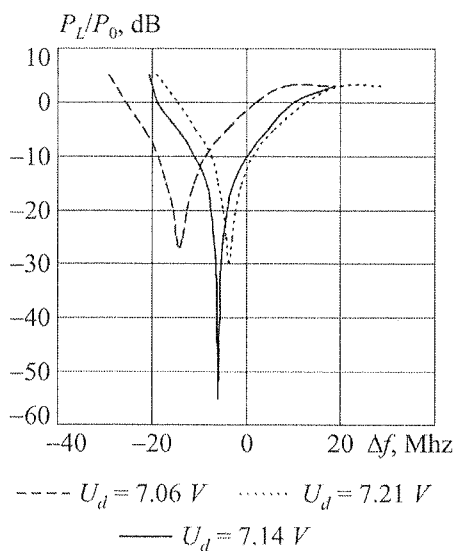
Fig. 9. Experimental power-frequency characteristics at the different values of
the Gunn oscillator active element bias voltage

Since at the frequency, corresponded to the minimum of PFC, the scheme under investigation has extremely high sensitivity to the change of the oscillator eigenfre-

quenc
freque
of the
oscilla
signal

The
the sync
at the c
frequenc
the detur
growth c
(fig. 10).

Thus
sensitivit
to the ch
to use thi
the bias v
The
the Russi

quency and power, come from it to the common load, then at the fixed synchrosignal frequency the change of the bias voltage U_d on 0.2 V, which cause insignificant change of the power (about 0.5 dB) and the frequency (about 5 MHz) of the synchronized oscillator output signal, results in considerable (up to 40 dB) change of the resultant signal power on the common load (fig. 10).
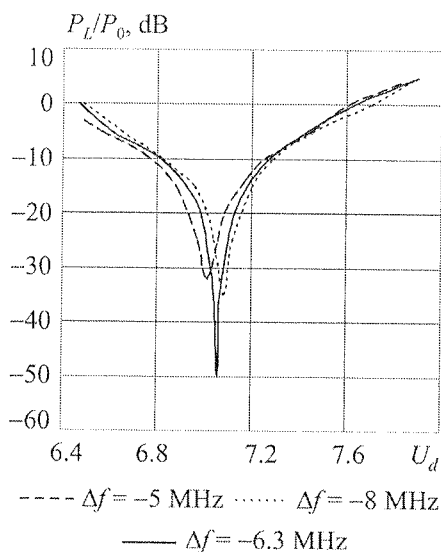

Fig. 10. Experimental dependencies of the power of the signal in the load on
the Gunn oscillator active element bias voltage at the fixed detunings Δf

The experimental dependencies of the first harmonic of the output power P_L/P_0 of the synchronized oscillator on the bias voltage of the Gunn oscillator active element at the constant values of the detuning $\Delta f = f - f_0$, where f is the synchrosignal frequency and f_0 is the Gunn oscillator eigenfrequency, are shown in fig. 10. Selecting the detuning Δf one can achieve both decrease and increase of the output power at the growth of the Gunn diode bias voltage at the constant frequency of the output signal (fig. 10).

5. CONCLUSION

Thus, the carried out experimental investigations and calculations show the high sensitivity of the investigated microwave scheme on the base of synchronized oscillator to the change of the bias voltage of the Gunn oscillator active element. It allows one to use this scheme to realize an effective method of the control of the output power by the bias voltage of the Gunn diode.

6. REFERENCES

1. M . S h u r: GaAs Devices and Circuits. New York and London: Plenum Press, 1987 p. 632.
2. D . P . T s a r a p k i n: Microwave oscillators on Gunn diodes. M.: Ravio i Svyas, 1982.
3. D . A . U s a n o v, Al . V . S k r i p a l, An . V . S k r i p a l : Physics of semiconductor radio and laser autodynes. Saratov: Saratov Univ. Press., 2003.
4. D . A . U s a n o v, A . V . S k r i p a l: Physics of semiconductor devices operation in microwave circuits. Saratov: Saratov Univ. Press., 1999.
5. B . S . P e r l m a n, C . L . U p a d h y a y u l a, W . W . S i e k a n o w i c z: Microwave Properties and Applications of Negative Conductance Transferred Electron Devices // Proc. IEEE. 1971. Vol. 59, No.8, pp. 1229-1237.
6. T . M a k i n o ć: Effects of the operational modes on the temperature dependence of the Gunn diode admittance// Solid State Electron. 1979, Vol. 22, No. 9, pp. 761-769.
7. Microwave Devices. Device Circuit Interactions/ Ed. by M.J. Howes, D.V. Morgan (John Wiley 57890 & Sons, London, New York, Sydney, Toronto, 1976).
8. G . I . H a d d a d, R . J . T r e w: Microwave Solid-State Active Devices // IEEE Trans. Microwave Theory Tech. 2002, Vol. MTT-50, N 3, pp. 760-779.
9. O . M u l l e r, W . G . F i g e l: Stability Problems in Transistor Power Amplifiers// Proc. IEEE. 1967, Vol. 55, N 8, pp. 1458-1466.
10. W . C . T s a i, F . I . R o s e n b a u m: Bias circuit oscillations in Gunn devices// IEEE Trans. Electron Dev. 1969, Vol. ED-16, No. 2, pp. 196-202.
11. D . A . U s a n o v, S . S . G o r b a t o v, A . V . S k r i p a l: Features of the low-frequency microwave oscillations of Gunn diodes // Izv. VUZ. Radioelectronics. 1981, T. 24, N 10, pp. 67-69.
12. A . S u á r e z, A . M e d i a v i l l a, J . F . L u y: Period doubling route to chaos in SiGe IMPATT diodes// IEEE Microwave Guided Wave Lett. 1998, Vol. 8, N 4, pp. 170-172.
13. B . I n g r u b e r, W . P r i t z l, D . S m e l y, M . W a c h u t k a, G . M a g e r l High-Efficiency Harmonic-Control Amplifier// IEEE Transactions on Microwave Theory and Techniques. 1998, Vol. 46, N 6, pp. 857-862.
14. D . A . U s a n o v, A . V . S k r i p a l: The physics of semiconductor devices operation in microwave circuits. Saratov: Publishing house of Saratov State University, 1999, pp. 376.
15. D . A . U s a n o v, A . V . S k r i p a l, A . V . A b r a m o v, A . A . K l e t z o v: Nonlinearity of the frequency characteristics of the MESFET in the large signal mode // Izv. VUZ. Electronics. 2003, N 5, pp. 50-56.
16. D . A . U s a n o v, S . S . G o r b a t o v, A . A . S e m e n o v, V . D . T u p i k i n: Active microwave filters on the base of semiconductor microwave oscillators operated in synchronization mode // Devices and Technique of the Experiment. 1991, N 5, pp. 121-122.
17. D . A . U s a n o v, A . V . S k r i p a l, A . V . A b r a m o v: Optical control of semiconductor synchronized microwave oscillators in the signals subtraction scheme // Izv. VUZ. Electronics. 2002, N 5 pp. 31-39.
18. D . A . U s a n o v, A . V . S k r i p a l, A . V . A b r a m o v: Optical control of semiconductor synchronized microwav? oscillators in the power suppression mode// Journal of Telecommunications and Information Technology// 2003, N 1, pp. 30-35.
19. D . A . U s a n o v, A . V . S k r i p a l, A . V . A b r a m o v: Optical control of semiconductor synchronized microwave oscillators in the power suppression mode // Proc. of 33rd European Microwave Conference. Munich, Germany. 7-9th October 2003, Vol. 3, pp. 1405-1408.

20. A
    cɾ
    oʃ
    Pₑ
21. A
    uł
    ci
    M
22. V
    wɪ
23. H
    flʊ

20. A. V. Abramov, D. A. Usanov, A. V. Skripal, V. A. Pozdnyakov: A microwave method for measurement of free charge carriers mobility in semiconductor structures// Proc. of XV International Conference on Microwaves, Radar and Wireless Communications MIKON-2004, Poland, Warszawa, May 17-19, 2004, Vol. 2, pp. 667-770.

21. A. V. Abramov, D. A. Usanov, A. V. Skripal, V. A. Pozdnyakov: Modulation of the output power of semiconductor microwave oscillators by changing the voltage in bias circuit// Proc. of XV International Conference on Microwaves, Radar and Wireless Communications MIKON-2004, Poland, Warszawa, May 17-19, 2004, Vol. 3, pp. 874-877.

22. V. S. Andreev : To the theory of synchronization of self-oscillators on the base of devices with negative resistance // Radioengineering. 1975, N 2, pp. 43-53.

23. H. W. Thim : Computer study of bulk GaAs devices with random one-dimensional doping fluctuations // J. Appl. Phys. 1968, Vol. 39, N 8, pp. 3897-3904.

Dyna

Abs
distr
entia
of co
but a
and a
diffe
tion
equa
obtai
ones.

Stable
sirable to
coupled (C
compared
suppressio
feedback,
reliability.
mation abo
operation u
ysis reveal
waveform,
Relative in
parameters

[1] Departm
vilius.pa

Dynamic characteristics of gain-coupled ingaasp laser diodes and their reliability

E. ŠERMUKŠNIS[1], J. VYŠNIAUSKAS[1], V. PALENSKIS[1], J. MATUKAS[1], AND S. PRALGAUSKAIT[1]

Abstract — Dynamic characteristics of partly gain-coupled multiple-quantum-well InGaAsP distributed feedback laser diodes have been investigated. Basic dynamic parameters (differential gain, K-factor, differential carrier lifetime) were found out. It is shown that the increase of coupling coefficient results not only in both oscillation and damping frequency increasing, but also in time-resolved frequency chirp oscillation decreasing. Relation between K-factor and differential carrier lifetime and their correlation with differential gain indicates essential differential gain role in dynamic parameter variance. A possibility to simulate the modulation characteristics of partly gain-coupled distributed feedback laser diodes using simple rate equations for carrier and photon density has been shown. Chirp and optical power pulses obtained by time-resolved frequency chirp measurements were compared with modelled ones.

1. INTRODUCTION

Stable single-mode lasers with a narrow linewidth and low chirp are highly desirable to prevent pulse variance in long-haul telecommunication systems. Partly gain-coupled (GC) distributed feedback (DFB) laser diodes (LDs) show better performance compared to index-coupled ones [1]: they have high single mode yield, high side mode suppression ratio, reduced spatial hole burning and sensitivity to the external optical feedback, low frequency chirp, large intrinsic modulation bandwidth, good long term reliability. Laser dynamic characteristic measurements provide comprehensive information about their suitability for the particular application as well as deeper device operation understanding. With respect to the other methods time-resolved chirp analysis reveals more detailed information because it enables to observe specific chirp waveform, while other methods usually show only time-averaged optical frequency. Relative intensity noise (RIN) measurements enable to extract some key LD dynamic parameters such as oscillation-relaxation frequency and damping, which determine

[1] Department of Radiophysics, Vilnius University, Sauletekio 9, 2040 Vilnius, Lithuania; E-mail: vilius.palenskis@ff.vu.lt

direct modulation speed and provide information about intrinsic material properties. The aim of this work was to find out the dynamic characteristics of gain-coupled DFB laser diodes and to investigate their behaviour during long time ageing. In addition, computer simulation of LDs transient characteristics was made. Simulation of laser physical processes is very relevant today because it can help better to understand the operation of such devices.

2. EXPERIMENTAL METHOD

The LD chirp characteristics were carried out from the time-resolved frequency chirp measurements [2]. For that purpose the DFB laser was directly modulated with 2.5 Gbit/s rate rectangular pulses by using pseudorandom pulse sequence pattern generator. Direct current and current pulse amplitude levels were chosen in such way, that mean laser optical power and extinction rate were 5 mW and 8.5 dB, respectively. The electrical signal was passed through a microwave cable and applied directly to the laser microwave input strip line by using a microwave RF probe. Bias-tee has been connected to the RF line and direct current was applied using the same microwave probe. The investigated samples were fed from low noise current source. For light beam coupling, tapered fiber was precisely positioned near the laser output facet, so, that reflections from the fiber input lens were minimal in compromise with coupled power. In addition, entire laser-fiber system was covered with plastic in order to decrease air circulation around fiber end because it causes slow fiber end position movements. Such movements occur due to some local air temperature variations as well as to air pressure variations. Such protection helps to hold constant laser beam coupling to the fiber for a long time interval, which is sufficient for one laser chirp measurement. The Advantest Q7606B Optical Chirpform Test Set as Mach-Zehnder interferometer and Tektronix TDS800 digital sampling oscilloscope with optical input block were used for further modulated optical beam chirp measurements. Data acquired with the scope were averaged with 1024 samples and the software mathematical low frequency filter $f_c = 50$ GHz was applied for signal transmission and digital scope noise reduction. By arranging the interferometer, two different interferometer frequency transfer function areas can be chosen and two different waveforms $V_{AM} + V_{FM}$ and $V_{AM} - V_{FM}$ were loaded to the digital scope. There, V_{AM} and V_{fM} mean the optical beam power modulation and optical beam frequency modulation terms, respectively. By taking into account that frequency transfer function has sinusoidal form, frequency deviation Δf can be calculated:

$$\Delta f = \frac{\mathrm{FSR}\,\sin^{-1}\left(\frac{V_{FM}}{V_{AM}}\right)}{2\pi};$$ (1)

where FSR is the Free Spectral Range of the interferometer [2] .Linewidth enhancement factor (chirp parameter) was extracted from the time-resolved chirp waveform. In this case 10 Gbit/s pulse sequences were generated and corresponding chirp waveforms,

which consisted of several periods, were analyzed by using PC. Optical beam power RIN of DFB LDs was measured using HP spectrum analyser in the frequency range from 0.5 GHz to 22 GHz. Since RIN of LD is very sensitive to the reflections, optical isolator was applied. Thermal noise and shot noise were measured by using an HP supplied routine (for the HP-70004A controller). Relaxation-oscillation frequency, f_r, and damping, Γ, were extracted by fitting measured RIN to the equation:

$$\mathrm{RIN}(f) = \frac{A + Bf^2}{\left(f_r^2 - f^2\right)^2 + \left(\frac{\Gamma}{2\pi}\right)f^2};$$
(2)

where A and B are the fitting constants, and f is the frequency [3].

3. INVESTIGATED DEVICES

Object for the measurements was gain coupled distributed feedback semiconductor laser, where gain coupling is achieved by periodical several quantum well (QWs) truncating: first-order grating cuts two or three quantum wells. The active region of measured LDs consists of six undoped InGaAsP compressively strained (1.3 %) QWs and five lattice matched p-doped InGaAsP barriers. The composition, strain and thickness of QWs were adjusted to have maximum photo-luminescence intensity within (1500-1605) nm range. Below and above the active region there are separate confinement layers.

4. EXPERIMENTAL RESULTS

The measurements of relative intensity noise at room temperature have been carried out for different LD bias up to 80 mA, while coupled power did not exceed 0 dBm. RIN spectrum shows resonant behaviour (Fig. 1). As it is shown in Fig. 1, equation (2) quite well fits measured RIN spectra in the whole investigated frequency range from 0.5 GHz to 22 GHz. A peak frequency increases with bias current increasing. Oscillation-relaxation frequency, f_r, and damping, γ, goes up as well. It is well known that oscillation-relaxation frequency square and damping have linear dependence on bias current [3]:

$$f_r^2 = D(I - I_{th}),$$
(3)

$$\Gamma = 1/\tau' + Kf_r^2;$$
(4)

where I is the bias current, I_{th} is the threshold current, and τ' is the differential carrier lifetime. In order to find from these linear dependencies the parameters D, K and τ', the RIN spectra were measured at different laser bias values. Measurement results with excellent accuracy match eqs. (3) and (4) as it is presented in Fig. 2.
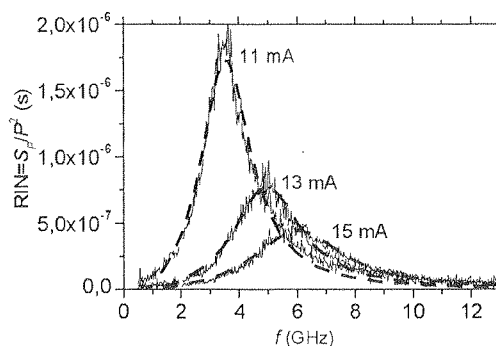
Fig. 1. RIN dependency on frequency at different laser bias (at room temperature):
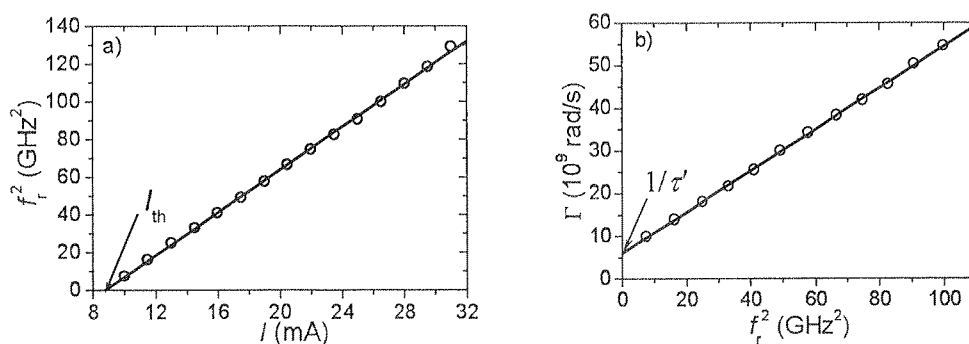solid line —— experimental data, dashed line —— fitting results

Fig. 2. Oscillation frequency dependency on laser bias current (a) and damping dependency on
oscillation frequency (b) at room temperature: dots —— experimental data,
solid line —— fitting results

Oscillation frequency and damping linear fitting was done in low bias current range (not exceeding 40 mA) in order to achieve better accuracy (at higher current region the resonance is less remarkable in RIN spectra, so, data points scattering increases and fitting is less precise). Multiple investigations of the same sample have shown, that measurements have had good repeatability, so, scattering of parameters between different LDs can be evaluated, even if samples RIN characteristics are quite similar. Therefore, linear fitting parameters I_{th}, D, $1/\tau'$ and K can be found in good accuracy. The threshold current, I_{th}, of investigated lasers (extracted from RIN characteristics (Fig. 2a)) is distributed in the range from 7 mA to 12 mA. Differential carrier lifetime, τ', ranges from 0.12 ns to 0.26 ns. Product of carrier and photon lifetimes, $\tau_{ph} \tau_e$, extracted from f_r^2 vs. I curves [4], was found in the range $(1.6 \cdot 10^{-20}$–$2.9 \cdot 10^{-20})$s. Parameter D, which is proportional to the differential gain, spreads from 4 GHz^2/mA to 6 GHz2/mA. Damping factor K is distributed from 0.42 ns to 0.57 ns. The maximum intrinsic modulation bandwidth, f_{max}, for investigated lasers can be expressed as [3]:

$f_{\max}$ = 8.88/K=20 GHz. Laser diode chirp shows some differences with respect to electrooptical modulators [5] due to nonlinear gain. While electrooptical modulator chirp has only transient part, LD chirp has transient and adiabatic term. Relatively plain region in chirp waveform (Fig. 3) is referred as adiabatic chirp and oscillations (blue or red shifts) corresponding to both power pulse edges referred as transient chirp. While adiabatic chirp pulse shape is the same as optical power pulse shape, transient chirp is proportional to the optical power P derivative:

$$\Delta f(t) = \frac{\alpha}{2\pi}\left[\frac{\dot{P}(t)}{P(t)} + G_P P(t)\right];\qquad (5)$$

where P is the optical power, G_P is the nonlinear gain, α is the chirp parameter. Chirp parameter affects both transient and adiabatic chirp, while nonlinear gain affects only adiabatic chirp. This chirp parameter can be found from time-resolved chirp measurements. If dependency $\Delta f/P$ vs. $\dot{P}/P^2]$ (here Δf is the frequency chirp) is found to be linear (Fig. 4), the eqs. (5) actually takes place, and the chirp parameter can be found from the slope of this dependency. For measured LDs the chirp parameter is spread in the range from 2 to 2.8. For comparison, the several tens of LDs from different wafers (all samples have had the same processing and structure) have been measured. The same structure lasers have obvious and measurable differences in RIN and chirp characteristics. If two different lasers do not have equal differential gain, this affects on mostly all dynamic parameters. Different lasers can have slightly different facets reflectivity (that is included in photon lifetime) or different density and/or distribution of defects that can decrease carrier lifetime.
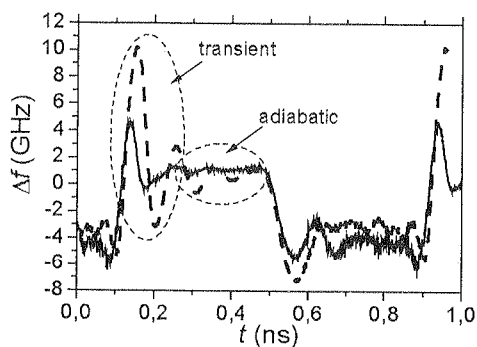

Fig. 3. Time-resolved chirp waveforms of two lasers with different damping: solid line — $\Gamma = 88 \cdot 10^9$ rad/s and dashed line — $\Gamma = 50 \cdot 10^9$ rad/s

Also, in gain-coupled DFB lasers the gain coupling is achieved by periodically truncated quantum wells, so, QWs cutting depth and form can vary from sample to sample and affect coupling coefficient, κ, as well as photon lifetime. Answer to the question, which parameter's variation has the largest effect on LD dynamic parameter
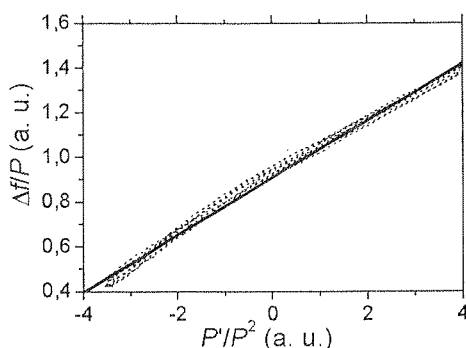
Fig. 4. Linearized time-resolved chirp (in order to reach better accuracy
several waveform periods are plotted)

dispersion between different samples, could help focus more attention on these pa-
rameters during development and processing steps as well as better understanding of
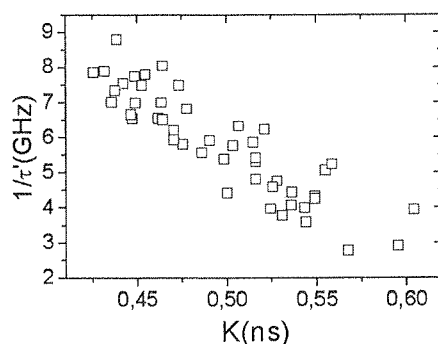dynamic characteristics.

Fig. 5. Correlation between K-factor and $1/\tau^?$ for different samples

In some cases, quite clear correlation between two fitting parameters can be seen
(Figs. 5 and 6). It was observed that amplitude of chirp rings depends on oscillation
frequency and damping of different samples (it is shown in Figs. 3 and 6). It is always
desirable to make chirp rings smaller, particularly in these cases when rings make most
contribution to the pulse power.

In order to find chirp ring amplitude analytically one should account a lot of
factors, such as amplitude and extinction rate of optical power pulse, amplitude of
power pulse rings, which all depend on the earlier mentioned key dynamic parameters
on their own. Besides, analytical analysis of large signal is especially complicated. By
measuring many LDs chirp pulses and RIN it was observed that chirp rings amplitude,
which in large part contribute transient chirp, is smaller in lasers with large damping
and oscillation-relaxation frequencies (Fig. 3 and 6). On the other hand, it was found

that these two frequencies seem to be mutually correlated as well as both correlated with coupling coefficient or stopband, what can be explained by photon lifetime variation versus coupling [6] or differential gain variations per sample. In latter case, differential gain can influence both frequencies through K-factor and D parameter (eqs. (3, 4, 6)):

$$K = (2\pi)^2(\tau_{ph} + \varepsilon/\upsilon_g g_n);\qquad\qquad(6)$$

where D and K are the constants which act as figures of merit for the frequency response of the laser, D is proportional to the differential gain, g_n, and τ_{ph} is the photon lifetime, ε is the nonlinear gain coefficient, υ_g is the group velocity [3]. It was found that K and τ' are both mutually correlated with differential gain, as well (Fig. 5). Weak correlation between stopband and differential gain were observed, too. The latter correlation can occur due to different detuning of LD with different stopbands. On
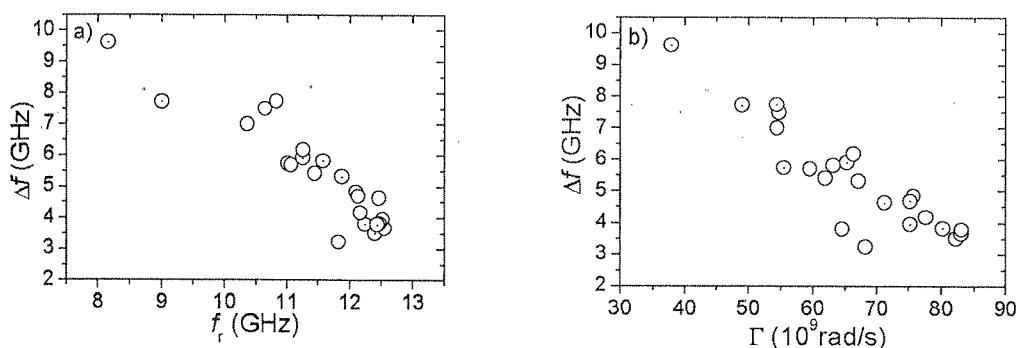

Fig. 6. Time–resolved frequency chirp waveform ring amplitude dependencies on oscillation-relaxation frequency (a) and damping (b) for different samples

the other hand, the volume of active region can slightly variate when the cutting deep variates and it also potentially can affect to D parameter or differential gain spread.

LD ageing was achieved by applying high bias current (150 mA) at elevated temperature (100°C) for a long time interval (1500 h). The RIN measurements were done and dynamic parameters of LDs were extracted during each 500 h step of ageing. Degradation of almost all investigated parameters was comparable with the measurements errors, except obvious threshold current increasing (interception with X-axis) that leads to a small decreasing of oscillation relaxation frequency at constant bias current (Fig. 7). Slope of f_r^2 vs. I dependency (parameter D) seems to remain the same during device ageing (Fig. 7). So, the product $\tau_{ph}\,\tau_e$ degrades. It can be explained in the way that during ageing more defects appear in the LD active region, what leads to the carrier lifetime decreasing [7]. It seems that damping characteristics are more resistant to the ageing or at least there is no obvious tendency (Fig. 8).
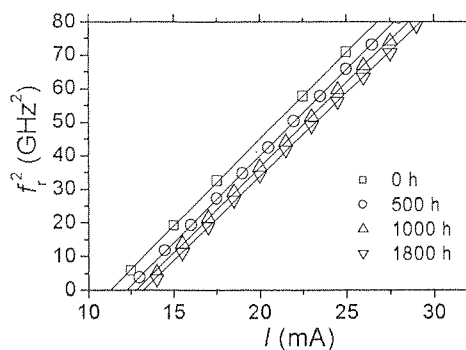
Fig. 7. f_r^2 vs. I dependency evolution during LD ageing
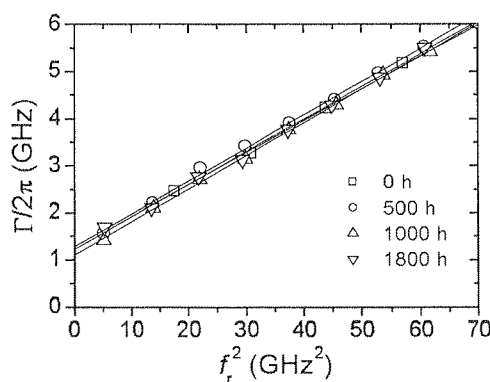
Fig. 8. Γ vs. f_r^2 dependency evolution during LD ageing

5. COMPUTER SIMULATION RESULTS

In order to numerically simulate LDs dynamic characteristics, various differential equation solving methods can be used, such as Euler's method or the Fourth-Order Runge-Kutta method. Different methods can have various modelling accuracy and computation time. These two methods were compared and it was found that Runge-Kutta is preferable. If time step Δt, which was used for modelling, is about 10^{-14} s, both methods give the same accuracy. But in the case when $\Delta t = 4 \cdot 10^{-12}$ s, the accuracy of Euler's method became obviously worse while the accuracy of the Runge-Kutta method did not change. When model describes the actual device operation quite well, then, by proper simulation parameters selection, one should obtain, that simulated characteristics match the real device characteristics.

Ordinary rate equations for carrier and photon density were used to describe and simulate the LDs dynamic behavior [3, 4]. For carrier density it is:

$$\frac{\mathrm{d}n}{\mathrm{d}t} = \frac{J}{qd} - \frac{n}{\tau_s} - G_n (n - n_{ot}) p; \qquad (7)$$

where n is the carrier density in the active region, p is the photon density. There we use the bias current density J and electron charge q, d is the active region width, τ_s represents the carrier lifetime and G_n is the differential optical gain per second, n_{ot} is the carrier density at transparent. The rate equation for the photon density is:

$$\frac{dp}{dt} = G_n\,(n - n_{ot})\,p - \frac{p}{\tau_p} + \beta\frac{n}{\tau_s};$$ (8)

where τ_p is the photon lifetime and β is the spontaneous emission factor. The first term on the right side of eqs. (7) accounts for injected carriers, the second for losses of carriers due to spontaneous recombination. There $G_n(n - n_{ot})$ describes optical gain per second. The term p/τ_p describes the photon loss through facets and absorption in the active region. A part of the photons is emitted spontaneously, that is why the last term in eqs. (8) takes place. For simplicity, the optical gain is supposed to be linear and depends only on carrier density. Carrier lifetime is supposed to be constant, i.e. it does not depend on carrier density.

Emitted optical power is proportional to the photon density in the active region and the chirp is proportional to the carrier density [8]. Optical power and time-resolved chirp pulses, which were obtained from time-resolved chirp measurements, were used for simulation (Fig. 9). By simulating various current signals LDs dynamic response was obtained (Fig. 10 and 11). By direct current pulse simulation, carrier and photon density pulses were obtained and compared with experimental optical power and chirp pulses. By proper equation (7) and (8) parameters variation and selection, simulated pulses were matched up with experimental ones till the best matching between simulated and experimental data was reached; see Fig. 9 and Fig. 10.
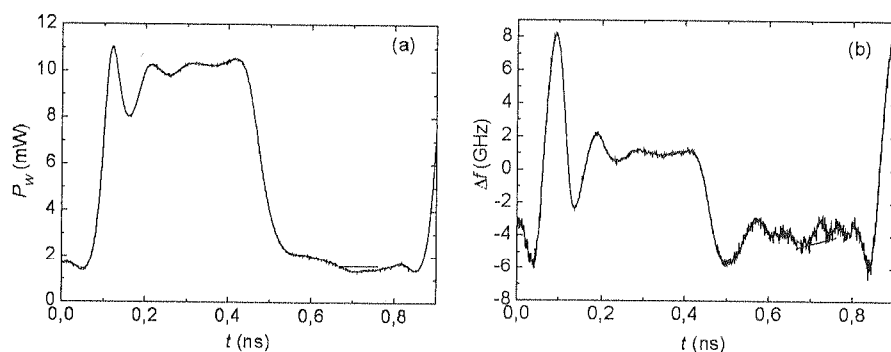

Fig. 9. Optical power (a) and chirp (b) pulses obtained from time-resolved frequency chirp measurements

Differential gain G_n variation obviously changes carrier and photon density oscillation amplitude as well large signal oscillation and damping frequencies. Carrier density at '0' and '1' levels shows dependence on differential gain, too, while photon density at these levels stays almost constant. Oscillation amplitude for both carrier

[left margin:] lifferential rth-Order uracy and at Runge-)⁻¹⁴s, both e accuracy inge-Kutta quite well, simulated

scribe and

(7)

and photon densities versus G_n has the maximum. Oscillation frequency shows nearly $f_r^2 \sim G_n$ dependence for both carrier and photon densities. Differential gain G_n variation helped to match simulated and experimental oscillation frequency. Experimental pulse oscillation frequency of selected LD was fitted best, when $G_n = 6 \cdot 10^{-7}$ cm^3/s. In this case, differences between photon and carrier modelled and measured oscillation frequency were 0.5 % and 4.2 %, respectively.

The product of carrier and photon lifetime was taken so that these two parameters would correspond to the real possible LDs values. It was noticed that by changing τ_p and τ_s values, '0' and '1' levels for both p and n densities varied. Dependence of carrier and photon density oscillation amplitude versus photon lifetime shows the maximum, too. In the case of carrier density oscillation amplitude maximum, the photon lifetime is equal to 5 ps and the photon density oscillation amplitude reaches the maximum when the photon lifetime is equal to 10 ps. Carrier and photon density oscillation frequency depends on photon lifetime as well. The main criterion for choosing both lifetimes was simulated and measured carrier and photon density matching at levels '0' and '1'. For the measured LD pulses in Fig. 9, these two parameters became equal to $\tau_S = 3,82 \cdot 10^{-9}$ s and $\tau_P = 5 \cdot 10^{-12}$ s, respectively.
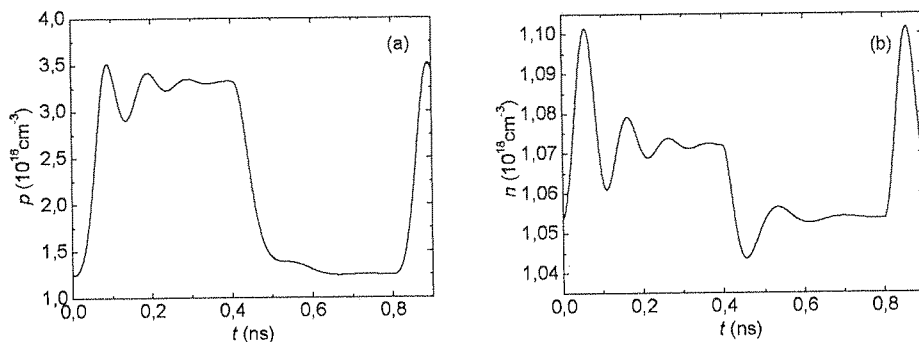

Fig. 10. Modelled photon (a) and carrier density (b) pulses

Spontaneous emission factor β was also varied in a wide interval. The main effect of β variation was a change in the oscillation amplitude and damping frequency. It also has a weak effect on the carrier density at '0' and '1' levels. Spontaneous emission factor variation helps finally match the oscillation amplitude and the damping frequency, while the oscillation frequency stays almost constant.

The model supposes that bias current pulses are strictly of rectangular form. In experiment conditions it was very problematic to measure the form of LD's bias current pulse. In part it was related to small laser input dimensions and in part to the non-ideal laser interface and RF probe impedance matching. On the other hand, simulated pulses showed that the introduction of semi-rectangular pulse could substantially improve simulated and experimental data matching. Two kinds of pulses were tested, bell form

pulse and pulse with exponential trailing edges. The latter pulse showed obviously better matching.
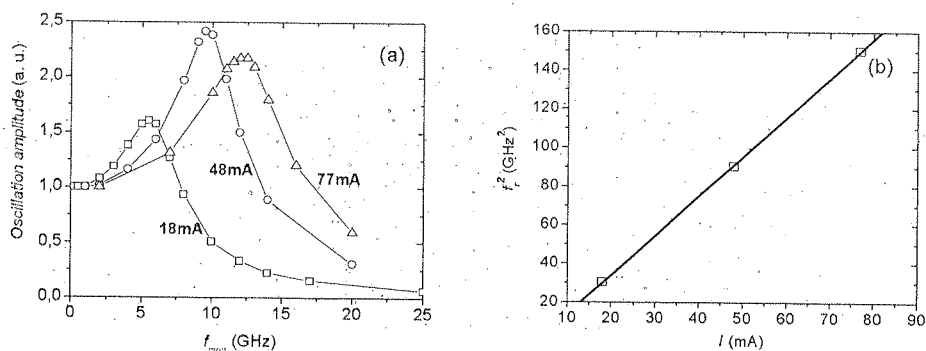

Fig. 11. Simulated LD transfer function corresponding to different bias current (a). Each transfer function resonant frequency square is proportional to corresponding bias current (b)

Several LDs were simulated and dynamic parameters were extracted. For some samples, the simulated and measured pulses matched quite well. Computer simulation difficulties appeared mostly with samples, which damping frequency is higher and the oscillation amplitude is smaller. Small signal theory predicts that large damping can be achieved by introducing nonlinear gain. So, including a nonlinear gain into the model could help to make proper simulation of LDs with large damping.

Some of LDs dynamic parameters that were extracted from RIN data were compared to those obtained by modelling.

By small signal harmonic current source simulation, the LD transfer function can be calculated and the oscillation-relaxation frequency dependence on the bias current can be found. Fig. 11 shows that transfer function has resonant behaviour and peak frequency increases together with DC. Peak frequency square versus bias current shows linear dependence. It is the same behaviour as that of the real LD. It was noticed that peak frequency in Fig. 11a, which corresponds to the current pulse 1 level, is nearly the same as the large signal photon density oscillation frequency in Fig. 10a., in both cases the frequency was approximately equal to 10 GHz. From the peak frequency square versus bias current slope, the D parameter can be found. In this case, D parameter is equal to 2 GHz^2/mA. Simple equation relates D parameter with differential gain G_n:

$$D = G_n/q = \Gamma v_g g_n/(Vq); \tag{9}$$

where Γ represents the fact that the optical mode spatial dimension is larger than the active region volume V and is referred to as the mode confinement factor. Further, v_g is the group velocity. There g_n means the differential gain per centimetre.

The D parameter extracted from RIN measurements was proportional to the differential gain, which was used in simulation.

6. CONCLUSIONS

Comprehensive studies of dynamical characteristics such as relaxation-oscillation frequency, damping, chirp characteristics and relative intensity noise of gain-coupled multiple-quantum-well InGaAsP distributed feedback laser diodes have been carried out. Their behavior during long time ageing has been investigated, too. From the investigated characteristics the key dynamic parameters such as differential gain, K-factor and differential carrier lifetime were extracted. Simple chirp parameter extraction from LDs time-resolved frequency chirp waveform technique was proposed and the chirp parameter was found to be in the range 2-2.8. Increase of coupling coefficient, which can be achieved by deepening QWs truncating, results not only in increasing of oscillation and damping frequencies, but also in decreasing of time-resolved frequency chirp oscillation amplitude that is desirable for pulse propagation in fiber. Relationship between K-factor and differential carrier lifetime and their correlation with differential gain shows on essential differential gain role in dynamic parameter spread. It is also emphasized on possible differential gain tie-in with stopband through detuning or due to the active region volume variations. Ageing experiment results have shown that dynamic characteristics of investigated LDs do not remarkably degrade during 1800 h ageing at direct current 150 mA at temperature 100°C. Carrier and photon density pulses were simulated using the same boundary conditions for rate equations as the measured pulses had. It was shown that transient processes in the distributed feedback semiconductor lasers could be described and simulated by simple rate equations within about 5 % tolerance even if some important factors are not accounted for. By varying such model parameters as carrier and photon lifetime, differential optical gain and spontaneous emission factor, the simulated pulses matched the measured ones. The best results were obtained for samples where carrier and photon oscillation amplitude was larger and the damping was lower, i. e. in samples with negligible nonlinear gain effect on the pulse form. Frequency transfer function simulation shows that simulated oscillation frequency well coincide with that obtained from relative intensity noise measurements.

7. REFERENCES

1. H. Lu, T. Makino, and G. P. Li, "Dynamic properties of partly gain-coupled 1.55-μm DFB lasers", *IEEE J. Q. E.*, vol. 31, (1995), pp. 1443-1450.
2. R. A. Saunders, J. P. King, and I. Hardcastle, Wideband chirp measurement technique for high bit rate sources, *Electron. Lett.*, vol. 30,(1994), pp. 1336-1338.
3. M. C. Tatham, I. F. Lealman, C. P. Seltzel, L. D. Westbrook, and D. M. Cooper, "Resonance frequency, damping and differential gain in 1.55-μm multiple quantum-well lasers", *IEEE J. Q. E.*, vol. 28, (1992), pp. 408-414.
4. G. P. Agrawal and N. K. Dutta "Long Wavelength Semiconductor Lasers" (van Nostrand Reinhold Co., N. Y., 1986).

5. F .
    vol.
6. J .
    unc
    vol.
7. M .
    USA
8. C .
    (198

5. F. K o y a m a a n d K. I g a, "Frequency chirping in external modulators", *J. Lightwave Technol.*, vol. 6, (1988), pp. 87-93.

6. J. K. W h i t e, C. B l a a u w, P. F i r t h, a n d P. A u k l a n d, "85 C investigation of uncooled 10-Gb/s directly modulated InGaAsP RWG GC-DFB lasers", *IEEE Photon. Technol. Lett.*, vol. 13, (2001), pp. 773-775.

7. M. F u k u d a, Reliability and degradation of semiconductor lasers and LEDs (Artech House 1991, USA, 1996).

8. C. H. H e n r y, "Theory of the linewidth of semiconductor lasers", *IEEE J. Q. E.*, vol. QE-18, (1982), pp. 259-264.

T

Ex
erties l
scattere

─────────────

[1] 1
Ph.
Tec
He
199
tion
[2] Was
Mo.
resp
in M
His
and

Technique of Ultra Wideband Radar Target Discrimination Using Natural Frequencies and Cumulant Preprocessing

ANDREY B. BAEV[1], YURY V. KUZNETSOV[2]

Abstract — A modification of ultra wideband aspect independent radar target discrimination method using fourth-order cumulant preprocessing is introduced. It based on the natural frequencies of the objects. The increasing of the accuracy of parameter estimation can be achieved if the correct choice of one-dimensional slice of 3-D fourth-order cumulant sequence is made. The usage of this technique with signature algorithm leads to the increasing of the true discrimination probability if the space of attributes includes the most informative parameters of the objects. The results of experimental research of the signals scattered by the scaled aircraft models by using the signature algorithm with fourth-order cumulant preprocessing are presented.

Index Terms — Cumulants, signal processing, target recognition (radar), time domain analysis.

1. INTRODUCTION

Experimental and theoretical researches of electromagnetic field scattering properties by various objects in wide frequency band have shown essential distinction of scattered signals' spectral and time characteristics for bodies with various geometrical

---

[1] 1 Was born in Moscow, Russia, on December 3, 1975. He received M.Sc.E. and Ph.D. degrees from the Moscow Aviation Institute (State University of Aerospace Technology), Russia, in 1999, and 2002, respectively, all in electrical engineering. He has worked for the Theoretical Radioelectronics Chair of the Moscow Aviation Institute since 1996. He is currently Associate Professor. His current research interests deal with system identification, signal processing, higher order statistics, and spectral analysis.

[2] Was born in Kursk, Russia, on December 28, 1951. He received M.Sc.E. and Ph.D. degrees from the Moscow Aviation Institute (State University of Aerospace Technology), Russia, in 1974, and 1981, respectively, all in electrical engineering. He is the Head of the Theoretical Radioelectronics Chair in Moscow Aviation Institute (State University of Aerospace Technology) from 2001. His current research interests deal with system identification, signal processing, higher order statistics, and spectral analysis.

form [1]-[3]. It confirms the fact that the ultra wideband (UWB) echo-signals preserve the information about the geometrical sizes and form of the objects.

According to the Baum's singular expansion method (SEM) [4] the transient impulse response of radar target can be divided into two parts: early-time and late-time portions. Early-time reaction consists of the entire function, and for finite time duration of excitation pulse and limited size of the object can be bounded in time.

Late-time portion of scattered field contains only damping oscillations defined by the natural frequencies of the object and its aspect angle. So the late-time reaction can be presented as a sum of damping harmonics which can be depicted by pairs of complex-conjugated poles on a complex frequency plane. In [4] it is shown that positions of these poles are practically independent from the aspect angle of excitation pulse and the initial conditions of the scattered field. Thus the interaction of exciting field with the target can be approximately described by transfer function or the impulse response of the object.

The suppression of additive Gaussian noise in received radar echo-signals is traditionally based on autocorrelation (the second-order statistics). However in such processing of UWB signals some information contained in the response, for example, the phase information is lost. The application of higher-order statistics for estimation of UWB signals parameters can help to increase the accuracy and suppress the noise [5], [6]. It is known that cumulants of the order higher than two for Gaussian processes are equal to zero. That can be used for Gaussian noise suppression through the process of parameter estimation of objects' natural frequencies.

The definition of the resonant model parameters for the data corrupted by noise can be implemented by known parametrical methods, such as modified Prony's method, Matrix Pencil Method, ESPRIT, MUSIC etc [7], [8]. The combination of cumulant preprocessing and time domain parameter estimation methods research is required in respect with the radar targets discrimination.

In this article the signature recognition algorithm of radar targets is proposed. Thus it is necessary to provide effective formation of objects' signature to develop criterion of referencing the scattered signal to one of the predetermined classes. The quality of recognition can be estimated by the true discrimination probability. This allows to determine the influence of parameter estimation accuracy on the quality of recognition and to define the alphabet of attributes used for construction of radar target discrimination algorithm.

In section II, the resonant model of ultra wideband radar targets is presented. The higher-order statistics of resonant model is discussed in Section III. Section IV describes the radar target discrimination algorithm. The results of experimental research of signals scattered by the scaled aircraft models are given in Section V. Concluding remarks are drawn in Section VI.

2. THE RESONANT MODEL OF RADAR TARGETS

In accordance with Baum's SEM the structure of the scattered electromagnetic field has rather complex character depending on the shape, polarization and aspect angle of the exciting transient pulse and the geometrical form and size of the radar target. The surface currents caused by incident field form the scattered field in all directions and on all frequencies existing in transient exciting signal.

The linear model of late-time portion of received echo-signal can be presented by a sum of exponentially damped harmonics x[n] corrupted by noise w[n] as following

$$y[n] = x[n] + w[n] = \sum_{k=1}^{K} A_k e^{-\sigma_k n T_0} \cos(2\pi f_k n T_0 + \psi_k) + w[n], \qquad (1)$$

where $s_k = \sigma_k + j2\pi f_k$ is the k-th aspect-independent natural complex frequency of the target, and A_k and psi_k are the aspect- and excitation-dependent amplitude and phase of the k-th target mode, respectively, $w[n]$ are samples of additive Gaussian band-limited noise, N is a number of samples. T_o is a period of sampling.

Research of different targets' resonant properties showed the following:

— The positions of the natural frequencies on complex s-plane are practically independent on the aspect angle and polarization of the exciting wave.

— The diagram of poles for each object is unique.

That allows distinguishing objects of various classes if the parameters of natural frequencies are determined.

To make the analysis of ultra wideband radar target discrimination algorithm we have selected resonance frequencies [1], [9], appropriate to resonances of scaled models of aircrafts F-4 and MIG-27.
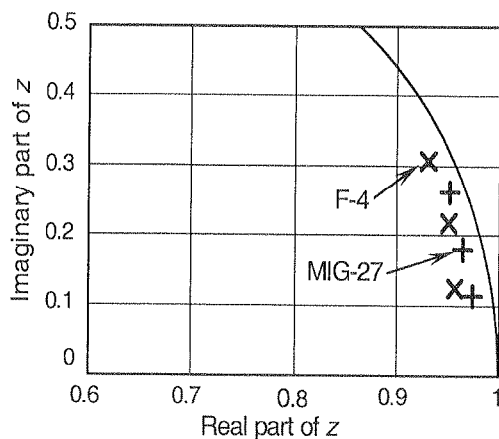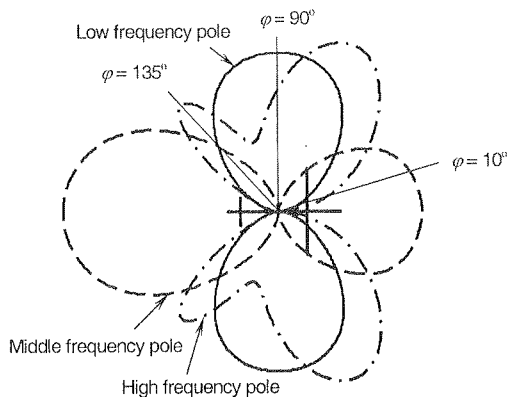

Fig. 1. Complex z-plane plot of aircraft models

Fig. 2. The dependence of resonant poles' residues on the aspect angle

Fig. 1 shows the locations of resonant poles on the complex z-plane for these targets. The values of poles on complex z-plane can be expressed

$$z_k = \exp\{(\sigma_k + j2\pi f_k)\,T_o\}.\tag{2}$$

The signal-to-noise ratio (SNR) was estimated as

$$q = 10\lg\left\{\frac{1}{N \cdot \sigma_w^2}\sum_{n=0}^{N-1} x^2[n]\right\},\tag{3}$$

where σ_w is the standard deviation of the Gaussian noise $w[n]$.

Fig. 2 shows the poles' residues A_k dependence on aspect angle according to [1, p. 487]. Fig. 3 shows the power spectrum of these resonant models for different aspect angles φ. From this Fig. 3 it is visible that at some aspect angles power spectrum peaks appropriate to some poles of the object may vanish. Thus new resonant maxima do not occur.
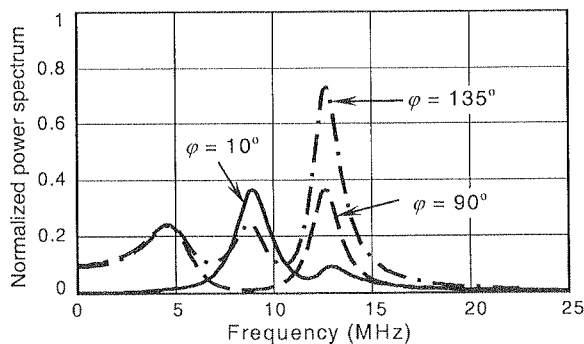
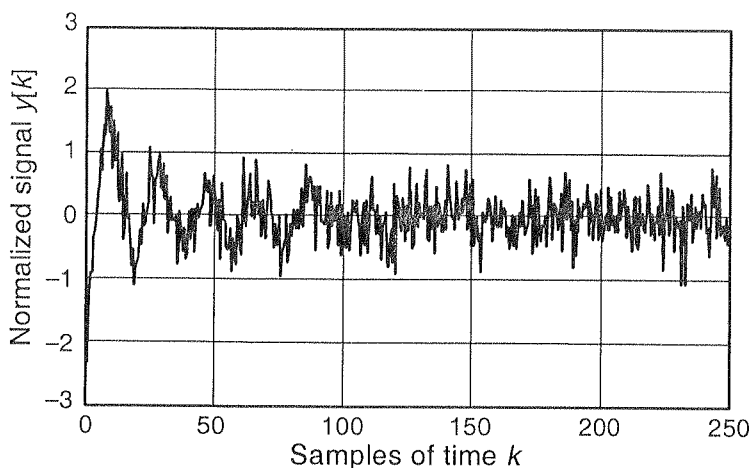Fig. 3. Power spectrum of resonant model for different aspect angles

Fig. 4. Scatters signal of F-4 scaled aircraft model, SNR = 5 dB

3. THE HIGHER-ORDER STATISTICS OF RESONANT MODEL

Fig. 4 shows realization of received echo-signal's (1) resonant model for the scaled aircraft F-4 described earlier. We assumed that the signal (1) periodically repeats with period N, so this signal concerns to signals with bounded mean power. It is clear that for this SNR the signal is highly corrupted with noise and as been shown in our previous article [6] the accuracy of parameter estimation even for the best known methods is pure.

As the echo signal has zero average value, its cumulants $c(\tau)$ up to the third order will coincide with the moments $r(\tau)$. The third-order cumulants and moments are defined by equation:

$$c_3^y(\tau_1, \tau_2) = r_3^y(\tau_1, \tau_2) = \frac{1}{N} \sum_{k=0}^{N-1} y[k] \, y[k + \tau_1] \, y[k + \tau_2]. \tag{4}$$

It's clearly seen the third-order cumulants is two-dimensional sequence, shown in Fig. 5.

As we can use only one-dimensional function in the parameter estimation algorithm, it is necessary to determine the slice, which can represent the model with undisturbed parameters and less corrupted by noise. We've determined experimentally the best 1-D slice of third-order cumulants sequence, which is shown in Fig. 6. From this figure it is seen, that simultaneously with redaction of noise level there is a significant reduction of the echo-signal level. It conforms the statement that third-order cumulants for symmetric signals tends to zero and therefore third-order statistics gives
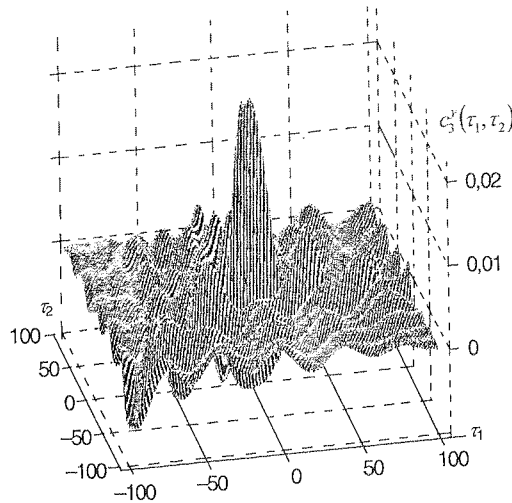
Fig. 5. Third-order cumulants of F-4 resonant model

not good results [6] when it used with parameter estimation algorithms. So we needed to use fourth-order cumulants, which are defined by equation:

$$c_4^y(\tau_1, \tau_2, \tau_3) = r_4^y(\tau_1, \tau_2, \tau_3) - r_2^y(\tau_1) r_2^y(\tau_3 - \tau_2) - r_2^y(\tau_2) r_2^y(\tau_3 - \tau_1) - \quad (5)$$

$$-r_2^y(\tau_3) m_2^y(\tau_2 - \tau_1), \quad r_4^y(\tau_1, \tau_2, \tau_3) = \frac{1}{N} \sum_{k=0}^{N-1} y[k] y[k+\tau_1] y[k+\tau_2] y[k+\tau_3].$$

The best 1-D slice of fourth-order cumulant sequences for the F-4 resonant model is shown in Fig. 7. It is visible that the level of Gaussian noise has considerably decreased. The results of accuracy comparison for different order cumulant preprocessing will be presented in section V.
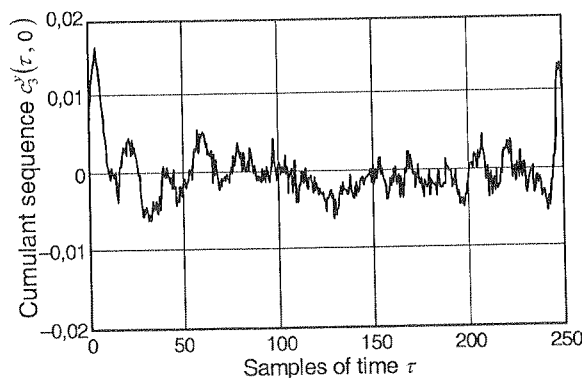

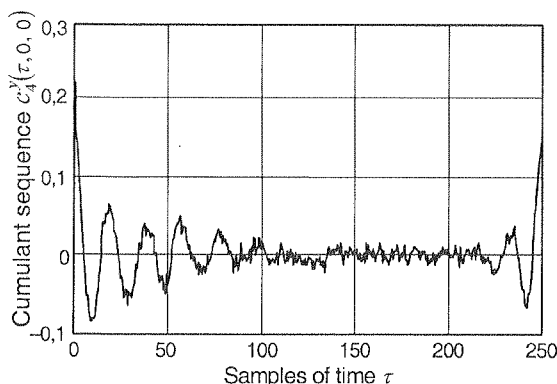Fig. 6. 1-D slice of third-order cumulant sequence of F-4 resonant model

Fig. 7. 1-D slice of fourth-order cumulants sequence of F-4 resonant model

4. RADAR TARGET DISCRIMINATION ALGORITHM

In this paper the following task is considered. It is necessary to discriminate the given number of radar targets by using measured ultra wideband responses of objects [9]. It is supposed that these objects are a priori divided into M classes. The set of the measured natural poles $z_1, z_2, \ldots, z_K$ is used as attributes of the chosen targets' classes, or as a dictionary of attributes.

The quantity of attributes K (the dimension of the attributes' dictionary) is determined by the given set of classes and depends on used discrimination algorithm. The expression determining classes of radar targets can be written in language of these attributes.

Generally it is necessary to minimize the attributes quantity K, which is describing the object, because it simplifies discrimination algorithm of ultra wideband radar targets. Definition of optimum number K is one of the tasks of our research.

A point in K-dimensional space of attributes represents each class of identified objects

$$\bar{S}_j = \left\{ S_{j1}, S_{j2}, \ldots, S_{jK} \right\}, \tag{6}$$

where S_{ji} is the appropriate coordinate in space of attributes, $j = 1 \ldots M$.

The measured set of attributes for the real response from ultra wideband radar target differs from each set of classes' attributes, as the signal is corrupted by noise:

$$\bar{Y}_j = \bar{S}_j + \bar{W}, \tag{7}$$

where $\bar{Y}_j$ is the set of measured attributes $\bar{Y}_j = \{Y_{j1}, Y_{j2}, \ldots, Y_{jK}\}$, $\bar{W}$ is an error in attributes' estimation because the noise is present in the received signal.

The correspondence of the measured set of attributes $\bar{Y}_j$ to one of the given classes of the targets $\bar{S}_j$ (or the decision criterion) is following. The space of attributes is divided into M not crossed areas appropriate to chosen classes of the targets. The borders of these areas are determined by the solution of optimization problem: decision

γ_j on identification of j-th class of the targets is accepted for set of the measured parameters $\bar{Y}_i$ in case if the distances R_i between $\bar{Y}_i$ and $\bar{S}_j$ in space of attributes is minimum in comparison with distances up to all other signatures:

$$k = \arg\min_i R_i = \arg\min_i \left| \bar{Y}_i - \bar{S}_j \right|, j = 1, \dots, M. \tag{8}$$

Quality of ultra wideband radar targets discrimination algorithm is estimated by true discrimination probability for the targets of all classes:

$$P_{true} = \sum_{j=1}^{M} P_j \cdot P\left(\Gamma_j / H_j\right) \tag{9}$$

where p_j is a priori probability of j-th class, $P\left(\Gamma_j / H_j\right)$ is the conditional probability of decision making Γ_j provided that is put forward hypothesis H_j about identification of the j-th class is true.

The true discrimination probability is determined by dimension of the dictionary of attributes, i.e. the quantity of the measured natural frequencies of the target, and depends on noise level $w[n]$ presenting in the data. Therefore it is important to define the boundary signal-to-noise ratio at which the given level of probability of true discrimination is provided.

5. RESULTS OF DIGITAL MODELING

For an experimental research of ultra wideband radar target discrimination algorithm the responses of the scaled models of planes F-4 and MIG-27, described in section II, were used [9, 10]. The quantitative comparison of effectiveness of the discrimination algorithms can be made by using the relative poles' variance:

$$\Phi_{z_k} = 10 \cdot \lg \sum_{i=1}^{L} \left\{ \frac{1}{L} \frac{|z_{k,i} - z_k|^2}{|\sigma_k|^2} \right\}, \tag{10}$$

where z_k is k-th pole of the signal; z_k, i is estimation of k-th pole for i-th trial run of $y[n]$ (1); L is a number of independent trial runs. Each sample of variance was computed by $L = 500$ trial runs. Independent Gaussian band-limited noise sequence each run was perturbed.

Fig. 8 shows the dependences of a total resonant models poles' variance on the signal-to-noise ratio for the higher order cumulant sequences of ultra wideband radar targets. One can see that for all signal-to-noise ratios the best quality of resonant model poles' estimation provides the 1-D slice of the fourth-order cumulant sequence $c_4^y(\tau, 0, 0)$. So the higher order cumulants can be used as an effective tool for improving the discrimination of ultra wideband radar targets.

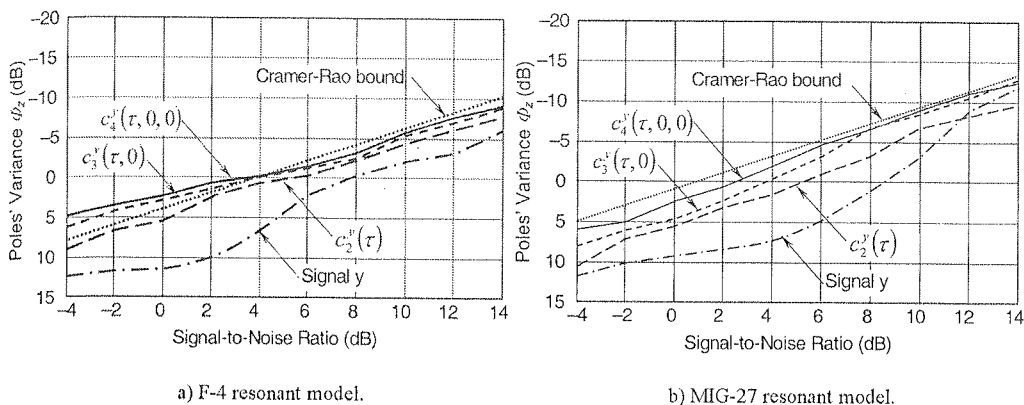a) F-4 resonant model.　　　　　　　　b) MIG-27 resonant model.

Fig. 8. The variance of the resonant model's poles

The results of F-4 resonant model's poles estimation by Matrix Pencil Method for 500 independent realizations of signal with Gaussian band-limited noise with signal-to-noise ratio SNR = 10 dB are depicted in Fig. 9. The true signal poles locations are depicted as circles, the estimations are shown as points. From the figure it is visible that estimations for high-frequency (HF) poles are concentrated near the true value while estimations of mid-frequency (MF) and low-frequency (LF) poles have much more dispersion.
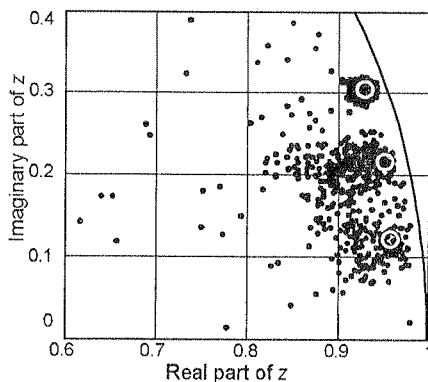
Fig. 9. The estimates of F-4 resonant model's poles for 500 independent runs using Matrix Pencil Method, SNR = 10 dB

The set of the measured natural poles on complex plane were used as information parameters in a dictionary of attributes for the radar targets. The resonant models of both targets consist of three pairs of complex conjugate poles, so a maximum quantity of attributes is $N = 6$.

At the first stage of digital modeling we analysed dependence of probability of true discrimination of radar targets on the signal-to-noise ratio at different quantity of

the information attributes N, depicted on Fig. 10. From the figure it is visible, that at reduction N for the fixed signal-to-noise ratio the probability of true discrimination is increased. It shows that the task of discrimination of ultra wideband radar targets may be solved by the best way at $N = 2$, if the HF pole is present in each case.
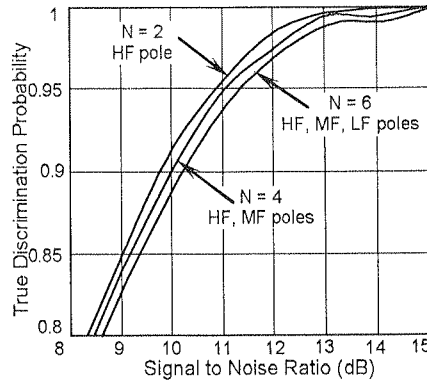

Fig. 10. Probability of true discrimination for several numbers of quantities of attributes N

Further dependence of probability of true discrimination of two radar targets was researched at $N = 2$ for LF, MF and HF poles of resonant model. Discrimination was carried out for each type of a pole independently. Probabilities of true discrimination of the radar targets from the signal-to-noise ratio for the specified types of poles are presented on Fig. 11. From figure it is visible that the maximal probability of true
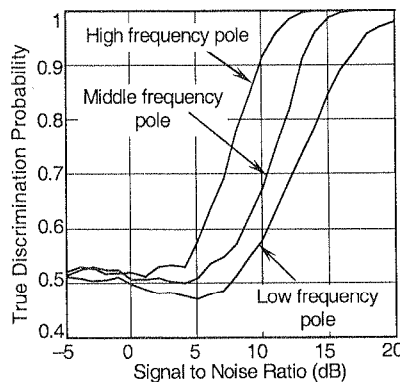
Fig. 11. True discrimination probability for single poles of resonant model

discrimination is provided with a high-frequency pole. It is possible to explain this by that the high frequency pole in our model corresponds to the higher level of Q-factor. The Q-factor of a resonant model's pole is the following ratio:

$$Q_k = \frac{\omega_k}{2\,|\sigma_k|} = \frac{\pi f_k}{|\sigma_k|}, \tag{11}$$

Dependence of probability of true discrimination of radar targets on Q-factor of poles for the fixed values signal-to-noise ratio was analyzed and depicted on Fig. 12. From figure it is visible, that for the higher values of signal-to-noise ratio the true discrimination of radar targets is possible with Q-factor of poles about 2-3. At small values of signal-to-noise ratio the acceptable level of probability of true discrimination is achieved at Q-factor of poles more than 6.
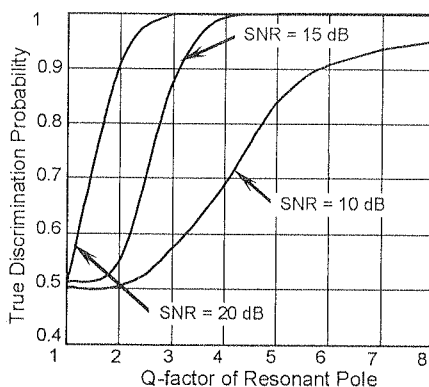

Fig. 12. True discrimination probability for one pole of F4 resonant model

6. CONCLUSION

An aspect independent radar target discrimination method based on the natural frequencies of ultra wideband radar targets in addition with cumulant preprocessing is introduced. The sets of natural resonances were offered to use as signatures of radar targets. These signatures are the points in multi-dimensional attribute space, each axis of which is proportional to the true value of poles' coordinate on a complex z-plane for the expected target.

The distance between an estimation of a point in attribute space for the identified object and the signatures of objects stored in a databank is the criterion for its discrimination. Such approach allows creating the automated system of ultra wideband radar target discrimination.

The main new results of our researches are following:
1. The application of fourth-order cumulant for preprocessing of received echo-signal leads to the increasing of SNR and therefore to the higher accuracy of parameter estimation.
2. The correct usage of fourth-order cumulant demands the choice of the best 1-D slice of three-dimensional cumulant sequence, which is preserving the information on the parameters of the objects and obtain the lowest level of noise.

3. The usage of signature algorithm for identification of the radar targets with fourth-order cumulant preprocessing allows increasing the true discrimination probability if the correct choice of the alphabet of attributes for the targets was made.

7. REFERENCES

1. J. D. Taylor, *Introduction to Ultra-Wideband Radar Systems* / editor J.D. Taylor, CRC Press, 1995.
2. E. Rothwell, B. Drachman, "A Continuation Method for Identification of the Natural Frequencies of an Object Using a Measured Response", *IEEE Trans. on Antennas and Prop.*, vol. AP-33, No. 4, April 1985, pp. 445-450.
3. T. K. Sarkar, D. D. Weiner, V. K. Jain, and S. A. Dianat, "Impulse Response Determination in the Time Domain – Theory", *IEEE Trans. on Antennas and Prop.*, vol. AP-30, No. 4, Jul. 1982, pp. 657-663.
4. C. E. Baum, "The Singularity Expansion Method", in *Transient Electromagnetic Fields*, L. B. Felson, Ed. New York: Springer-Verlag, 1976, pp. 129-179.
5. J. M. Mendel, "Tutorial on Higher-Order Statistics (Spectra) in Signal Processing and System Theory: Theoretical Results and Some Applications", *Proceedings IEEE*, vol. 79(3), March 1991, pp. 278-305.
6. Y. Kuznetsov, A. Baev, and V. Chtchekatourov, "Parameter Estimation of the Resonant Model in Passive and Active Radar Systems by Using Third-Order Statistics", in 29th *European Microwave Conference*, Oct. 1999, pp. 395–398.
7. T. K. Sarkar, and Y. Hua, "Matrix Pencil Method for Estimating Parameters of Exponentially Damped/Undamped sinusoid in Noise", *IEEE Trans. on Antennas Propag.*, vol. 38, No 5, May 1990.
8. T. K. Sarkar, and Y. Hua, "On SVD for Estimating Generalised Eigen values of Singular Matrix Pencil in Noise", *IEEE Trans. on Signal Processing*, vol. 39, No. 4, Apr. 1991, pp. 892-900.
9. Y. Kuznetsov, A. Baev, and A. Aleksandrov, "Ultra Wideband Radar Target Discrimination Using the Signatures Algorithm", in 33th *European Microwave Conference*, Oct. 2003, pp. 987-990.
10. Y. Kuznetsov, and A. Baev, "Technique of Ultra Wideband Radar Target Discrimination Using Natural Frequencies", in 15th *International Conference on Microwaves Radar, and Wireless Communications*, May 2004.

spaw
the r
Indus
empl
band
with
has e
many
2.4 C
acces

I
vance
seen
show

¹ S
B
m

A Low-Profile Dual-Band Antenna for a Wireless LAN Access Point

KONSTANTY BIALKOWSKI[1], SERGUEI ZAGRIATSKI[1] ADAM POSTULA[1]
AND MAREK BIALKOWSKI[1]

Abstract — The design of a dual-band 2.45/5.2 GHz antenna for an access point of a Wireless Local Area Network (WLAN) is presented. The proposed antenna is formed by a Radial Line Slot Array (RLSA) operating at 2.4 GHz and a microstrip patch working at 5.2 GHz, both featuring circular polarization. The design of this antenna system is accomplished using commercially available Finite Element software, High Frequency Structure Simulator (HFSS) of Ansoft and an in-house developed iteration procedure. The performance of the designed antenna is assessed in terms of return loss (RL), radiation pattern and polarization purity in the two frequency bands.

1. INTRODUCTION

In recent years, a wide expansion of Wireless Local Area Networks (WLAN) has spawned a considerable number of wireless communication protocols. As for today, the most widely spread WLAN protocols are IEEE 802.11b, which utilizes 2.4 GHz Industrial, Scientific and Medical (ISM) frequency band, and IEEE 802.11a, which employs 5.2 GHz Unlicensed National Information Infrastructure (UNII) frequency band in the USA. In Europe, an analogous ETSI unlicensed band is allocated for use with another standard named HIPERLAN. In addition, a new IEEE 802.11g standard has emerged that utilizes the 2.4 GHz frequency band. As a result of such availability, many WLAN providers are interested in offering access to the two frequency bands of 2.4 GHz and 5.2 GHz. In order to use this opportunity, both mobile transceivers and access points have to feature dual-band 2.4 GHz/5.2 0 GHz operation.

It has to be noted that the growing popularity of WLAN has ignited rapid advances in multi-band antennas for mobile transceivers. However, less activity has been seen with regard to developing access point (AP) antennas. Recent studies [1] have shown that access point antennas are an important part of WLAN systems, as they

[1] School of Information Technology and Electrical Engineering, University of Queensland, Brisbane, Australia. Email: konstanty@ieee.org, zagr@itee.uq.edu.au, adam@itee.uq.edu.au, meb@itee.uq.edu.au

are responsible for their efficient performance. The reason is that, as these systems use free frequency bands, where the maximum level of power is limited, the only available means in the physical layer to improve the quality of communication link are the radiation properties of antennas. These include such parameters as gain and polarization. From the commercial and user point of views, these antennas should feature a nice aesthetic appearance (preferably being of low profile) and low cost.

Here we propose a low profile antenna which operates in both 2.4 GHz (ISM) and 5.2 GHz (UNII/ETSI) frequency bands. This antenna consists of two different antenna elements, which are combined in one body. The first antenna element is a Radial Line Slot Array (RLSA) antenna operating at 2.4 GHz. The second antenna is a microstrip patch antenna operating at 5.2 GHz. Both antennas are aimed for producing circular polarization in the horizontal plane, when they are flat mounted at the ceiling of a room. The choice of circular polarization is intentional, as it permits freedom of orientation for the user-end antenna and enhances immunity against adverse effects of multi path propagation [2]. This is because when the transmitted wave undergoes an uneven number of reflections it changes the sense of polarization (for example from left hand circular to the right hand circular one) and as such is rejected by a receiving circularly polarized antenna. Through this property the Line Of Sight communication link is enhanced.

In order to perform an electromagnetic analysis and optimization of the proposed antenna system, Ansoft High Frequency Structure Simulator (HFSS) and in-house developed software are used.

2. DESIGN

Antenna Configuration

The dual-band antenna under investigation is shown in Fig. 1. As seen in this figure, a RLSA aimed for operation at the 2.4 GHz band [3] forms its base. The RLSA antenna consists of two metal plates separated by a suitable distance and a conducting wall which closes it. This radial cavity is partially filled with air and dielectric material to achieve rigidity of the mechanical structure and at the same to provide more degrees of freedom during optimizing of the RLSA antenna electrical performance. The feed position at the bottom plate of the antenna is implemented as a coaxial disc-ended probe. This feeding structure, when operating as a coaxial-to-radial guide transition, provides an operational bandwidth exceeding the one required for the IEEE 802.11b or g standards. Its advantage is the ease of manufacture [4].

Fig. 1. The top plate bears radiating slots, which are positioned in a circular ring. By varying orientation and position of the slots different radiation patterns and polarization can be produced. Here we aim at the RLSA design that produces a conical radiation pattern with circular polarization. This goal is achieved by using a suitable set of slot pairs, which are separated by a quarter-wavelength in the radial direction
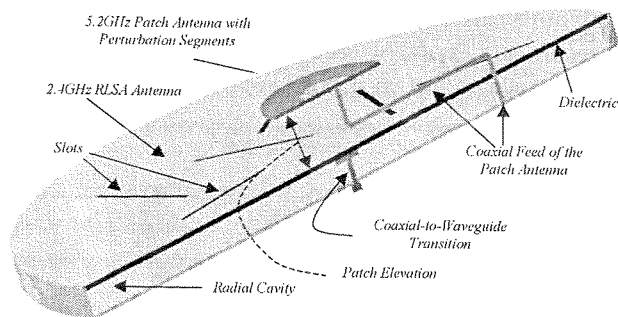
Fig. 1. Dual Band 2.4 GHz and 5.2 GHz Antenna

with the tilt of 45 degrees with respect to the radial line from the centre of the radial cavity towards to the wall [5]. The lengths of the slots are chosen to be slightly smaller than half wavelength at the design frequency of 2.4 GHz [6].

In order to achieve the operation at 5.2 GHz a conducting circular patch supported by a dielectric substrate is included at the top of the RLSA antenna [7]. To achieve circular polarization the patch includes perturbation segments (Fig.3) which excite two dominant TM_{11} modes in quadrature. The presence of the two modes (being in quadrature over a certain range of frequencies) results in a circularly polarized wave that is radiated by this antenna. It has to be noted that the patch size is restricted by the maximum available space in the center region of the RLSA. The use of dielectric substrate reduces the patch size and thus helps meeting this important design constraint.
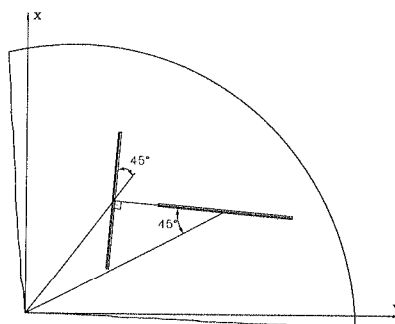
Fig. 2. Slot geometry

A challenging task concerns incorporating a suitable feeding arrangement of the patch when it is combined with the RLSA. Similarly as the RLSA antenna, the patch has to be fed from its bottom side. The other end of the feed has to be connected to the WLAN access point transceiver. The close proximity of the patch and the RLSA causes mutual coupling, which has to be taken into account during the design process. In order to avoid adverse effects, the mutual coupling needs to be minimized. Here, the feeding
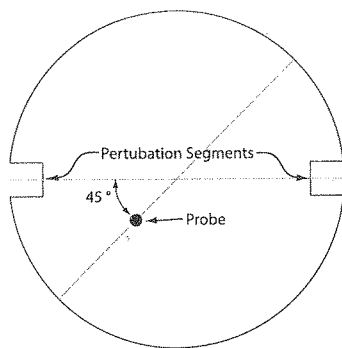
Fig. 3. Patch antenna geometry

structure is chosen in the form of a semi-rigid coaxial probe, which goes through the bottom part of the radial cavity to the patch (Fig. 1). In order to obtain impedance match to a 50 ohm system, the inner conductor of this line has to be connected to the patch slightly off its centre. The part of the coaxial cable going through the radial cavity has to be properly located to minimize interactions with the feed of the RLSA antenna. This location has to be chosen at least a quarter-wavelength away from the RLSA feed.

In order to obtain an optimal performance of the proposed dual-band antenna, the design procedure outlined above requires suitable adjustments. Here, this task is accomplished using the CAD procedure, which is described next.

Design Procedure

At the initial stage, the two antennas are designed in isolation with the aim of obtaining good RL, axial ratio (AR) and gain. When combined in one body, performances of these two antennas are expected to degrade.

To overcome the problem of dealing with too many parameters affecting the performance of the combined structure, its idealized version is considered first. In this step, the RLSA antenna including its actual feed is left unchanged but the patch assumes an ideal coaxial feed of zero height under the patch. Such an idealized feeding structure can be assumed in HFSS. This idealized structure can provide vital information on the effect of close proximity of the RLSA and the patch antenna on their return losses and radiation patterns in the two considered frequency bands.

Having performed the assessment of performance of the antenna with the idealized patch feed the next step concerns inclusion of a physically realizable feed.

Both the idealized and physically realizable antenna structures are simulated with the use of High Frequency Structure Simulator of Ansoft [8]. Using the Finite Element Method (FEM), the HFSS views the simulated structure as an assembly of dielectric and conducting objects. These objects are divided into small tetrahedrons (finite elements). The convenience of simulating arbitrarily shaped objects is offset by usually lengthy

computations due to many finite elements included in this process. This is especially true with regard to radiating structures, as the FEM requires an inclusion of an extra region to form an absorbing surface emulating an open space.

In order to simplify the simulation process, which can include a large number of iterations, the authors developed extra software to work in conjunction with HFSS. The software is similar in principle to the HFSS Optimetrics and handles such tasks as generating input data for HFSS and post-processing of the output data. The undertaken strategy and details of this in-house developed software are given in the next section.

Design Iteration

Ansoft HFSS has a scripting feature which controls the simulation procedure. This scripting feature uses the Windows OLE mechanism. Ansoft recommends VBScript (based on Visual Basic) to interact with HFSS. However, this recommendation does not impose strict limitations on the type of language to be used. Here the language 'Perl' was applied.

The design of the software was done in modular form. Fig. 4 explains how the different modules of the developed software interact to perform HFSS simulations.
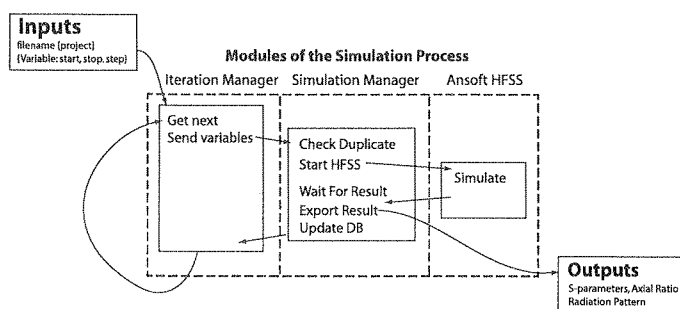
Fig. 4. Typical simulation procedure using in-house developed iterator and Ansoft HFSS

HFSS makes it possible to assign variables to certain attributes of the antenna, such as lengths, angles, positions and electric parameters of various parts of the antenna. The in-house developed software uses these attributes to vary the simulated structure. Before the in-house developed software is started, a set of variables are added to the Iteration Manager, which include the start, stop and step size. In addition a set of simulation variables is required, which include the frequencies necessary to simulate (for example, RL and radiation pattern).

The Iteration Manager is responsible for generating new sets of simulation variables for every new simulation task. The simulation task is sent to the Simulation Manager, which first makes sure that an identical simulation has not been done before. Every completed Simulation is recorded with the project filename, hash (summary of the geometry parts of the project file), and the set of variables of the simulation. The hash, being a summary of the project file, allows differences to be monitored. This is

accomplished by doing an MD5 hash of the geometry parts of the file. Once confirmed that the simulation has not been done before, the simulation job is sent to HFSS. Once HFSS completes a given simulation the results are exported into a CSV formatted file. The simulation results are also added to the result database. Once any particular simulation is complete the results can be viewed straight away – even when there are more iterations left to be done. The Result Viewing can include displaying the scattering matrix parameters on screen (or exporting them to a plotter or printer), as well as generating 2D or 3D radiation patterns and axial ratio, which gives a measure of circular polarization purity of the simulated antenna.

Due to the modular approach used here, it is possible to add other modules such as an Optimizer module. In this case, optimization methods such as Quasi-Newton method or equivalent can be employed. The implementation of such an extra procedure would require defining a set of goals and an error function. The other possible extension, which would be simple to make, is to automatically distribute the simulation jobs among multiple computers.

3. RESULTS

The first part of the work undertaken here concerned the separate designs of the RLSA and the patch antenna. This task was accomplished in an iterative manner using HFSS working in conjunction with the in-house developed software, which was described in the previous section of this paper. Following this stage, the two antennas were manufactured and experimentally tested. The experimental stage was necessary to confirm the validity of the HFSS design.

Fig. 5 shows the simulated and measured return losses over the frequency range from 2 to 3 GHz while Fig.6 reveals the simulated and measured radiation patterns (at 2.4 GHz) of the RLSA antenna operating in stand-alone configuration. The di-
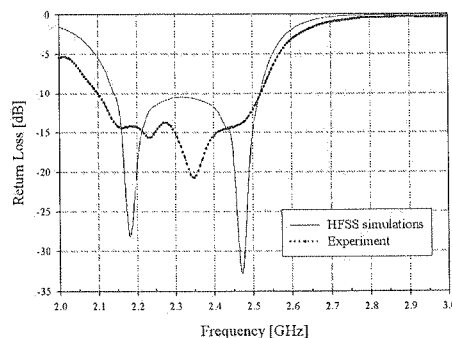
Fig. 5. Return loss of the RLSA antenna operating in isolation

mensions of the RLSA antenna were as follows: radius and height of the radial guide $H_g = 15.0$mm and $R_g = 125.0$mm respectively, slot's width and length W=3.0mm and L=53.0mm respectively. It can be observed that the simulated and experimental 10 dB RL bandwidth is about 15%.
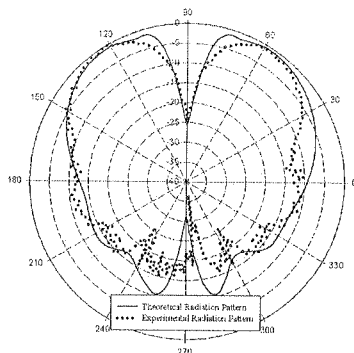

Fig. 6. Radiation pattern of the RLSA antenna in isolation

Fig. 6 shows that the antenna produces a conical radiation pattern and this feature is confirmed both by simulations and experiment. Similarly, Fig. 7 indicates both via simulations and measurements a high quality circular polarization that is achieved in the 2.4 GHz frequency band by the RLSA antenna.
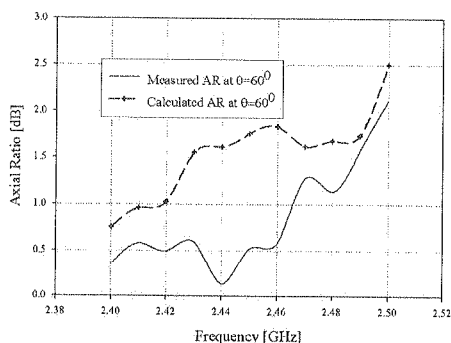
Fig. 7. Axial ratio of the RLSA operating in isolation

Fig. 8, 9 and 10 show analogous results (for return loss, radiation pattern and axial ratio) of the patch antenna operating in the stand-alone mode at the 5.2 GHz frequency band. The dimensions of the patch, which produced the presented results were as follows: patch radius $R_{patch} = 10.0$mm, probe position (measured from the centre of the patch) R – probe = 3.5mm, perturbation segment size 2mm $\times$ 2mm, and

the angle between the perturbation segments and the probe $\varphi = 45°$. The patch assumed ULTRALAM $^{\circledR}$ 2000 substrate with the thickness h= 1.5mm and the relative dielectric constant of 2.45.
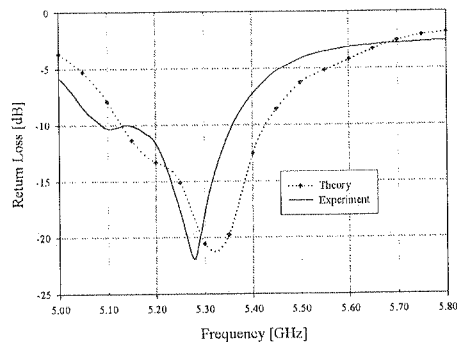
Fig. 8. Return loss of the patch antenna operating in isolation
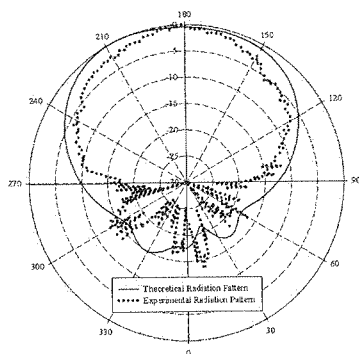
Fig. 9. Radiation pattern of the patch antenna at 5.2 GHz, as obtained in stand-alone configuration

Fig. 8 shows about a 5% 10 dB RL bandwidth of the patch both for simulation and experimental results. Fig. 9 indicates that the antenna produces broadside radiation pattern. Fig. 10 shows that the patch antenna exhibits good quality circular polarization, similarly as the RLSA antenna. Good agreement between the simulated and measured results in all of the presented cases confirms the validity and good accuracy of HFSS. Due to these reasons all of the other presented results only concern HFSS simulation results.

Figure 11 and 12 reveal the simulated return loss and radiation pattern characteristics when the RLSA and the patch are combined in one body. In this case, an idealized coaxial feed of zero height below the ground of the patch is assumed. It
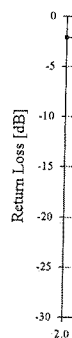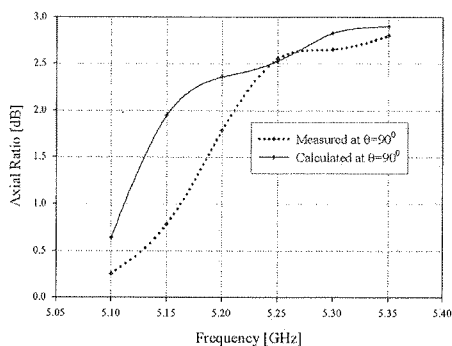
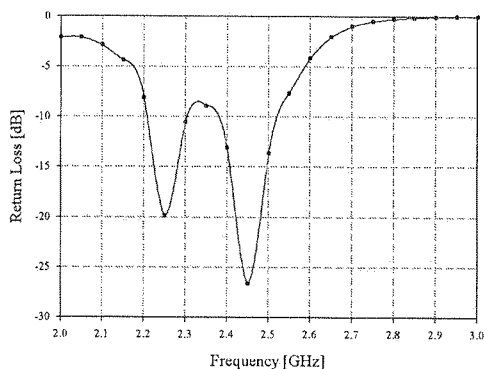Fig. 10. Axial ratio of the patch antenna in stand-alone configuration

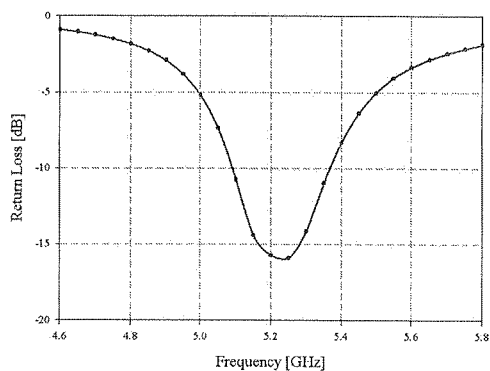Fig. 11(a). RL of the RLSA antenna in the presence of the patch with an idealised coaxial feed,

Fig. 11(b). RL loss of the patch antenna with an idealized feed as obtained in the presence of RLSA

can be seen that for the RLSA the 10 dB RL bandwidth is reduced to 4%. However the 2.4 GHz ISM band is still adequately covered. The RL characteristic of the patch remains almost unchanged in the presence of the RLSA antenna, when compared with the results presented in Fig. 8.

Fig. 12 (a) shows the simulated radiation pattern of the RLSA antenna when it is combined with the patch. The conical radiation pattern is preserved. However, a slight perturbation of symmetry of this pattern is observed when compared with the one shown in Fig. 6.

The radiation pattern of the patch antenna, shown in Fig. 12 (b), is affected only with respect to backward direction. This is expected because the patch is now supported by a large ground plane formed by the upper plate of the RLSA.

Fig. 13 (a) shows the dependence of the return loss characteristic of the RLSA
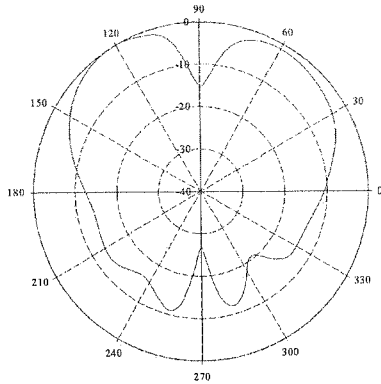
Fig. 12(a). Radiation pattern of the RLSA antenna
in the presence of the patch with an idealised
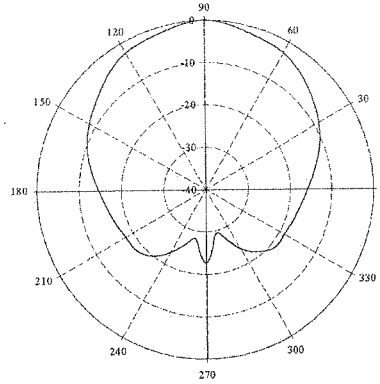coaxial feed, as obtained at 2.4 GHz,

Fig. 12(b). Radiation pattern of the patch antenna
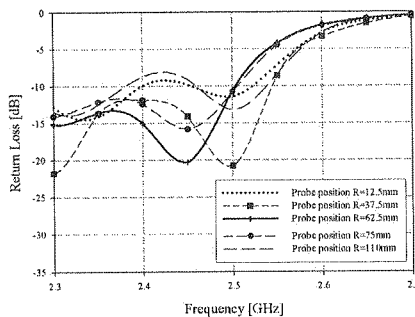with an idealized feed as obtained in the presence
of RL at 5.2 GHz

Fig. 13(a). Return loss of the RLSA antenna in in
the presence of the patch when location of the
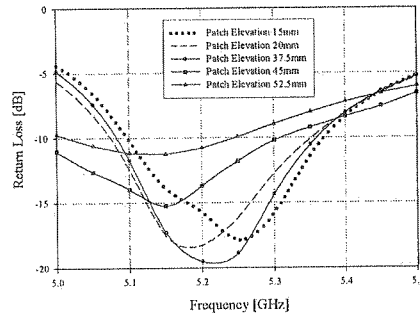coaxial cable through the radial cavity is varied,

Fig. 13(b). Return loss of the patch antenna as a
function of its height above the RLSA antenna

antenna when the location of the coaxial cable going through the radial cavity is moved
away from the centre of the RLSA. It can be seen that coaxial cable has a small effect
on the RLSA return loss when its location becomes larger than 37.5mm (a quarter-
wavelength at 2.4 GHz) from the centre of the RLSA. It has been found that for such
locations, the radiation pattern followed that of the idealized feed case, as shown in
Fig. 12 (a).

Fig. 13 (b) represents the calculated return loss of the patch antenna when it is
elevated at a certain height above the RLSA antenna. Note that the presented results
correspond to the case when the RLSA antenna is terminated in a matched load. It is
observed that the RL of the patch is slightly dependent on the choice of the height

of the patch above the RLSA. Small heights in the range of 15-30mm are optimal. In order to satisfy the low-profile design as well as to guarantee enough space for accommodating a co-axial bend or L-shape connector feeding the patch antenna an elevation of 20-25mm can be chosen.

Fig. 14 shows that the results for circular polarization as measured in terms of axial ratio. As seen in this figure, high quality circular polarization is maintained both at 2.4 GHz and 5.2 GHz frequency bands when the two antennas are combined in one structure.
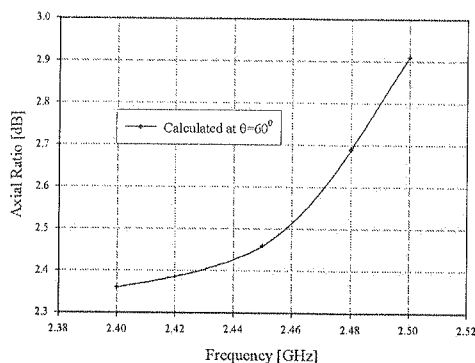

Fig. 14(a). Axial ratio of the RLSA antenna in the presence of the patch antenna with a physically realizable coaxial feed,
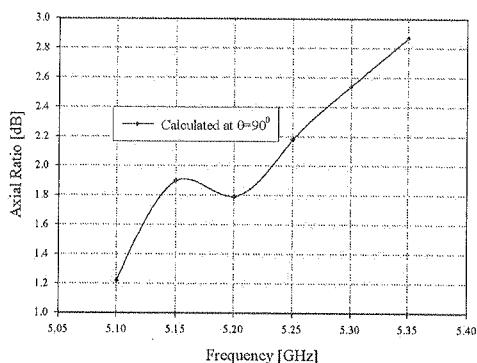
Fig. 14(b). Axial ratio of the patch antenna with physically realizable coaxial feed when operating in the presence of RLSA

4. CONCLUSIONS

In this paper, the design of a dual-band (2.45/ 5.2 GHz) antenna with circular polarization for operation as an access point antenna of a WLAN has been described. A Radial Line Slot Array antenna operating at 2.4 GHz combined with a circular patch antenna operating at 5.2 GHz forms this dual-band antenna system. The design of this radiating structure has been accomplished using commercially available Ansoft HFSS and in-house developed software. The investigations have included two cases, one when the two antennas operate in stand-alone configurations and two, when they are combined in one body. The main problem that has been overcome in this design concerns a suitable feeding arrangement for the patch without adversely affecting the operation of the RLSA. Using the proposed feeding arrangement, which includes a suitable positioned coaxial line going through the radial cavity, it has been shown that the radiation patterns of the combined structure are similar to those produced by the two antennas in the stand-alone arrangements. The dual-band antenna produces fine performances in terms of return losses and radiation patterns in both frequency bands.

The obtained results indicate that the proposed antenna should be attractive for use as an access point antenna in dual-band 2.45/5.2 GHz WLAN systems.

5. ACKNOWLEDGEMENTS

6. REFERENCES

1. K. S. Bialkowski, A. Postula, "Demonstrating the effects of multi-path propagation and advantages of diversity antenna techniques", *Proc. Antennas and Propagation Society International Symposium*, vol. 3, June 2003, pp. 654-657, 22-27.
2. K. Fujimoto, J. R. James, "Mobile Antenna Systems Handbook", Norwood, MA: Artech House, 1994.
3. S. Zagriatski, M. E. Bialkowski, "Radial Line Slot Array Antenna for IEEE 802.11 b/g Wireless LAN Applications", *Proc. 7th International Symposium on DSP and Communication Systems, DSPCS'03*, December 2003, pp. 153-158.
4. M. E. Bialkowski, "Analysis of a Coaxial-to-Waveguide Adaptor Including Disc-Ended Probe and a Tuning Post", *IEEE Trans. Microwave Theory Tech.*, vol. 43, Feb. 1995, pp. 344-349.
5. J. Takada et al., "Circularly Polarised Conical Beam Radial Line Slot Antenna", *Electronics Letters*, vol. 30, no. 21, Oct. 1994, pp. 1729-1703.
6. M. S. Castaner, "Low-Cost Monopulse Radial Line Slot Antenna", *IEEE Trans Antennas Propagat.*, vol. 51, no. 2, February 2003, pp. 256-263.
7. H. Nakano, K. Vichien, T. Sugiura, J. Yamaychi, "Singly-Fed Patch Antenna Radiating a Circularly Polarized Conical Beam", *Electronics Letters*, vol. 26, no. 10, May. 1990, pp. 638-639.
8. Ansoft ® HFSS™ Version 9.0 Full Manual

Modelling of mutual coupling in microstrip antenna arrays fed by microstrip line

MARIUSZ KOSOWSKI[1], WŁODZIMIERZ ZIENIUTYCZ[1]

Abstract — The results of modelling of the coupling between the rectangular microstrip patches in linear arraty are presented. The equivalent circuit in form of a combination of the transmission lines stubs is proposed. It is then applied to model the coupling between two subsequent patches and two patches separated by third one. It is shown that such circuit well represents the mutual coupling in the narrow frequency band (4%). The equivalent circuit was applied to examine how the coupling modified the signals in the input ports of the array and as a consequence how the radiation pattern of the array is changed due to the coupling between the patches. Two linear arrays with cocecans radiation pattern were next designed to verify the theory: first which included proposed equivalent circuit and second one without the coupling (reference array). The results of measurements of VSWR and the radiation pattern for both arrays are presented and compared with theory.

1. INTRODUCTION

The mutual coupling between radiating elements in the antenna arrays is an important factor which should be taken into account in small arrays [1] as well as in classical microstrip arrays [2] and multi-element antennas oriented to wireless communications [3]. The complete structure of the array of rectangular patch antennas can be currently simulated by fullwave simulators but such procedure is very time consuming if a feeding structure is included into simulations. It is worthwhile to mention that fullwave professional simulators cannot include all physical phenomena so even in this case the numerical results should be treated only as a good approach. The simplified synthesis methods based on an array factor seem to be still attractive and sufficiently accurate for the cases when requirements for radiation pattern are not too excessive.

In this paper we proposed a simple method which permitted to include the mutual coupling between rectangular patch radiators into the procedure of an array synthesis. An equivalent circuit in the form of the combinations of the transmission lines with

---

[1] Mariusz Kosowski and Wodzimierz Zieniutycz are with Gdańsk University of Technology, Faculty of Electronics, Telecommunications, and Informatics (ETI), Department of Microwave and Antenna Engineering, ul. Narutowicza 11/12, 80-952 Gdańsk, Poland, e-mail: wlz@pg.gda.pl

shorted and open stubs was introduced between the input ports of the patch radiators to simulate the electromagnetic mutual coupling between the patches. The elements of such circuit were found by fullwave simulation of the mutual coupling between the patches. The results of simulations were presented for the cases of the couplings between two subsequent patches and between two patches separated by third ones. Once the elements of the equivalent circuits for mutual couplings were found we used them in the circuit simulator to examine the influence of the coupling on radiation pattern of the array efficiently. The equivalent circuit permitted us to design the feeding structure of an array including the effects of the couplings between the radiators using the circuit simulator. Such procedure led to substantial reduction of calculation time.

In order to verify the procedure an exemplary case of 8 element linear array of rectangular patch antennas with cosecans radiation pattern designed for frequency f=13 GHz was discussed. The results of measurements of reflection coefficient and the radiation pattern of the fabricated array were presented and compared with theory and with the parameters of the reference array which was designed neglecting the effect of mutual couplings.

2. THEORY AND RESULTS OF SIMULATIONS

We considered 8 element linear array of patch radiators designed for frequency f=13 GHz (Fig. 1). The patches were placed in such way that the radiating edges of two subsequent patches are against each other. The distance between the patches was $\lambda_0/2$ (λ_0 — free space wavelength). We expected that the mutual coupling could not be neglected for this structure. The patches were matched to 50Ω input ports by quarter wavelength transformers. For simulation and for fabrication we used as a substrate TACONIC TLC-30 ($\varepsilon_r = 2.99$, h=0.508).

We treated the array from Fig. 1 as 8-port network and the scattering matrix elements were calculated with a help of electromagnetic simulator. Agilent ADS MOMENTUM was used for all simulations.
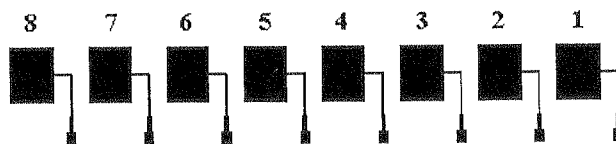

Fig. 1. Linear array of 8 rectangular patches fed by microstrip line

The typical results of calculations of the scattering matrix elements are shown in Table 1.

We can observe from Table 1 that the coupling coefficients $-S_{12}|$ and $|S_{13}|$ are similar however they are less then -20 dB. The absolute value of next coefficient ($|S_{14}|$) differs about 3 db from $|S_{13}|$. The calculations also showed that the coupling

Table 1

The exemplary scattering matrix S parameters calculated for 8-port from Fig. 1.
The first figures in lower row concern the absolute values and they are in [dB]
whereas the second ones are the phases (in [deg])

S_{12}	S_{13}	S_{14}	S_{15}	S_{16}	S_{17}
−21.9/−147.7	−23.3/−61.9	−26.1/111	−28.5/−75.2	−30.2/100	−31.5/−82

coefficients were similar for other combinations of the ports. It is worthwhile to mention that the reflection coefficient $|S_{11}|$ calculated for isolated patch was about −43 dB. The coupling effect deteriorated the matching so when the coupling was taken into account we obtained $|S_{11}| = -29.7$ dB. The data presented in Table1 suggested that for the first approximation we could take into account the coupling between two subsequent patches and two patches separated by the third one.

In order to model electromagnetic coupling between the patches we proposed the equivalent circuit in the form of the transmission lines (T1, T2, T3) with opened (TO) and shorted (TS) stubs (Fig. 2). Such circuit was an effect of a number of the numerical
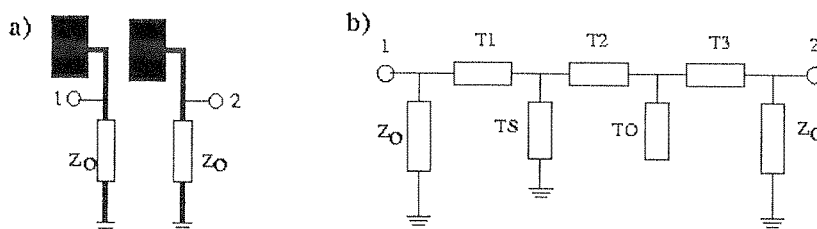

Fig. 2. Physical structure of the coupled patches (a) and the equivalent circuit (b)

experiments. We calculated from MOMENTUM the characteristics of isolated patch and they were introduced together with equivalent circuit to circuit simulator Agilent ADS. Optimizing procedure were used to find the parameters of equivalent circuit which permitted to fit the circuit model to the results of fullwave simulations. In Fig. 3 there are shown the exemplary absolute values $|S_{ii}|$ and $|S_{ii+1}|$ calculated from MOMENTUM, compared with these ones obtained from circuit simulation by Agilent ADS.

The differences between the results of electromagnetic simulations and modeled values are less 0.4 dB for mutual coupling in the frequency range 12.8-13.2 GHz. The modeled reflection coefficients agreed very well with fullwave simulations. The characteristics of the reflection coefficient $|S_{i+1i+1}|$ was similar to $|S_{ii}|$ so we do not showed them here. We also used equivalent circuit from Fig. 2 to model the coupling between two patches separated by the third one. The results of simulations are shown in Fig. 4. One can observe similar behaviour of the characteristics as compared to these ones presented in Fig. 3 but the coupling is about 2 dB weaker.
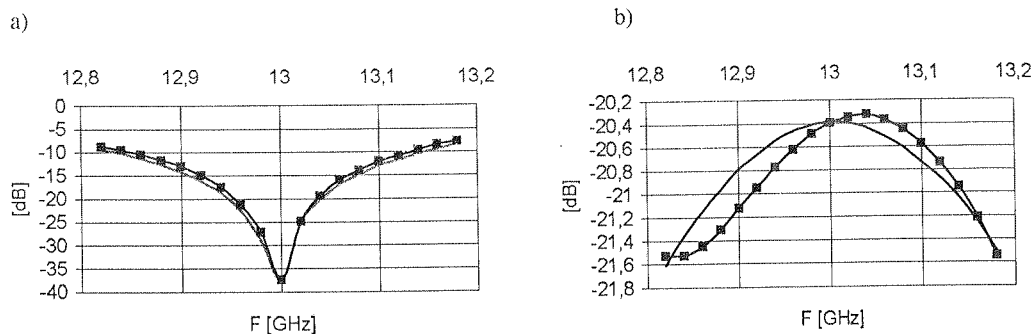
a)   b)

The

Fig. 3. Reflection (a) and coupling (b) of two subsequent coupled patches: simulated by
Agilent ADS MOMENTUM (thin solid line) and modeled by the equivalent circuit
from Fig. 2b (squared line)
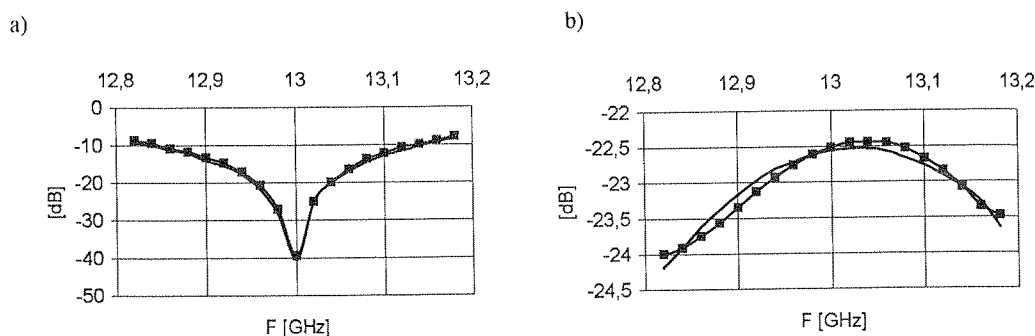
a)   b)

Fig. 5.
for an

Fig. 4. Reflection (a) and coupling (b) of two coupled patches separated by third one: simulated by
Agilent ADS MOMENTUM (thin solid line) and modeled by the equivalent circuit
from Fig. 2b (squared line)

It
of the
leads

Once the equivalent circuits for both couplings were determined they were introduced between the input ports of the array and we examined the influence of the coupling on the operation of the array. In the first step we applied equivalent circuits to calculate the excitation coefficients which were modified to the coupling effects. We used for simulation an array with series feed [4] (see Fig. 6) with quarter wavelength transformers to excite properly each element of the array. In Table 2 there are compared the normalized excitation coefficients a_{n+1}/a_n for cosecans pattern calculated for both cases: without and with mutual coupling between radiating patches. We can observe from Table 2 that the coupling modifies considerably absolute value of a_3/a_2 whereas other coefficient are only slightly changed. More important are the changes of the phases, however to examine the influence of the amplitudes and phases changes we calculated the radiation patterns for arrays with original and modified excitation coefficient. The results of calculations are shown in Fig. 5.

Th
linear
were
coupli
two pa
in whi
differe
the co
It
proced

Table 2

The normalized excitation coefficients a_{n+1}/a_n for 8-element array (from Fig.8) with cosecans pattern calculated without coupling (second row) and with coupling (third row). The first figures concern the absolute values whereas the second are the phases (in [deg])

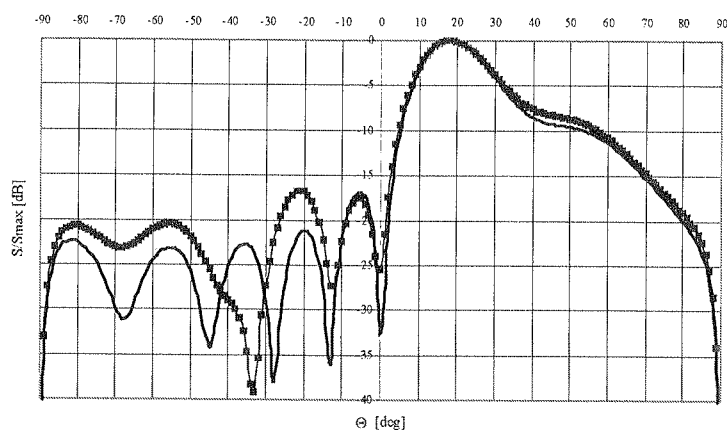| a_8/a_7	a_7/a_6	a_6/a_5	a_5/a_4	a_4/a_3	a_3/a_2	a_2/a_1
1.14/42.5	0.51/19	0.56/74.4	1/84.3	1.78/74.4	1.97/19	0.88/42.5
1.11/52.4	0.66/13.8	0.56/74.4	1.07/78.3	1.98/87.5	2.75/3.3	0.86/25.8

Fig. 5. Radiation patterns calculated for the array with undisturbed excitation coefficients (solid line) and for array in which mutual coupling between the patches was taken into consideration (squared line)

It can be seen from Fig. 5 that mutual coupling does not change the cosecant part of the pattern but modifies the maximum values of minor lobe even about 5 dB and leads to higher levels of minimums of the pattern.

3. EXPERIMENT

The procedure described in previous section was applied in design of 8 element linear array with the cosecans radiation pattern. First the equivalent circuit elements were determined so feeding structure could be designed taking into account mutual coupling between radiators. The mutual couplings between two subsequent patches and two patches separated by the third one were taken into account. The reference array in which the mutual couplings between the patches were neglected was designed. The differences of the dimensions between the arrays were smaller then 1mm so in Fig. 6 the common layout for the antennas is shown.

It should be noted that for structure from Fig. 6 the computation time for such procedure was estimated to be about 10 time smaller then fullwave simulation of
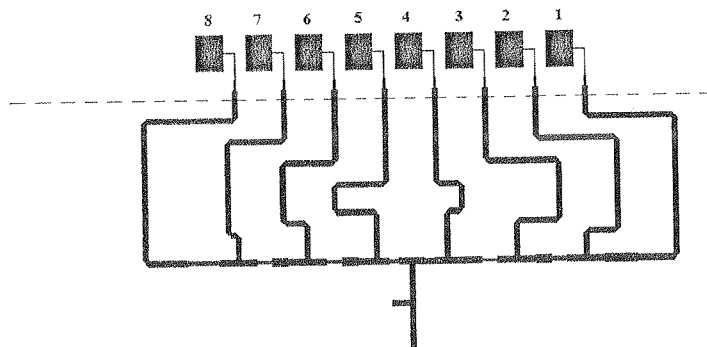
Fig. 6. The layout of array with the feeding system

total structure. Additionally, some elements of feeding system were also simulated by MOMENTUM to establish the distance between microstrips to eliminate the mutual coupling between them. In order to prevent the parasitic radiation from feeding system we covered it with an absorbing material.

The reflection coefficients for both arrays are shown in Fig. 7. It can be observed that the resonant frequencies are shifted towards the higher frequencies for both arrays. The proposed procedure leads to the results which for lower frequencies agree slightly better then the results for the reference array.
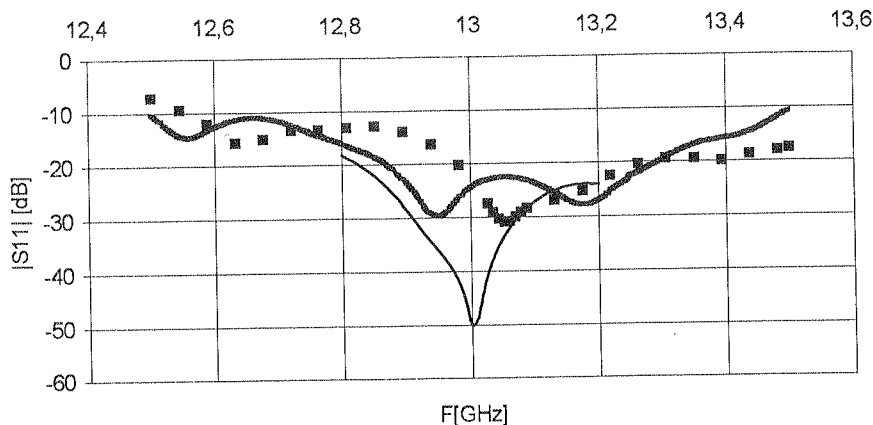

Fig. 7. Reflection coefficients: theoretical (thin solid line), measured for the array designed with the proposed procedure (thick solid line) and for the reference array (squares)

The measurement of radiation patterns showed that the operation frequency of the arrays is slightly moved towards the higher frequencies (exactly to 13.2 GHz) so in Fig. 8 E-plane radiation patterns of the arrays measured for this frequency are shown and compared with the theoretical one calculated for f=13 GHz. It is observed that

the
hor
thec
mea

patc
the
patc
prop
simu
cann
gain
linea
was
belie
SLL

the proposed procedure gives the pattern which agrees better with the theory near the horizontal plane ($\theta = 0$). The shape of the curve for $\theta < 0$ seems to be closer to the theoretical one then the curve for reference array. It should be noted however, that the measured values of SLL are about 4 dB higher then the theoretical ones.
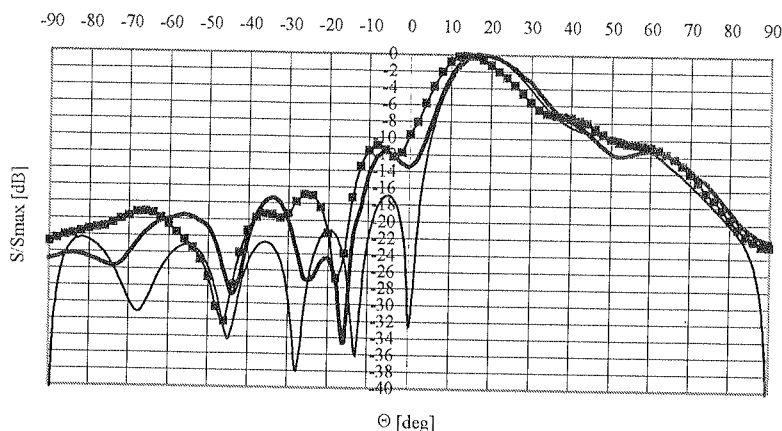

Fig. 8. The radiation patterns: theoretical (thin solid line), measured for the array designed with proposed procedure (thick solid line) and for the reference array (squared line)

4. SUMMARY

The equivalent circuit for modeling the effect of the mutual coupling between the patches in linear array was proposed. It consists of the sections of the transmission lines, the open and shorted stubs. It permits to model the coupling between two subsequent patches or two patches separated by third one in the frequency range of about 4% properly. The model of the coupling is useful in the design of feeding system by circuit simulator if the feeding system is integrated with radiating patches and the coupling cannot be neglected. Application of the proposed procedure leads to the substantial gain in the computation time. The procedure was verified for the case of 8 element linear array with cosecans radiation pattern. A slight improvement of the parameters was observed for the characteristics of the reflection and for the radiation pattern. It is believed that the proposed method would be more effective for the patterns with small SLL but it needs further studies.

5. REFERENCES

1. H . S t e y s k a l , J . S . H e r d "Mutual Coupling Compensation in Small Array Antennas", IEEE Trans. Antennas Propagat., vol. AP-38, December 1990, pp. 1971-1975.

2. P. B. Katehi "Mutual Coupling between Microstrip Dipoles in Multielement Arrays", IEEE Trans. Antennas Propagat., vol. AP-38, December 1990, pp. 1971-1975.

3. R. R. Ramirez, F. De Flaviis, "A Mutual Coupling Study of Linear and Circular Polarized Microstrip Antennas for Diversity Wireless Systems", IEEE Trans. Antennas Propagat., vol. AP-51, February 2003, pp. 238-248,.

4. E. Penard, C. Terret, "Design and Technology of Low-Cost Printed Antennas", In *Handbook of Microstrip Antennas*, Vol. 1 J. R. James and P. S. Hall Peter Peregrinus, London, UK, 1989.

syst
mill
spat
able
abst
exar
ing
giga
achi
whe
or j
of p
higl

Multi Scale Multi Physics Modeling of Microwave Circuits and Systems

(Invited Paper)

MICHAEL B. STEER[1]

Abstract — Modeling of complex systems requires that a systematic approach be adopted for multi scale and multi physics modeling. The current state of physical modeling tools in the arena of microwave and electromagnetic model is considerably mature enabling discrete problems to be considered. The real need is for hybridization of discrete modeling systems to obtain a seamless simulation environment from atoms to systems. The paper explores a strategy for multi physics multi scale modeling of microwave circuits and systems. It presents a framework guiding research in the development of electromagnetic and microwave modeling tools

1. INTRODUCTION

We have reached the stage where we can entertain the design of very complex systems that involve the interaction of a variety of physical effects and that can involve millions of elements. Examples include modeling of the microprocessor chip and of spatial power combining systems. These are enormously complex systems yet we are able to design fabricate and utilize these systems. Success has been achieved using abstract models and operating a system at significant back-off from its potential. For example, a microprocessor could contain transistor elements that have ultimate switching speeds (the transistors f_T) of hundreds of gigahertz yet clock them at just a couple of gigahertz. We compensate for the uncertainties with tremendous sacrifices in ultimate achievable performance. The same back-off can be seen in nearly all other systems where it may be called a safety margin, over-engineering, gain margin, phase margin or just engineering margin. No matter what the term, the concept betrays our lack of precise understanding, fluctuations of characteristics, and design tolerances. Much higher performance would be achieved if we had a precise understanding resulting in

[1] M.B. Steer is with the Department of Electrical and Computer Engineering, North Carolina State University, Raleigh, North Carolina, U.S.A. (email: m.b.steer@ieee.org)

both reduced engineering margin and engineering of systems hitherto not realized. Now we are at the point where we can envision the capture of a range of physical effects in determining performance. We are at the point where we must link the probabilistic world and deterministic worlds and must solve the problem of interfacing disparate physics and widely divergent scales.

If we could achieve precise multi physics and multi scale modeling we could reliably design systems without fabricating and characterizing individual components, and we could achieve optimization at a level of sophistication that is beyond the wildest of imaginings with our current process of technology and system development. It seems unreasonable to model every atom and electron yet the atomic level properties affect the composite performance. A systematic procedure based on multiple models at different scales, with models at adjacent scales linked to each other by defined parameterized interfaces that can be calibrated to measurement, is one reasonable approach. Thus multi scale modeling will involve very many organizations and disciplines leading to many seemingly incompatible approaches. It seems essential that an object-oriented approach be followed meaning in this context that there are well defined interfaces to models capturing a particular scale, and that the various scales are captured, most likely, by stand alone programs. Multiscale modeling is a grand scientific and engineering challenge. This paper presents a review of what is involved in modeling components of an electronic system; various strategies for modeling different types of electronic systems; and present examples of efforts that implement limited multi scale modeling strategies.

In this paper we will first consider the electronic design process. Then we will consider the integration of electronic circuits and the electromagnetic environment before considering a general long term strategy for multi physics and multi scale modeling.

2. REALIZATION OF ELECTRONIC SYSTEMS

We need to stand back and consider how we engineer systems. So that we are not too far ranging, the discussion here will be restricted to electronic systems but we will consider all aspects that affect the performance of such systems including the materials, the thermal, chemical and electromagnetic environments, mechanical stresses, and levels of abstraction or architecture. Since the middle of the twentieth century the essence of semiconductor-based microelectronic design has been the useful capability of predicting the circuit- level behavior before building circuits and systems. This is achieved by hiding physical details in a circuit simulator and invoking ever-increasing levels of abstraction see Figures 1 and 2. The fundamentally important abstractions are the Spice (and derivative) circuit simulators with their underlying device models. These device models capture, in a phenomenological sense, the underlying physics which are probabilistic being based on quantum mechanics. Technology Computer Aided Design (TCAD) tools that model the underlying processes yield continuum parameters such as

mobility which is a key parameter in our most advanced device models. Large systems are built using a hierarchical design methodology and our electronic system design process is based on behavioral models of ever increasing abstraction at the transistor, gate, amplifier, register, transceiver, etc., levels. Currently at each level much inherent performance information is lost but this is the trade-off we have been happy to live with to entertain the realization of very complex systems. We could continue to develop with this hierarchical design process but we have reached the point where we can integrate circuit and electromagnetic models for example, and as we become better at this we will achieve dramatic increases in the performance of systems.
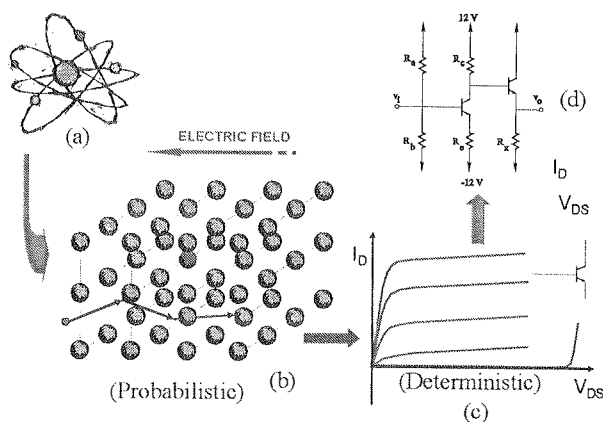
Fig. 1. Multiple scales: (a) atomic level; (b) at the crystal level illustrating scattering; (c) phenomenological terminal characteristics of a transistor; and (d) circuit-level
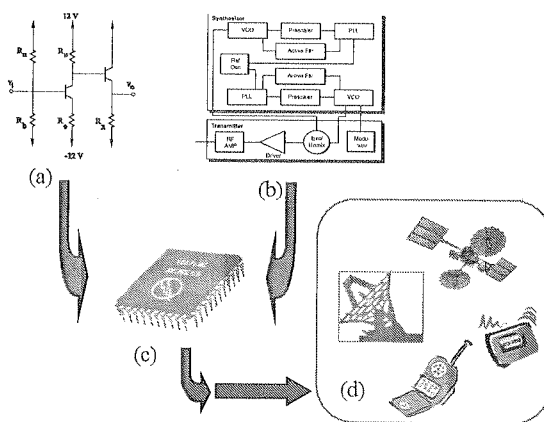
Fig. 2. Increasing scales: (a) circuit level; (b) architectural level; (c) subsystem level; and (d) system level

3. STRATEGY FOR INTEGRATING ELECTROMAGNETIC
AND CIRCUIT MODELS

The behavioral model of simple electromagnetic structures such as discrete capacitors and inductors described by first order integro-differential equations. However we need to be able to incorporate in the circuit abstraction the electrically significant spatial distributions of electromagnetic (EM) fields. That is, the accurate simulation of these circuits requires an integration of EM and electrical circuit models. One approach is to incorporate the lumped element devices of the circuit into traditional EM simulations. The device and circuit element equations are inserted into a time stepping EM simulator such as a Finite Difference Time Domain (FDTD) or Transmission Line Matrix (TLM) simulator [1]. Here the constitutive relations of the conventional circuit elements are embedded in the analysis grid of the FDTD or TLM method, and lumped elements are incorporated as equivalent current or voltage sources. Nonlinear effects are addressed by the predictor algorithm inherent in the FDTD or TLM methods. At this point we should consider the numerical strategies used in circuit simulators which must deal with large numbers of nonlinear devices with generally very strong nonlinear relations between voltages and currents. Circuit simulators, including Spice-like and harmonic balance tools, use Newton or quasi-Newton nonlinear solvers. These solvers are known as predictor-corrector strategies and provided that the step from one iteration to the next is sufficiently small, these can be rendered as globally convergent. It was found in the 1960's that predictor strategies alone cannot be used to analyze general circuits. In a predictor algorithm what has happened at past times or iterations is used to predict the state of the circuit at the next step. This is unstable in most cases unless a corrective iteration takes place. In the correction phase, a measure of error is utilized to improve the prediction. Thus unless the discrete time-domain field solvers evolve to use predictor-corrector algorithms they cannot be used to model any but the simplest of circuits. Even then, use of the discrete-time field solvers alone to solve device-field interactions has significant problems as in effect the linear electromagnetic environment would be solved repeatedly using an iterative nonlinear solver. Hybridization of the field solver is required in any case to handle general microwave structures, and it is this author's opinion that hybridization of the field solver with a circuit solver using the many advances in circuit simulation technology developed over the last five decades is absolutely required. One of the central cases in the development of a multi physics modeling environment is that we cannot afford to develop a single simulator to model all-things. We must develop a strategy that utilizes established modeling tools where possible and focus development efforts on interface technologies and on the tools that are compatible with hybridization. What we will describe in the following is alternative approach is to incorporate the EM environment as part of the circuit and to use a conventional circuit solver to integrate the EM and electrical effects.

One fundamental issue that arises in modeling electrically large systems in a circuit representation is that the topology of a circuit is based on nodes or terminals

and these, as well as the circuits themselves have zero dimension. By the very nature of the problem being solved EM simulators are three dimensional although we can collapse the number of dimensions in some cases, e.g. with planar circuits. So an essential problem interfacing circuit and EM modeling tools is resolving the discrepancy between terminals and spatially distributed structures. This problem has been resolved by defining port connections whereby the interface a single interface between the EM environment and a circuit is two terminals (being a port) which are sufficient close together that the physical separation of the two terminals can be ignored. The next most significant problem is the assignment of system ground. Currently circuit simulators use a nodal approach in which voltages are assigned to nodes and each of these voltages is referred to a common reference point commonly called ground. In a spatially distributed system, a common reference point cannot always be defined as the (electrically significant) spatial separation of a node and its reference point cannot be tolerated. If the separation is an appreciable fraction of a wavelength, it is not possible to uniquely define voltage. Introduction of the new concept of Local Reference Terminal (LRT) and Local Reference Group (LRG) are essential extensions to circuit theory required to enable the general merging of electromagnetic models with circuit models. The concept can be illustrated with respect to Fig. 3. Here a
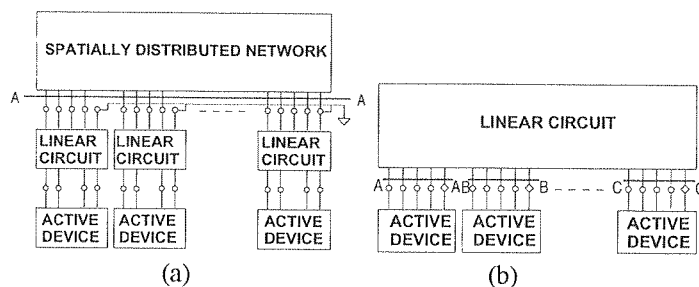

Fig. 3. Cutsets showing the application of Kircho's ⓡ current law to the circuits with: (a) a global reference node; and (b) with local reference nodes. The cuts are indicated by the lines with corresponding letters at the ends

spatially distributed structure modeled using EM techniques is connected to a circuit containing linear and nonlinear elements. In Fig. 3 (a) a single ground is used so that at the interface between the spatially distributed structure and the conventional circuit, a cutest (A-A) is performed. Conventional circuit analysis is such that the sum of the currents crossing the cutest must be zero. However, since the reference terminal for each interface group is distinct the correct way of representing this connection is using LRTs as shown in Fig. 3 (b). Note that all terminals that share an LRT form an LRG of terminals. With the introduction of LRTs there are now a number of cutsets at the interface (A-A) (B-B) etc. and for each of these the sum of the currents crossing each cutest is zero. These are quite different constraints. These constraints relate directly to nodal admittance parameters which are also the basis of circuit simulation techniques.

Thus the convenient way of representing the distributed circuit is by way of port-based Y parameters. This is similar to the modeling of N-port networks where conventionally there are two terminals at each port. Now we extend the concept to multiple terminals at each port sharing a common reference terminal. Details on the impact on circuit theory are documented in [2]. One of the issues that this example illustrates is that hybridization generally requires the development of new concepts that enable supposedly disjoint techniques to be interfaced.
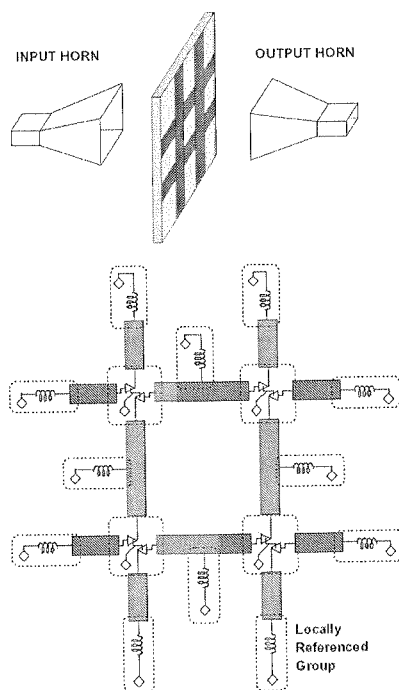
Fig. 4. An active antenna array (a grid amplifier) with four differential amplifier stages located at the intersections of a 2 × 2 grid

A spatial power combining system shown in Fig. 4 (a) illustrates the need for the LRG concept. Here a horn illuminates a planar array containing amplifiers located at the intersections of a grid. Horizontal elements of the grid are attached to the amplifier input while vertical components of the grid are attached to the amplifier outputs. The amplified output signal is orthogonally polarized with respect to the input signal and collected by the right hand horn. Shown in Fig. 4 (b) are the LRGs required to model this structure with the active devices and associated linear circuitry. Detail of the Method of Moments formulation to capture the port-based Y parameters of the grid amplifier structure is shown in Fig. 5. If this circuit were to be modeled with a common ground terminal located at each of the conventional circuits then this is the same as saying that there was no spatial separation of the circuitry. The circuit-oriented analysis

of distributed structures using the concepts presented here can be found in a number of publications [2–7].
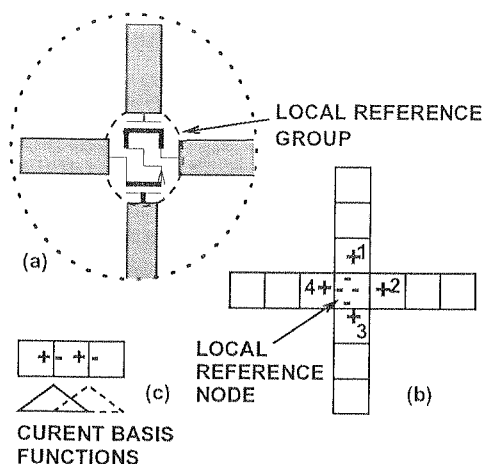

Fig. 5. Definition of differential ports: (a) a locally referenced group; (b) cells used in MOM analysis; and (c) current basis

4. STRATEGY FOR MULTI SCALE MODELING

The previous section presented one aspect of multi physics modeling, integrating circuit modeling with electro-magnetic modeling. It illustrates many of the commonalities in multi physics modeling in general. It is critically important to define the interfaces well. In this case the interface is defined by port-based admittance parameters and appropriate circuit analysis algorithms [2]. Also inherent in the circuit modeling has been multi scale modeling. Here the linkage between the phenomenological (or terminal) characteristics of the transistors are captured in device models incorporated in the circuit simulator. The link to the lower scale (at the material and transistor geometry level) has been captured by the transistor model parameters. The transistor model itself is derived through physical insight quite independently of circuit configurations. In many cases the transistor model uses geometry and material parameters but in all cases experimental verification is used to fine tune the transistor parameters. It is simply not possible to use physical modeling alone to develop sufficiently accurate models at a higher scale. This parameter calibration must also be a characteristic of multi scale modeling.

Let's step back a minute and consider the origins of microwave network analysis. Microwave computer aided engineering was born out of a strategy for multi physics modeling with the use of the circuit abstraction. Electrical engineers are so comfortable with this abstraction that few pause to realize its significance and the constraints that

it imposes on modeling the physical world. One viewpoint is that a circuit — of say resistors, inductors and capacitors — is a graphical way of specifying the coupling of first order algebraic, first order differential, and first order integral equations:

$$(I = V/R), \qquad (I = CdV/dt), \qquad (I = L \int V.dt).$$

At each coupling point, that is a shared terminal in circuit terms, a mathematical coupling is established using Kirchoff's current law (KCL), stating that the sum of the currents entering each node is equal to zero. There are elaborations to this procedure to accommodate more complex constitutive relations but, if at all possible, these are described by interconnections of primitives describing simpler, lower-order interactions. What we are talking about here is a dramatic expansion of the type of abstraction undertaken. In the case of the element abstractions described above characterizations of physical objects, e.g. a parallel plate capacitor is used. When it comes to multi scale modeling we are referring to modeling the material properties and coupling this with geometry to establish the model (e.g. capacitor) parameters. Microwave, and circuit engineering in general, has evolved so that transistor and circuit elements are collected to form an amplifier and other subsystems. Subsystems then become part of systems and as the scale (or abstraction level) goes higher fewer and fewer attributes are retained. Just as it would be impossible to simulate the voltages and currents of a circuit if individual electrons were considered, it is not possible to determine system parameters such as bit-error-rate by considering circuits at the system level. In the end it is the system level parameters that really matter but it is the very basic material parameters and nanometer scale structure that ultimately determine the overall performance. Some time in the near future we will be able to examine the effect on system performance by changing material parameters, say doping level, entirely using modeling. Multi scale modeling will make this possible.

The real solutions are system solutions and the maintenance of a vibrant engineering economy requires that we maintain rapid development of capability. This has traditionally been achieved through technology selection but in the foreseeable future this will be largely achieved through sensing, intelligence, multifunctionality, and adaptivity. Thus an important part of maintaining the health of the engineering profession will be supported by advances in multi scale modeling. A representation of a multi scale modeling approach is illustrated in Figure 6. Here lower scale models are closer to the physics while higher numbered scales are at increasing levels of abstraction. In going from one scale to a higher scale information must be dropped and well defined interfaces are required. It seems clear that no one organization let alone an individual will be able to cope with all of the scales. Thus an object-oriented approach must be strictly adhered to. In this context this really means well–defined interfaces but also means that there must be a minimum amount of knowledge required to traverse from one level in the hierarchy to the next. Adaptive modeling and multi scale generic modeling techniques must be adopted. Adaptive modeling must support [8–10]:

Mathematical statement of the problem

Formulation of model uncertainty estimators

Uncertainty/error management, and

Various model creation strategies.

Within each scale there can be considerable physical and heuristic knowledge but this cannot traverse scales. As such there must be compact support for a variety of multi scale modeling representations at least for the parameterized interfaces. Not many of the current modeling representations seem appropriate. Some that do include:

Describing functions

Power series

Volterra series

Multi Resolution functions (e.g. wavelets)

As an example, with respect to transistor modeling, describing functions are typically used although table-based models are also important. The describing functions (e.g. describing a transistors current-voltage relation) need only be loosely based on device physics. What is important is that the describing functions get the trends right and the coefficients of the describing function can be traced to attributes at the lower scale (e.g. geometry in the case of a transistor model). There is a major problem at lower scales as at some point probabilistic behavior must be captured in a deterministic way. We have some examples of this being done such as the representation of mobility based on Monte Carlo simulations but there is no general solution. Multi scale model development seems to be a tractable problem except for the apparent need to capture different effects in different model domain. As a result, multi resolution modeling approaches seem to be of critical importance because of their inherent compact support in different domains (with frequency and time domains being the most obvious). This is an important point; while multi resolution techniques have been important in specific application areas it has been possible to achieve solutions using alternative approaches. In EM analysis the Fixed Multipole Method can be substituted for multi resolution analysis to achieve similar or even better results as less a priori knowledge about a problem is required. However in joining models at different scales multi resolution analysis seems to be unrivaled and deserves close examination.

5. MULTIRESOLUTION MODELING

It is apropos to demonstrate the key concepts in the application of multi resolution representations. We will do this for a circuit application. In a circuit the circuit quantities at different terminals can be varying at vastly different rates. In conventional transient analysis the basic unit of analysis is defined by the time step and the same time step is used at every terminal in the circuit. In wavelet-based transient analysis different time steps can be used in different parts of the circuit and the time step adjusted according to activity. A generic waveform is shown in Fig. 7 and different parts of the waveform vary at different rates. Instead of a waveform we could consider any quantity

that must be represented using basis functions. Ideally it would be possible to directly utilize the basis functions at various scales this providing the parameterized interfaces indicated in Fig. 6. First we will consider a number of basis function representations.
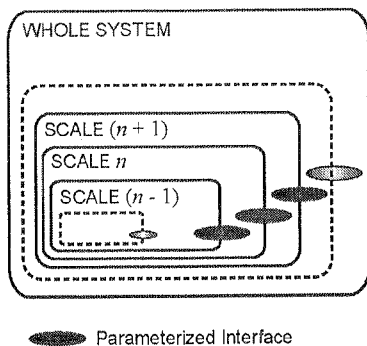

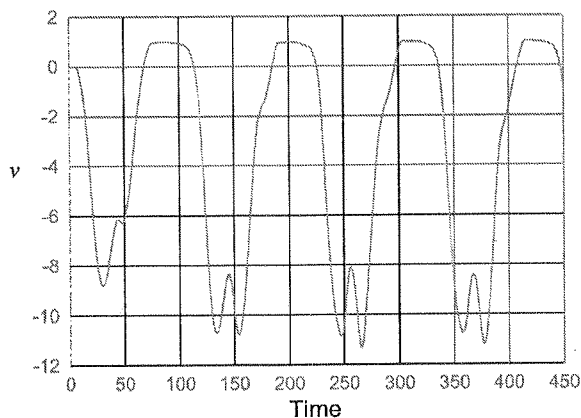Fig. 6. Representation of the multi scale modeling approach adopted here

Fig. 7. A waveform in a circuit

Fig. 8 shows the representation of the waveform using sub domain basis functions. In a circuit simulator these would be individual time steps where the inherent representation of the basis function from one time step to the next is a trapezoid rather than a pulse. Similar sub domain representations are used in electromagnetic analysis with discrete modeling methods such as finite element or finite difference methods. This is also the representation used in the EM Method of Moments. Fig. 9 presents the whole domain basis function representation. This is the EM representation used in the spectral domain representation. It is a good representation but does not capture transient (local) effects. Finally Figures 10 and 11 present two views of a multi resolution representation but at different order. The multi resolution representation shown in Fig. 10 has lower
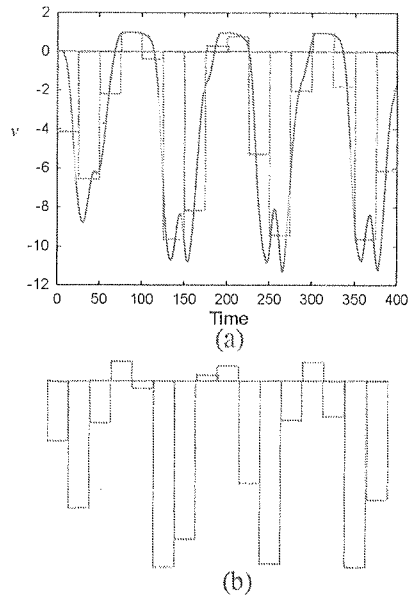
Fig. 8. Representation of the waveform using Sub domain basis function s: (a) superimposed on waveform; and (b) individual basis functions
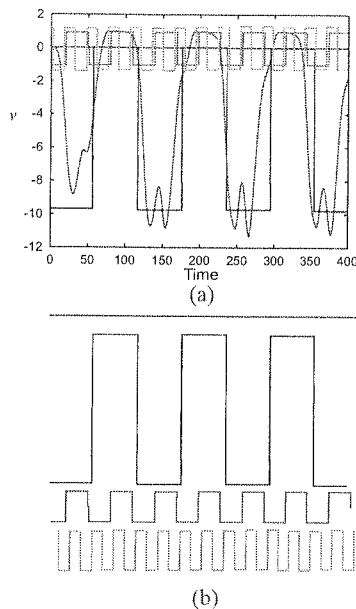
Fig. 9. Whole domain basis function representation: (a) superimposed on waveform; and (b) individual basis functions
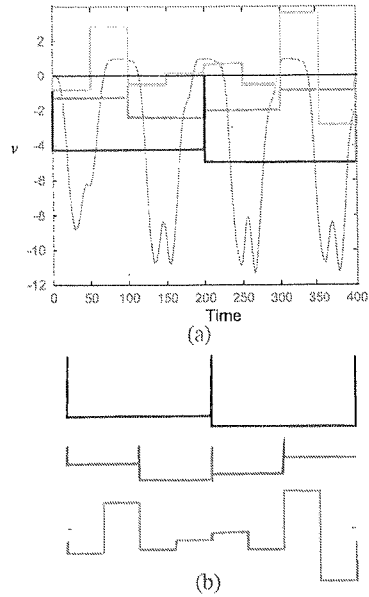
Fig. 10. Multiresolution representation: (a) superimposed on waveform;
and (b) individual basis functions

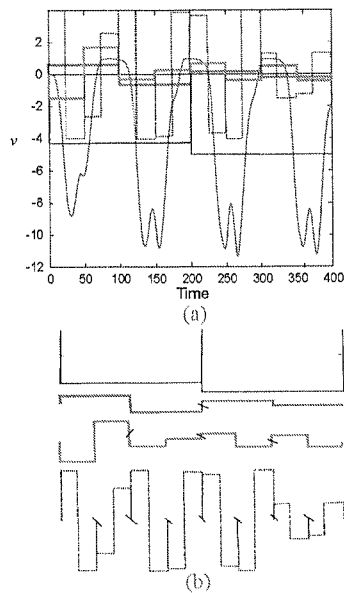Fig. 11. Multresolution representation but at higher order than that shown in Figure: (a) superimposed
on waveform; and (b) individual basis functions

ord
hap
at j
mo
Hig
cap
is o
crit
basi
of t
with
indi
and
at t
harr
the

in F
elec
thro

hybr
each
can
worl

order functions than does the representation of Figure 11 and is easier to see what is happening. In modeling a waveform a span of time is considered. Now we are looking at just pulse functions and these do not have compact support (limited width in two or more domains) however they do illustrate the principle of multi resolution modeling. Higher order multi resolution basis functions (increasing as we move down in Fig. 10 capture localized characteristics. At lower order a broad approximation of the waveform is obtained. Fig. 11 just adds another order of the multi resolution basis functions. The critical aspect here is that very fine resolution can be achieved by using high order basis functions. However in the interface to a higher level modeling scale, only a few of the low order multi resolution bases need be retained. Fine resolution is required within a scale to capture fine features. As an example consider an amplifier circuit. The individual transistors comprising the amplifier have strongly nonlinear characteristics and so it is important to represent many harmonics, perhaps twenty or thirty. However at the external terminals of the amplifier, the response can be quite linear and little harmonic distortion may be evident. Thus low order resolution is needed to capture the essential response of the amplifier.

6. STRATEGY FOR MULTI SCALE MULTI PHYSICS MODELING

A strategy for combining multi physics and multi scale modeling is illustrated in Fig. 12. Two domains are illustrated. These domains could be the electronic and electromagnetic domains. At the circuit level there are scales ranging from the atomic through transistor, circuit and subsystem level. At the electromagnetic level there are
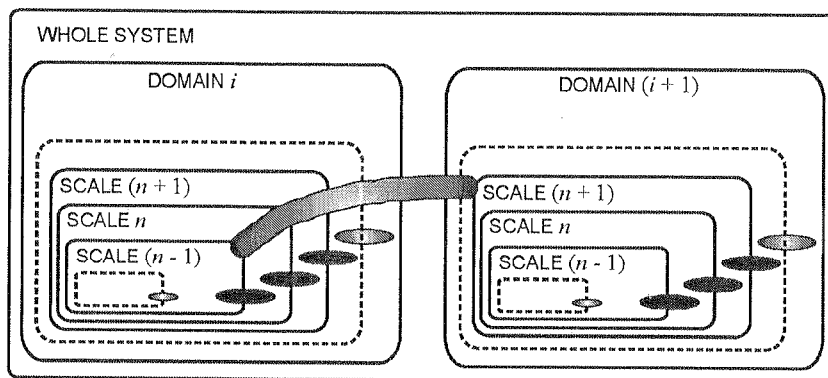

Fig. 12. Multi physics and multi scale modeling

hybridized EM analyses. At some level in each scale the domain are linked. Between each scale in each domain are parameterized interfaces. It is unlikely that modeling can ever be undertaken in isolation and regular calibration with the actual physical world is required. Space Mapping [11] is a strategy for enabling this calibration. It is

traditionally been used for the calibration of fine and coarse models and it in the multi physics multi scale context it can be used to provide calibration of models at different scales.

An example of multi scale multi physics modeling, albeit it in a primitive form, is modeling of the spatial power combining system reported in [4] and shown in Fig. 13. In a spatial power combining system the output of multiple amplifiers are combined in an EM mode to achieve large output powers. Only outline details can be provided here. Separate electromagnetic models are used for the input and output horns, planar patch
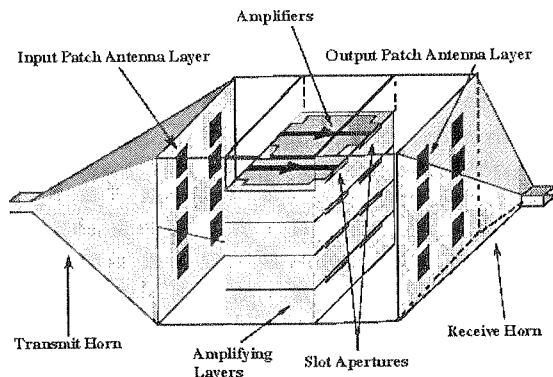
Fig. 13. A spatial power combining system reported in [5]

antenna array, and of the amplifier tiles. The electromagnetic models are combined using Generalized Scattering Matrices (GSM). In [4] the complete EM model was combined with a circuit level simulator using electro-thermal transistor models yielding the modeled responses of the system which correspond well with measurements. The key result here is that we are able to do limited multi scale and multi physics modeling.

7. CONCLUSION

RF and microwave CAE will benefit from advances in computing power and memory, the migration to new computer architectures such as highly parallel computers, and algorithmic advances. Current analysis schemes are limited to portions of circuits and not able to handle real world excitations such as digitally modulated signals without significant simplification. In the future we must be able to model accurately real world signals and whole RF front ends with the full dynamic resolution significantly exceeding the performance expected of the actual circuit. New approaches to CAE development and to the integration of dissimilar simulation and computation techniques will be developed. We have progressed from spaghetti programming to structured programming to object-oriented programming. At the same time non-CAE specific numerical algorithms have been developed and are being incorporated in evolving

CAE environments. Our views of what a circuit is (and so how it is to be modeled) have changed so we can utilize of the shelf numerics without customizing numerical algorithms to our specific requirements. Object-oriented programming is a significant paradigm shift enabling new CAE concepts to be implemented with much less effort than in the past.

8. REFERENCES

1. S. M. S. Imtiaz, and S. M. El-Ghazaly, "Global modeling of millimeter-wave circuits: electromagnetic simulation of amplifiers", *IEEE Trans. on Microwave Theory and Techn.*, vol. 45, Dec. 1997, pp. 2208–2217.
2. M. B. Steer, J. F. Harvey, J. W. Mink, M. N. Abdulla, C. E. Christoffersen, H. M. Gutierrez, P. L. Heron, C. W. Hicks, A. I. Khalil, U. A. Mughal, S. Nakazawa, T. W. Nuteson, J. Patwardhan, S. G. Skaggs, M. A. Summers, S. Wang, and A. B. Yakovlev, "Global modeling of spatially distributed microwave and millimeter-wave systems", *IEEE Trans. Microwave Theory Techn.*, vol. 47, June 1999, pp. 830-839.
3. M. B. Steer, J. W. Bandler and C. M. Snowden, "Computer-aided design of RF and microwave circuits and systems", *IEEE Trans. Microwave Theory Techn.*, vol. 50, Mar. 2002, pp. 996–1005,.
4. W. Batty, C. E. Christoffersen, A. B. Yakovlev, J. F. Whitaker, M. Ozkar, S. Ortiz, A. Mortazawi, R. Reano, K. Yang, L. P. B. Katehi, C. M. Snowden and M. B. Steer, "Global coupled EM-electrical- thermal simulation and experimental validation for a spatial power combining MMIC array", *IEEE Trans. Microwave Theory and Techn.*, vol. 50, Dec. 2002, pp. 2820–2833.
5. C. E. Christoffersen and M. B. Steer, "State-variable-based transient circuit simulation using wavelets", *IEEE Microwave and Guided Waves Letters*, Vol. 11. April 2001, pp. 161–163.
6. A. I. Khalil and M. B. Steer, "Circuit theory for spatially distributed microwave circuits", *IEEE Trans. On Microwave Theory and Techn*, vol. 46, Oct. 1998, pp. 1500-1502.
7. C. E. Christoffersen, S. Velu and M. B. Steer, "A universal parameterized nonlinear device model formulation for microwave circuit simulation", *2002 IEEE MTT-S Int. Microwave Symp. Dig.*, June 2002.
8. M. S. Shepard, M. W. Beall, R. M. O'Bara, B. E. Webster, "Toward Simulation-Based Design", submitted for publication, 2003. http://intranet.scorec.rpi.edu/reports/2003-14.pdf
9. D. Datta, R. C. Picu and M. S. Shephard, "Multigrid Atomistic Continuum Method: An adaptive approach to bridge continuum with atomistic analysis", submitted for publication, 2003.
10. R. Wentorf, R. Collar, M. S. Shephard and J. Fish, "Automatic modeling of complex woven mesostructures", *Comp. Meth. Appl. Mech. Engng.*, vol. 172, 1999, pp. 273–291.
11. J. W. Bandler, R. M. Biernacki, S. H. Chen, R. H. Hemmers and K. Madsen, "Electromagnetic optimization exploiting aggressive space mapping", *IEEE Trans. Microwave Theory Tech.*, vol. 43, Dec. 1995, pp. 2874-82.

Efi

an i
today
perfo
in th
trimn
num
class

solut
late e
long
use o

N
beam
segm
them

[1] T
e
[2] T
u

Eficient multimode mixed time-frequency domain analysis and optimization of waveguide structures

A. KRĘCZKOWSKI[1] , M. MROZOWSKI [2]

Abstract — Application of full-wave analysis and optimization method of waveguide structures having a desired topology is presented. Modeling of waveguide discontinuities by generalized scattering matrices are effi- ciently performed utilizing the modified FDTD-IBC method. Numerical optimization and model measurements of the 7-th order waveguide direct coupled cavity filter validate the presented approach.

1. INTRODUCTION

Because of low losses and high power handling waveguide structures still play an important role in the military and commercial microwave systems. Demands of today's market enforce reducing manufacturing costs, development time and improved performance. These requirements can only be met by introducing CAD-CAM methods in the whole development process and elimination of any postproduction tuning and trimming elements. The crucial factor in the whole design chain is a very efficient numerical tools that allows rigorous full-wave analysis and optimization of a wide class of waveguide components with the required accuracy.

The commercially available general purpose CAD tools do not provide an optimal solution for the design of specific microwave components. Frequently these tools simulate electrically large structures only as a whole and this often leads to the unacceptably long time of analysis. In consequence, long simulation time practically prevents the use of any optimization procedures in the design process.

Meanwhile, many microwave components like waveguide filters, multiplexers or beam- forming networks can easily be divided into smaller segments. Some of these segments must be analyzed using rigorous full-wave numerical methods, but some of them can be characterized analytically. In a few last years the above-mentioned ap-

[1] Telecommunications Research Institute, Gdansk Division, ul. Hallera 233A, 80-502 Gdańsk, Poland, e-mail: alexk@pit.gda.pl
[2] Technical University of Gdańsk, Department of Electronics, Telecommunications and Informatics, ul. Narutowicza 11/12, 80-952 Gdańsk, Poland, e-mail: mim@pg.gda.pl

proach has been gaining significant popularity among electro-magnetic computational community [1].

In this paper we introduce a new methodology of waveguide component design method which has been developed based on the following principles:

- Decomposition of the analyzed structure in the two groups of segments (discontinuities and homogeneous waveguide sections);
- Modeling discontinuities of arbitrary shape in time domain using the concept analogous to the Generalized Scattering Matrix (GSM);
- Modeling homogenous waveguide sections by GSM's using analytical formulas in the frequency domain;
- Modeling the whole structure by adopting the Connection Scattering Matrix (CSM) concept;
- Utilizing efficient gradient-based optimization strategy based on Adjoint Network Method (ANM).

2. ANALYSIS

Most of practically used waveguide components consist of discontinuities separated by sections of a homogeneous waveguide. Usually, we are interested in establishing scattering parameters of the structure in the given frequency band for the dominant mode only. Depending on the distance between adjacent discontinuities higher order modes exited at each discontinuity can interact. Therefore, to achieve a satisfactory accuracy each segment (discontinuity and homogeneous waveguide segments) of the decomposed structure has to be modeled by generalized multimodal matrix. For example, if the considered network consists of the set of two-port sections (physical ports) than each section, characterized by its individual GSMi can be represented as multiport circuit. Therefore, with every physical port there are assigned a few the so-called modal-ports. This approach is not only restricted to the physical two-ports but can easily be generalized to more complicated cases where the factor of modal port multiplication is the number of modes that one wish to take into account.

GSM's modeling of homogeneous waveguide sections, placed between discontinuities, can be easily carried out by well-known analytical formulas with virtually no numerical costs. However the discontinuities require a full wave numerical method. For simple discontinuities one may use the mode matching, but if the modeling tool is to be general one has to develop a technique that can handle discontinuities of arbitrary shape, In this paper we propose to carry out the GSM modeling of discontinuities by a hybrid PEE-FDTD [4] method with Impedance Boundary Conditions (IBC) at the section extremities. The FD-TD allows one to analyze discontinuities of any shape and PEE technique that can be used in waveguide structures yields significant acceleration of the numerical analysis.

The fundamental problem concerning numerically efficient introduction of FDTD method for wave-guiding systems consist in implementation of appropriate Absorbing

Boundary Conditions (ABC). To minimize the volume of the simulation space required by the algorithm, and hence also reduce the simulation time, one has to introduce ABC of good quality not only for the propagating mode but also for higher-order waveguide modes. Such modal ABC's can be efficiently applied using for example the concept of prediction digital filters [2]. However, Shibata and Itoh [3] have shown that the problem of multi-modal ABC can be avoided altogether if the scattering matrix of a discontinuity is calculated under the assumption of ports loaded with fixed impedances rather than for the matched ports. To obtain faster convergence by elimination of the higher order mode interaction (higher than assumed rank of GSM) we used modified algorithm by introducing FDTD-PEE scheme [4].

In our approach (Fig. 1) we introduced IBC for the first M-modes at the planes assigned to the physical ports #1 and # 2. These planes for modes M+1 to M+L+1 are simultaneously interface planes between the FDTD and PEE regions allowing energy removal of L higher modes from the vicinity of discontinuity (FDTD region).
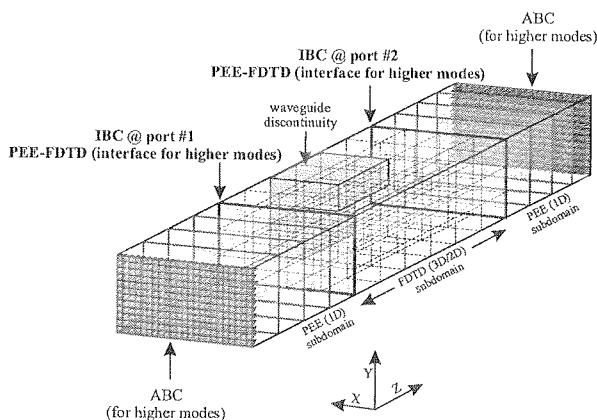
Fig. 1. Simulation space in modeling of waveguide discontinuity

The L higher-order modes are next attenuated along PEE regions and finally are absorbed at theirs extremities by simplified ABC [5]. Applying the extra homogeneous waveguide sections beyond the IBC planes, where the field behavior is modeled by PEE (Partial Eigenfunction Expansion) method, does not result in excessive increase of numerical costs because of considerably better performance of the PEE algorithm over the FDTD [4] (in the case of homogeneous waveguide).

By this approach one can minimize the volume of FDTD region containing the discontinuity and limit the number of independent simulations to a maximum of 2M runs. If discontinuity is symmetrical M-runs are sufficient to establish GSM of the rank 2M×2M. In the case of the method originally introduced by Shibata and Itoh, when discontinuities having very high reflection coefficients, (for example irises used in waveguide filters) are modeled to achieve satisfactory results for M-modes GSM one usually needs to perform much more independent simulations to account for inter-
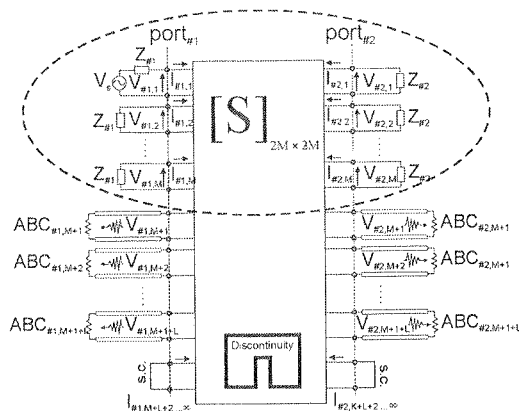
Fig. 2. Equivalent circuit of the modeled discontinuity

action of higher (than M) order modes which are reflected from IBCs. Fig. 2. shows an equivalent circuit of discontinuity with distinguished modal ports associated with physical ports #1 and #2. Time series of the equivalent 2M modal voltages at ports #1&2 registered during the simulation process allow one to obtain parameters of the GSM [3, 6].

Because all considered modal ports are generally not matched so one cannot distinguish the incident and reflected waves and in consequence the obtained GSM matrix is inconsistent with the classical one (where the matched ports loading is assumed). To obtain the classical form of GSM one has to introduce the proper matrix transformation taking into consideration change in the modal ports reference impedances [6].

Once the GSM of individual discontinuities and the homogeneous sections are known the scattering parameters of the whole structure can be computed. To this end we applied the concept of the Connection Scattering Matrix (CSM) [7].

The CSM method relies on creating W matrix containing both the information about GSM parameters of every sub-circuit and the global topology of the net. the system response can be used. The idea of creating CSM matrix and the structure of W matrix are shown in fig. 3 for the case of cascaded connection of two four-ports (we can interpret them as two-ports with two modal ports associated with every physical port). Because of the double port numbering scheme (fig.3.) dimensions of the W matrix in the case of components consisted of many discontinuities (sections) could be significant but the careful investigation of the W matrix structure reveals that this matrix is sparse and thus efficient numerical methods for obtaining

The response of the circuit represented by vector of waves incident at every port of the net for excitation placed in any desired port is given by (1):

$$\vec{a} = [W]^{-1} \cdot \vec{c} \tag{1}$$

Where vector c represents the unitary source of excitation. For example if $c = [1, 0, \ldots, 0]^{T}$ than using formula (1) one can obtain a complete system response for
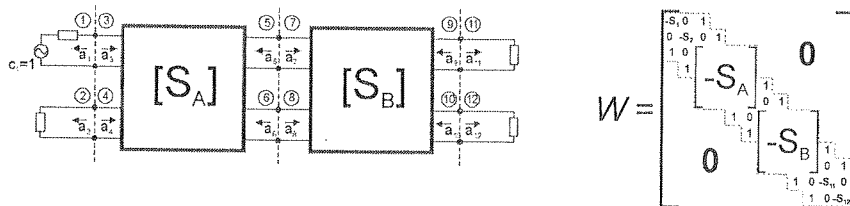
Fig. 3. An example of building connection scattering matrix of the system with a simple circuit topology. S_A and SB represent GSM matrices of two sections. Connections between modal ports are represented by "1" on crosscuts of rows and columns corresponding to the unique port pairs numbers

excitation placed at port number 1. This response is contained in the first column of inverted W matrix. It is obvious that next columns of W^{-1} could be interpreted as system's response for excitation placed in corresponding ports. Therefore only one inversion of W matrix is sufficient to obtain complete system's response to any excitation. It is worth to mention that CSM method is not restricted to cascaded connection of multi-ports but can be used to analyze systems having an arbitrary topology.

By using the CSM modeling, well established in circuit theory, together with segmentation technique described above one can significantly reduce the time of full-wave analysis of waveguide networks, compared to a classical FD-TD method, especially in the case when one can observe multiply reflections occurring between discontinuities (band-pass waveguide filters). In the hybrid approach that we propose in this paper, time domain analysis is used for individual discontinuities and hence the simulation time of the whole structure does not depend on the internal reflections or the Q-factor of the structure, while the versatility and accuracy of FD-TD is retained.

3. OPTIMIZATION METHOD

The most efficient optimization techniques involve the gradient of the objective function (derivatives with respect to geometrical parameters). For this reason we decided to adopt the ANM [7] method. With this approach one can easily find the partial derivatives of the global network. When the considered network is described by W matrix it can be shown that sensitivity of the wave amplitude at the i-th port with respect to the geometrical parameter –p can be given by (2).

$$\frac{\partial a_i}{\partial p} = \vec{\alpha}^T \cdot \left[\frac{\partial S}{\partial p} \right] \cdot \vec{a} \qquad (2)$$

Transposed vector α in ANM terminology is interpreted as a response of the adjoint network to the excitation incident at the i-th port. It suggests that besides the calculation of the original network response (a) one needs additional calculation of the adjoint network. A careful investigation of intermediate steps required to derive formula

(2) reveals that factor α is simply the i-th row of $\mathbf{W}^{-1}$ matrix of the original network and thus there is no need for additional calculations. Matrix of the partial derivatives in (2) has the rank of the $\mathbf{W}$ matrix and is expressed in terms of the partial derivatives of the GSM's of con- stituent subnetworks. Sensitivities of the wave amplitudes at the selected ports (external and usually corresponding to the fundamental mode) are used to establish the gradient of objective function expressed in terms of basic network parameters ($S_{1,1}$ and/or $S_{2,1}$).

The derivatives of the GSM's matrix with respect to the geometrical dimensions of waveguide discontinuities segments have to be approximated by finite difference. This is associated with a significant numerical expenditure. However, analogous derivatives for homogeneous waveguide segments can be evaluated analytically with a negligible numerical effort. Formula (3) represents an example of waveguide section S matrix (dominant mode only) sensitivity with respect to the section length (l).

$$\frac{\partial S}{\partial l} = -\gamma_{10} \begin{bmatrix} 0 & \exp(-\gamma_{10} \cdot l) \\ \exp(-\gamma_{10} \cdot l) & 0 \end{bmatrix} \tag{3}$$

Because ANM method allows one to limit determination of GSM's matrix derivatives only to the segments directly connected with optimized variable thus presented approach is by far more efficient compared to traditional methods which need at least one additional full-wave simulation of the entire network for each optimized variable.

4. NUMERICAL AND EXPERIMENTAL RESULTS

To illustrate the validity of presented approach the waveguide narrow band-pass filter using 8 unsymmetrical H-plane diaphragms (7 cavities) was investigated. An exploded view of the waveguide direct coupled cavity filter based on waveguide standard WG-90 (a=22.86 mm; b=10.16 mm) is presented in fig. 4.

Fig. 4. 7-th order waveguide direct coupled cavity filter

Fig.

Fig.
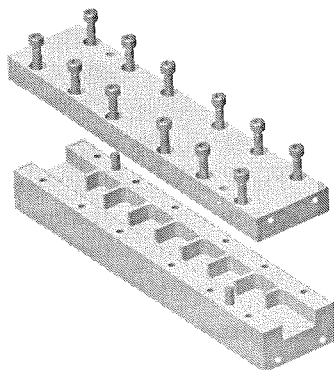
filter
slot
const
was
Duri
TE$_{10}$

The design parameters and nominal responses of the Chebyshev type filter are presented in fig. 5. The synthesis procedure based on a distributed step-impedance
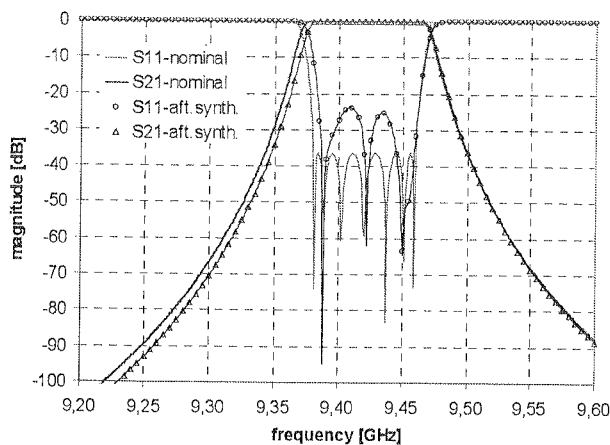
Fig. 5. Responses of the filter: nominal and the one obtained of after synthesis. Design parameters are: Center frequency = 9.42 GHz, Bandwidth = 80 MHz; Ripple= 0.001 dB
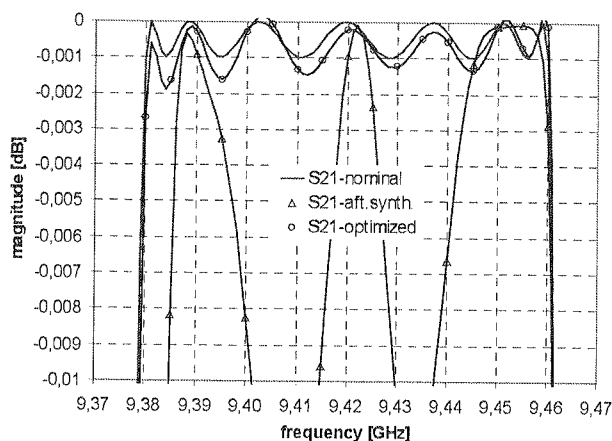

Fig. 6. Comparison of: transmission characteristics in pass-band . There curves correspond to nominal characterisitics and the characterisitics obtained after synthesis and after optimisation

filter prototype [8] resulted in 8 geometrical parameters of the structure (4 diaphragm slot widths and 4 resonator lengths). The thickness of diaphragms was assumed to be constant (d=2 mm) in whole design process. The response of the filter after synthesis was calculated (fig. 4–5) using full-wave analysis method described in paragraph II. During the analysis each segment of the structure was modeled by GSM's for modes $TE_{10} \div TE_{30}$. The calculation time of the filter response was about 2 min. on an 866

MHz PC. The deviation of the calculated response of the synthesized filter from the nominal characteristics is due to the interaction of higher-order modes between adjacent diaphragms that not taken into consideration in the synthesis procedure. To achieve design goals 8 geometrical parameters were optimized using gradient-based strategy with ANM. The starting point of the optimization procedure was parameters obtained at the synthesis stage. The results after optimization process are presented in fig. 6–7 showing little discrepancy between the optimized and nominal parameters.

The optimization time of the filter was about 3.5 h. with 3 first modes used in the GSM's modeling of each segment. Finally, the filter with optimized parameters was fabricated (fig. 4) and measured (fig. 7). Comparing the responses of simulated and measured filters one can observe high agreement of characteristics both in pass- and stop-bands. Some discrepancy can be observed with regard to the measured attenuation (–0.6 dB) and matching in the pass-band that are believed to be caused mainly by imperfect calibration of the network analyzer (lack of proper calibration kit) rather than by fabrication errors.
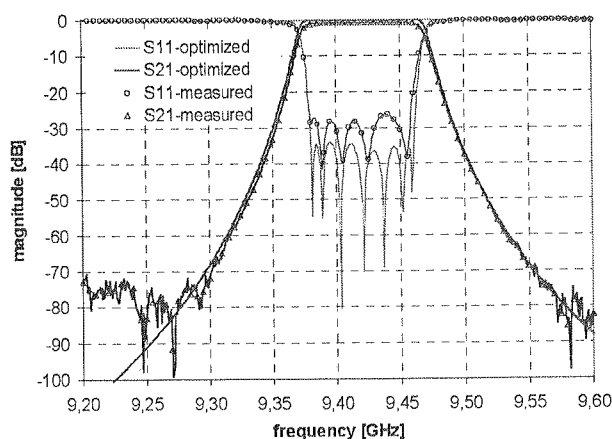
Fig. 7. Comparison of: optimized and measured filter responses

5. CONCLUSION

A method involving mixed time-frequency domain full-wave analysis and optimization of waveguide structures was introduced. The segmentation approach combined with the CSM method lets one to significantly shorten the calculation time in comparison with methods operating in the whole simulation domain (orthodox FDTD method). The FDTD-IBC is used to characterize the discontinuities so the approach can be applied to the structures having discontinuities of arbitrary shape. The adjoint network method facilitates the analytic computation of derivatives of the objective function with respect to the geometrical parameters of the homogeneous waveguide

segments. Due to this property full-wave optimization of quite complicated structure can be done in reasonable time. Since the optimization operates directly on the full-wave microwave model the component designed is ready to fabrication without the need of any post-manufacturing tuning.

6. REFERENCES

1. F. A l e s s a n d r i, M. D i o n i g i, R. S o r e n t i n o, "A fullwave CAD Tool for Waveguide Components Using a High Speed Direct Optimizer", IEEE Trans. on MTT, Vol. 43, No. 9, September. 1995.
2. M. M r o z o w s k i, M. N i e d ź w i e c k i, P. S u c h o m s k i, "Application of digital filters to the construction of wide- band dispersive boundary condition", IEEE MTT-S Int. Microwave Symp., Orlando, FL, 1995, pp. 801- 804.
3. T. S h i b a t a, T. I t o h, "Generalized-Scattering-Matrix Modeling of Waveguide Circuits Using FDTD Field Simulations", IEEE Trans. on MTT, Vol. 46, No. 11, November 1998.
4. M. M r o z o w s k i, "A hybrid PEE-FDTD algorithm for accelerated time domain analysis of electromagnetic waves in shielded structures", IEEE Microwave and Guided Wave Letters, Vol. 4, No. 10, Oct. 1994.
5. A. K r ę c z k o w s k i, T. R u t k o w s k i, M. M r o z o w s k i, "Fast Modal ABC'c in the hybrid PEE-FDTD analysis of waveguide discontinuities", IEEE Microwave and Guided Wave Letters, May 1999, Vol. 9, No. 5, pp. 186-188
6. A. K r ę c z k o w s k i, M. M r o z o w s k i, "Multimode analysis of waveguide discontinuities using the concept of generalised scattering matrix and power waves", Conf. Proceed. XIII International Conference on Micro- waves, Radar and Wireless Communications, Poland, Wroclaw, May 22-24, 2000, Vol. 2, pp. 569-572
7. V. A. M o n a c o, P. T i b e r i o, "Computer aided analysis of microwave circuits", IEEE Trans. on MTT, Vol. 22, 1974, pp. 249-263
8. Y i - C h i S h i h, "Design of Waveguide E-Plane Filters with All-Metal Inserts", IEEE Trans. on MTT, Vol. 32, 1984, pp. 695-704

its
dor
typ
wit
nor
———
wit
———
or
nod
acr
y n
the
Cor
———

A study of FDTD solutions on variable
and subgridded meshes

JANUSZ RUDNICKI[1], MAŁGORZATA CELUCH-MARCYSIAK [1]

Abstract — Numerical artifacts caused by 1D and 2D mesh refinements in the FDTD method are investigated. The effect of numerical reflections previously known from simulation practice is mathematically confirmed. It is shown that the magnitude of reflections can be accurately predicted by combining the numerical dispersion relations in the two mesh subregions with the electric field continuity condition at the interface. To this end, numerical emulation of Snell's law and non-orthogonality of the numerical field and propagation vectors are addressed. The theory is validated for the 2D TE modes at normal and oblique incidence

1. INTRODUCTION

The FDTD method is a well established tool for electromagnetic modelling, and its properties are well known for the case of uniform meshing of the computational domain. However, practical application to the analysis and design of microwave devices typically requires non-uniform meshing, so that fine geometrical details can be resolved without unnecessarily boosting the required computer resources. Two basic kinds of non-uniform meshes are in use:

— variable mesh, where the discretisation is one-dimensionally refined, in accor-- dance with the formulae $\Delta x = \Delta x(x)$, $\Delta y = \Delta y(y)$, $\Delta z = \Delta z(z)$, e.g. Fig. 1 a) and c),

— subgridding, where the mesh is simultaneously refined in two – Fig. 1 b) and d), or three dimensions.

In the variable mesh any two cells may have either a common edge, or a common node, but not both. This enforces a rather straightforward field continuity condition across the mesh interface. With reference to Fig. 1a, the E_y field at $x = 0$ and any y must be common for the coarse mesh ($x < 0$) and fine mesh ($x > 0$) solutions. In the case of subgridding, one coarse-mesh edge is split into several fine-mesh edges. Consequently, one has more options for "sewing" the coarse and fine mesh solutions

---

[1] Instytut Radioelektroniki Politechniki Warszawskiej, 00-665 Warszawa, ul.Nowowiejska 15/19, E-mail: m.celuch@ire.pw.edu.pl

across the interface. This gives rise to a variety of subgridding FDTD algorithms, see [1]–[3] and references therein.
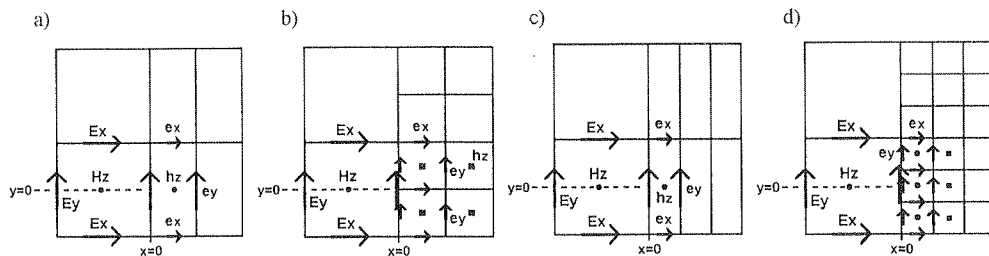
Fig. 1. Meshes considered in this paper: a) 2:1 variable mesh, b) 2:1 subgridding, c) 3:1 variable mesh, d) 3:1 subgridding

FDTD algorithms on locally refined meshes allow economising the computer effort for the required overall accuracy level. However, they also induce uncontrolled numerical artifacts such as numerical reflections. For subgridded FDTD, several concepts for reducing the level of reflections through spline interpolation [1], field collocation [2] or minimisation of a rather arbitrary reflection-based goal function [3] have been proposed and practically applied, but not mathematically validated so far. On the other hand, a theoretical study for predicting the magnitude of numerical reflections has been proposed in [4] for variable meshes and normal incidence. Our target here is to extend the methodology of [4] to oblique incidence and subgridding. For clarity, we shall concentrate on the case of TE waves and equal time-steps being used in the coarse and fine mesh subregions.

2. FDTD EIGENWAVES AT OBLIQUE INCIDENCE

We consider a TEM wave of parallel polarisation incident from coarse to fine mesh region. Its magnetic field is:

$$H_1^+ = H_{10}^+ exp[j(\omega t - \beta_{1x}x - \beta_{1y}y)] \tag{1}$$

where:

$$\beta_{1x} = \beta_x \cos \vartheta_1, \ \beta_{1y} = \beta_y \sin \vartheta_1 \tag{2}$$

β_1 — numerical propagation constant, ϑ_1 — angle of incidence, and the numerical dispersion relation dictates:

$$r_2 \sin^2(0.5\omega\Delta t) = \sin^2(0.5\beta_{1x}a) + \sin^2(0.5\beta_{1y}a) \tag{3}$$

where a denotes the coarse cell size, Δt — time-step, $r = a/(v\Delta t)$, v — phase velocity in the continuum. The E_y field of this wave is given by:

$$E_{1y}^+ = (E_{10}^+ \cos \vartheta_{1P})exp[j(\omega t - \beta_{1x}x - \beta_{1y}y)] = \tag{4}$$
$$= (Z_0 H_{10}^+ \cos \vartheta_{1P})exp[j(\omega t - \beta_{1x}x - \beta_{1y}y)]$$

It follows from [5] that the ratio of total E- and H-field amplitudes is conserved in FDTD, and therefore Z_0 in (4) is the physical medium intrinsic impedance. However, the numerical emulation of the divergence relation reads [5]:

$$\sin(0.5\beta_{1x}a)E_{1x}^{+} + \sin(0.5\beta_{1y}a)E_{1y}^{+} = \qquad (5)$$
$$= E_{10}^{+}[\sin\vartheta_{1P}, \cos\vartheta_{1P}]\sin(0.5\beta_{1x}a), \sin(0.5\beta_{1y}a)] = 0$$

and entails that the numerical E- field vector is perpendicular to the $[\sin(0.5\beta_{1x}a), sin(0.5\beta_{1y}a)]$ vector, and not to $[\beta_{1x},\beta_{1y}]$. Thus in a general case polarisation angle deviates from that in the continuum: $\vartheta_{1P} \neq \vartheta_1$.

A transmitted wave on the fine mesh has an analogous form:

$$e_{2y} = (e_{20}\cos\vartheta 2P)exp[j(\omega t - \beta_{2x}x - \beta 2yy)] = \qquad (6)$$
$$= (Z_0 h_{20}\cos\vartheta 2P)exp[j(\omega t - \beta_{2x}x - \beta_{2y}y)]$$

and obeys the fine mesh dispersion relation: for $p : 1$ subgridding:

$$(r/p)^2 \sin^2(0.5\omega\Delta t) = \sin^2(0.5\beta_{2x}a/p) + sin_2(0.5\beta_{2y}a/p) \qquad (7)$$

for $p : 1$ variable mesh:

$$r^2 \sin^2(0.5\omega\Delta t) = p^2 \sin^2(0.5\beta_{2x}a/p) + sin^2(0.5\beta_{2y}a) \qquad (8)$$

3. NUMERICAL EMULATION OF SNELL'S LAW

In the continuum, Snell's law states:

$$\beta_{1y} = \beta_{2y} \qquad (9)$$

A plane wave propagating on the variable mesh in the y-direction does not "see" mesh refinement in the x- direction and (9) still applies. Actually, this complies with what the relations (3) and (8) require for $\beta_{1x} = \beta_{2x} = 0$:

$$\sin(0.5\beta_{1y}a) = r\sin(0.5\omega\Delta t) = sin(0.5\beta_{2y}a) \qquad (10)$$

In the case of subgridded meshes, a conflict appears. For the separate, uncoupled meshes of a and a/p cell size, and with the assumed $\beta_{1x} = \beta_{2x} = 0$, the numerical dispersion relations (3) and (7) suggest:

$$\sin(0.5\beta_{2y}a) = r\sin(0.5\omega\Delta t) = p\sin(0.5\beta_{2y}a/p) \qquad (11)$$

However, for any finite discretisation, $\vartheta_1 \neq 0$, and $p \neq 1$, formulae (9) and (11) cannot be simultaneously met. With our problem understanding of today we cannot exclude that a numerical Snell's law will tend to (11) rather than (9) in a hypothetical

FDTD space unbounded in the y-direction. It remains as a topic for future investigation.

In this paper, we shall consider oblique propagation with reference to rectangular waveguide modes. This leads to an eigenproblem in the y-direction and following [5] the boundary conditions force:

$$\beta_{1y} = \beta_{2y} = n\pi/L \tag{12}$$

where L is waveguide y-dimension and n is a modal y-index determined by the applied source template. For completeness, let us mention that the physical solution (12) may be superimposed by a spurious pattern with:

$$\beta_{1ys} = \beta_{2ys} = 2\pi/a \tag{13}$$

4. NUMERICAL REFLECTION COEFFICIENTS

As in [4] we allow for a reflected wave, and require that the tangential E-field be continuous across $x = 0$:

$$E_{10} + \cos\vartheta_{1P}(1 + \Gamma) = e_{20}\,\cos\vartheta_{2P} \tag{14}$$

Enforcing (14) into the FDTD update equation at $x = 0$, we obtain the formulae for the reflection coefficient. For the 2:1 variable mesh (Fig. 1a) where a natural continuity condition is $E_{1y}(0,0) = e_{2y}(0,0)$:

$$jr\sin(\frac{\omega\Delta t}{2})(1 + \Gamma) = \tag{15}$$

$$= \frac{2}{3}\left[\frac{\exp(j0.5\beta_{1x}a) - \Gamma\exp(-j0.5\beta_{1x}a)}{\cos\vartheta_{1P}} - \frac{(1 + \Gamma)\exp(-j0.25\beta_{2x}a)}{\cos\vartheta_{2P}}\right]$$

For the basic 2:1 subgridded mesh (Fig. 1b) where:
— $e_{2y}(0, \pm0.25a)$ are updated from $H_{1z}(-0.5a, 0)$ and $h_{2z}(0.25a, \pm0.25a)$, respectively,
— the continuity condition is set as $E_{1y}(0,0) = 0.5[e_{2y}(0, 0.25a) + e_{2y}(0, -0.25a)]$ we also derive (15) and at $\vartheta_1 = 0$ the variable and subgridded meshes produce identical reflections. At $\vartheta_1 \neq 0$ different y-resolution leads to different β_{2x}, ϑ_2, ϑ_{2P} by virtue of (7) and (8), and different reflections result from (15).

For the 3:1 collocated scheme after [2] we have:
— the continuity condition is set as $E_{1y}(0,0) = e_{2y}(0,0) = e_{2y}(0, \pm0.333a)$,
— $E_{1y}(0,0)$ is updated from $H_{1z}(-0.5a, 0)$ and arithmetic average of the three
    components: $h_{2z}(0.5a, 0)$ and $h_{2z}(0.5a, \pm0.333a)$, marked as a squares in Fig. 1d:

$$jr\sin(\frac{\omega\Delta t}{2})(1 + \Gamma) = \tag{16}$$

$$= \frac{1}{2}\left[\frac{\exp(j0.5\beta_{1x}a) - \Gamma\exp(-j0.5\beta_{1x}a)}{\cos\vartheta_{1P}} - \frac{(1 + \Gamma)\exp(-j0.5\beta_{2x}a)}{\cos\vartheta_{2P}}\right]$$

For comparison, we also construct a collocated 2:1 scheme such that:

— the continuity condition is set as $E_{1y}(0,0) = e_{2y}(0, 0.25a) = e_{2y}(0, -0.25a)$,

— $E_{1y}(0,0)$ is updated from $H_{1z}(-0.5a, 0)$ and arithmetic average of the four $h_{2z}(0.5a, \pm 0.25a, \pm 0.25a)$ components, marked as a squares in Fig. 1b:

$$jr \sin(\frac{\omega \Delta t}{2})(1 + \Gamma) = \tag{17}$$

$$= \frac{1}{2}\left[\frac{\exp(j0.5\beta_{1x}a) - \Gamma \exp(-j0.5\beta_{1x}a)}{\cos \vartheta_{1P}} - \frac{(1 + \Gamma)\exp(-j0.5\beta_{2x}a)\cos(0.25\beta_{2x}a)}{\cos \vartheta_{2P}}\right]$$

5. MATHEMATICAL PREDICTIONS AND SIMULATED RESULTS

For the coarse-to-fine mesh propagation (further denoted by $c \to f$) our prediction algorithm proceeds as:

[A] For the assumed ω and ϑ_1 solve (3) for β_1 and get ϑ_{1P} from (5).

[B] Apply Snell's law (9) —— or, for comparative purposes, (11).

[C] Get β_{2x} from the dispersion relation in the second region (7) or (8), and there from β_x, ϑ_2, ϑ_{2P}.

[D] Solve (15) or (16) or (17) for Γ.

An analogous procedure is constructed for the fine-to-coarse case ($f \to c$).

In FDTD simulations, we model a matched section of a parallel-plate line of width 10 mm, with mesh discontinuity set at its half-length. We apply pulsed excitation with spatial template of either TEM mode (for normal incidence) or the first waveguide mode (with H_z, E_x and E_y fields and frequency-dependent angle of incidence). The frequency-dependent reflection coefficient is extracted by the method of [6].

Reflection coefficients at normal incidence are plotted in Fig. 2. Note that now (15) correctly reduces to eq.(3) of ref. [4], and the $f \to c$ and $c \to f$ variable mesh and subgridding cases produce the same reflection magnitude. The 3:1 collocated scheme of [2] is confirmed as ultra low-reflecting. Simulated results perfectly agree with predictions. At 45° incidence (Fig. 3) variable mesh reflections are lower than at 0° (curve 1). In fact, as shown in Fig. 4, curve 5, they monotonously decrease to zero with the increasing incidence angle. This prediction has been confirmed by simulating a waveguide mode starting at its cutoff frequency.

The 2:1 subgridding scheme behaves differently. With Snell's law analytically enforced by waveguide boundary conditions, reflections are non-monotone and grow for large incidence angles. We predict full reflection at $\vartheta_1 = 90°$ for the $f \to c$ (curve 3 in Fig. 4) and already at $\vartheta_1 < 90°$ for the $c \to f$ case (curve 1 in Fig. 4). A numerical quasi-Brewster angle minimising the reflections is also expected. FDTD waveguide simulations of Fig. 5 confirm both effects.

Parallel-plate line model has produced results for the normal incidence reflections. Now we will try to investigate the oblique incidence case. There are well know similar-
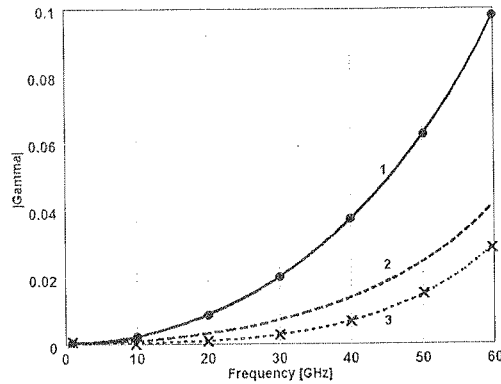
Fig. 2. Reflections at 0°, $a = 1$ mm: 1–2 : 1 variable and subgridded mesh (15);
2–collocated 2:1 (17); 3–collocated 3:1 (16);
lines–predicted, dots– simulated
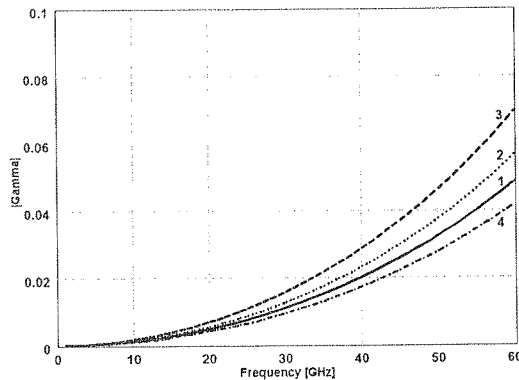
Fig. 3. Predicted reflections on 2:1 meshes, $a = 1$ mm, 45° incidence: variable mesh –1;
subgridding: 2 - $c \rightarrow f$ and $f \rightarrow c$ with (9); 3 - $f \rightarrow c$ with (11);
4 - $c \rightarrow f$ with (11)

ities between a wave propagating in a waveguide along its axis and a wave propagating in free space at some angle with respect to that axis. Thus analysis versus frequency of a wave incident at a wall across the waveguide is equivalent to the analysis of a free-space wave analyzed versus the angle of incidence. At very high frequencies in the waveguide we have quasi-normal incidence. At the cutoff frequency of the guide we have incidence angle of 90°.

Full reflections would not occur, and subgridding would perform more like variable mesh, if decoupled y-directed dispersion relations were maintained —— eq.(11), curves 2, 4 in Fig. 4. This is impossible due to waveguide boundary conditions, as shown by the different asymptotic behaviour of curves 1 and 2 in Fig. 5 near cutoff. Development
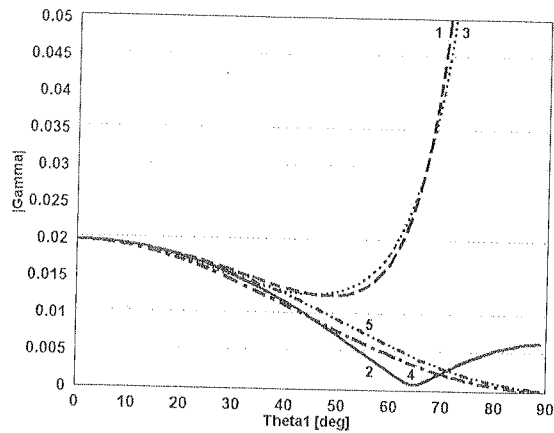
Fig. 4. Predicted numerical reflections on 2:1 meshes, $a = 1$ mm, $f = 30$ GHz, as a function of incidence angle: 1 — $c \to f$ (9), 2 – $c \to f$ (11), 3 – – $f \to c$ (9), 4 — $f \to c(11)$, 5 — variable mesh $c \to f$
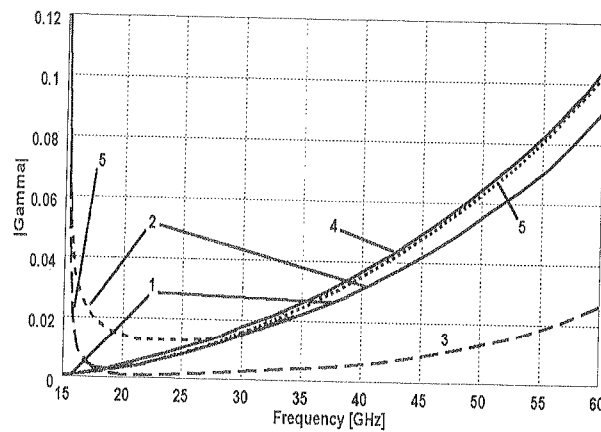
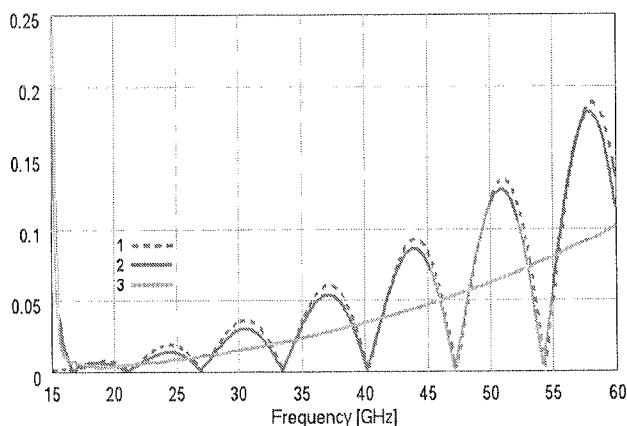Fig. 5. Reflections for fundamental waveguide mode in a rectangular waveguide of 10 mm width, modelled with $a = 1$ mm: 1 —— variable mesh 1:2 (predicted and simulated) and subgridding 2:1 (predicted with (11)), 2 —— subgridding 2:1 (simulated), 3 — subgridding 3:1 collocated (predicted and simulated), 4 — variable mesh 3:1 (simulated), 5 —— subgridding 3:1 non-collocated (simulated)

of FDTD subgridding schemes with Snell's law emulated by (11) in place of (9) may be a worthwhile topic for studies.

Let us consider an example of a waveguide of the width of 10 mm (with 15 GHz cut-off frequency) with mesh discontinuity set at its half-length. We apply sinusoidal excitation (50GHz – much above the cut-off and 16 GHz —- near the cut-off) with spatial template of the first waveguide mode.

variable mesh plane
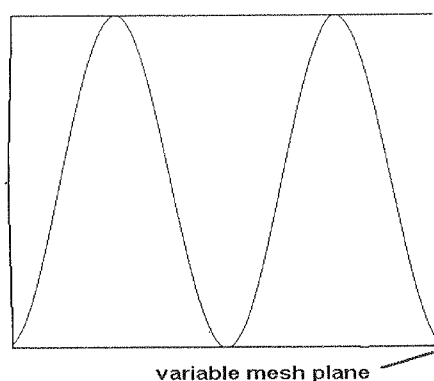
Fig. 6. Envelope of the electric field of a wave incident on variable mesh at f=16 GHz

Fig. 6 shows the envelope of the electric field in the waveguide modelled with FDTD cell size $a = 1$ mm and sinusoidal excitation at the frequency f=16 GHz. The wave is incident from the left side on a variable mesh wall on the right side of the picture. Because the excitation frequency is close to the cut-off frequency, according to curve 4 on Fig. 5 there is no reflection from the mesh discontinuity and thus no ripples appear on the field envelope. Similar numerical experiment performed for the same frequency but with incidence on a 3:1 subgridding wall is illustrated in Fig. 7. We can
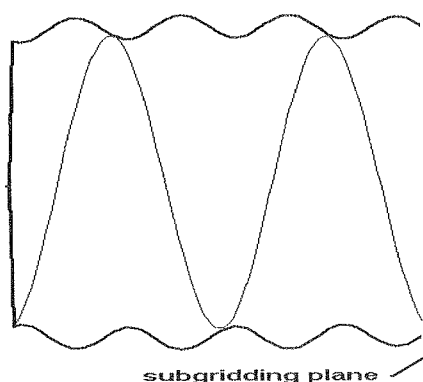
subgridding plane

Fig. 7. Envelope of the electric field of a wave incident on 3:1 subgridding at f=16 GHz

observe there important reflections from the subgridding plane — the result which is in agreement with the theoretical predictions of Fig. 5.
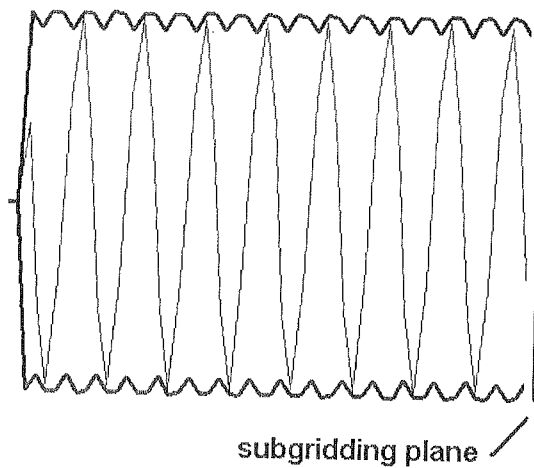
subgridding plane

Fig. 8. Envelope of the electric field of a wave incident on non-collocated 3:1 subgridding or variable mesh at f=50 GHz
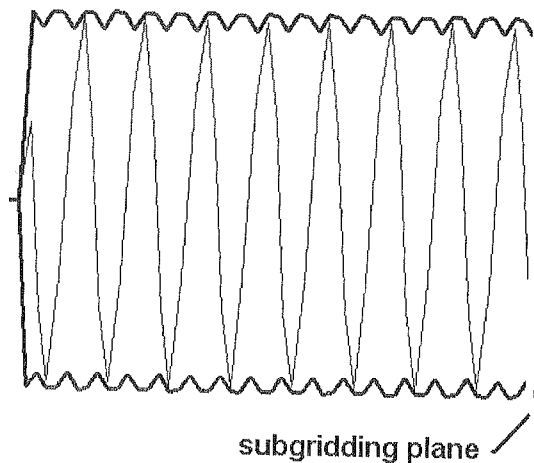
subgridding plane

Fig. 9. Envelope of the electric field of a wave incident on 3:1 collocated subgridding at f=50 GHz

Fig. 8 presents the shape of the electric field envelope in the same waveguide for the excitation frequency of 50GHz. The same result is obtained in the case of a wave incident at a variable mesh wall as well as in a case of a wave incident at a subgridding wall obtained with non-collocated scheme. This is also in agreement with Fig. 5 where curves 4 and 5 are overlapped.

The difference in the collocated and non-collocated schemes can be observed by comparison of Fig. 8 and Fig. 9. In Fig. 9 we present the envelope of the electric field for waveguide mode in a rectangular waveguide for 3:1 subgridding collocated scheme for the frequency of 50 GHz. Comparison with Fig. 8 shows that collocated scheme produces about four times lower reflections. This again confirms good properties of the collocated scheme of [2] predicted in Fig. 5.

a)

b)

c)
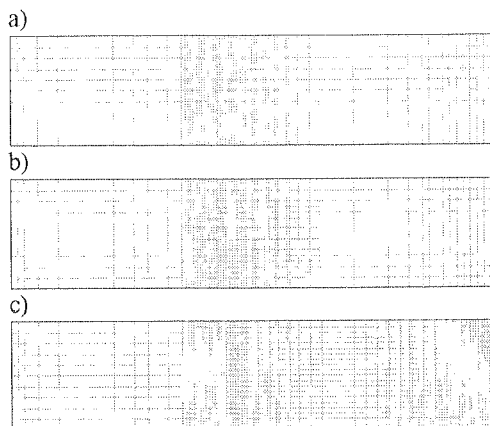
Fig. 10. A rectangular waveguide example with variable mesh and subgridding configurations: a) 3:1 variable mesh with two mesh interfaces, b) 3:1 subgridding with two mesh interfaces, c) 3:1 subgridding with one mesh interface

Fig. 11. Reflections for fundamental waveguide mode in a rectangular waveguide of 10 mm width, modelled with $a = 1$ mm: 1 — 3:1 variable mesh with two mesh interfaces, 2 — 3:1 subgridding with two mesh interfaces, 3 — 3:1 subgridding with one mesh interface

Fig. 11 shows the reflections for fundamental waveguide mode in a rectangular waveguide of 10 mm width, modelled with $a = 1$ mm for 3:1 subgridding with one mesh interface (curve 3), according to Fig. 10 c), and for 3:1 variable mesh (curve 1) and subgridding (curve 2) with two mesh interfaces, according to Fig. 10 a) and 10 b) respectively. For two mesh interfaces we can observe influence of multiple reflections from coarse–fine and fine– coarse mesh interfaces.

6. CONCLUSIONS

We have proposed a methodology for predicting the level of reflections in FDTD techniques on variable and subgridded meshes. It has been validated for TEM and 2D waveguide mode propagation in a parallel-plate line. At normal incidence, sub-gridded (non-collocated) and variable meshes exhibit equal reflections. For increasing incidence angles reflections on variable mesh decrease to zero and reflections on sub-gridded meshes increase and the effect of total reflection occurs. Ultra low reflections of the collocated 3:1 scheme after [2] have been mathematically confirmed, and other existing or future schemes can be similarly evaluated. Reflections are generally lower in collocated schemes where the boundary fields are updated with a symmetric spatial stencil. However, all the considered subgridding algorithms exhibit the effect of total reflection at large incidence angles, which does not occur for variable meshes. This must be taken into account when applying the FDTD method to the analysis of waveg-uide circuits close to the cutoff frequency or structures in which the wave is incident at a subgridding boundary at high angles.

Furthermore, interesting theoretical concepts have been posed, such as numerical emulation of Snell's law and non-orthogonality of the numerical electric field and propagation vectors.

7. REFERENCES

1. M. Okoniewski, E. Okoniewska, M. A. Stuchly, "Three-dimensional subgrid-ding algorithm for FDTD" *IEEE Trans.Antennas Propag.*, vol. 45, No. 3, March 1997, pp. 422-428.
2. Ł. Kulas, M. Mrozowski, "A simple high-accuracy subgridding scheme", 33rd *European Microwave Conf. Proc.*, Munich, Germany, October 2003, pp. 347-350.
3. S. Wang, F. L. Teixeira, R. Lee, J.-F. Lee, "Optimization of subgridding schemes for FDTD" *Microwave and Wireless Components Lett.*, vol. 12, No. 6, June 2002, pp. 223-225.
4. M. Celuch-Marcysiak, "Evaluation and enhancement of supraconvergence effects on nonuni-form and conformal FDTD meshes", *2001 IEEE MTT-S IMS Dig.*, Phoenix, May 2001, pp. 745- 748
5. M. Celuch-Marcysiak, W. K. Gwarek, "On the nature of solutions produced by finite difference schemes in time domain", *Int.J.Numer.Model.*, vol. 12, No. 1/2, Jan.-April 1999, pp. 23-40.
6. M. Celuch-Marcysiak, W. K. Gwarek, "Wide-band S-parameter extraction from FD-TD simulations for propagating and evanescent modes in inhomogeneous guides", *IEEE Trans. Microwave Theory Tech.*, vol. 51, No. 8, Aug. 2003, pp. 1920-1928.

7. S. S. Zivanovic, K. S. Yee, K. K. Mei, "A subgridding method for the time-domain finite-difference method to solve Maxwell's equations", *IEEE Trans.Microwave Theory Tech.*, vol. 39, No. 3, March 1991, pp. 471-479.

8. K. M. Krishnaiah, C. J. Railton, "A stable subgridding algorithm and its application to eigenvalue problems", *IEEE Trans.Microwave Theory Tech.*, vol. 47, No. 5, May 1999, pp. 620-628.

9. M. J. White, Z. Yun, M. F. Iskander, "A new 3-D FDTD multigrid technique with dielectric transverse capabilities", *IEEE Trans.Microwave Theory Tech.*, vol. 49, No. 3, March 2001, pp. 422-430.

lin
the

Nonlinear Dielectrics for
Tunable Microwave Components

(Invited Paper)

ROLF JAKOBY[1], PATRICK SCHEELE[1], STEFAN MÜLLER[1]
AND CARSTEN WEIL[2]

Abstract — Agile materials and technologies based on nonlinear dielectrics like ferro-electrics or liquid crystals offer a line of passive tunable microwave components such as varactors, filters and phase shifters, suitable as key components in phased-array antennas e.g. for automotive radar sensors and in future reconfigurable (frequency agile) RF-frontends, e.g. in mobile communication systems with multiband operation. The trend towards these commercial microwave applications involves a demand for cheaply integrated, compact devices with both, high tunability and low insertion loss. Therefore, distinct research interests have been focused on agile materials for tunable microwave components as promising alternatives to active semiconductor devices or MEMS varactors. Starting with some results of ferroelectric thin-film devices from literature, the focus of this paper will be on our research of tunable microwave components based on (1) ferroelectric thick-films on Al2O3-substrate and (2) liquid-crystals. Up to now, only very few approaches used an anisotropy at microwaves, e.g. for phase shifting purposes. However, with recently developed, novel highly-anisotropic microwave LCs, a figure-of-merit of above 110°/dB at 24 GHz has been achieved for a inverted- microstrip line phase shifter with comparatively low control voltages less than 30 V. At the same frequency, this exceeds by far the figure-of-merit of 30 to 50°/dB of BST-coplanar waveguide phase shifters, however, much lower tuning speed. This substantial progress opens up totally new low-cost LC applications beyond optics.

1. INTRODUCTION

Agile materials and technologies offer a line of tunable components that use non-linear dielectrics such as FerroElectric (FE) material or Liquid Crystal (LC), where the dielectric constant of FEs or the anisotropy of LCs can be adjusted by applying

[1] Technische Universität Darmstadt, Institut für Hochfrequenztechnik, Merckstr. 25, 64283 Darmstadt, Germany; Email: jakoby@hf.tu-darmstadt.de
[2] Advanced Ferrite Technology GmbH, Spinnerei 44, 71522 Backnang, Germany

Table 1

Some parameters for microwave components for currently competing technologies. The entries reflect data from different literature. IMD= intermodulation distortion; [1] at high volume; [2] at low volume; [3][Cha2], [Kir2]; [4][Wei8], [Mue1]

Technology 1...40 GHz	Tunability	FoM [°/dB] @24 GHz	Q@10 GHz (RF losses)	Power consumption	DC-control voltage	Response time (speed)	IMD	Cost
Semi Cond. PIN/Schottky GaAs FET GaAs Varac.	High	30 > 50?	Moderate 30...60	Poor 1–5 mW 1–5 mW 100-300 mW	1-10 V 1-10 V 10-40 V	Fast 1-5 ns 2.10 ns 1-5 μs	Poor	Moderate[1] to High[2]
MEMS-varactor	Low		Very good 100–1000 < 200 (typ)	Excellent $\ll 1\ \mu W$	10–100 V	Slow > 5 μs	Excellent Power Handling?	Low[1] to Moderate[2]
Ferroelectrics Thin film Thick film	Moderate to High	30...50 < 30(50)	Moderate < 30; 100[3] < 20	Excellent $\ll 1\mu W$ $\ll 1\mu W$	< 20 V 10–100 V	Very Fast < 1 ns < 1 ns	Poor Good	Low[1] Low[2]
Liquid Crystals	Moderate	< 25, 110[4]	–	Good $\ll 100\mu W$	< 30 V	Very slow > 10 ms	?	Low[2]

a DC-voltage. This technique is used in a family of tunable varactors, filters, phase shifters and impedance matching networks [10], [1], [2], [8], [12], [14], [18], [19], [21], [22], [23], [24] [25], [27], [29], [29], [30], [31], [8], [15], [32], [34], [17]. Circuits using this tuning method may be manually tuned, computer-controlled or tuned via a feedback loop in the system. Tunable microwave components such as varactors and phase shifters are needed as key components in phased-array antennas e.g. for automotive radar sensors and in future reconfigurable (frequency agile) RF-frontends, e.g. in mobile communication systems with multiband operation. The trend towards these commercial microwave applications involves a demand for cheaply integrated, compact devices with both, high tunability and low insertion loss. According to Tab. 1, the so far favored concepts such as active semiconductor devices and circuits or MEMS varactors partly do not meet these requirements. Therefore, distinct research interests have been focused on passive, tunable microwave components based on nonlinear dielectric materials as promising alternatives.

2. APPLICATIONS OF NONLINEAR DIELECTRICS

Dielectric materials, whose relative dielectric constant strongly depends on the electrical-field strength are commonly denoted as nonlinear dielectrics. Their internal dielectric polarization can be changed by applying a DC-voltage. This allows various applications at microwaves that might be divided into two classes:
1. A control of a small-signal dielectric constant by an externally applied DC-voltage for tunable linear microwave components such as varactors and phase shifters.

2. A large signal modulation of the dielectric constant for frequency-conversion devices such as frequency multipliers, up-converters or modulators.

The most popular room temperature nonlinear dielectrics studied so far at microwave frequencies are ferroelectrics, mainly Barium-Strontium-Titanate (BST), a Perovskite-type oxide. Since bulk crystals and dense bulk ceramics of BST are less suited for microwave applications because of their very high relative permittivity ($\varepsilon_r > 10000$!), mostly epitaxial thin films of BST on single-crystal substrates have been investigated for microwave purposes e.g. in [10], [4], [20], [26], [35]. BST thin-films have been developed and optimised specifically for microwave integrated circuits, using both MOCVD-grown and RF magnetron-sputtered films. The material optimization efforts have concentrated on achieving high tunability and simultaneous low loss, and also on developing robust electrode systems for circuit fabrication on silicon substrates [36]. BST- films have several properties that make it attractive for high-frequency applications, including [36]:

- *High dielectric constant*: in the range of 100-300 typically, useful for small-area bypass capacitors and MEMS switches
- *Field dependent permittivity*: as much as 4:1 variation in permittivity, useful for tunable RF circuits such as varactors, phase-shifters, filters and VCOs.
- *"Fast" polarization response*: allows for rapid tuning and frequency conversion devices.
- *High breakdown field strength*: allows for large bi-polar voltage swings and hence good power-handling.

Few results shall be summarized in the following for CoPlanar Waveguide (CPW) phase shifters based on thin-film technology, operating at room temperature:

1. A monolithic reflection-type phase shifter fabricated on BST/sapphire achieved a Figure-of- Merit (FoM) of 89°/dB at 1.87 GHz and better than 44°/dB from 1.52 to 2.56 GHz with 160 V [11].
2. Simple transmission-line phase shifters obtained a FoM between 30°/dB and 45°/dB at 31.34 GHz with high field strength $E_{max} > 20$ V/mm [3].
3. Complex loaded-line phase shifters with distributed parallel plate or interdigital capacitors, compatible with monolithic processes provided 240°-phase shift with insertion losses of 3 dB at 10 GHz. The circuit has demonstrated a FoM of 93°/dB at 6.3 GHz, 87°/dB at 8.5 GHz and 60 to 80°/dB at 10 GHz at voltages below 20 V, but with very high field strength $E_{max} > 40$ V/mm [1], [2].

Some parameters are roughly summarized in Tab. 1 for currently competing technologies. The entries reflect data from different literature, e.g. [9], [35], [13], [5], [34], [17], appropriate to general-purpose, continuously variable varactors and phase shifters, suitable for microwave operation in a wide assortment of applications.

It is apparent from Tab. 1 that there are pros and cons for each technology, and therefore the choice depends strongly on the particular application. BST dielectrics are favored for applications: 1) which require rapid, continuous tuning, and 2) frequency-conversion devices, that exploit the "fast" capacitive non-linearity. Neither of these

applications can be addressed by MEMS-varactor and LC-devices, which are too slow. In both categories, BST-based components can be designed for much higher capacity than a comparable GaAs-based varactor at higher frequencies. On the other hand, applications demanding very high Q-factors —— such as narrowband tunable filters for communications, or even phase shifters if lowest possible insertion loss is an important objective —— are not yet appropriate for implementation with BST-components, due to persistently high material losses in the microwave range. This might be overcome by strained-relieved BST-thin films, which achieved significantly high dielectric quality factors $Q > 100$ at 8 GHz as recent work exhibited in [5], [13].

Furthermore, the same non-linearity that is used in frequency conversion devices can be a drawback for linear components such as phase shifters due to Inter-Modulation Distortion (IMD) —— the generation of unwanted third-order mixing products. In comparison to semiconductors, BST devices promise to be extremely competitive in terms of cost, in particular at mm-waves, without a significant sacrifice in performance for many applications.

Apart from this, we have focused our efforts on ceramic thick-films of BST on common Al_2O_3 substrates [29], [30], [31], because of mainly two reasons: (1) the screen-printing technique used is much cheaper than the above thin-film techniques, thus being really low-cost, (2) the ability of integration into LTCC (Low Temperature Cofired Ceramics) technology, which is widely used to fabricate cost-effective and reliable microwave components and devices. Incorporation of ceramics with tunable dielectric properties will enhance LTCC technology, enabling the integration of components such as compact varactors, filters and phase shifters.
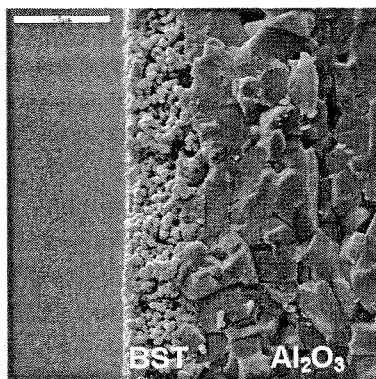
Fig. 1. Ceramic BST film of 3 μm thickness on an 99%-alumina substrate

A rather novel and promising option for nonlinear microwave dielectrics are anisotropic nematic Liquid Crystals (LCs), well known from optical Liquid Crystal Displays (LCD). Up to now, only very few approaches have been made to make direct use of a microwave dielectric anisotropy, e.g. for phase shifting purposes. However, with recently developed, novel highly-anisotropic microwave LCs, a figure-of-merit

above 110°/dB at 24 GHz has been achieved for a phase shifter [34], [17], which is superior to BST-phase shifters [1], [3], however, at much lower tuning speed.

3. FERROELECTRIC THICK-FILM DEVICES

The high dielectric nonlinearity of ferroelectrics like the Barium-Strontium-Titanate ($Ba_xSr_{1-x}TiO_3$) material system is the consequence of the orientational polarization of a small Ti-ion in a Perovskite-type crystal by applying an external electrical field. Due to the high electrical charge of the Ti-ion, a high dipole moment is induced that results in both, a very high absolute value and a high relative change of the dielectric constant. At the Curie-point — the temperature of maximum relative permittivity — the crystal changes from a polar, ferroelectric phase to a non-ferroelectric or paraelectric phase. For applications as tunable microwave dielectrics these materials should always be used in the paraelectric phase close to the Curie-point only, since additional losses due to spontaneous polarization and hysteresis are prevented there. In this paraelectric phase much lower dielectric dispersion is observed at microwave frequencies. The best trade-off among dieletric tunability and losses is achieved in a certain temperature region of the paralectric phase of about 20°C higher than the Curie-point [37], [28], [30].

A well-suited candidate that exhibits a paraelectric phase at room temperature is given by the $Ba_{0.6}Sr_{0.4}TiO_3$ — material composition. In order to make use of the dielectric tunability of such a room temperature paraelectric in combination with planar integrated microwave components, ceramic thick-films of $Ba_{0.6}Sr_{0.4}TiO_3$ — partly doped with Fe-additives —- have been processed by using a low- cost screen-printing technique on Al_2O_3 — microwave substrates with subsequent pressing and sintering [30]. The screen printing technique can be used to prepare BST film thicknesses of 3 to 30μm, depending on the number of printings.

To characterize the BST-thick films over a large frequency range, model-based scattering-parameter measurements are used with InterDigital Capacitors (IDC) from 1 MHz up to 2 GHz and CoPlanar Waveguide (CPW) structures up to 40 GHz [28], [32]. They will be described in section 3.1 and 3.2, respectively. Fig. 2 depicts the relative permittivity of two BST ceramics with different percentage of Ba as a function of the applied electrical field strength E measured with an IDC at 1 MHz and room temperature ($T = 25°C$). As expected, both parameters decrease with E, where the $B_{60}ST$ indicates nearly the same tunability $\tau_\varepsilon = [\varepsilon_r(0) - \varepsilon_r(E_{max})]/\varepsilon_r(0)$ as $B_{65}ST$, but accompanied with lower losses. Hence the material quality factor $\eta_\varepsilon = \tau_\varepsilon/\tan\delta$ is higher.

The relative permittivity and losses of a $Ba_{0.6}Sr_{0.4}TiO_3$ — thick film vs. frequency is shown in Fig 3 at room temperature ($T = 25°C$) for two values of the applied electrical field strength: $E = 0$ and 10 V/μm. While the relative permittivity remains nearly constant over the whole frequency range, the losses steeply increase with frequency. According to Fig. 2, both parameters decrease with the field strength.
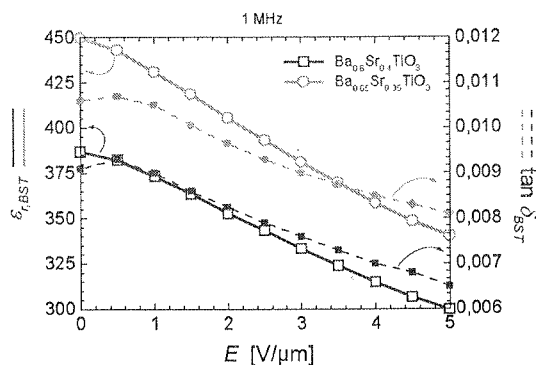
Fig. 2. Relative permittivity of two BST ceramics with 60% and 65% of Ba as a function of the field strength at 1 MHz and $T = 25°C$
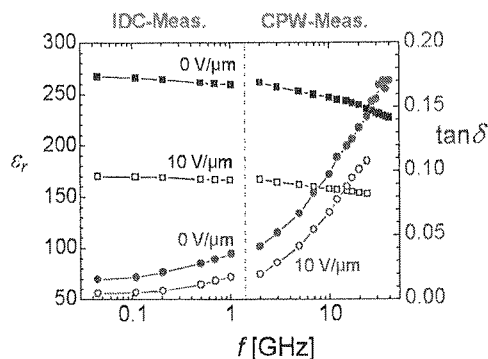
Fig. 3. Relative permittivity and losses of a $Ba_{0.6}Sr_{0.4}TiO_3$ —— thick film as a function of frequency at room temperature ($T = 25°C$). Parameter is the applied electrical field strength $E = 0$ and 10 V/μm. *IDC: InterDigital Capacitor, CPW: CoPlanar Waveguide*

3.1. INTERDIGITAL VARACTORS

InterDigital Capacitors (IDC) as shown in Fig. 4 are very appropriate to realize varactors in connection with tunable BST-thick films, since the electric field is mainly concentrated in the paraelectric film at the substrate surface. For the dielectric tuning of the film in addition a DC-voltage is applied between the finger gaps. Since the spacings of the interdigital fingers can be chosen very narrow, here typically 10 to 20 μm, high electric field strengths can be achieved in the ferroelectric film at moderate DC-voltages.

IDCs can easily be fabricated on top of a multilayer BST-thick film / Al_2O_3 substrate by standard photolithography, thin-film technology and gold plating [29], [30], [31]. In connection with appropriate models they were used to evaluate the dielectric properties of BST films at 1 MHz and from 45 MHz to 2 GHz. As an example Fig. 5 exhibits measurement results for the small signal relative permittivity ε_r of

a $Ba_{0.6}Sr_{0.4}TiO_3$ —-- thick film vs. the applied electrical DC-field strength E_{DC} at 1 MHz extracted with an IDC at room temperature. By sweeping the applied dielectric field strength in different directions one obtains a very symmetrical curve with a strong quadratic portion and a saturation for very high electrical field strengths near dielectric breakdown. The small hysteresis is assumed to be caused by sporadic ferroelectric phases, i.e. local microdomains of spontaneous polarization. A relative change of permittivity of more than 60% can be achieved for an electrical field strength of 20 V/μm.

The dielectric loss tangent $\tan \delta$ of BST-thick films also decreases while increasing the applied electrical field strength. At 1 MHz, $\tan \delta$ amounts to moderate values between 0.01 and 0.005 for a field strength of $E = 0$ V/μm and $E = 20$ V/μm, respectively. In the microwave region from 45 MHz to 2 GHz no significant frequency dispersion of the dielectric constant can be observed and a high dielectric tunability is main- tained. The dielectric loss tangent of BST-thick films increases with frequency and depends on the film quality.

First realizations of varactors on different BST-thick films have resulted in dielectric quality factors of up to about 40, 25, 15 and 11 at 1, 2.5, 5 and 10 GHz, respectively, and room temperature. However, a great potential of improvement is presumed in the optimization of the material preparation and film processing. Dielectric varactors based on tunable BST films are a quite promising alternative to semiconductor varactor diodes, in particular with increasing frequency. Whereas the quality factor of semiconductor varactors decreases strongly with increasing frequency due to the dominating series resistance of the active semiconductor, the quality factor of a BST varactor is mainly determined by the film-loss tangent. Furthermore, paraelectric varactors exhibit the benefits of very low power consumption ($P_{DC} < 1\mu$W) and high tuning speed (< 1 ns).
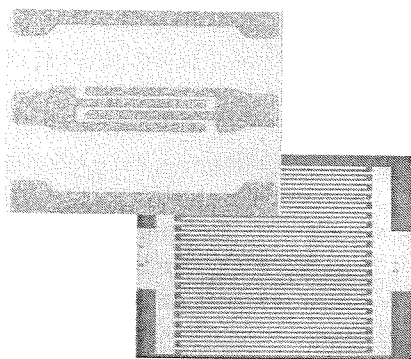
Fig. 4. Photographs of gold InterDigital Capacitors (IDC) on BST–thick and thin films. The finger gap width is typically between 10 μm and 20 μm

Concerning a linear operation, the introduced interdigital BST varactors seem to have further advantages compared to semiconductor varactors diodes. First simulations
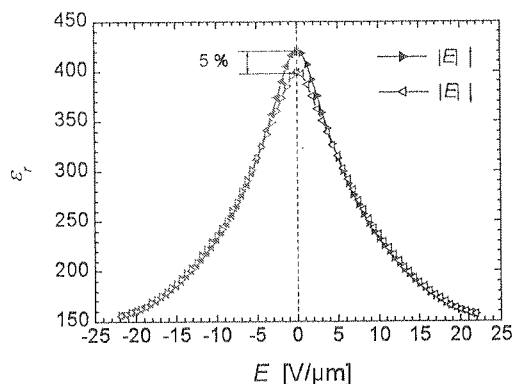
Fig. 5. Relative permittivity of a paraelectric, ceramic $Ba_{0.6}Sr_{0.4}TiO_3$ ---- thick film as a function
of the applied electrical field strength measured with an interdigital capacitor at 1 MHz
and room temperature ($T = 25°C$)

indicate that the tunability compression and intermodulation distortion is typically moderate, since RF voltages, e.g. in 2-W-transmitters, are much smaller compared to the applied DC-control voltages (100 to 200 V).

It seems to be reasonable that a miniaturization of the varactor is needed to obtain high film tunability with lower DC-voltages as well. This can either be achieved by decreasing the interdigital gaps between fingers to sub-micron dimensions, or by using Metal-Insulator-Metal (MIM) capacitors in connection with thick films or multilayer structures (see Fig. 6). But one has to be aware that lowering the DC-control voltage will always result in increased nonlinear signal distortion, unwanted for linear device operation.
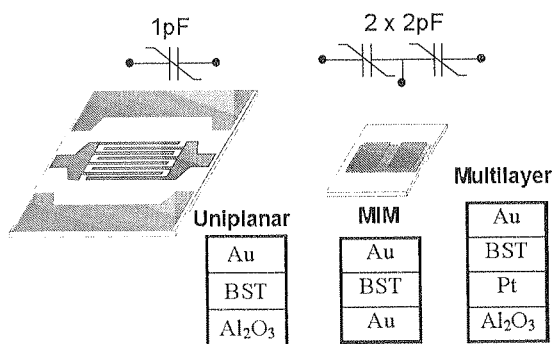
Fig. 6. Different structures to realize BST varactors

3.2. COPLANAR WAVEGUIDE PHASE SHIFTERS

As far as high-permittivity paraelectric thin or thick films are concerned, the uniplanar concept of the CoPlanar Waveguide (CPW) provides several preferences compared to the microstrip technology, since the electric field is mainly concentrated between the line slots and in the tunable dielectric film. As indicated in the schematic presentation of a CPW-phase shifter according to Fig. 7 (above), the dielectric constant of the BST film can be controlled by simply applying a DC-voltage UDC between the inner conductor and the ground metallizations of the CPW, perpendicular to the direction of propagation of the microwave signal. Hence, CPWs using BST-thick films are very promising candidates for low-cost tunable dielectric transmission-line phase shifters, in particular at mm-wave frequencies. Fig. 7 (below) is the top view of a realized CPW-phase shifter.
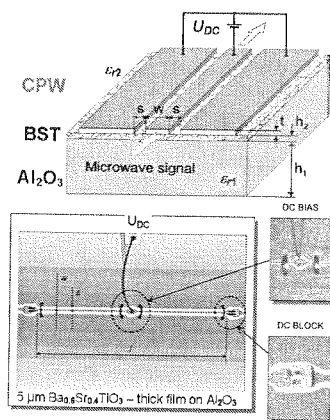
Fig. 7. Voltage controlled dielectric CoPlanar Waveguide (CPW) phase shifter
on a $Ba_{0.6}Sr_{0.4}TiO_3$ —— thick film

3.2.1. Modeling

Quasi-TEM models of homogenous CPW structures with multiplayered dielectrics as shown in Fig. 7 can be derived by the well known conformal mapping technique and the method of partial capacitances, if the lateral dimensions of the CPW cross-section $(w + 2s)$ are sufficiently small compared to the guided wavelength. Based on these static approaches a more sophisticated Quasi-TEM-model for CPWs on multilayered dieletrics, including dielectric losses and metallic conductor losses, has been derived in closed form. This enhanced model shows excellent agreement with a FDFD (Finite Difference Frequency Domain) numerical full wave analysis including metallic and dielectric losses for a typical high-permittivity thick-film [29]. It provides a fast simulation algorithm that can easily be implemented in CAD tools. In addition, the models

have proved to be very appropriate to extract the BST-thick film dieletric properties and tunability from measurements of coplanar waveguides and coplanar resonators at microwave frequencies up to 26.5 GHz.

3.2.2. Measurement Results

A dielectric CPW-phase shifter device based on a room-temperature paraelectric $Ba_{0.6}Sr_{0.4}TiO_3$ — thick film was fabricated and measured. The CPW geometry on a 5 μm thick $Ba_{0.6}Sr_{0.4}TiO_3$ film was chosen to be $w = 15$ μm and $s = 30$ μm, so as to achieve high electrical field strengths with reasonable dc voltages, while having simultaneously a fair matching compared to a 50 Ω-line impedance. A 100 V DC-bias is implemented by a long, inductive bond wire of 25 μm diameter to the center conductor of the CPW. Two ceramic single-layer chip capacitors bonded to the inner CPW conductors were used as DC-blocking elements according to Fig. 7 (below). The physical line length of the active phase shifter section is $l = 18$ mm.
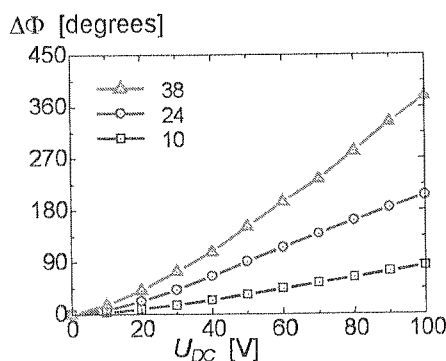
Fig. 8. Measured differential phase shift of a BST-CPW phase shifter vs. the applied voltage for different frequencies at room temperature

The scattering parameters of this phase-shifter device were measured at room temperature with a network analyzer up to 40 GHz. The return loss of this CPW-phase shifter device is below −10 dB over K- and Ka-band. Fig. 8 shows the measured differential phase shift $\Delta\Phi$ vs. the applied voltage U_{DC} at different frequencies. The differential phase shift can be controlled continuously and exceeds 360° at 38 GHz for a maximum DC voltage of 100 V, corresponding to an electrical field strength of 3.3 V/μm. The best phase shifter figure-of-merit values, i.e. the quotient of differential phase shift and insertion loss, amounts 15 to 28°/dB at 24 GHz for a maximum field strength of 10 V/μm. This can be increased up to 50°//dB at 24 GHz for field strength above 20 V/μm. If the same field strength is considered, these results are comparable to the reported performance of epitaxial ferroelectric thin-film phase shifters (see [10]).

A more efficient use of paraelectric films is mainly limited by the high dielectric loss tangent of BST thick films at microwave frequencies according to Fig. 3.

4. NEMATIC LIQUID CRYSTAL PHASE SHIFTER

LCs generally exhibit three characteristic phases with increasing temperature: *crystalline* (solid) $\rightarrow$ mesophase (liquid crystalline) $\rightarrow$ *isotropic* (liquid). Based on the degree of orientational and/or positional order, the mesophase can be classified as: (1) nematic, (2) cholesteric and (3) smectic. The structure of a nematic LC consists of long one?dimensional polar molecules. In the nematic phase there is a long-range orientation order of the anisotropic molecules according to Fig. 9, causing different dielectric constants $\varepsilon_\parallel$ and $\varepsilon_\perp$ in the microwave region, parallel and perpendicular to the preferred axis N.

$$\Delta\varepsilon_r = \varepsilon_{r,\parallel} - \varepsilon_{r,\perp}$$
$$\Delta n = n_\parallel - n_\perp = \sqrt{\varepsilon_{r,\parallel}} - \sqrt{\varepsilon_{r,\perp}}$$
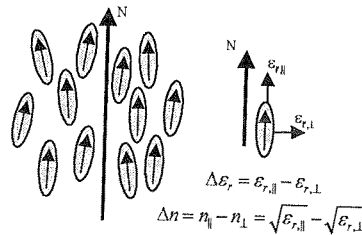
Fig. 9. Perpendicular and parallel permittivity of director N compared to the RF-field as well as the defined anisotropy of the permittivity and the refractive index

The dielectric anisotropy of nematic LCs is based upon the orientation of its long polar molecules by means of externally applied electro-static or magneto-static fields with respect to an RF-field. The differen-tial permittivity between the LC molecule orientations parallel and perpendicular to the RF-field is defined as dielectric anisotropy $\Delta\varepsilon_r = \varepsilon_{r,\parallel} - \varepsilon_{r,\perp}$. Analog to the optical region, a refractive index of the material in the microwave frequency region is given by the Maxwell relation: $\Delta n = \sqrt{\varepsilon_\parallel} - \sqrt{\varepsilon_\perp}$. Three different measurement setups have been developed and applied for a microwave characterization of nematic LCs for low volumes:

- (M1) Broadband parallel-plate capacitor measurements with a HP 4191A LCR-impedance analyzer from 1 MHz to 1 GHz.
- (M2) Broadband S-Parameter measurements with a miniaturized coaxial line up to 26.5 GHz.
- (M3) A circular-cavity resonator using a pertubation method for the TM_{010}-mode at 8.5 GHz. Fig. 10 shows the applied setup, where the LC is filled in a thin PTFE-tube placed in the center of the cavity.

A standard nematic LC structure K15 (5CB) of Merck was chosen for the first step demonstration of a LC microwave anisotropy at room temperature [32], [33].
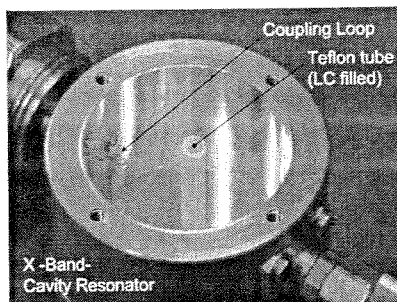
Fig. 10. Circular cavity resonator for precise characterization of LCs at 8.5 GHz
using an cavity pertubation approach

According to Fig. 11 it offers a nematic phase between 15°C to 35°C with high dielectric anisotropy at low frequencies (< 1 kHz) and a relatively high optical anisotropy $\Delta n = 0.212$ at $\lambda = 589$ nm and 20°C.
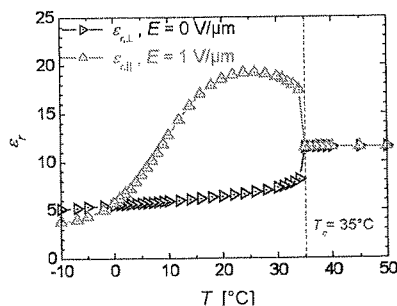
Fig. 11. Measured anisotropy of K15 as a function of the temperature at 1 MHz

A broadband RF characterization of LC K15 has shown a dominant relaxation absorption band in the frequency region below 400 MHz, due to a molecular rotation around the short and long molecule axis according to Fig. 12 (top), as typical for nematic LCs [Wei4] [Wei6]. Therefore, nematic liquid crystals are less qualified for MHz frequencies, but the results are very encouraging for applications above 1 GHz. For LC K15, the mean values $\varepsilon_r = 2.75$ and $\tan \delta = 0.037$ were measured with a cavity (M3) at 8.5 GHz according to Fig. 10. Fig. 12 (bottom) exhibits the measured anisotropy of K15 with (M2), which increases up to a value of approximately 0.1 at 26 GHz at room temperature.

The relatively good performances for this commercially available standard nematic LC K15 encouraged us to carry out further investigations of LCs in close cooperation with Merck research [32], [34], [17]. These were focused on well-directed synthesis of nematic LCs optimized for microwave frequencies, leading to several novel complex LC mixtures with a very high anisotropy Δn of up to 0.37 at 26 GHz according to Fig. 12 (bottom) [34]. This is by far the highest anisotropy for LCs at microwaves and

room temperature known from literature. Tab. 2 exhibits the anisotropy and the losses.
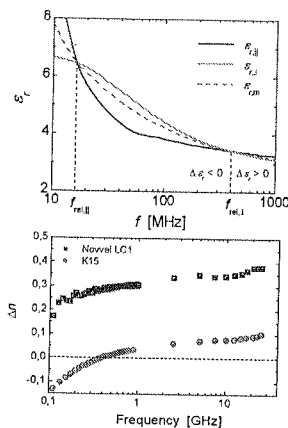
Fig. 12. Dielectric constants $\varepsilon_{r,\parallel}$ and $\varepsilon_\perp$ (top) as well as dielectric anisotropy Δn at microwaves (bottom) of nematic LC K15 at room temperature. The anisotropy of the novel mixture probe LC1 is plotted in addition in the lower figure

Table 2

Permittivity, dielectric anisotropy Δn and losses $\tan\delta_\parallel$ and $\tan\delta_\perp$ of K15 and two novel nematic LCs all measured at room temperature.

LC	$\varepsilon_{r,\parallel}$	$\varepsilon_{r,\perp}$	Δn	$\tan\delta_\parallel$	$\tan\delta_\perp$
(M1)-characterization at 1 GHz					
K15 (5CB)	3.27	3.13	0.04	0.084	0.151
NovelLC1	3.94	2.62	0.37	0.017	0.067
(M2)-characterization at 26 GHz					
K15 (5CB)	–	–	0.1	–	–
Novel LC1	–	–	0.37	–	–
(M3)-characterization at 8.5 GHz					
Novel LC2	3.68	2.56	0.32	0.009	0.026

4.1. INVERTED-MICROSTRIP LINE PHASE-SHIFTER DESIGN

The concept of the planar integrated Inverted-Micro-Strip transmission Line (IM-SL) fits the goal of forming a low cost liquid crystal microwave phase shifter very well. It offers the benefit of very low requirements of LC, where the microwave signal

is dominantly guided in the LC dielectric to make best use of its anisotropy. A cross-section of the inverted-micro-strip phase shifter is illustrated in Fig. 13. The upper microstrip-line and the ground plane consist of $17\mu m$ gold-plated copper metallizations.

The upper and lower substrates of the inverted microstrip lines consist of low permittivity composite ceramic substrates (TMM3) of Rogers Corp. ($\varepsilon_r = 3.27$), supporting the metallization. The LC is filled in one of the two filler plugs on the upper substrate using capillary attraction, whereas the second filler plug deaerates the LC volume. The RT-Duroid substrate satisfies different functions:

- sealing a fixed volume to be filled with LC,
- separating the stripline and the ground plane, and
- contacting stripline and ground plane to the connectors of a microstrip test-fixture in Fig 14.
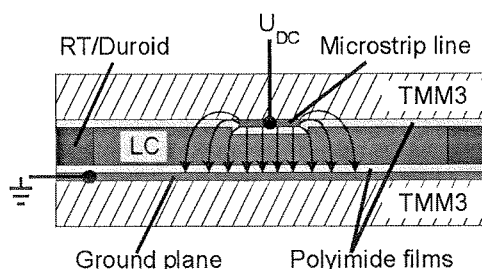
Fig. 13. Cross-sectional view of the phase shifter device. The LC molecules are pre-aligned by mechanically rubbed polyimide films and can be oriented by a DC-voltage parallel to the polarization of the microwave field

Thin polyimide films of approximately 300 nm thick-ness are spin coated on both ceramic substrate surfaces. The polyimide surfaces were mechanically rubbed with a nylon velvet in order to obtain a planar alignment of the LC-molecules parallel to the surfaces, leading to a perpendicular orientation to the electrical RF-field of the IMSL. In this default state, the effective minimum relative permittivity in the phase shifter is $\varepsilon_{r,eff,\perp}$. If a sufficiently high tuning voltage is applied between the stripline and the ground metallization, the orientation of the nematic LC molecules is forced to rotate continuously with an increasing DC-voltage, up to the saturation point of a complete parallel orientation to the polarization of the microwave field at about 30 V. In this case the maximum relative permittivity $\varepsilon_{r,eff,\parallel}$ is measured, due to the maximum available electrical dipole moment. This voltage-controlled tuning of the relative permittivity with a maximum effective anisotropy $\Delta n_{eff} = \sqrt{\varepsilon_{r,eff}} - \sqrt{\varepsilon_{r,eff,\perp}}$ can be used directly for continuous phase shifting of the microwaves. The IMSL geometry is designed to match a line impedance of 50Ω. Nevertheless, due to a shift in the permittivity the characteristic impedance causes some mismatch of a few Ohms. Using a TRL-calibration in connection with a microstrip test-fixture, the calibra- tion plane
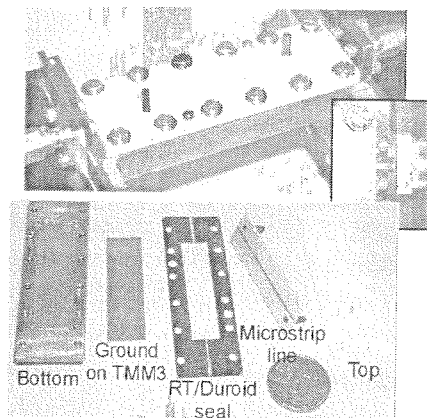
Fig. 14. Inverted-microstrip line phase shifter using a nematic LC. Above: Fully packaged LC phase shifter device and coaxial SMA connectors and filler plugs. Below: View of each separated part of the phase shifter device. The parts will be mounted from left to the right

is placed at the transition from the conven- tional feeding microstrip line to the LC loaded IMSL.

4.2. MEASUREMENT RESULTS

To demonstrate the functionality of nematic LCs, a tunable phase shifter has been realized in IMSL technique with a length $l = 48$ mm and height $h = 0.254$ mm. This phase shifter has been filled with K15 and the novel mixture LC2 and characterized by a network analyzer HP8510B from 3.5 GHz up to 24 GHz at room temperature. The input reflection of the phase shifter is always below -10 dB over the whole frequency range for both orientations, except around 18 GHz it increases to -8 dB affected by a resonance due to impedance mismatch to the coaxial feeding system. The attenuation for the novel mixture LC2 is well below the one for K15, due to lower $\tan \delta$ as shown in Fig. 15.
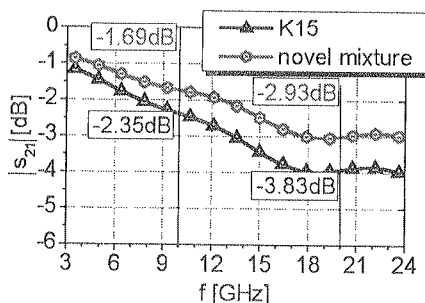
Fig. 15. Insertion losses for K15 and the novel LC2

To point out the functionality of the device, the differential phase shift $\Delta\Phi =$ $\dfrac{360° \cdot f \cdot l}{c_0} \cdot \Delta n_{eff}(U_{DC})$ is plotted vs. the applied control voltage in Fig. 16 for K15 and LC2 at 10 GHz and 20 GHz. Above the Fréedericks threshold voltage $U_F \approx 3$ V ($E_F \approx 0.022$ V/μm) an increase of phase shift is observed that is limited by a saturation of polarization above 30 V ($E \approx 0.1$ V/μm), i.e. the LC molecules are completely oriented in parallel to the microwave field. Only a very small hysteresis was observed for the measured differential phase shift vs. an increasing or decreasing control voltage. In addition, Fig. 17 depicts $\Delta\Phi$ vs. frequency for both LCs. An increase of $\Delta\Phi$ occurs over the whole frequency range. To state a performance of the phase shifter device, a Figure-of-Merit (FoM) is defined by $FoM = \dfrac{\Delta\Phi}{|s_{21}|}$ [°/dB] . The measured FoM is shown in Fig. 18.
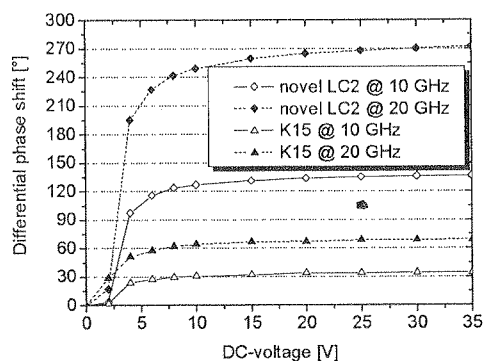
Fig. 16. Insertion losses for K15 and the novel LC2
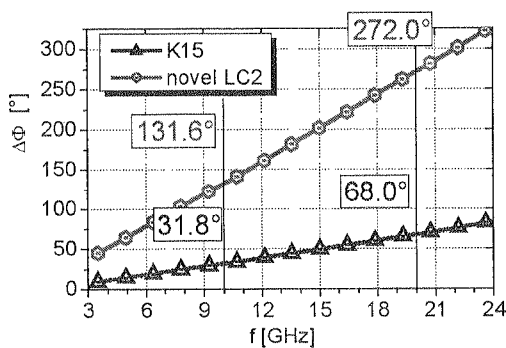
Fig. 17. Measured differential phase shift of the LC-phase shifter device filled with K15 and the novel mixture LC2 as a function of the applied DC-voltage at 10 and 20 GHz

The FoM increases with frequency, except for a drop at about 18 GHz, which is a result of a resonance of the device due to a mismatch to the coaxial feeding system.
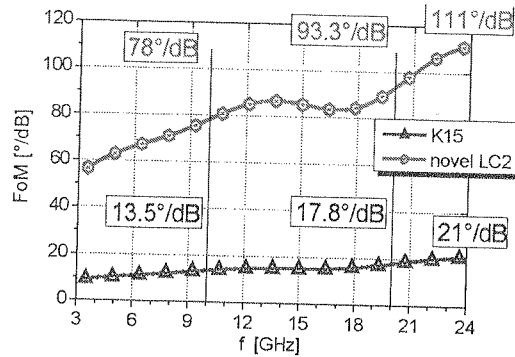
Fig. 18. Measured Figure-of-Merit (FoM) as a function of frequency for a tuning voltage of 30 V

Compared to K15, the FoM has been increased steeply from 18°/dB up to 93°/dB at 20 GHz, and even 21°/dB up to 111°/dB at 24 GHz due to a higher Δn and a lower $\tan \delta$ (see Tab. 2) [34], [17]. To our knowledge, this is the best value reported for a tunable LC microwave phase shifter. It even goes beyond the best results for thin-film ferroelectric phase shifters above 20 GHz. As an additional benefit, the FoM of LC rises with increasing frequency, as obvious from Fig. 18, whereas it decreases for ferroelectrics and semiconductor phase-shifter devices.

5. CONCLUSION AND OUTLOOK

Generally, the principle functionality of BST-films and nematic liquid crystals has been demonstrated at microwave frequencies with varactors and phase shifter devices. The focus has been on two different low-cost planar integrated, voltage-controlled tunable phase shifter devices based on (1) coplanar waveguide on a ferroelectric thick film ceramics and Al_2O_3-microwave substrate and (2) inverted-microstrip line with novel liquid crystal in-between. For the first type, the differential phase shift can be controlled continuously and exceeds 360° at 38 GHz. The best phase shifter figure-of-merit values, i.e. the quotient of differential phase shift and insertion loss, amounts to 15 to 28°/dB at 24 GHz for a field strength of 10 V/μm. This can be increased up to 50°/dB at 24 GHz for very high field strengths of above 20 V/μm. This is comparable to the results in the figure-of-merit using epitaxial thin-film technology.

In contrast, with comparatively low control voltages of less than 30 V (0.1 V/μm), the phase shifter figure-of-merit of the second type amounts above 110°/dB at 24 GHz for a novel LC, however with very low response time above 10 ms. Nevertheless, this could open up totally new fields of LC applications besides optics, requiring low tuning speed. Therefore, besides the synthesis of LCs with higher figure-of-merit at microwaves, our research is additionally aimed for LCs and device configurations that allows higher tuning speed and standard processes.

In particular for ferroelectrics (but also for LCs), the most crucial issue up to now is the high dielectric-loss tangent of those materials at microwave frequencies that still limits the application potential of nonlinear dielectrics. Thus, one of our current research activities – in close interdisciplinary cooperation with materials scientists and chemists – is aimed for a more sophisticated understanding of material and microstructure related polarization and loss mechanisms. The first experiences have already led to promising starting points for further improvement of both, the dielectric material properties and device concepts. Not until these systematic investigations have been conducted, one can estimate the full capability and the physical limits of nonlinear dielectrics at microwave frequencies.

6. REFERENCES

1. B. Acikel, T. Taylor, P. Hansen, J. Speck und R. York, A New X Band 180° High Performance Phase Shifter using BaSrTiO$_3$ Thin Films. *IEEE MTT-S Int. Microw. Symp.*, 2002, pp. 1467-1469.
2. B. Acikel, T. Taylor, P. Hansen, J. Speck, R. York, A New High Performance Phase shifter using Ba$_x$Sr$_{1-x}$TiO$_3$ Thin Films. *IEEE Microwave and Wireless Components Letters*, Vol. 12, No. 7, July 2002.
3. C. M. Carlson, T. V. Rivkin, P. A. Parilla, J. D. Perkins, D. S. Ginley, A. B. Kozyrev, V. N. Oshadchy, A. S. Pavlov, A. Golovkov, M. Sugak, D. Kalinikos, L. C. Sengupta, L. Chiu, X. Zhang, Y. Zhu und S. Sengupta, 30 GHz Electronically Steerable Antennas Using Ba$_x$Sr$_{1-x}$TiO$_3$ — Based Room- Temperature Phase Shifters. *Mat. Res. Soc. Symp. Proc.*, Vol. 603, 2000, pp. 15-25.
4. W. Chang, J. S. Horwitz, A. C. Carter, J. M. Pond, S. W. Kirchoefer, C. M. Gilmore und D. B. Chrisey, The effect of annealing on the microwave properties of Ba$_{0.5}$Sr$_{0.5}$TiO$_3$ thin films. *Appl. Phys. Lett.*, Vol. 74, No. 7, Feb. 1999, pp. 1033-1035.
5. W. Chang, S. W. Kirchoefer, J. F. Pond and J. S. Horwitz, L. Sengupta, Strain-relieved Ba$_{0.6}$TiO$_3$ thin films for tunable microwave applications. *J. of Applied Physics*, Vol. 92, No 3, Aug. 2002.
6. A. Deleniv, S. Gevorgian, Tunable Power Splitters and Matching Networks based on LTCC Ferroelectric Ceramic Films. *Workshop WS 6 — Tunable Ferroelectric Materials and Devices for Microwave Applications, EuMC 2003*, Munich.
7. D. Demus, J. Goodby, G. W. Gray, H.-W. Spiess, V. Vill, *Hanbook of Liquid Crystals, Volumes 1, 2A, 2B, 3*, Wiley- VCH 1998.
8. D. Dolfi, M. Labeyrie, P. Joffre und J.P. Huignard, Liquid Crystal Microwave Phase Shifter. *Electronics Letters*, Vol. 29, No. 10, May 1993, pp. 926-928.
9. D. Galt, T. Rivkina und M. W. Cromar, Microwave Tuning Quality and Power Handling of Voltage-Tunable Capacitors: Semiconductor Varactors versus Ba$_{1-x}$Sr$_x$TiO$_3$ Films. *Mat. Res. Soc. Symp. Proc.*, Vol. 493, 1998, pp. 341-346.
10. S. S. Gevorgian und E. L. Kollberg, Do We Really Need Ferroelectrics in Paraelectric Phase Only in Electrically Controlled Microwave Devices, *IEEE Trans. Microwave Theory Tech.*, Vol. 49, No. 11, 2001, pp. 2117-2124.
11. D. Kim, et. al., A Wide Bandwidth Monolithic BST Reflection-Type Phase Shifter Using A Coplanar Waveguide Lange Coupler. *IEEE MTT-S Int. Microwave Symp. Dig.*, 2002, pp. 1471-1474.

12. S. W. Kirchoefer, J. M. Pond, H. S. Newman W.-J. Kim und J. S. Horwitz, Ferroelectric- Ferrite Tunable Phase Shifters. *IEEE MTT-S Int. Microwave Symp. Dig.*, 2000, pp. 1359-1362.

13. S. W. Kirchoefer, W. Chang, J. A. Bellotti and J. M. Pond, Dependence of microwave tuning and loss on materials properties and strain in BST thin films. *Workshop WS 6 — Tunable Ferroelectric Materials and Devices for Microwave Applications, EuMC*, Munich, 2003.

14. Kozyrev, A. Ivanov, V. Keis, M. Khazov, V. Osadchy, T. Samoilova, O. Soldatenkov, A. Pavlov, G. Koepf, C. Mueller, D. Galt und T. Rivlin, Ferroelectric Films: Nonlinear Properties and Applications in Microwave Devices. *IEEE MTT-S Int. Microwave Symp*, 1998, pp. 985-988.

15. K. C. Lim, J. D. Margerum und A. M. Lackner, Liquid crystal millimeter wave electronic phase shifter. *Appl. Phys. Lett.*, 62 (10), March 1993, pp. 1065-1067.

16. Y. Liu, A. S. Nagra, E. G. Erker, P. Periaswamy, T. R. Taylor, J. Speck und R. A. York, BaSrTiO$_3$ Interdigitated Capacitors for Distributed Phase Shifter Applications. *IEEE Microwave and Guided Wave Letters*, Vol. 10, No. 11, Nov. 2000, pp. 448-450.

17. S. Müller, P. Scheele, C. Weil, M. Wittek, C. Hock, R. Jakoby, Tunable Passive Phase Shifter for Microwave Applications using Highly Anisotropic Liquid Crystals, accepted for *IEEE MTT-S Int. Microwave Symp.*, 2004.

18. J. B. L. Rao, D.'P. Patel und V. Krichevsky, Voltage-Controlled Ferroelectric Lens Phased Arrays. Ferroelectric Materials For Phased Array Applications. *IEEE Trans. Ant. and Prop.*, Vol. 47, No. 3, March 1999, pp. 458-468.

19. R. R. Romanofsky, J. Bernhard, G. Washington, F. Van Keuls, F. Miranda und C. Cannedy K- Band Phased Array Antennas Based On Ba$_{0.60}$Sr$_{0.40}$TiO$_3$ Thin-Film Phase Shifters, *IEEE Trans. Microwave Theory Tech.*, Vol. 48, Dec. 2000, pp. 2504- 2510.

20. S. Sengupta, S. C. Sengupta, S. Stowell, E. Ngo, W. E. Kosik und D. K. Vijay, Analysis of Ferroelectric Thin Films Deposited by Pulsed Laser Deposition on Oxide and Fluoride Substrates. *Proceedings of 9th Int. Symp. on Applications of Ferroelectrics*, 1994, pp. 70-73.

21. V. Sherman, K. Astafiev, A. Tagantsev, N. Setter, I. Vendik, O. Vendik Design and Investigation of Ferroelectric Digital Phase Shifter. Proc. of the 31th *EuMC*, London, Sept. 2001.

22. G. Subramanyam, F. A. Miranda, R. R. Romanofsky, F. W. Van Keuls, C. L. Canedy, S. Aggarwal, T. Venkatesan und R. Ramesh, A Ferroelectric Tunable Microstrip Lange Coupler for K-Band Applications. *IEEE MTT-S Int. Microwave Symp. Dig.*, 2000, pp. 1363- 1366.

23. G. Subramanyam, N. Mohsina, A. Al Zaman, F. Miranda, F. W. Van Keuls, R. Romanofsky und J. Warner, Ferroelectric Thin-film Based Electrically Tunable Ku-band Coplanar Waveguide Components. *IEEE MTT-S Int. Microwave Symp. Dig.*, 2001, pp. 471-474.

24. F. W. Van Keuls, C. H. Mueller, F. A. Miranda, R. R. Romanofsky, C. L. Canedy, S. Aggarwal, T. Venkatesan, R. Ramesh, J. S. Horwitz, W. Chang und W. J. Kim, Room Temperature Thin Film Ba$_x$Sr$_{1-x}$TiO$_3$ Ku-Band Coupled Microstrip Phase Shifters: Effect of Film Thickness, Doping, Annealing and Substrate Choice. *IEEE MTT-S Int. Microwave Symp. Dig.*, 1999, pp. 737-740.

25. V. K. Varadan, D. K. Ghodgaonkar, V. V. Varadan, J. F. Kelly und P. Glikerdas, Ceramic Phase Shifter for Electronically Steerable Antenna Systems. *Microwave Journal*, Jan. 1992, pp. 116-127.

26. V. K. Varadan, V. V. Varadan, F. Selmi, Z. Ounaies und K. A. Jose, Multilayer Tunable Ferroelectric Materials and Thin Films. *SPIE Proceedings*, Vol. 2189, pp. 433-447, 1994.

27. V. K. Varadan, K. A. Jose, V. V. Varadan, R. Hughes und J. F. Kelly, A Novel Microwave Planar Phase Shifter. *Microwave Journal*, April 1995, pp. 244-254.
28. M. Voigts, W. Menesklou und E. Ivers-Tiffee, Dielectric Properties and Tunability of BST and BZT Thick Films for Microwave Applications. *Integr. Ferroelectrics*, Vol. 39, 2001, pp. 383-392.
29. C. Weil, P. Wang, H. Downar, J. Wenger und R. Jakoby, Ferroelectric Thick Film Ceramics for Tunable Microwave Coplanar Phase Shifters. *FREQUENZ*, Vol. 54, 11-12/2000, pp. 250-256.
30. C. Weil und R. Jakoby, Tunable Coplanar Waveguide Phase Shifters Using Thick Films of Barium Strontium Titanate. *Proc. of the 11th MIOP Conf.*, Stuttgart, pp. 176-181, May 2001.
31. C. Weil, S. Müller, P. Scheele, Y. Kryvoshapka, R. Jakoby, Ferroelectric- and Liquid Crystal- Tunable Microwave Phase Shifters, *IEEE EuMW*, Munich, Oct. 2003, pp. 1431-1434.
32. C. Weil, G. Lüssem und R. Jakoby, Tunable Inverted-Microstrip Phase Shifter Device Using Nematic Liquid Crystals. *IEEE MTT-S Int. Microwave Symp.*, June 2002, pp. 367-370.
33. C. Weil und R. Jakoby, Studies of Nematic Liquid Crystals for Dielectric Tunable Microwave Phase Shifters. *5th Int. Symposium on Relaxation Phenomena in Dielectric, Magnetic and Superconducting Systems*, Darmstadt, Oct. 2002.
34. C. Weil, St. Müller, P. Scheele, P. Best, G. Lüssem, R. Jakoby, Novel highly anisotropic liquid-crystal mixtures for tuneable microwave devices, *Electronics Letters*, V. 39, No. 24, Nov. 2003, pp. 1732-1734.
35. B. York, Thin-Film Ferroelectrics: Deposition Methods and Applications. *IEEE MTT-S Int. Microwave Symp.*, Workshop WFE "Ferroelectric Materials and Microwave Applications", 2000.
36. B. York, A. Nagra, E. Erker, T. Taylor, P. Periaswamy, J. Speck, S. Streiffer, O. Auciello, Microwave Integrated Circuits using Thin-Film BST. *IEEE MTT-S Int. Microwave Symp.*, 2001.
37. F. Zimmermann, M. Voigts, C. Weil, R. Jakoby, P. Wang, W. Menesklou und E. Ivers-Tiffée, Investigation of barium strontium titanate thick films for tunable phase shifters. *J. of the European Ceramic Society*, 21, 2001, pp. 2019-2023.

INFORMATION FOR AUTHORS OF K.E.T.

The editorial stuff will accept for publishing only original monographic and survey papers concerning widely understood electronics. Because of the fact that KWARTALNIK ELEKTRONIKI I TELEKOMUNIKACJI is a journal of the Committee for Electronics and Telecommunications of Polish Academy of Scince, it presents scientific works concerning theoretical bases and applications from the field of electronics, telecommunications, microelectronics, optoelectronics, radioelectronics and medical electronics.

Articles should be characterised by original depiction of a problem, its own classification, critical opinion (concerning theories or methods), discussion of an actual state or a progress of a given branch of a technique and discussion of development perspectives.

An article published in other magazines can not be submitted for publishing in K.E.T. TThe size of an article can not exceed 30 pages, 1800 character each, including figures and tables.

Basic requirements

The article should be submitted to the editorial stuff as a one side, clear, black and white computer printout in two copies. The article should be prepared in English or Polish. Floppy disc with an electronic version of the article should be enclosed. Preferred wordprocessors: WORD 6 or 8.

Layout of the article.
- Title.
- Author (first name and surname of author/authors).
- Workplace (institution, adress and e-mail).
- Concise summary in a language article is prepared in (with keywords).
- Main text with following layout:
  - Introduction
  - Theory (if applicable)
  - Numerical results (if applicable)
  - Paragraph 1
  - Paragraph 2
  - . . . .
  - . . . .
  - Conclusions
  - Acknowledgements (if applicable)
  - References
- Summary in additional language:
  - Author (firs name initials and surname)
  - Title (in Polish, if article was prepared in English and vice versa)
  - Extenstive summary, hawever not exceeching 3600 characters (along with keywords) in Polish, if artide wos prepared in English and vice versa). The summary should be prepared in a way allowing a reader to obtaoin essential information contained in the artide. For that reason in the summary author can place numbers of essential formulas, figures and tables from the article.

Pages should have continues numbering.

Main text

Main text can not contain formatting such as spacing, underlining, words written in capital letters (except words that are commonly written in capital letters). Author can mark suggested formatting with pencil on the margin of the article using commonly accepted adjusting marks.

Text should be written with double line spacing with 35 mro left and right margin. Titles and subtitles should be written with small letters. Titles and subtitles should be numberd using no mor than 3 levels (i.e. 4.1.1.).

Tables

Tables with their titles should be places on separate page at the end of the article. Titles of rows and columns should be written in small letters with double line spacing. Annotations concerning tables

should be placed directly below the table. Tables should be numbered with Arabic numbers on the top of each table. Table can consist algorithm and program listings. In such cases original layout of the table will be preserved. Table should be cited in the text.

Mathematical formulas

Characters, numbers, letters and spacing of the formula should be adequate to layout of main text. Indexes should be properly lowered or raised above the basic line and clearly written. Special characters such as lines, arrows, dots should be placed exactly over symbols which they ar attributed to. Formulas should be numbered with Arabic numbers place in brackets on the right side of the page. Units of measure, letter and graphic symbols should be printed according to requirements of IEE (International Electronical Commission) and ISO (International Organisation of Standardisation).

References

References should be placed at the and of the main text with th subtitle „References". Refrences should be numbered (without brackets) adequately to references placed in the text. Examples of periodical [@], non-periodical [2] and book [3] references:
1. F. Valdoni: A new milimetre wave satelite. E.T.T. 1990, vol. 2, no 5, pp. 141–148
2. K. Anderson: A resource allocation framework. XVI International Symposium (Sweden). May 1991. paper A 2.4
3. Y.P. Tvidis: Operation and modeling of the MOS transistors. Nw York. McGraw-Hill. 1987. p. 553

Figures

Figures should be clearly drawn on plain or milimetre paper in the format not smaller than 9×12 cm. Figures can be also printed (preferred editor – CorelDRAW). Photos or diapositives will be accepted in black and whit format not gratd than 10×15 cm. On th margin of each drawing and on th back side of each ohoto authorp name and abbreviation of the title of article should be placed. Figure's captures should be given in two longuaqes (first in the language the article is writtes in and then in additional language). Figure's captures should be also listed on separate page. Figures should be cited in the text.

Additional information

On the separate page following information should be placed:
– mailing address (home or office),
– phone (home or/and office),
– e-mail.
Author is entiled to free of charg 20 copies of articl. Additional copies or the whole magazine can be ordered at publisher at th one's expense.
Author is obliges to perform the author's correction, which should be accomplished within 3 days starting from the date of receiving of the text from the ditorial stuff. Corrected text should be return to the editorial stuff personally or by mail. Correction marks should be placed on th margin of copies received from the editorial stuff or if needed on separate pages. In the case when the correction is not returned in said time limit, correction will be performed by technical editorial stuff of the publisher.
In case of changing of workplace or home address Authors are asked to inform the editorial stuff.

INFORMACJE DLA AUTORÓW

Redakcja przyjmuje do publikowania prace oryginalne, przeglądowe i monograficzne wchodzące w zakres szeroko pojętej elektroniki. Ponieważ KWARTALNIK ELEKTRONIKI I TELEKOMUNIKACJI jest czasopismem Komitetu Elektroniki i Telekomunikacji Polskiej Akademii Nauk, w związku z tym na jego łamach znajdują się prace naukowe dotyczące podstaw teoretycznych i zastosowań z zakresu elektroniki, telekomunikacji, mikroelektroniki, optoelektroniki, radiotechniki i elektroniki medycznej.

Artykuły powinno charakteryzować oryginalne ujęcie zagadnienia, własna klasyfikacja, krytyczna ocena (teorii lub metod), omówienie aktualnego stanu, lub postępu danej gałęzi techniki oraz omówienie perspektyw rozwojowych. Artykuły publikowane w innych czasopismach nie mogą być kierowane do druku w Kwartalniku Elektroniki i Telekomunikacji w drugiej kolejności zgłoszenia.

Objętość artykułu nie powinna przekraczać 30 stron po około 1800 znaków na stronie, w tym rysunki i tabele.

Wymagania podstawowe.

Artykuły należy nadsyłać na wyraźnym, jednostronnym, czarno-białym wydruku komputerowym. Wydruk w formacie A4 powinien mieć znormalizowaną liczbę wierszy i znaków w wierszu (30 wierszy po 60 znaków w wierszu), w dwóch egzemplarzach, w języku polskim lub angielskim wybranym przez autora. Do wydruku powinna być dołączona dyskietka z elektronicznym tekstem artykułu. Preferowane edytory to WORD 6 lub 8. Układ artykułu (w wersji podstawowej) musi być następujący:
- Tytuł.
- Autor (imię i nazwisko autora/ów).
- Miejsce pracy (nazwa instytucji, miejscowość, adres. + ew. adres elektroniczny (e-mail).
- Zwięzłe streszczenie powinno być w języku takim, w jakim jest pisany artykuł (wraz ze słowami kluczowymi).
- Tekst podstawowy powinien mieć następujący układ:
    1. WPROWADZENIE
    2. np. TEORIA
    3. np. WYNIKI NUMERYCZNE
    3.1. ....
    3.2. ....
    4. ....
    5. ....
    6. PODSUMOWANIE
    7. ew. PODZIĘKOWANIA
    8. BIBLIIOGRAFIA
- Układ streszczenia w dodatkowej wersji językowej powinien być następujący:
    AUTOR (inicjał imienia i nazwisko).
    TYTUŁ (w języku angielskim – o ile artykuł pisany jest w języku polskim i na odrwót).
Obszerne do 3600 znaków streszczenia (wraz z słowami kluczowymi) w języku:
    a. angielskim, gdy artykuł pisany jest w języku polskim.
    b. polskim, gdy artykuł pisany jest w języku angielskim.
Streszczenie to powinno pozwolić czytelnikowi na uzyskanie istotnych informacji zawartych w pracy. Z tego względu w streszczeniu tym mogą być cytowane numery istotnych wzorów, rysunków i tabel zawartych w podstawowej wersji językowej.
- Wszystkie strony muszą mieć numerację ciągłą.

Sposób pisania tekstu.

Tekst powinien być pisany bez używania wyróżnień, a w szczególności nie dopuszcza się spacjowania, podkreślania i pisania tekstu dużymi literami z wyjątkiem wyrazów, które umownie pisze się dużymi literami (np. FORTRAN). Proponowane wyróżnienia Autor może zaznaczyć w maszynopisie zwykłym ołówkiem za pomocą przyjętych znaków adjustacyjnych, np. podkreślenie linią przerywaną oznacza spacjowanie (rozstrzelenie), podkreślenie linią ciągłą – pogrubienie, podkreślenie wężykiem — kursywa.

Tekst powinien być napisany z podwójnym odstępem między wierszami, tytuły i podtytuły małymi literami. Marginesy z każdej strony powinny mieć około 35 mm. Wielkość czcionki wydruku powinna być zbliżona co najmniej co wielkości czcionki maszyny do pisania (minimum 12 punktów). Przy podziale pracy na rozdziały i podrozdziały cyfrowe ich oznaczenia nie powinny być większe niż II stopnia (np. 4.1.1.).

Sposób pisania tabel.

Tabele powinny być pisane na oddzielnych stronach. Tytuły rubryk pionowych i poziomych powinny być napisane małymi literami z podwójnym odstępem między wierszami. Przypisy (notki) dotyczące tabel należy pisać bezpośrednio pod tabelami. Tabele należy numerować kolejno liczbami arabskimi, u góry każdej tabeli podać tytuł dwujęzyczny. W pierwszej kolejności w podstawowej wersji językowej, a później w dodatkowej wersji językowej. Tabele umieścić na końcu maszynopisu. Przyjmowane są tabele algorytmów i programy na wydrukach komputerowych. W tym przypadku zachowany jest ich oryginalny układ. Tabele powinny być cytowane w tekście.

Sposób pisania wzorów matematycznych.

Rozmieszczenie znaków, cyfr, liter i odstępów powinno być zbliżone do rozmieszczenia elementów druku. Wskaźniki i wykładniki potęg powinny być napisane wyraźnie i być prawidłowo obniżone lub podwyższone w stosunku do linii wiersza podstawowego. Znaki nad literami i cyframi, całkami i in. symbolami (strzałki, linie, kropki, daszki) powinny być umieszczone dokładnie nad tymi elementami, do których się odnoszą. Numery wzorów cyframi arabskimi powinny być kolejne i umieszczone w nawiasach okrągłych z prawej strony. Nazwy jednostek, symbole literowe i graficzne powinny być zgodne z wytycznymi IEE (International Electronical Commision) oraz ISO (International Organization of Standarization).

Powołania.

Powołania na publikacje powinny być umieszczone na ostatnich stronach tekstu pod tytułem „Bibliografia", opatrzone numeracją kolejną bez nawiasów. Numeracja ta powinna być zgodna z odnośnikami w tekście artykułu. Przykłady opisu publikacji:

– periodycznej   1. F. Valdoni: A new milimetre wave satelite. E.T.T. 1990, vol. 2, no 5, pp. 141–148
– nieperiodyczne 2. K. Andersen: A resource allocation framework. XVI International Symposium, Stockholm (Sweden), may 1991, paper A 2,4
– książki   3. Y.P. Tvidis: Operation and modeling of the MOS transistors. New York, McGraw-Hill, 1987, p. 553

Materiały ilustracyjne.

Rysunki powinny być wykonane wyraźnie, na papierze gładkim lub milimetrowym w formacie nie mniejszym niż 9×12 cm. Mogą być także w postaci wydruku komputerowego (preferowany edytor Corel Draw). Fotografie lub diapozytywy przyjmowane są raczej czarno-białe w formacie nie przekraczającym 10×15 cm. Na marginesie każdego rysunku i na odwrocie fotografii powinno być napisane ołówkiem imię i nazwisko Autora oraz skrót tytułu artykułu, do którego są przeznaczone oraz numer rysunku. Spis podpisów pod rysunki i fotografie powinny być umieszczone na oddzielnej stronie. Podpisy pod rysunkami (fotografiami) powinny być dwujęzyczne: w pierwszej kolejności w podstawowej wersji językowej, a później w dodatkowej wersji językowej. Rysunki powinny być cytowane w tekście.

Uwagi końcowe.

Na odrębnej stronie powinny być podane następujące informacje:
– adres do korespondencji z kodem pocztowym (domowy lub do miejsca pracy),
– telefon domowy i/lub do miejsca pracy,
– adres e-mailowy (jeśli autor posiada).

Autorowi przysługuje bezpłatnie 20 odbitek artykułu. Dodatkowe egzemplarze odbitek, lub cały zeszyt Autor może zamówić u wydawcy na własny koszt.

Autora obowiązują korekta autorska, którą powinien wykonać w ciągu 3 dni od daty otrzymania tekstu z Redakcji oraz zwrócić osobiście lub listownie pod adres Redakcji. Korekta powinna być naniesiona na przekazanych Autorowi szpaltach na marginesach ew. na osobnym arkuszu w przypadku uzupełnień tekstu większych niż dwa wiersze. W przypadku nie zwrócenia korekty w terminie, korektę przeprowadza Redakcja Techniczna Wydawcy. Redakcja prosi Autorów o powiadomienie ją o zmianie miejsca pracy i adresu prywatnego.

KWARTALNIK
ELEKTRONIKI I TELEKOMUNIKACJI

ELECTRONICS AND
TELECOMUNICATIONS

QUARTERLY

SPIS TREŚCI – TOM 50/2004

SPIS TREŚCI DO TOMU 50 – 2004

Nr 1

Nr 2

Nr 3

Nr 4

(Zawiera referaty w języku angielskim z Konferencji MIKON 2004)

CONTENTS

Nr 1

Nr 2